Universidade do Porto

Faculdade de Engenharia

FEUP

Ductile Damage Prediction in Sheet Metal Forming and Experimental Validation

Dissertation presented to the Faculty of Engineering, University of Porto, as a requirement to obtain the Ph.D. degree in Mechanical Engineering, carried out under the supervision of Professor Abel Dias dos Santos, Assistant Professor, Faculty of Engineering, University of Porto, Professor José Manuel de Almeida César de Sá, Full Professor, Faculty of Engineering, University of Porto and Professor Francisco Manuel Andrade Pires, Associate Professor, Faculty of Engineering, University of Porto.

Pedro Manuel Cardoso Teixeira

Faculdade de Engenharia da Universidade do Porto

Porto

2010

Investigação financiada pela Fundação para a Ciência e a Tecnologia (Ministério da Ciência, Tecnologia e Ensino Superior) através da Bolsa de Doutoramento SFRH/BD/31341/2006, no âmbito do POS_C - Desenvolver Competências - Medida 1.2 e do QREN - POPH - Tipologia 4.1 - Formação Avançada (comparticipado pelo Fundo Social Europeu e por fundos nacionais do MCTES).

À minha família

"(...) it is sometimes difficult to select the proper model for a given application. The simplest is often the more efficient event, even if it is not the most accurate."

In: Jean Lemaitre
Handbook of Materials Behaviour Models, Academic Press, 2001

AGRADECIMENTOS

Ao Professor Doutor **Abel Dias dos Santos** desejo exprimir a minha sincera gratidão pela oportunidade concedida de trabalhar nesta área científica, através desta dissertação. A sua orientação, apoio e disponibilidade, e por fim, o seu espírito crítico na revisão minuciosa do presente texto foram fundamentais para a coerência e concretização desta dissertação.

Ao Professor Doutor **José Manuel de Almeida César de Sá** agradeço o incentivo e o seu esforço para proporcionar as melhores condições para a realização desta dissertação. Queria igualmente agradecer o apoio financeiro concedido para a participação em conferências, fundamental para a divulgação do trabalho realizado nesta dissertação.

Ao Professor Doutor **Francisco Manuel Andrade Pires** desejo agradecer a disponibilidade e auxílio prestado nas implementações numéricas. A sua revisão crítica do presente texto foi igualmente fundamental para a coerência do mesmo.

Ao **INEGI** - Instituto de Engenharia Mecânica e Gestão Industrial desejo agradecer, na pessoa do Presidente e Director do CETECOP - Unidade das Tecnologias de Conformação Plástica, Professor Doutor **Augusto Duarte Campos Barata da Rocha**, a disponibilidade de meios concedida durante a realização deste trabalho. As facilidades de acesso a diversas capacidades científicas e tecnológicas do INEGI tornaram possível a realização do trabalho experimental apresentado nesta dissertação.

A toda a minha família, os meus verdadeiros amigos, que sempre me apoiaram e incentivaram nas alturas mais difíceis, quero exprimir os meus profundos agradecimentos pela vossa compreensão e amizade ao longo desta caminhada. A vós dedico este trabalho.

À **Fundação para a Ciência e Tecnologia**, pelo apoio financeiro concedido através da Bolsa de Doutoramento SFRH/BD/31341/2006.

Finalmente, a todos os que directamente ou indirectamente contribuíram com o seu esforço e apoio na realização deste trabalho, o meu muito obrigado.

RESUMO

Os processos tecnológicos de conformação plástica de chapa são hoje correntemente utilizados em diversas áreas de produção. A complexidade crescente dos produtos, a constante redução dos ciclos de desenvolvimento e as tendências actuais de utilização de materiais mais leves e mais resistentes colocaram novos desafios aos processos de conformação plástica de chapa. Para fazer face a estes desafios, existe uma crescente aproximação ao conceito de produção virtual, e em particular ao uso da simulação numérica por elementos finitos. Nas últimas décadas, tem sido dedicado um extenso esforço no desenvolvimento destas ferramentas numéricas e no estabelecimento de modelos matemáticos que permitam modelar o comportamento da chapa quando sujeita ao processo de conformação plástica. Um dos desafios principais está relacionado com a previsão da ocorrência de rotura, especialmente importante para a nova classe de materiais mais leves e mais resistentes. A presente dissertação pretende ser uma contribuição para a melhoria e desenvolvimento de modelos de previsão de rotura em processos de conformação plástica de chapas metálicas, no âmbito da teoria da Mecânica do Dano Contínuo. São introduzidas as definições escalar e de ordem superior para a variável de dano e são desenvolvidos os modelos constitutivos correspondentes, seguindo uma formulação termodinamicamente consistente. É dedicada uma atenção especial aos aspectos computacionais da implementação numérica dos modelos constitutivos desenvolvidos e aos temas relacionados com a sua integração num programa de elementos finitos comercial. Para avaliar o desempenho da estratégia proposta, foram realizados vários testes numéricos e os ensaios experimentais correspondentes de modo a determinar a precisão dos modelos propostos na previsão de rotura. Com o objectivo de determinar o evento mais restritivo no processo de conformação plástica de chapas metálicas, estricção ou rotura, é proposta uma abordagem conjunta entre um critério de instabilidade e um modelo de dano. O algoritmo para a integração numérica do modelo é descrito e a importância da abordagem é ilustrada por intermédio da comparação dos resultados numéricos com resultados experimentais obtidos por outros autores.

Palavras-Chave: Dano dúctil; Conformação Plástica; Modelação Numérica; Rotura; Instabilidade plástica.

ABSTRACT

Sheet metal forming processes are widely used in several production areas. The growing complexity of the products, the shortening of development cycles and the actual trends of using lighter and higher strength materials has placed new challenges to the sheet metal forming processes. To face these challenges, a successive approach to virtual production has arisen, namely to finite element numerical simulation. In last decades, an extensive effort has been dedicated in the development of these numerical tools and in the establishment of mathematical models that allow a better modelling of sheet metal behaviour under plastic deformation. One key challenge is related with failure prediction, especially important for the new class of lighter and more resistant materials. The present dissertation intends to provide a contribution in the improvement and development of reliable failure prediction models for the simulation of metal forming processes, within Continuum Damage Mechanics theory. Scalar and high-order definitions for the damage variable are introduced and the derivation of corresponding constitutive models is addressed, following a thermodynamically consistent framework. Particular attention is devoted to the computational issues of the numerical implementation of derived constitutive models and to aspects related to its integration into a commercial finite element code. To evaluate the performance of the proposed framework, several numerical tests and corresponding experimental testings were carried out in order to assess the robustness and accuracy of the proposed models in the failure prediction in sheet metal forming processes. With the aim of determining the most restrictive event in sheet metal forming, necking or fracture, an integrated approach between an instability criterion and a damage model is proposed. The algorithm for numerical integration of the model is addressed and the importance of the coupled approach is illustrated by means of a comparison with experimental results obtained by other authors.

Keywords: Ductile damage; Sheet Metal Forming; Numerical modelling; Failure; Plastic instability.

RÉSUMÉ

Les procédés de mise en forme de tôles minces sont largement utilisés dans plusieurs areas de la production. La complexité croissante des produits, la diminution des cycles de développement et les tendances actuelles de l'utilisation de matériaux plus légers et plus résistants ont engendré de nouveaux défis pour les procédés de mise en forme de tôles minces. Pour affronter ces défis, il ya un approchement à la notion de production virtuelle, et, particulièrement, à la utilisation de la simulation numérique par éléments finis. Dans les dernières décades, un grand effort a été consacré au développement de ces outils numériques et a l'établissement de modèles mathématiques qui permettent un meilleur modelage du comportement de la tôle sous déformation plastique. Un des principaux défis se rapporte à la prévision de la survenue de rupture, particulièrement important pour la nouvelle classe de matériaux plus légers et plus résistants. Cette dissertation aspire de offrir une contribution à l'amélioration et le développement de modèles de prévision de rupture en la simulation de procédés de mise en forme, en vertu de la théorie de la mécanique des l'endommagent continu. Les définitions scalaire et tensorielle pour la variable d'endommagement sont introduites et les modèles de comportement correspondants sont développés, à la suite d'une formulation thermodynamique cohérente. C'en porte une spéciale attention aux aspects de mise en œuvre du calcul numérique des modèles de comportement développés et aux questions liées à son intégration dans un programme commercial d'éléments finis. Pour évaluer la performance de la stratégie proposée, ont été effectuées plusieurs tests numériques et des essais expérimentaux correspondants pour déterminer l'exactitude des modèles proposés pour prédire la rupture. Afin de déterminer l'événement plus restrictif dans les procédés de mise en forme de tôles minces, striction ou rupture, on propose une approche commune entre un critère d'instabilité et un modèle d'endommagement. L'algorithme d'intégration numérique du modèle est décrit et l'importance de l'approche est illustrée par la comparaison des résultats numériques avec les résultats expérimentaux obtenus par d'autres auteurs.

Mots-clés: Endommagement ductile; Mise en forme; Modélisation numérique; Rupture; Instabilité plastique.

CONTENTS

AGRADECIMENTOS v

RESUMO vii

ABSTRACT ix

RÉSUMÉ xi

CONTENTS xiii

1. INTRODUCTION 1
  - 1.1 Motivation 1
  - 1.2 Scope and layout of the thesis 6

2. TOPICS IN CONTINUUM MECHANICS AND THERMODYNAMICS 9
  - 2.1 Kinematics of deformation and strain measures 9
  - 2.2 Forces and stress measures 15
  - 2.3 Fundamental laws of thermodynamics 19
    - 2.3.1 Conservation of mass 19
    - 2.3.2 Momentum balance 19
    - 2.3.3 The first principle 20
    - 2.3.4 The second principle 20
    - 2.3.5 The Clausius–Duhem inequality 20
  - 2.4 Constitutive theory 21
    - 2.4.1 Constitutive axioms 21
    - 2.4.2 Thermodynamics with internal variables 23
    - 2.4.3 Phenomenological and micromechanical approaches 26
    - 2.4.4 The purely mechanical theory 27
    - 2.4.5 The constitutive initial value problem 27
  - 2.5 Weak equilibrium. The principle of virtual work 28

3. FINITE ELEMENT METHOD 29
3.1 Definition of the initial boundary value problem 29
3.2 Spatial discretization of initial boundary value problem 30
3.3 Time integration and incremental solution procedures 32
3.3.1 Explicit dynamic finite element solution strategy 34
3.4 Local integration of constitutive equations 38
3.5 Contact with friction modelling 41

4. ISOTROPIC DAMAGE MECHANICS 45
4.1 Introduction 45
4.2 Physical aspects of internal damage in solids 46
4.3 Continuous Damage Mechanics developments 47
4.3.1 Original developments 47
4.3.2 Ductile damage 50
4.4 Lemaitre's elasto-plastic isotropic damage theory 53
4.4.1 State potential and state relations 53
4.4.2 Dissipation potential and associated evolution equations 56
4.4.3 Damage threshold 59
4.4.4 Critical damage criterion 59
4.4.5 Computational aspects 60
4.5 Elasto-plastic isotropic damage model with anisotropic flow 60
4.5.1 Constitutive model 61
4.5.2 Integration algorithm 63
4.6 Simplified elasto-plastic isotropic damage model with crack closure 70
4.6.1 Crack closure effect definition 71
4.6.2 Tensile / compressive split of stress tensor 72
4.6.3 Crack closure effect on damage evolution 73
4.6.4 Simplified integration algorithm 74
4.7 Remarks on non-local formulations 79

5. ANISOTROPIC DAMAGE MECHANICS 81
5.1 Introduction. Higher-order nature of damage variables 81
5.2 Physical interpretation of a second order damage variable 83
5.3 Coupled elasto-plastic anisotropic damage theory 86
5.3.1 The constitutive model 87
5.3.2 Integration algorithm 95
5.4 Sensitivity analysis of anisotropic damage model 102
5.4.1 Influence of damage evolution law parameters 102
5.4.2 Influence of hardening parameters 105
5.4.3 Influence of normal anisotropy 107

6. APPLICATION OF DAMAGE TO FAILURE PREDICTION 111
6.1 Tensile test 111
6.1.1 Numerical modelling 118
6.1.2 Results and discussion 119
6.2 Bulge test 122
6.2.1 Numerical modelling 124
6.2.2 Results and discussion 125
6.3 U shape geometry 130
6.3.1 Experimental failure 130
6.3.2 Numerical modelling 131
6.3.3 Results and discussion 131
6.4 Warping geometry 136
6.4.1 Experimental failure 136
6.4.2 Numerical modelling 137
6.4.3 Results and discussion 137
6.5 Axisymmetric cup 141
6.5.1 Experimental failure 142
6.5.2 Numerical modelling 142
6.5.3 Results and discussion 143
6.6 Cross shape geometry 152
6.6.1 Experimental failure 152
6.6.2 Numerical modelling 153
6.6.3 Results and discussion 154
6.7 Concluding remarks 160

7. APPLICATION OF DAMAGE TO NECKING OCCURENCE 163
7.1 Introduction 163
7.2 Forming limit diagrams modelling review 166
7.2.1 Hill's localized necking criterion 167
7.2.2 Swift's diffuse necking criterion (MFC) 169
7.2.3 Marciniak-Kuczynski analysis (M-K analysis) 172
7.2.4 Modified maximum force criterion (MMFC) 176
7.2.5 Other theoretical methods of necking prediction 180
7.3 Forming limit calculation with damage consideration review 181
7.4 Proposed damage-coupled criterion (MMFC+AD) 184
7.5 Application of MMFC+AD for forming limit diagrams prediction 187
7.6 Concluding remarks 199

8. CONCLUSION AND FINAL REMARKS 201
8.1 General conclusions 201
8.2 Future work 204

NOTATION, NOMENCLATURE AND ABBREVIATIONS 205
- List of symbols 205
- List of abbreviations 209

LIST OF FIGURES 211

LIST OF TABLES 215

LIST OF BOXES 217

REFERENCES 219

1. INTRODUCTION

This chapter establish the overall framework of the problems associated with the numerical simulation of metal forming processes, emphasizing on aspects such as the technological challenges and industrial interest. The objectives for the work developed in this thesis, based on the described challenges, are defined. The structure and contents of this dissertation, in order to guide the reader and to assist the consultation, are also presented.

1.1 Motivation

Metal forming processes are characterized by the ability to obtain mechanical parts with high production rates with a minimum waste of material (near net-shape technology). Moreover, it is their high production rates that make these processes especially suitable for the production of components on a large scale. Among these technological processes, we may include those for making sheet metal parts. Terms like deep drawing, press working and press forming are used commonly in industry to describe general sheet forming operations, since they are performed usually on presses using a set of dies. Typically, a deep drawing operation implies the presence of three main components: a punch, a die and a blank holder. The principle of the process is illustrated in Figure 1.1.

The punch moves towards an initially flat metal sheet and deforms it in order to achieve a desired shape. The blank holder transfers an external force to the metal sheet, preventing wrinkling and allowing the control of the flow of the material. The two principal deformation modes in this process may depend directly on the blank holder action and its corresponding force. In the example presented in Figure 1.1, a tool used to draw an axisymmetric part is shown. However, deep drawing is also used to produce complex geometry parts, and, for some products and due to its inherent complexity, several deep drawing stages may be required to obtain a single final product, using several tool sets, one for each stamping stage.

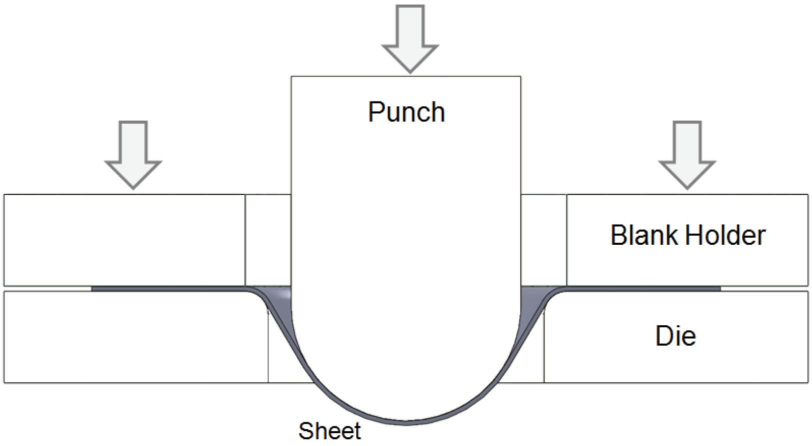

Figure 1.1 Deep drawing process.

Sheet metal forming processes are used in several production areas and industries such as automotive, household appliances (washing machines, refrigerators, grills, stoves, etc.), domestic and decorative elements (bathtubs, dishwashers, containers, lamps, LPG cylinders, etc.), electrical and electronics (switches, computer and lamp socket components, etc.), food utensils (cookware, tableware, lids, trays, etc.), aerospace, ships, etc.

Current trends in these industries may be characterized by the flexibility and increasing complexity of products due to the demands imposed by the market. The strong competition among several producers coupled with increasing shortening of product life requires a rapid development of economic and high quality products, demanding a high flexibility for changes in design in order to fulfil the imposed innovation on such products [Yang 2002].

This reduction in development time cycle has left an extremely short period to the design of new tools and their correction and tuning. Typically, it takes many cycles and several costly trial-and-error stages in the development phase using prototype tools. The time consumption and press shop equipment occupation, needed for production, increase these development costs, compromising the necessary reduction in product-to-market cycle.

Among the industries that make use of sheet metal forming technology, we may emphasize the automotive industry due to its large production volumes and high variety of stamped components. The economic significance of this industry in developed countries associated with the strong competition among many producers creates vitality for the development of several knowledge areas including metal forming technologies.

Current main concerns in the automotive industry include environmental protection issues, fuel economy and safety specifications. The overall strategy incorporates the reduction of total vehicle weight, thus permitting to achieve better performances and fuel consumption reductions as well as decreasing greenhouse gas emissions. At the same time, the passenger's safety must be continuously improved by addressing increasingly demanding safety specifications imposed by legislation. All these requirements have forced a policy of low weight concepts and structures prepared to withstand impacts [Pickett 2004], making use of lighter and / or more resistant materials.

However, the trend is not to have a single approach on the use of materials. The light, safe, clean and financially accessible car follows a multi-material concept, where different materials are used in body-in-white components of the vehicle, depending on the required strength for the part. The concept includes mild steels (MS), aluminium alloys (AA), conventional high strength steels (HSS) and advanced high strength steels (AHSS) such as dual phase steels (DP), transformation induced plasticity steels (TRIP) and martensitic steels (MS) [IISI 2006]. The introduction of new materials in the automobile industry has brought new challenges for metal forming technologies. The behaviour observed with conventional steels does not apply to these new materials and the empirical knowledge acquired over the years with conventional steels cannot be extrapolated to these new alloys, being needed the definition of new operating conditions.

These factors combined with the growing complexity of deep drawing technology led to a successive approximation to the virtual production concepts, in particular, the numerical simulation of metal forming processes by the finite element method and the extension of its use throughout all the production chain [Roll 2002].

The numerical simulation of metal forming has, therefore, assumed a vital role in satisfying the industry needs. The interest shown in these methods by the industry is evident: it allows to virtually validate a forming tool, reducing (or even replacing) the experimental tests on press, thus reducing the time-to market for new products and consequently the costs involved in its development. Still, the contribution of numerical simulation can go further, rather than being only confined to the simulation of the metal forming process and the validation of the manufacturability of the part. The optimization of the entire chain of production through the numerical simulation, starting from the raw material up to the final product, passing through assembling steps, aiming a cost reduction in each stage, can lead to significant gains in both economic and technical terms, crucial in the current highly competitive market. To achieve these higher objectives, several requirements are imposed to the numerical simulation [Makinouchi 2001]:

- Simulation of all plastic forming process including stamping, cutting and folding;
- Reliability of numerical results in the prediction of forming defects including springback, wrinkling and fracture;
- Applicability to the wide variety of products produced by metal forming;
- Use of different materials such as mild steels, aluminum alloys, high strength steels and advanced high strength steels;
- Obtaining results in reasonable time.

An extensive effort has been devoted over the last decades in the development of the numerical simulation codes focusing on the fulfilment of these requirements. Several areas are currently subject of intense research in order to approximate numerical simulation results to experimental reality: mechanical behaviour of materials and the establishment of constitutive laws to describe it, optimization of existing simulation codes, tribological aspects related to sheet / tool contact and the corresponding modelling, among others. The integration and interaction of information and developments collected in all these areas (extremely difficult) makes it possible the prediction of forming defects in the early stages of product development. The typical forming defects may range from small dimensional defects to extremely evident defects such as cracks and rupture. According to Lange [1985], forming defects can be classified into three distinct classes: dimensional defects, surface defects and defects related with unsatisfactory final mechanical properties. Other criteria such as aesthetic defects vs. functional defects or causes that originated them are also used to establish a distinction between different defects. A particularly broad criterion was proposed by Ajmar *et al.* [2001] that sets a differentiation between global and local defects. A defect is considered as a global defect if affects all the stamped part. A local defect is any defect that is limited to a restricted area of the part. This classification seems more appropriate to classify all forming defects, and can be applied to all types of defects, either aesthetic or functional, and can even be applied to defects for which the cause is unknown or is not perfectly defined. Following this classification, a list and classification of typical forming defects are presented in Table 1.1.

Traditionally, the major challenge was raised by the forming defects that were affecting the final geometry of the stamped part, namely the prediction of global defects related to springback [Santos 2008]. However, in the last years, fracture has assumed a prominent position. This trend is directly connected with the use of new materials, especially the Advanced High Strength Steels (AHSS), which present a distinct mechanical behaviour, for which there is a smaller experience and prediction capability.

Table 1.1 Typical forming defects classification.

Forming defect	**Global**	**Local**
Twisting	●	
3D Springback	●	
Wrinkles	●	●
2D Springback		●
Surface deflection	●	●
Excessive thinning		●
Rupture / cracks		●
Marks		●
Spoilers		●

The application of these materials is intimately related with the obvious advantages that those materials can offer in terms of yield stress and tensile strength when compared to deep-drawing quality mild steels and conventional high-strength steels (HSS), as shown in Figure 1.2 [IISI 2006]. Their advantageous mechanical properties allow to produce lighter and more resistant components through the use of thinner sections, thus reducing the total structure weight and, in some cases, also allow the reduction of the number of components.

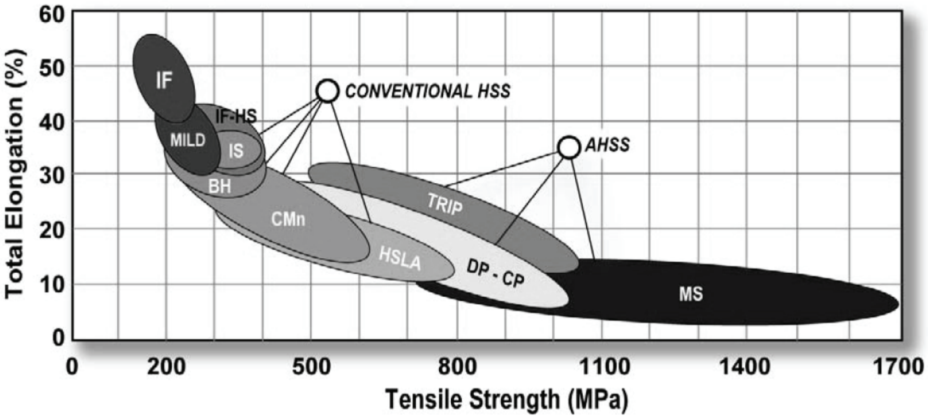

Figure 1.2 Different types of steels and their mechanical characteristics: Advanced high strength steels (AHSS) compared to mild steels (MS) and low-resistance and conventional high-strength steels (HSS).

But, these advantages in terms of weight, strength and stiffness of such components must be balanced with their lower ductility and premature rupture during processing. Fractures that rarely occurred a decade ago in resistance testings of the components, have become frequent with the AHSS steels due to their lower ductility and its higher work hardening when compared with conventional steels. In these materials, failure often occurs before any necking occurrence and, therefore, without any notice, as seen in Figure 1.3.

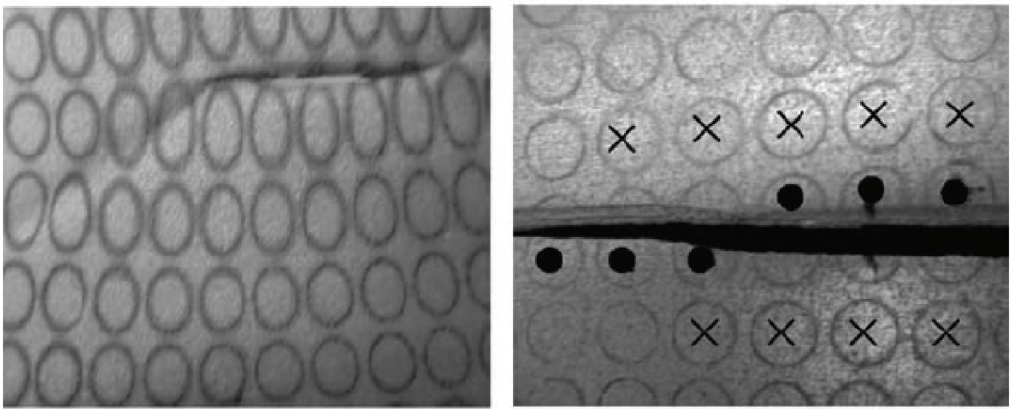

Figure 1.3 Localized necking prior to the rupture in a DP600 steel (left) and fracture without any visible necking in a DP980 steel (right) [Shi 2006].

This behaviour raises questions to the applicability of conventional methods to assess forming limits, such as the well-established forming limit diagram (FLD) concept, which is defined for the occurrence of localized necking.

Therefore, the theoretical analysis of plastic instability and the initiation of fracture is of paramount importance for these materials in order to determine forming limits either by necking onset or by premature fracture occurrence. To model fracture initiation, a successive approximation is observed to theories that consider material inhomogeneities and describe the mechanism of internal damaging in ductile materials, either by using a micromechanics-based formulation [Gurson 1977] or a Continuous Damage Mechanics approach [Lemaitre 1985a]. The current trend for the failure prediction in forming simulations is to attempt the replacement of the common use of FLDs by a generalized incremental stress state dependent damage model, able to account for load-path dependent failure behaviour and to provide reliable prediction of the stress and strain histories, indispensable for predicting the onset of fracture in metals [Roll 2008].

1.2 Scope and layout of the thesis

The driven-force of this thesis is the ability enhancement of numerical codes for failure prediction in metal forming processes by the development of more advanced numerical models based on the Continuum Damage Mechanics theory. Therefore, the main objective of the present work is to contribute to the improvement and development of reliable failure prediction models for the simulation of sheet metal forming processes, emphasizing issues related to continuum modelling as well as to the computational aspects relevant to the application of the proposed models in large scale numerical simulations in explicit time integration schemes.

In order to face this main goal, this thesis is divided into eight chapters. After this introductory one, Chapter 2 sets out the basic concepts of continuum mechanics and thermodynamics which form the basis for the constitutive model developments in the subsequent chapters. Also, with an introductory nature, the principles of finite element methods are introduced in Chapter 3.

Chapter 4 deals with the isotropic damage mechanics theory. A review of the basic concepts of internal damage in solids is provided and the developments under the Continuum Damage Mechanics theory are reviewed concerning different state and dissipation couplings. The original isotropic damage model proposed by Lemaitre [1985a] is presented and an enhancement of the model is introduced by the inclusion of plastic anisotropy described by the Hill48 criterion. A simplified partial coupling algorithm is proposed, which allows introducing additional effects without increasing dramatically the analysis time, namely the quasi-unilateral effect on damage evolution.

Chapter 5 introduces anisotropic damage mechanics. A review of higher order damage variables used to describe internal damage state of the material is presented and the physical interpretation of a second-order representation is provided. Using this latter definition, the thermodynamically consistent anisotropic damage model proposed by Lemaitre *et al.* [2000a] is described and its implementation into a commercial finite element code is addressed, also considering plastic anisotropic behaviour, as previously done for the isotropic damage theory. A sensitivity analysis of the implemented model is presented regarding the influence of several parameters on damage evolution and mechanical properties degradation.

Chapter 6 is mainly devoted to a qualitative validation of the implemented damage models and a discussion of the obtained results. Some basic classical testings and complex applications are considered in order to evaluate the performance of the models in the prediction of the ductile damage and failure that is expected to occur during metal forming processes. Intrinsically, a complete characterization of adopted damage models is achieved aiming to propose a methodology to virtually reproduce (or simulate) metal forming processes in order to predict when and where ductile failure will take place inside the stamped part.

Chapter 7 introduces a new criterion for forming limits prediction based on an integrated approach between the presented anisotropic damage model and the necking criterion proposed by Hora *et al.* [1996], combining the determination of the onset of the two last phases of plastic deformation: necking and failure. A review on forming limit diagrams modelling is provided and the most important criteria are presented.

The importance of the proposed coupled approach is shown by providing improved prediction in necking occurrence and allowing to determine which phenomenon, necking or failure, is the most restrictive event in a sheet metal forming operation, especially important in materials where fracture can occur before required conditions for necking are achieved.

Chapter 8 summarizes the main issues addressed in the thesis and cast the general conclusions of this work, along with suggestions for future research.

2. TOPICS IN CONTINUUM MECHANICS AND THERMODYNAMICS

This chapter reviews some basic concepts of mechanics and thermodynamics of continuous media. The objective is not to enter in full detail on the subjects, but to focus precisely on the points that have been employed and implemented throughout this work. The definitions and notation introduced will be systematically employed throughout the subsequent chapters of this thesis. The material presented here is well established in the continuum mechanics literature [Lemaitre 1994] [Simo 1998] [Doghri 2000] [Souza Neto 2008] and an effort has been made to follow the notation and nomenclature used in standard textbooks.

2.1 Kinematics of deformation and strain measures

Consider a body $\mathcal{B}$ embedded in the three dimensional Euclidian space $\mathbb{R}^3$ in its reference (undeformed) configuration with boundary $\partial\mathcal{B}$ as represented in Figure 2.1 [Souza Neto 2008]. Each material particle $\boldsymbol{p}$ can be labelled by its position in the orthogonal basis $\boldsymbol{E}_i$. In its current (deformed) configuration, $\mathcal{B}$ occupies the region $\boldsymbol{\varphi}\left(\mathcal{B}\right)$ defined by the deformation map $\boldsymbol{\varphi}$. The corresponding current position of particle $\boldsymbol{p}$ can be defined as [Souza Neto 2008]:

$$\boldsymbol{x} = \boldsymbol{\varphi}\left(\boldsymbol{p}\right). \tag{2.1}$$

This description based on material coordinates is known as Lagrangian description. The corresponding vector field, which is the displacement, is defined by:

$$\boldsymbol{u}\left(\boldsymbol{p}\right)=\boldsymbol{\varphi}\left(\boldsymbol{p}\right)-\boldsymbol{p} \tag{2.2}$$

and, thus, one may write that:

$$\boldsymbol{x}=\boldsymbol{p}+\boldsymbol{u}\left(\boldsymbol{p}\right). \tag{2.3}$$

Due to the physical meaning of $\boldsymbol{x}$ and $\boldsymbol{p}$ and by the fact that map $\boldsymbol{\varphi}\left(\cdot\right)$ is a one-to-one relation, deformation map can be uniquely inverted:

$$\boldsymbol{p}=\boldsymbol{\varphi}^{-1}\left(\boldsymbol{x}\right) \tag{2.4}$$

where $\boldsymbol{\varphi}^{-1}$ is called reference map. This description, based on spatial coordinates, is known as Eulerian description.

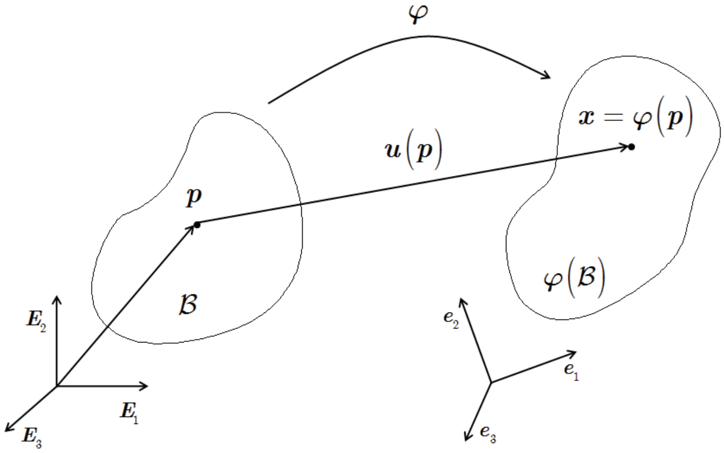
φ
$\boldsymbol{u}(\boldsymbol{p})$
$\boldsymbol{x}=\varphi(\boldsymbol{p})$
$\boldsymbol{p}$
$\mathcal{B}$
$\varphi(\mathcal{B})$
$\boldsymbol{E}_2$
$\boldsymbol{E}_1$
$\boldsymbol{E}_3$
$\boldsymbol{e}_2$
$\boldsymbol{e}_1$
$\boldsymbol{e}_3$

Figure 2.1 Configurations of a deformable body.

Now, consider an infinitesimal vector $d\boldsymbol{p}$ in the reference configuration. This infinitesimal vector $d\boldsymbol{p}$ is transformed to its deformed state $d\boldsymbol{x}$, by the deformation gradient $\boldsymbol{F}$, as:

$$d\boldsymbol{x}=\boldsymbol{F}d\boldsymbol{p}\Leftrightarrow\boldsymbol{F}=\frac{d\boldsymbol{x}}{d\boldsymbol{p}} \tag{2.5}$$

or, alternatively, due to relation shown in Equation (2.3), deformation gradient can also be written as:

$$\boldsymbol{F}=\boldsymbol{I}+\nabla\boldsymbol{u} \tag{2.6}$$

where $\nabla\boldsymbol{u}$ represents the gradient of displacement field.

Consider, now, an infinitesimal volume inside body $\mathcal{B}$, defined by the infinitesimal vectors $d\boldsymbol{a}$, $d\boldsymbol{b}$ and $d\boldsymbol{c}$. In the reference configuration, volume is expressed by:

$$dV_0=\left(d\boldsymbol{a}\times d\boldsymbol{b}\right)\cdot d\boldsymbol{c}. \tag{2.7}$$

By applying the deformation gradient to the infinitesimal vectors, the deformed infinitesimal volume, denoted as dV, becomes:

$$dV = \left(\boldsymbol{F}d\boldsymbol{a} \times \boldsymbol{F}d\boldsymbol{b}\right) \cdot \boldsymbol{F}d\boldsymbol{c}\,. \tag{2.8}$$

Making use of tensor algebra, it follows that:

$$\frac{dV}{dV_0} = \frac{\left(\boldsymbol{F}d\boldsymbol{a} \times \boldsymbol{F}d\boldsymbol{b}\right) \cdot \boldsymbol{F}d\boldsymbol{c}}{\left(d\boldsymbol{a} \times d\boldsymbol{b}\right) \cdot d\boldsymbol{c}} = \det \boldsymbol{F} = J \tag{2.9}$$

where J denotes the determinant of $\boldsymbol{F}$, representing, locally, the volume after deformation per unit reference volume [Pires 2005]. In order to have a physically acceptable situation, in any deformation of a body, J must be always greater than zero (otherwise infinitesimal volume would collapse into a point).

The deformation gradient relates, therefore, quantities before deformation to quantities after deformation and provides a complete description of deformation including stretch as well as rigid body rotations. As rigid body rotations do not contribute for size and shape change of body $\mathcal{B}$, it is imperative to decompose the deformation gradient $\boldsymbol{F}$ into stretch and rotation components [Pires 2005]. By applying the polar decomposition theorem, schematically represented in Figure 2.2, to the deformation gradient $\boldsymbol{F}$, one obtains:

$$\boldsymbol{F} = \boldsymbol{R}\boldsymbol{U} = \boldsymbol{V}\boldsymbol{R} \tag{2.10}$$

where $\boldsymbol{U}$ is the right stretch tensor and $\boldsymbol{V}$ is the left stretch tensor. The tensor $\boldsymbol{R}$ is the local orthogonal rotation tensor and connects both configurations, reference and deformed configurations.

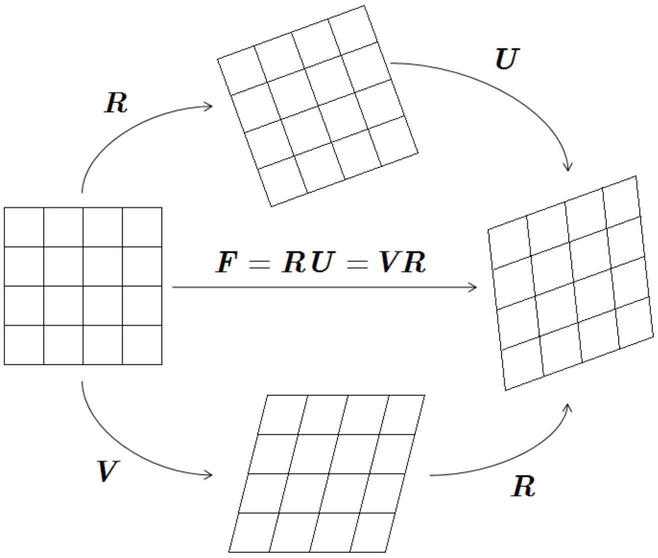

Figure 2.2 Schematic representation of the polar decomposition theorem.

The two stretch tensors, $\boldsymbol{U}$ and $\boldsymbol{V}$, represent, in fact, measures of stretch itself since they only contain the stretch part of the deformation gradient. Therefore, polar decomposition is extremely important in the definition of strain measures, i.e., to define and quantify the change of distance between two particles between reference and deformed configurations. Before introducing strain measures, let us define the right and left Cauchy-Green stretch tensors $\boldsymbol{C}$ and $\boldsymbol{b}$, respectively given by:

$$\boldsymbol{C} = \boldsymbol{U}^2 = \boldsymbol{F}^T\boldsymbol{F}\,,\ \boldsymbol{b} = \boldsymbol{V}^2 = \boldsymbol{F}\boldsymbol{F}^T. \tag{2.11}$$

Based on the right Cauchy-Green stretch tensor $\boldsymbol{C}$, one can define an important family of strain measures, the Lagrangian strain tensors $\boldsymbol{E}$. The most particular member of this family is the Green-Lagrange tensor, which is obtained as:

$$\boldsymbol{E}^{(2)} = \frac{1}{2}\left(\boldsymbol{U}^2 - \boldsymbol{I}\right) = \frac{1}{2}\left(\boldsymbol{F}^T\boldsymbol{F} - \boldsymbol{I}\right). \tag{2.12}$$

Based on the left stretch tensor $\boldsymbol{b}$, the Eulerian counterpart of the Lagrangian family tensors, denoted by $\boldsymbol{\varepsilon}$, are defined as:

$$\boldsymbol{\varepsilon}^{(m)} = \begin{cases} \dfrac{1}{m}\left(\boldsymbol{V}^m - \boldsymbol{I}\right) & m \neq 0 \\ \ln\left[\boldsymbol{V}\right] & m = 0 \end{cases} \tag{2.13}$$

where m is a real number and $\ln\left[\cdot\right]$ denotes the tensor logarithm of $\left[\cdot\right]$. Both Lagrangian and Eulerian strain tensors are related by:

$$\boldsymbol{\varepsilon}^{(m)} = \boldsymbol{R}\boldsymbol{E}^{(m)}\boldsymbol{R}^T \tag{2.14}$$

where $\boldsymbol{R}$ is a local rotation.

So far, all these quantities were considered time-independent. However, many plasticity formulations are developed in terms of rate quantities [Dunne 2005], even the rate-independent plasticity models. Thus, it is important to consider a time-dependent deformation of body $\mathcal{B}$, also called as motion. In this case, a deformation map $\boldsymbol{\varphi}\left(\bullet, t\right)$ defines the deformation of $\mathcal{B}$ for each time t. Due to the time dependence of the motion, one can define velocity and acceleration of particle $\boldsymbol{p}$ as being the first and second derivatives with respect to time as:

$$\dot{\boldsymbol{x}}\left(\boldsymbol{p}, t\right) = \frac{\partial \boldsymbol{\varphi}\left(\boldsymbol{p}, t\right)}{\partial t};\ \ddot{\boldsymbol{x}}\left(\boldsymbol{p}, t\right) = \frac{\partial^2 \boldsymbol{\varphi}\left(\boldsymbol{p}, t\right)}{\partial^2 t}, \tag{2.15}$$

or, using an Eulerian description as:

$$\boldsymbol{v}\left(\boldsymbol{x}, t\right) = \frac{\partial \boldsymbol{\varphi}^{-1}\left(\boldsymbol{x}, t\right)}{\partial t};\ \boldsymbol{a}\left(\boldsymbol{x}, t\right) = \frac{\partial^2 \boldsymbol{\varphi}^{-1}\left(\boldsymbol{x}, t\right)}{\partial^2 t} \tag{2.16}$$

where $\boldsymbol{v}$ and $\boldsymbol{a}$ are the spatial description of the velocity field and acceleration field, respectively.

Considering a spatially varying velocity field $\boldsymbol{v}$, it is also possible to calculate its spatial rate of change, given by the derivative of the velocity with respect to spatial coordinates as:

$$\boldsymbol{l} = \nabla_x \boldsymbol{v} \tag{2.17}$$

where $\boldsymbol{l}$ is called the velocity gradient tensor. Considering the derivative of the deformation gradient $\boldsymbol{F}$ with respect to time and applying the derivative chain rule, one may equivalently write that:

$$\boldsymbol{l} = \dot{\boldsymbol{F}}\boldsymbol{F}^{-1}. \tag{2.18}$$

Therefore, velocity gradient maps the deformation gradient onto its rate of change. The velocity gradient tensor can be further decomposed into a symmetric tensor, $\boldsymbol{d}$, called rate of deformation tensor or stretching tensor and a skew-symmetric tensor, $\boldsymbol{w}$, called continuum spin or vorticity tensor, defined as:

$$\boldsymbol{d} = \operatorname{sym}\left(\boldsymbol{l}\right) = \frac{1}{2}\left(\boldsymbol{l} + \boldsymbol{l}^T\right);\ \boldsymbol{w} = \operatorname{skew}\left(\boldsymbol{l}\right) = \frac{1}{2}\left(\boldsymbol{l} - \boldsymbol{l}^T\right). \tag{2.19}$$

Another definition is the skew-symmetric tensor $\boldsymbol{\Omega}$, also called angular velocity tensor. This tensor derives from tensor $\boldsymbol{w}$ and defines only the rigid body rotation and its rate of change and is independent of the stretch. The angular velocity tensor is given by the expression:

$$\boldsymbol{\Omega} = \dot{\boldsymbol{R}}\boldsymbol{R}^T. \tag{2.20}$$

The importance of this tensor will be shown in the definition of stress rates. Further decomposition of the deformation gradient $\boldsymbol{F}$ can be performed, using the classical multiplicative decomposition theorem.

Consider, again, a generic body $\mathcal{B}$ embedded in the three dimensional Euclidian space $\mathbb{R}^3$ in its reference (undeformed) configuration, containing an infinitesimal vector $d\boldsymbol{p}$, and the same body in its current (deformed) configuration, and the corresponding deformed infinitesimal vector $d\boldsymbol{x}$ as seen in Figure 2.3 [Dunne 2005]. Additionally, consider an intermediate fictitious configuration of body $\mathcal{B}$, corresponding to a stress-free state which infinitesimal vector $d\boldsymbol{p}$ has undergone only purely plastic deformation to become $d\boldsymbol{X}$. The transformation mapping of $d\boldsymbol{p}$ to $d\boldsymbol{X}$ is the plastic deformation gradient so that [Dunne 2005]:

$$d\boldsymbol{X} = \boldsymbol{F}^p d\boldsymbol{p} \tag{2.21}$$

and the plastic deformation gradient is defined as:

$$\boldsymbol{F}^p = \frac{d\boldsymbol{X}}{d\boldsymbol{p}}. \tag{2.22}$$

Considering the current configuration $d\boldsymbol{X}$, the transformation map of $d\boldsymbol{X}$ to $d\boldsymbol{x}$ is the elastic deformation tensor $\boldsymbol{F}^e$ given by:

$$\boldsymbol{F}^e = \frac{d\boldsymbol{x}}{d\boldsymbol{X}}. \tag{2.23}$$

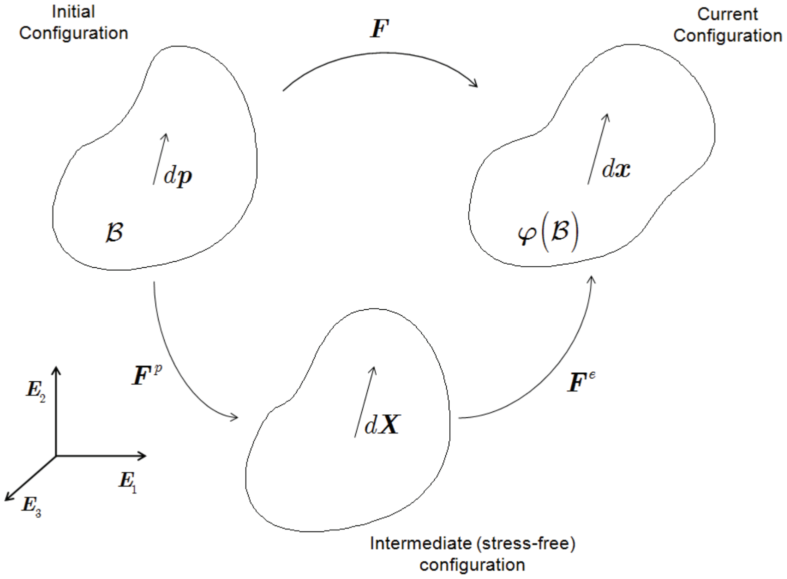
Initial Configuration
$\boldsymbol{F}$
Current Configuration
$d\boldsymbol{p}$
$\mathcal{B}$
$d\boldsymbol{x}$
$\varphi(\mathcal{B})$
$\boldsymbol{E}_2$
$\boldsymbol{F}^p$
$\boldsymbol{F}^e$
$d\boldsymbol{X}$
$\boldsymbol{E}_1$
$\boldsymbol{E}_3$
Intermediate (stress-free) configuration

Figure 2.3 Schematic representation of the multiplicative decomposition theorem.

Thus, one may write:

$$d\boldsymbol{x} = \boldsymbol{F}^e d\boldsymbol{X} = \boldsymbol{F}^e \boldsymbol{F}^p d\boldsymbol{p}, \tag{2.24}$$

and, therefore:

$$\boldsymbol{F} = \boldsymbol{F}^e \boldsymbol{F}^p \tag{2.25}$$

being this relation the classical multiplicative decomposition of the deformation gradient, into its elastic and plastic components. Using this decomposition, both the elastic and plastic deformation gradients may contain stretch and rigid body rotation resulting in a non-uniqueness intermediate configuration. By convention, and in order to achieve a unique intermediate configuration, rigid body rotations are affected to the plastic deformation gradient and as a result, $\boldsymbol{F}^e$ and $\boldsymbol{F}^p$ can be written as:

$$\boldsymbol{F}^e = \boldsymbol{V}^e; \ \boldsymbol{F}^p = \boldsymbol{V}^p \boldsymbol{R} \tag{2.26}$$

where $\boldsymbol{R}$ represents the total rigid body rotation between the initial and current configuration and $\boldsymbol{V}^e$ and $\boldsymbol{V}^p$ denote the elastic and plastic components of the left stretch tensor. Using this decomposition, one can redefine the velocity gradient $\boldsymbol{l}$ and address the decomposition of the elastic and plastic rates of deformation. From Equation (2.18) and Equation (2.25) and after some straightforward tensor algebra, one may write the elastic and plastic components of the velocity gradient as a function of the elastic and plastic deformation gradients:

$$\boldsymbol{l}^e = \dot{\boldsymbol{V}}^e \left(\boldsymbol{V}^e\right)^{-1};\ \boldsymbol{l}^p = \dot{\boldsymbol{F}}^p \left(\boldsymbol{F}^p\right)^{-1}. \tag{2.27}$$

So, the velocity gradient can be rewritten as:

$$\boldsymbol{l} = \boldsymbol{l}^e + \boldsymbol{V}^e \boldsymbol{l}^p \left(\boldsymbol{V}^e\right)^{-1}. \tag{2.28}$$

Performing the decomposition of this new definition of the velocity gradient into the rate of deformation tensor $\boldsymbol{d}$ and the skew-symmetric continuum spin tensor, $\boldsymbol{w}$, (see Equation (2.19)), one has:

$$\begin{aligned} \boldsymbol{d} &= \boldsymbol{d}^e + \operatorname{sym}\left[\boldsymbol{V}^e \boldsymbol{d}^p \left(\boldsymbol{V}^e\right)^{-1}\right] + \operatorname{sym}\left[\boldsymbol{V}^e \boldsymbol{w}^p \left(\boldsymbol{V}^e\right)^{-1}\right] \\ \boldsymbol{w} &= \boldsymbol{w}^e + \operatorname{skew}\left[\boldsymbol{V}^e \boldsymbol{d}^p \left(\boldsymbol{V}^e\right)^{-1}\right] + \operatorname{skew}\left[\boldsymbol{V}^e \boldsymbol{w}^p \left(\boldsymbol{V}^e\right)^{-1}\right] \end{aligned}. \tag{2.29}$$

Thus, it is possible to verify that elastic and plastic rates of deformation are not additively decomposed:

$$\boldsymbol{d} \neq \boldsymbol{d}^e + \boldsymbol{d}^p. \tag{2.30}$$

However, if elastic strains can be considered small, which is the case of metal forming processes, then the elastic part of the left stretch tensor $\boldsymbol{V}$ is almost equal to $\boldsymbol{I}$:

$$\boldsymbol{V}^e = \left(\boldsymbol{V}^e\right)^{-1} \approx \boldsymbol{I}, \tag{2.31}$$

and it is possible to postulate the additive decomposition of the rate of deformation tensor as:

$$\boldsymbol{d} = \boldsymbol{d}^e + \boldsymbol{d}^p. \tag{2.32}$$

2.2 Forces and stress measures

In this section, the stress and equilibrium concepts for a large deformation analysis of a body will be introduced. The natural starting point for any description of stress measures is the Cauchy stress tensor. In order to introduce this definition, consider a body $\mathcal{B}$ in the deformed configuration, Figure 2.4 [Pires 2005]. Let $\mathcal{S}$ be an oriented surface of $\mathcal{B}$ with unit normal vector $\boldsymbol{n}$ at a point $\boldsymbol{x}$.

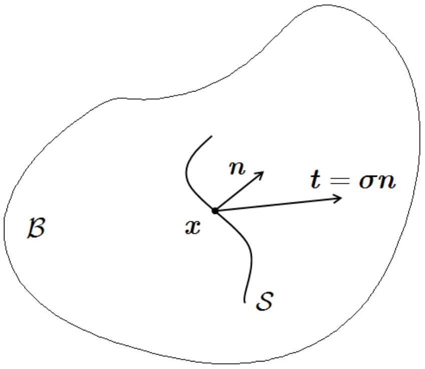

Figure 2.4 Surface forces. The Cauchy stress.

Cauchy's axiom states that: "At $\boldsymbol{x}$, the surface force, i.e., the force per unit area, exerted across $\mathcal{S}$ by the material on the side of $\mathcal{S}$ into which $\boldsymbol{n}$ is pointing upon the material on the other side of $\mathcal{S}$ depends on $\mathcal{S}$ only through its normal $\boldsymbol{n}$." This means that identical forces are transmitted across any surfaces with normal $\boldsymbol{n}$ at $\boldsymbol{x}$. This force (per unit area) is called the Cauchy stress vector and will be denoted as [Souza Neto 2008]:

$$\boldsymbol{t}\left(\boldsymbol{n}\right) \tag{2.33}$$

with dependence on $\boldsymbol{x}$ and time omitted for notational convenience. In the particular case when surface $\mathcal{S}$ belongs to the boundary of $\mathcal{B}$, the Cauchy stress vector represents the contact force exerted by the surrounding environment on $\mathcal{B}$. Furthermore, the dependency of the surface force $\boldsymbol{t}$ on the normal $\boldsymbol{n}$ is linear. This implies that there exists a tensor field $\boldsymbol{\sigma}\left(\boldsymbol{x}\right)$ such that the Cauchy stress vector is given by (Figure 2.4):

$$\boldsymbol{t}\left(\boldsymbol{x},\boldsymbol{n}\right) = \boldsymbol{\sigma}\left(\boldsymbol{x}\right)\boldsymbol{n}\,. \tag{2.34}$$

The tensor field $\boldsymbol{\sigma}$ is symmetric:

$$\boldsymbol{\sigma} = \boldsymbol{\sigma}^T \tag{2.35}$$

and is called the Cauchy stress tensor. It is often referred as the true stress tensor or, simply, stress tensor. Two important definitions (particularly convenient for the purpose of constitutive modelling) are obtained from the decomposition of the Cauchy stress tensor: the deviatoric stress or stress deviator and the spherical stress tensor. The deviatoric stress $\boldsymbol{s}$ is the traceless component of the stress tensor $\boldsymbol{\sigma}$ and is given by:

$$\boldsymbol{s} = \boldsymbol{\sigma} - p\boldsymbol{I} = \left(\mathbf{I} - \frac{1}{3}\boldsymbol{I} \otimes \boldsymbol{I}\right) : \boldsymbol{\sigma} \tag{2.36}$$

while the spherical stress tensor $p\boldsymbol{I}$, related with the first invariant of the stress tensor $\boldsymbol{\sigma}$, is the remainder component, computed as:

$$p\boldsymbol{I} = \frac{1}{3}\left(\boldsymbol{I} \otimes \boldsymbol{I}\right) : \boldsymbol{\sigma} \tag{2.37}$$

where p is the hydrostatic pressure (also referred as hydrostatic stress) calculated as:

$$p = \frac{1}{3}\operatorname{tr}\left(\boldsymbol{\sigma}\right). \tag{2.38}$$

Other common definitions for stress tensors can be found in the literature. In practical nonlinear analysis, the most used alternative stress measures are the Kirchhoff stress tensor $\boldsymbol{\tau}$ and the first and second Piola-Kirchhoff stress tensors, $\boldsymbol{P}$ and $\boldsymbol{S}$, respectively given by:

$$\boldsymbol{\tau} = J\boldsymbol{\sigma}\,, \tag{2.39}$$

$$\boldsymbol{P} = J\boldsymbol{\sigma}\boldsymbol{F}^{-T}\,, \tag{2.40}$$

$$\boldsymbol{S} = J\boldsymbol{F}^{-1}\boldsymbol{\sigma}\boldsymbol{F}^{-T} \tag{2.41}$$

where J is the volume ratio, as defined in Equation (2.9), and $\boldsymbol{F}$ is the deformation gradient. From Equations (2.9) and (2.39), it is evident that, for incompressible deformation states ($J = 1$), there is no numerical distinction between the Cauchy and Kirchhoff stress tensors. Due to the symmetry of the Cauchy stress tensor, Kirchhoff stress is also a symmetric tensor. This is not usually the case of the first Piola-Kirchhoff stress tensor, Equation (2.40), which is generally unsymmetric. However, it is possible to devise a symmetric stress tensor by using the second Piola-Kirchhoff stress definition, Equation (2.41). In spite of the mathematical convenience, this tensor does not admit a physical interpretation in terms of surface tractions as the Cauchy stress.

Despite these alternative stress tensors, Cauchy stress tensor is the most commonly used stress measure to establish equilibrium or constitutive equations. As for the strains, it is imperative to inquire the objectivity of tensor $\boldsymbol{\sigma}$. The objectivity concept can be assessed by studying the effect of a rigid body motion superimposed on the deformed configuration (more details in Section 2.4.1.2) [Pires 2005]. A second order quantity $\boldsymbol{G}$ is said to be objective if transforms as:

$$\boldsymbol{G} \rightarrow \boldsymbol{Q}\boldsymbol{G}\boldsymbol{Q}^{T} \tag{2.42}$$

being $\boldsymbol{Q}$ an orthogonal tensor describing an arbitrary superimposed rigid body rotation.

To investigate material objectivity of Cauchy stress tensor, let us first apply a transformation to the normal and traction vectors by a rotation $\boldsymbol{Q}$:

$$\begin{aligned} \breve{\boldsymbol{t}}\left(\breve{\boldsymbol{n}}\right) &= \boldsymbol{Q}\boldsymbol{t}\left(\boldsymbol{n}\right) \\ \breve{\boldsymbol{n}} &= \boldsymbol{Q}\boldsymbol{n} \end{aligned}\,. \tag{2.43}$$

Using the relationship between the traction vector and stress tensor, $\boldsymbol{t}\left(\boldsymbol{n}\right) = \boldsymbol{\sigma n}$, in conjunction with the above quantities gives, one can write:

$$\breve{\boldsymbol{t}}\left(\breve{\boldsymbol{n}}\right) = \boldsymbol{Qt}\left(\boldsymbol{n}\right) \Leftrightarrow \breve{\boldsymbol{t}}\left(\breve{\boldsymbol{n}}\right) = \boldsymbol{Q\sigma n} \Leftrightarrow \breve{\boldsymbol{t}}\left(\breve{\boldsymbol{n}}\right) = \boldsymbol{Q\sigma Q}^T \breve{\boldsymbol{n}}\,, \tag{2.44}$$

and, so:

$$\boldsymbol{\sigma} \to \boldsymbol{Q\sigma Q}^T\,. \tag{2.45}$$

Therefore, Cauchy stress tensor satisfies the objectivity requirement for a second order tensor, as defined in Equation (2.42), and is said to be objective.

The same material objectivity, however, is not ensured by the time derivative of the Cauchy stress tensor, which transformation reads:

$$\dot{\boldsymbol{\sigma}} \to \dot{\boldsymbol{Q}}\boldsymbol{\sigma Q}^T + \boldsymbol{Q}\dot{\boldsymbol{\sigma}}\boldsymbol{Q}^T + \boldsymbol{Q\sigma}\dot{\boldsymbol{Q}}^T\,. \tag{2.46}$$

Only in the special case of a time-independent rotation, i.e., when $\dot{\boldsymbol{Q}} = \boldsymbol{0}$, it is possible to say that Cauchy stress rate $\dot{\boldsymbol{\sigma}}$ is objective. Since plasticity problems are often formulated in a rate form, it is mandatory to define objective stress rates that ensure a transformation in accordance to Equation (2.42). These objective stress rates are usually defined by a suitable modification of the time derivative in order to satisfy material objectivity. The most common objective stress rates are the Jaumann-Zaremba, Truesdell and Green-Naghdi stress rates.

The Jaumann-Zaremba stress rate, denoted as $\boldsymbol{\sigma}^{\nabla}$, is defined as:

$$\boldsymbol{\sigma}^{\nabla} = \dot{\boldsymbol{\sigma}} - \boldsymbol{w\sigma} + \boldsymbol{\sigma w} \tag{2.47}$$

where $\boldsymbol{w}$ is the continuum spin or vorticity tensor (Equation (2.19)).

The Truesdell rate of $\boldsymbol{\sigma}$, in the other hand, is defined as:

$$\boldsymbol{\sigma}^{\circ} = \dot{\boldsymbol{\sigma}} - \boldsymbol{l\sigma} - \boldsymbol{\sigma l}^T + \left(\mathrm{tr}\boldsymbol{l}\right)\boldsymbol{\sigma} \tag{2.48}$$

where $\boldsymbol{l}$ is the velocity gradient tensor.

The Green-Naghdi stress rate of tensor $\boldsymbol{\sigma}$, here denoted $\boldsymbol{\sigma}^{\Diamond}$, is obtained by rotating $\boldsymbol{\sigma}$ back to the reference configuration, taking the time material derivative of the rotated quantity and then rotating the resulting derivative forward to the deformed configuration. That is:

$$\boldsymbol{\sigma}^{\Diamond} = \boldsymbol{R}\left[\frac{d}{dt}\left(\boldsymbol{R}^T\boldsymbol{\sigma R}\right)\right]\boldsymbol{R}^T = \dot{\boldsymbol{\sigma}} - \boldsymbol{\Omega\sigma} + \boldsymbol{\sigma\Omega} \tag{2.49}$$

where $\boldsymbol{\Omega}$ is the skew-symmetric tensor or angular velocity tensor (Equation (2.20)).

2.3 Fundamental laws of thermodynamics

In order to model physical phenomena of deformation and failure, it is important to use a method based on the general principles that govern representative state variables of material continuum. In this section, some basic concepts in thermodynamics of continuum mechanics are introduced. For this purpose, let us define the scalar fields θ , e , s and r defined over body $\mathcal{B}$ which represent, respectively, the temperature, specific internal energy, specific entropy and the density of heat production. In addition, variables $\boldsymbol{f}$ and $\boldsymbol{q}$ denote vector fields of body force and heat flux, respectively.

2.3.1 Conservation of mass

The first law of conservation postulates the conservation of mass expressed as [Pires 2005]:

$$\dot{\rho} + \rho \operatorname{div}_x \dot{\boldsymbol{u}} = 0$$

where $\operatorname{div}_x \left[\cdot\right]$ denotes the spatial divergence. Expressing by words, this law states that mass of an isolated system cannot be changed as a result of processes acting inside the system.

2.3.2 Momentum balance

The second law of conservation expresses the momentum balance. In its local form, balance can be expressed by the following partial differential equation with boundary condition [Souza Neto 2008]:

$$\begin{aligned} \operatorname{div}_x \boldsymbol{\sigma} + \boldsymbol{f} = \rho \ddot{\boldsymbol{u}} \quad & \text{in } \boldsymbol{\varphi}\left(\mathcal{B}\right) \\ \boldsymbol{t} = \boldsymbol{\sigma}\boldsymbol{n} \quad & \text{in } \boldsymbol{\varphi}\left(\partial\mathcal{B}\right) \end{aligned} \tag{2.50}$$

where $\boldsymbol{n}$ is the outward unit vector normal to the deformed boundary of $\mathcal{B}$ and $\boldsymbol{t}$ is the boundary traction vector field. The above momentum balance equations are formulated in the spatial (deformed) configuration. The corresponding formulation in the reference configuration is expressed in terms of the first Piola-Kirchhoff stress tensor as:

$$\begin{aligned} \operatorname{div}_p \boldsymbol{P} + \overline{\boldsymbol{f}} = \overline{\rho} \ddot{\boldsymbol{u}} \quad & \text{in } \mathcal{B} \\ \overline{\boldsymbol{t}} = \boldsymbol{P}\boldsymbol{m} \quad & \text{in } \partial\mathcal{B} \end{aligned} \tag{2.51}$$

where $\operatorname{div}_p \left[\cdot\right]$ denotes the material divergence, $\overline{\boldsymbol{f}}$ is the body force measured per unit reference volume, $\overline{\rho}$ is the density in the reference configuration:

$$\overline{\rho} = J\rho \,. \tag{2.52}$$

$\bar{\boldsymbol{t}}$ is the boundary traction force per unit reference area and $\boldsymbol{m}$ is the outward normal to the boundary of $\mathcal{B}$ in its reference configuration.

2.3.3 The first principle

The first principle of thermodynamics constitutes the third law of conservation related with the conservation of energy. It can be mathematically expressed by the equation [Pires 2005]:

$$\rho \dot{e} = \boldsymbol{\sigma} : \boldsymbol{d} + \rho r - \operatorname{div}_x \boldsymbol{q} \tag{2.53}$$

where the product $\boldsymbol{\sigma} : \boldsymbol{d}$ stands for the stress power per unit volume in the deformed configuration. This principle states that the total energy inside an isolated system remains the same for any process occurring inside that system. Therefore, internal energy rate per unit deformed volume must be equal to the sum of stress power and heat production per unit deformed volume minus the spatial divergence of the heat flux.

2.3.4 The second principle

The second principle of thermodynamics postulates that "energy systems have a tendency to increase their entropy rather than decrease it" and, therefore, expresses the irreversibility of entropy production. This principle can be expressed by the inequality:

$$\rho \dot{s} + \operatorname{div}_x \left[\frac{\boldsymbol{q}}{\theta} \right] - \frac{\rho r}{\theta} \geq 0 \, . \tag{2.54}$$

2.3.5 The Clausius–Duhem inequality

The Clausius–Duhem inequality can be used to express the second law of thermodynamics for elastic-plastic materials and is a statement concerning the irreversibility of natural processes, especially when energy dissipation is involved. The Clausius–Duhem inequality derives from the fundamental inequality which, in turn, can be obtained by combining of the first and second principles of thermodynamics. Hence, the fundamental inequality is given by the expression:

$$\rho \dot{s} + \operatorname{div}_x \left[\frac{\boldsymbol{q}}{\theta} \right] - \frac{1}{\theta} \left(\rho \dot{e} - \boldsymbol{\sigma} : \boldsymbol{d} + \operatorname{div}_x \boldsymbol{q} \right) \geq 0 \, . \tag{2.55}$$

Introducing a new variable, the specific free energy ψ (also known as Helmholtz free energy per unit mass) given by [Pires 2005]:

$$\psi = e - \theta s \tag{2.56}$$

and the equality, obtained by derivation:

$$\operatorname{div}_x\left[\frac{\boldsymbol{q}}{\theta}\right]=\frac{1}{\theta}\operatorname{div}_x\boldsymbol{q}-\frac{1}{\theta^2}\boldsymbol{q}\cdot\nabla_x\theta \tag{2.57}$$

into the fundamental inequality, one obtains the Clausius–Duhem inequality written as:

$$\boldsymbol{\sigma}:\boldsymbol{d}-\rho\left(\dot{\psi}+s\dot{\theta}\right)-\frac{1}{\theta}\boldsymbol{q}\cdot\boldsymbol{g}\geq 0 \tag{2.58}$$

with $\boldsymbol{g}=\nabla_x\theta$. Assuming that intrinsic (mechanical) dissipation is decoupled from the thermal dissipation, both following equations must be satisfied simultaneously:

$$\begin{aligned}&\boldsymbol{\sigma}:\boldsymbol{d}-\rho\left(\dot{\psi}+s\dot{\theta}\right)\geq 0\\&-\frac{1}{\theta}\boldsymbol{q}\cdot\boldsymbol{g}\geq 0\end{aligned}\quad. \tag{2.59}$$

It should be noted that all presented principles are valid for all types of substances, either gases, fluids or solids as long as chemical and electromagnetic effects are not taken into account [Pires 2001].

2.4 Constitutive theory

The distinction between different types of material's behaviour is made by introducing a proper constitutive model. Before starting to introduce the principles that are the basis for the constitutive theories presented in subsequently chapters, let us define the three fundamental axioms that define a rather general class of constitutive models of continua.

2.4.1 Constitutive axioms

The axioms, briefly presented in this section, must be satisfied for any constitutive model. It is important to make a distinction between thermokinetic and calorodynamic processes [Truesdell 1969]. A thermokinetic process of a generic body $\mathcal{B}$ is specified by a pair of thermokinetic variables:

$$\boldsymbol{\varphi}\left(\boldsymbol{p},t\right)\text{ and }\theta\left(\boldsymbol{p},t\right). \tag{2.60}$$

For the body $\mathcal{B}$ at a given region of space $\mathbb{R}^3$ in which the thermokinetic process is occurring, the history of this process will be assumed to define a calorodynamic process or constitutive relations. The set of fields

$$\left\{\boldsymbol{\sigma}\left(\boldsymbol{p},t\right),e\left(\boldsymbol{p},t\right),s\left(\boldsymbol{p},t\right),r\left(\boldsymbol{p},t\right),\boldsymbol{f}\left(\boldsymbol{p},t\right),\boldsymbol{q}\left(\boldsymbol{p},t\right)\right\} \tag{2.61}$$

must satisfy the principles of thermodynamics and the momentum balance.

2.4.1.1 Thermodynamic determinism

Thermodynamic determinism postulates that "the history of the thermokinetic process to which a neighbourhood of a point $\boldsymbol{p}$ of $\mathcal{B}$ has been subjected determines a calorodynamic process for $\mathcal{B}$ at $\boldsymbol{p}$". For simple materials, the deformation gradient $\boldsymbol{F}$, the temperature θ and the spatial gradient of temperature $\boldsymbol{g}$ are sufficient to define the history of the thermokinetic process. Regarding all variables delivered by conservation laws and introducing the specific free energy, the principles of thermodynamic determinism implies the existence of constitutive functionals $\mathfrak{F}$, $\mathfrak{G}$, $\mathfrak{H}$ and $\mathfrak{I}$ of histories of $\boldsymbol{F}$, θ and $\boldsymbol{g}$ such that, for a point $\boldsymbol{p}$, [Souza Neto 2008]:

$$\begin{aligned} \boldsymbol{\sigma}(t) &= \mathfrak{F}\left(\boldsymbol{F}^t,\theta^t,\boldsymbol{g}^t\right) \\ \psi(t) &= \mathfrak{G}\left(\boldsymbol{F}^t,\theta^t,\boldsymbol{g}^t\right) \\ s(t) &= \mathfrak{H}\left(\boldsymbol{F}^t,\theta^t,\boldsymbol{g}^t\right) \\ \boldsymbol{q}(t) &= \mathfrak{I}\left(\boldsymbol{F}^t,\theta^t,\boldsymbol{g}^t\right) \end{aligned} \tag{2.62}$$

and the Clausius–Duhem inequality holds for every thermokinetic process of $\mathcal{B}$.

2.4.1.2 Material objectivity

Material objectivity axiom states that "material response is independent of the observer". Assuming a change in the observer, a motion $\boldsymbol{\varphi}^*$ is related with motion $\boldsymbol{\varphi}$ if it can be expressed as [Souza Neto 2008]:

$$\boldsymbol{\varphi}^*(\boldsymbol{p},t) = \boldsymbol{y}(t) + \boldsymbol{Q}(t)\left[\boldsymbol{\varphi}(\boldsymbol{p},t) - \boldsymbol{x}_0\right] \tag{2.63}$$

where $\boldsymbol{y}(t)$ is a point in space, $\boldsymbol{Q}(t)$ is a rotation and $\boldsymbol{\varphi}(\boldsymbol{p},t) - \boldsymbol{x}_0$ is the position vector of $\boldsymbol{\varphi}(\boldsymbol{p},t)$ relative to an arbitrary origin $\boldsymbol{x}_0$. The deformation gradient corresponding to motion $\boldsymbol{\varphi}^*$ is given by the transformation:

$$\boldsymbol{F}^* = \boldsymbol{Q}\boldsymbol{F}\,. \tag{2.64}$$

Scalar fields are unaffected by a change in observer but Cauchy stress $\boldsymbol{\sigma}$, heat flux $\boldsymbol{q}$ and temperature gradient $\boldsymbol{g}$ transform according to the rules:

$$\begin{aligned} \boldsymbol{\sigma} &\rightarrow \boldsymbol{\sigma}^* = \boldsymbol{Q}\boldsymbol{\sigma}\boldsymbol{Q}^T \\ \boldsymbol{q} &\rightarrow \boldsymbol{q}^* = \boldsymbol{Q}\boldsymbol{q} \\ \boldsymbol{g} &\rightarrow \boldsymbol{g}^* = \boldsymbol{Q}\boldsymbol{g} \end{aligned}\;. \tag{2.65}$$

This objectivity principle also imposes some restrictions to the functionals expressed in Equation (2.62), namely relations:

$$\begin{aligned}\boldsymbol{\sigma}^*\left(t\right) &= \mathfrak{F}\left(\boldsymbol{F}^{t^*},\theta^t,\boldsymbol{g}^{t^*}\right)\\ \psi\left(t\right) &= \mathfrak{G}\left(\boldsymbol{F}^{t^*},\theta^t,\boldsymbol{g}^{t^*}\right)\\ s\left(t\right) &= \mathfrak{H}\left(\boldsymbol{F}^{t^*},\theta^t,\boldsymbol{g}^{t^*}\right)\\ \boldsymbol{q}^*\left(t\right) &= \mathfrak{I}\left(\boldsymbol{F}^{t^*},\theta^t,\boldsymbol{g}^{t^*}\right)\end{aligned} \tag{2.66}$$

must hold for any transformation stated in Equations (2.64) and (2.65).

2.4.1.3 Material symmetry

The symmetry group of a material is the set of density preserving changes of reference configuration under which the material response functionals $\mathfrak{F}$, $\mathfrak{G}$, $\mathfrak{H}$ and $\mathfrak{I}$ are not affected. The symmetry group of a solid material is a subset of the proper orthogonal group $\mathcal{O}^+$. A subgroup $\mathcal{S}$ of $\mathcal{O}^+$ is a symmetry group of a material defined by functionals $\mathfrak{F}$, $\mathfrak{G}$, $\mathfrak{H}$ and $\mathfrak{I}$ if relations:

$$\begin{aligned}\mathfrak{F}\left(\boldsymbol{F}^t,\theta^t,\boldsymbol{g}^t\right) &= \mathfrak{F}\left(\left[\boldsymbol{F}\boldsymbol{Q}\right]^t,\theta^t,\boldsymbol{g}^t\right)\\ \mathfrak{G}\left(\boldsymbol{F}^t,\theta^t,\boldsymbol{g}^t\right) &= \mathfrak{G}\left(\left[\boldsymbol{F}\boldsymbol{Q}\right]^t,\theta^t,\boldsymbol{g}^t\right)\\ \mathfrak{H}\left(\boldsymbol{F}^t,\theta^t,\boldsymbol{g}^t\right) &= \mathfrak{H}\left(\left[\boldsymbol{F}\boldsymbol{Q}\right]^t,\theta^t,\boldsymbol{g}^t\right)\\ \mathfrak{I}\left(\boldsymbol{F}^t,\theta^t,\boldsymbol{g}^t\right) &= \mathfrak{I}\left(\left[\boldsymbol{F}\boldsymbol{Q}\right]^t,\theta^t,\boldsymbol{g}^t\right)\end{aligned} \tag{2.67}$$

hold for every time-independent rotation $\boldsymbol{Q}$. In an isotropic solid, its symmetry group $\mathcal{S}$ is the entire proper orthogonal group.

2.4.2 Thermodynamics with internal variables

The use of constitutive equations written in terms of history functionals, as presented in Section 2.4.1, are too general to have practical utility in describing dissipative thermodynamical processes undergoing by real materials. A more effective way is to add some simplifying assumptions by adopting the so-called thermodynamics with internal variables. The starting point of this theory is the hypothesis that, at any instant of a thermodynamical process, the thermodynamic state (defined by $\boldsymbol{\sigma}$, ψ, s and $\boldsymbol{q}$) at a given point $\boldsymbol{p}$ can be completely defined by the knowledge of the instantaneous value of a finite number of state variables and not on their history [Pires 2005]. This hypothesis is intimately connected with the assumption of the existence of a (fictitious) state of thermodynamic equilibrium known as the local accompanying state [Kestin 1977] described by the current value of the state variables. Every process can be considered to be a succession of thermodynamic equilibrium states [Lemaitre 1994].

2.4.2.1 The state variables

State variables can be seen as parameters from thermodynamic process history and as the replacement of the complex constitutive description in terms of functionals. Their nature and number will be determinant in the accuracy of the description of the physical phenomena. For the processes that we are concerned (metal forming processes), the thermodynamic state at a point is determined by the set of state variables:

$$\left\{ \boldsymbol{F}, \theta, \boldsymbol{g}, \boldsymbol{\alpha} \right\} \tag{2.68}$$

where $\boldsymbol{F}$, θ and $\boldsymbol{g}$ are instantaneous values of deformation gradient, temperature and temperature gradient and:

$$\boldsymbol{\alpha} = \left\{ \alpha_k \right\} \tag{2.69}$$

represent a set of internal variables containing, in general, entities of scalar, vectorial and tensorial nature associated with the dissipative mechanisms.

2.4.2.2 Thermodynamic potential. Stress constitutive equation

The state potential allows the derivation of the state laws and the definition of the associate variables or driving forces associated with the state variables that define the energy involved in each phenomenon. Assuming the above hypothesis (expressed in Equation (2.68)), the specific free energy is assumed to have the form [Souza Neto 2008]:

$$\psi = \psi\left(\boldsymbol{F}, \theta, \boldsymbol{\alpha} \right). \tag{2.70}$$

So, its rate of change is given by:

$$\dot{\psi} = \frac{\partial \psi}{\partial \boldsymbol{F}} : \dot{\boldsymbol{F}} + \frac{\partial \psi}{\partial \theta} \dot{\theta} + \frac{\partial \psi}{\partial \alpha_k} \dot{\alpha}_k \tag{2.71}$$

where summation over k is implied. In this case, using the relationship:

$$\boldsymbol{\sigma} : \boldsymbol{d} = \boldsymbol{\sigma} \boldsymbol{F}^{-T} : \dot{\boldsymbol{F}} \tag{2.72}$$

for the stress power, one obtains for the Clausius-Duhem inequality:

$$\left(\boldsymbol{\sigma} \boldsymbol{F}^{-T} - \rho \frac{\partial \psi}{\partial \boldsymbol{F}} \right) : \dot{\boldsymbol{F}} - \rho \left(s + \frac{\partial \psi}{\partial \theta} \right) \dot{\theta} - \rho \frac{\partial \psi}{\partial \alpha_k} \dot{\alpha}_k - \frac{1}{\theta} \boldsymbol{q} \cdot \boldsymbol{g} \geq 0 \,, \tag{2.73}$$

or, equivalently, in terms of power per unit reference volume, as:

$$\left(\boldsymbol{P} - \bar{\rho} \frac{\partial \psi}{\partial \boldsymbol{F}} \right) : \dot{\boldsymbol{F}} - \bar{\rho} \left(s + \frac{\partial \psi}{\partial \theta} \right) \dot{\theta} - \bar{\rho} \frac{\partial \psi}{\partial \alpha_k} \dot{\alpha}_k - \frac{J}{\theta} \boldsymbol{q} \cdot \boldsymbol{g} \geq 0 \,. \tag{2.74}$$

The principle of thermodynamic determinism requires that Equation (2.74) remains valid for any pair of functions $\left\{\dot{\boldsymbol{F}}\left(t\right),\dot{\theta}\left(t\right)\right\}$. This implies the constitutive relations:

$$\boldsymbol{P} = \bar{\rho}\frac{\partial \psi}{\partial \boldsymbol{F}}, \; s = -\frac{\partial \psi}{\partial \theta} \tag{2.75}$$

for the first Piola-Kirchhoff stress and entropy, respectively. The Cauchy stress tensor can be further obtained as:

$$\boldsymbol{\sigma} = \frac{1}{J}\bar{\rho}\frac{\partial \psi}{\partial \boldsymbol{F}}\boldsymbol{F}^{T}. \tag{2.76}$$

2.4.2.3 Thermodynamical forces

For each internal variable α_k of the set $\boldsymbol{\alpha}$, we define the conjugate thermodynamical force as [Pires 2005]:

$$A_k \equiv \bar{\rho}\frac{\partial \psi}{\partial \alpha_k}. \tag{2.77}$$

With this definition and the identities in Equation (2.75), the Clausius-Duhem inequality can be rewritten as:

$$-A_k\dot{\alpha}_k - \frac{J}{\theta}\boldsymbol{q}\cdot\boldsymbol{g} \geq 0. \tag{2.78}$$

In what follows, we will adopt for convenience the notation:

$$\boldsymbol{A} \equiv \left\{A_k\right\} \tag{2.79}$$

for the set of all thermodynamical forces.

2.4.2.4 Dissipation. Evolution of the internal variables

The thermodynamic potential allows the establishment of relations between each internal variable α_k and the corresponding conjugate thermodynamical force A_k. However, in order to fully describe the dissipative mechanisms and completely characterize the constitutive model, a complementary formalism is required, namely, the postulation of constitutive equations for the flux variables $1/\theta\,\boldsymbol{q}$ and $\dot{\boldsymbol{\alpha}}$. Assuming that flux variables are given functions of the state variables, one may write the following constitutive equations [Souza Neto 2008]:

$$\begin{aligned} \dot{\boldsymbol{\alpha}} &= f\left(\boldsymbol{F},\theta,\boldsymbol{g},\boldsymbol{\alpha}\right) \\ \frac{1}{\theta}\boldsymbol{q} &= h\left(\boldsymbol{F},\theta,\boldsymbol{g},\boldsymbol{\alpha}\right) \end{aligned}. \tag{2.80}$$

Naturally, the formulation of functions f and h is restricted due to the fact that Clausius-Duhem inequality as expressed in Equation (2.78) must hold for any process (further details in [Truesdell 1969]). To have a more general form of Equation $(2.80)_1$ accounting for different natures of internal variables (scalar, vectorial or tensorial), it is convenient to define it in terms of objective rates rather than in the standard material time derivative, in order to achieve frame invariant evolution laws for variables that represent physical states associated with material directions.

2.4.2.5 Dissipation potential. Normal dissipativity

An effective way to ensure that Equation (2.78) is satisfied consists in postulating the existence of a scalar-valued dissipation (pseudo-) potential, continuous, non-negative and convex with respect to each A_k and $\boldsymbol{g}$. The dissipation (pseudo-) potential takes the form:

$$\Xi = \Xi\left(\boldsymbol{A}, \boldsymbol{g}; \boldsymbol{F}, \theta, \boldsymbol{\alpha}\right) \tag{2.81}$$

where state variables $\boldsymbol{F}$, θ and $\boldsymbol{\alpha}$ are introduced in the dissipation potential but only as parameters. In addition, the hypothesis of normal dissipativity is introduced, i.e., the flux variables are assumed to be determined by the laws:

$$\dot{\alpha}_k = -\frac{\partial \Xi}{\partial A_k}, \ \frac{1}{\theta}\boldsymbol{q} = -\frac{\partial \Xi}{\partial \boldsymbol{g}}. \tag{2.82}$$

A constitutive model defined by Equations (2.70), (2.75) and (2.82) satisfies 'a priori' the dissipation inequality [Pires 2005]. It should be noted, however, that the constitutive description by means of convex potentials as described above is not a direct consequence of thermodynamics but rather an instrument for formulating constitutive equations without violating thermodynamics.

2.4.3 Phenomenological and micromechanical approaches

Any material behaviour can be stated as a mathematical model as long as an appropriate set of internal variables are chosen. The choice of those internal variables and the analytical expressions for the state and dissipation potentials must be carefully taken because the success of the constitutive model in the description of the phenomena depends crucially on such selection. There are no rules for this selection process but, in general terms, the choice must be guided by the type of material, phenomena and the identification of all the physical mechanisms involved, corresponding conditions and expected accuracy and predictions delivered by the developed model.

Two main approaches can be distinguished in constitutive modelling with internal variables: the micromechanical and the phenomenological approaches. The micromechanical approach involves the determination of mechanisms and related variables at the atomic, molecular or crystalline levels. In general, these variables are discrete quantities and their continuum (macroscopic) counterparts can be defined by means of homogenisation techniques. The phenomenological approach, on the other hand, is based on the study of the response of the representative volume element (RVE), i.e., the element of matter large enough to be regarded as a homogeneous continuum. The internal variables, in this case, will be directly associated with the dissipative behaviour observed at the macroscopic level in terms of continuum quantities (such as strain, stress, temperature, etc.). Despite the macroscopic nature of theories derived on the basis of the phenomenological methodology, it should be expected that "good" phenomenological internal variables will be somehow related to the underlying microscopic dissipation mechanisms [Souza Neto 2008].

2.4.4 The purely mechanical theory

Having cold sheet metal forming in mind and, therefore, thermal effects being disregarded, the general constitutive equations based in the internal variables approach for a pure mechanical case are given by:

$$\begin{cases} \psi = \psi\left(\boldsymbol{F}, \boldsymbol{\alpha}\right) \\ \boldsymbol{P} = \bar{\rho}\dfrac{\partial \psi}{\partial \boldsymbol{F}} \\ \dot{\boldsymbol{\alpha}} = f\left(\boldsymbol{F}, \boldsymbol{\alpha}\right) \end{cases} . \tag{2.83}$$

2.4.5 The constitutive initial value problem

Assuming a purely mechanical theory (as stated above) and the adoption of the internal variable approach in the formulation of constitutive equations, the mechanical constitutive initial value problem can be stated as follows:

"Given the deformation history $\boldsymbol{F}\left(t\right)$, $t \in \left[t_0, t\right]$ and the initial conditions for the internal values $\boldsymbol{\alpha}\left(t_0\right)$, determine functions $\boldsymbol{P}\left(t\right)$ and $\boldsymbol{\alpha}\left(t\right)$ for the first Piola-Kirchhoff stress and the set of internal variables such that the constitutive equations:

$$\begin{cases} \boldsymbol{P}\left(t\right) = \bar{\rho}\left.\dfrac{\partial \psi}{\partial \boldsymbol{F}}\right|_t \\ \dot{\boldsymbol{\alpha}}\left(t\right) = f\left(\boldsymbol{F}\left(t\right), \boldsymbol{\alpha}\left(t\right)\right) \end{cases} \tag{2.84}$$

are satisfied for $t \in \left[t_0, t\right]$."

2.5 Weak equilibrium. The principle of virtual work

The momentum balance, as expressed in Equations (2.50) and (2.51), cannot be discretized directly by the finite element method. In order to discretize this equation, a weak form, often called a variational form, is needed [Belytschko 2000]. The principle of virtual work, or weak form, which will be stated in this section, is fundamental to the definition of the basic initial boundary value problem (IVBP) and can be used to approximate the strong form by finite elements procedures, as reviewed in Chapter 3. The spatial version of the principle virtual work states that “the body $\mathcal{B}$ is in equilibrium if and only if its Cauchy stress field, $\boldsymbol{\sigma}$, satisfies the equation:

$$\int_{\varphi(\mathcal{B})}\left[\boldsymbol{\sigma} : \nabla_x \boldsymbol{\eta} - \left(\boldsymbol{f} - \rho \ddot{\boldsymbol{u}}\right) \cdot \boldsymbol{\eta}\right] dv - \int_{\varphi(\partial\mathcal{B})} \boldsymbol{t} \cdot \boldsymbol{\eta}\, da = 0\,,\ \forall \boldsymbol{\eta} \in \mathcal{V} \tag{2.85}$$

where $\boldsymbol{f}$ and $\boldsymbol{t}$ are the body force per unit deformed volume and boundary traction per unit deformed area and $\mathcal{V}$ is the space of virtual displacements of $\mathcal{B}$, i.e., the space of sufficiently regular arbitrary displacements:

$$\boldsymbol{\eta} : \boldsymbol{\varphi}\left(\mathcal{B}\right) \rightarrow \mathcal{U}\,.\text{”} \tag{2.86}$$

The equivalently expression of the principle virtual work in the reference configuration is given by:

$$\int_{\mathcal{B}}\left[\boldsymbol{P} : \nabla_p \boldsymbol{\eta} - \left(\overline{\boldsymbol{f}} - \overline{\rho} \ddot{\boldsymbol{u}}\right) \cdot \boldsymbol{\eta}\right] dv - \int_{\partial\mathcal{B}} \overline{\boldsymbol{t}} \cdot \boldsymbol{\eta}\, da = 0\,,\ \forall \boldsymbol{\eta} \in \mathcal{V} \tag{2.87}$$

where $\boldsymbol{P}$ is the first Piola-Kirchhoff stress field, $\overline{\boldsymbol{f}} = J\boldsymbol{f}$ is the reference body force and $\overline{\boldsymbol{t}}$ is the boundary traction per unit deformed area. Similarly, $\mathcal{V}$ is the space of virtual displacements defined as the space of sufficiently regular arbitrary displacements:

$$\boldsymbol{\eta} : \mathcal{B} \rightarrow \mathcal{U}\,. \tag{2.88}$$

3. FINITE ELEMENT METHOD

This chapter presents some basic concepts in the field of numerical methods, namely the finite element method, and addresses the most relevant issues and aspects for the sheet metal forming area. The material presented in this chapter is well-established in the specific literature devoted to finite element method and reader is referred to [Belytschko 2000] [Zienkiewicz 2000a] [Souza Neto 2008], among others, for further details.

3.1 Definition of the initial boundary value problem

A set of phenomena occurs simultaneous during metal forming operations: heat exchange, large plastic strains, nonlinear hardening, ductile damage, contact with friction between sheet metal and tools, etc. In addition these non-linear phenomena, it is crucial to add the imposed initial boundary conditions and to treat all the evolving boundary conditions (such is the case of contact-friction conditions). These phenomena and constraints define a highly non-linear initial boundary value problem (IBVP) that has to be solved, iteratively, by using a proper solution scheme. But, before addressing the required spatial discretization and the time-stepping integration scheme, it is important to define the initial boundary value problem to be solved in the case of metal forming processes. Let us suppose that a deformed body $\mathcal{B}$ occupies, at time t, a volume v delimited by the boundary $\partial\mathcal{B}$ [Saanouni 2007]. During processing, the part will be submitted to an imposed:

- Displacement field $\boldsymbol{u}$ acting on $\partial\mathcal{B}_u$ of $\partial\mathcal{B}$;
- Force field $\boldsymbol{t}_F$ acting on $\partial\mathcal{B}_F$ of $\partial\mathcal{B}$;
- Contact force $\boldsymbol{t}_C$ acting on $\partial\mathcal{B}_C$ of $\partial\mathcal{B}$;
- Body force field $\boldsymbol{f}$ acting on $\mathcal{B}$,

with $\partial\mathcal{B}_u \cup \partial\mathcal{B}_F \cup \partial\mathcal{B}_C = \partial\mathcal{B}$ and $\partial\mathcal{B}_u \cap \partial\mathcal{B}_F \cap \partial\mathcal{B}_C = \varnothing$. The problem to be solved can be casted in the weak form of the momentum balance, in its spatial description, as follows:

$$\begin{aligned}\int_{\varphi(\mathcal{B})} \boldsymbol{\sigma} : \nabla_x \boldsymbol{\eta}\, dv - \int_{\varphi(\mathcal{B})} \boldsymbol{f} \cdot \boldsymbol{\eta}\, dv + \int_{\varphi(\mathcal{B})} \rho \ddot{\boldsymbol{u}} \cdot \boldsymbol{\eta}\, dv \\ - \int_{\varphi(\partial\mathcal{B}_C)} \boldsymbol{t}_C \cdot \boldsymbol{\eta}\, da - \int_{\varphi(\partial\mathcal{B}_F)} \boldsymbol{t}_F \cdot \boldsymbol{\eta}\, da = 0, \ \forall \boldsymbol{\eta} \in \mathcal{V}\end{aligned} \tag{3.1}$$

where $\ddot{\boldsymbol{u}}$ is the acceleration field, $\boldsymbol{\eta}$ is the virtual displacement field, ρ is the density and $\nabla_x[\cdot]$ denotes the spatial gradient of $[\cdot]$. So, the displacement based finite element analysis consists in finding the set of kinematically admissible deformations of $\mathcal{B}$, defined as:

$$\mathcal{K} = \left\{ \boldsymbol{u} : \mathcal{B} \rightarrow \mathcal{U} \mid \boldsymbol{u} = \bar{\boldsymbol{u}} \text{ on } \partial\mathcal{B}_u \right\} \tag{3.2}$$

that, at time t, satisfies the momentum balance described in Equation (3.1). As we will see later, the Cauchy stress tensor $\boldsymbol{\sigma}$ has to satisfy the (non-linear) constitutive equation, and will be dependent of the displacement $\boldsymbol{u}$ (through the velocity gradient $\boldsymbol{l}$) and of a set of internal variables $\boldsymbol{\alpha}$ related to plasticity, hardening and other phenomena such as ductile damage.

With the introduction of a spatial and time discretization approximations, this original initial boundary value problem is reduced to a set of incremental (generally nonlinear) algebraic finite element equations to be solved at each time station of the considered time interval [Souza Neto 2008], as we will see in the following sections.

3.2 Spatial discretization of initial boundary value problem

In order to numerically analyse the IBVP, at first, it is required to discretize the continuum domain by a finite number of elements, n_{elem}, having each one an elementary volume such as:

$$\mathcal{B} \cong \mathcal{B}^h = \bigcup_{e=1}^{n_{\text{elem}}} \mathcal{B}_{(e)} \tag{3.3}$$

with $\mathcal{B}^h$ representing the discrete domain of $\mathcal{B}$ and $\mathcal{B}_{(e)}$ the domain of a generic finite element e. The operation $\bigcup$ stands for the addition operation between all elements. It is important to emphasize that the quality of this spatial discretization is one of the key points that can affect the rigor and accuracy of results obtained by numerical simulation. Essentially, there are two main aspects that should be considered when performing the spatial discretization of the computational domain: the mesh geometry (topology) and the finite element type adopted (typology) [Alves 2003]. The first aspect is concerned to issues related with the geometric boundary of the computational domain and the configuration of elementary finite element (structured or non-structured mesh, regular or non-regular mesh, isotropic or anisotropic mesh). A finite element mesh that presents distorted elements can affect negatively the accuracy of the solution. The latter aspect is related with the element type adopted for the spatial discretization (solid, shell, solid-shell, etc.), his behaviour and the way that equations are formulated at the elemental level.

Focussing our attention to a generic finite element e, it can be defined by a finite number of nodes $n_{\text{node}}^{(e)}$. Each node i from element e has an associated shape function (or interpolation function) $\mathrm{N}_i^{(e)}$ such as:

$$N_i^{(e)}\left(\boldsymbol{x}^j\right) = \delta_{ij} \tag{3.4}$$

where $\boldsymbol{x}^j$ is the node coordinate and δ_{ij} is the Kronecker symbol. In words, it means that the shape function is equal to one if $i = j$ and zero for all the other nodes of the element e. A generic field $a\left(\boldsymbol{x}\right)$ defined over the element domain can be obtained by the finite element interpolation:

$$a^h\left(\boldsymbol{x}\right) = \sum_{i=1}^{n_{\text{node}}^{(e)}} a_i N_i^{(e)}\left(\boldsymbol{x}\right) \tag{3.5}$$

and, for the entire domain, as:

$$a^h\left(\boldsymbol{x}\right) = \sum_{i=1}^{n_{\text{node}}} a_i N_i^g\left(\boldsymbol{x}\right) \tag{3.6}$$

where N_i^g is the global finite element shape function associated with global node i. Using this interpolation procedure, approximation to the boundary value problem defined in Equations (3.1) and (3.2) can be obtained by replacing the functionals $\mathcal{K}$ and $\mathcal{V}$ by their discrete counterparts $\mathcal{K}^h$ and $\mathcal{V}^h$ as:

$$\boldsymbol{u}^h = \sum_{i=1}^{n_{node}} N_i^g\left(\boldsymbol{x}\right)\boldsymbol{u}_i \text{ and } \boldsymbol{\eta}^h = \sum_{i=1}^{n_{node}} N_i^g\left(\boldsymbol{x}\right)\boldsymbol{\eta}_i\text{, } \forall \boldsymbol{x} \in \boldsymbol{\varphi}\left(\mathcal{B}\right) \tag{3.7}$$

where $\boldsymbol{u}_i$ is the nodal displacement. Inserting Equation (3.7) into the weak form in Equation (3.1), one obtains the semi-discrete system of equations:

$$\boldsymbol{M}\ddot{\boldsymbol{u}} + \mathbf{f}^{\text{int}}\left(\boldsymbol{u}\right) = \mathbf{f}^{\text{ext}} \tag{3.8}$$

where $\boldsymbol{u}$ are the nodal displacements, $\boldsymbol{M}$ is called the consistent mass matrix, in the sense that it is calculated from the same shape functions $\mathbf{N}^g$ that are used for the interpolation of the displacement field, and is given by:

$$\boldsymbol{M} = \int_{\mathcal{B}} \rho \left(\mathbf{N}^g\right)^T \mathbf{N}^g dv \,. \tag{3.9}$$

$\mathbf{f}^{\text{int}}\left(\boldsymbol{u}\right)$ represents the internal force contribution from the element stress field and the term $\mathbf{f}^{\text{ext}}$ represents external forces arising from the applied tractions and contact conditions. These force vectors are obtained also as assemblies [Souza Neto 2008]:

$$\mathbf{f}^{\text{int}} = \underset{e=1}{\overset{n_{\text{elem}}}{\mathbf{A}}} \left(\mathbf{f}^{\text{int}}_{(e)}\right) \tag{3.10}$$

$$\mathbf{f}^{\text{ext}} = \underset{e=1}{\overset{n_{\text{elem}}}{\mathbf{A}}} \left(\mathbf{f}^{\text{ext}}_{(e)}\right) \tag{3.11}$$

of the element vectors:

$$\mathbf{f}^{\text{int}}_{(e)} = \int_{\mathcal{B}^{(e)}} \mathbf{B}^T \boldsymbol{\sigma}\, dv \tag{3.12}$$

$$\mathbf{f}^{\text{ext}}_{(e)} = \int_{\mathcal{B}^{(e)}} \mathbf{N}^T \boldsymbol{f} dv + \int_{\partial\mathcal{B}^{(e)}} \mathbf{N}^T \boldsymbol{t} da \tag{3.13}$$

where $\mathbf{A}$ stands for the finite element assembly operator and matrix $\mathbf{B}$ is the standard discrete symmetric gradient operator.

3.3 Time integration and incremental solution procedures

For the solution of the boundary value problem, there are two fundamental methods for problem formulation and time integration. If inertial forces are neglected, then problem is said to be quasi-static. If, on the other hand, inertial forces are considered in the equilibrium equations, the problem is said to be transient dynamic. For time integration, the scheme can be called either implicit or explicit. The difference between these two schemes is mainly related with the time instant when the constitutive model integration and the formulation of equilibrium equations are made. In the case of an implicit time integration scheme, solution is carried out at time $t_{n+1} = t_n + \Delta t_{n+1}$ while in the explicit method, solution is performed at time t_n, without any verification of equilibrium conditions at time t_{n+1}. Any combination between problem formulation and time integration is possible. Thus, one can have the following solution procedures: Static Explicit (SE), Static Implicit (SI), Dynamic Explicit (DE) and Dynamic Implicit (DI). Although all solution procedures are feasible (as for example the static explicit code ITAS3D [Santos 1993]), in this work, we will restrict ourselves to the two most widely used procedures: the static implicit (SI) and the dynamic explicit (DE) methods and focused in the dynamic explicit procedure. The choice between the two procedures is far from being consensual; there are tenacious supporters for each strategy.

Inevitably, the selection is linked with the advantages and disadvantages presented by each procedure and, in some cases, the choice often tend to be oriented by the working group and biased by the researcher preferences. Without pretending to get into deep discussions on this subject, here we will limit the discussion just mentioning some of the advantages and disadvantages of each solution procedure.

A deep-drawing operation usually runs at a slow speed and can be classified as a quasi-static process, and, thus, inertia effects, related with gravity and accelerations fields, can be disregarded. This is the basic assumption made in the static solution procedure that considers that the work done by the inertial forces is very small when compared with the work associated with the plastic deformation [Alves 2003], and, consequently, it can be neglected and removed from equilibrium equations. Thus, the problem is reduced to the solution of the non-linear algebraic system:

$$\mathbf{r}\left(\boldsymbol{u}_{n+1}\right)=\mathbf{f}^{\text{int}}\left(\boldsymbol{u}_{n+1}\right)-\mathbf{f}_{n+1}^{\text{ext}}=\mathbf{0} \tag{3.14}$$

for the nodal displacement $\boldsymbol{u}_{n+1}$ at time t_{n+1}. Being Equation (3.14) a non-linear system and if an implicit time integration scheme is considered, the solution is undertaken by an iterative method, which, in general, is the Newton-Raphson algorithm, until the static equilibrium between internal and external global force vectors is achieved. This solution procedure needs the exact linearization of algebraic system of Equation (3.14). It should be mentioned that this linearization requires the computation of consistent tangent operators, which can be a challenging task, especially when complex integration algorithms and material models are involved [Pires 2005]. Nevertheless, static implicit methods are widely used in springback calculations since it is widely accepted that purely explicit methods are not able to deliver a reliable prediction of springback [Alves 2003]. They can be considered unconditionally stable and, so, time increment Δt can be virtually equal to the total time $t_{\max}$. However, in practice, it is limited by non-linearities of constitutive models and contact treatment. As disadvantages, one can point out the almost quadratic increase of calculating time with increasing degrees of freedom and the required physical memory for the solution of the system of equations. Also, the contact treatment (and friction) in implicit methods is considered to be one of the main causes responsible for non-convergence or slowness of convergence in implicit methods.

A numerically more efficient algorithm is given by the dynamic explicit method, which can handle reasonably well with all the nonlinearities and discontinuities of the constitutive laws that model the physical phenomena, such as material constitutive laws and contact with friction modelling. It is considered also efficient for dealing with extremely refined meshes, with large problems and a high number of degrees of freedom associated with those problems [Alves 2003].

However, due to the explicit formulation, these methods may incur in a successive deviation from the equilibrium state and, consequently, from the exact solution, mainly due to the accumulation of small errors during the incremental integration of the boundary value problem. Therefore, the accuracy of the results will be strongly dependent on the size of the time increment Δt, being this method conditionally stable. Nevertheless, in most situations, this is not a concern for explicit dynamic analysis because the stable time increment is usually sufficiently small to ensure good accuracy.

3.3.1 Explicit dynamic finite element solution strategy

For the sake of completeness and before addressing the explicit dynamic finite element solution strategy, it is imperative to state the incremental boundary value problem in the weak form of the equilibrium:
"Given the set $\boldsymbol{\alpha}_n$ of internal variables at time t_n, and given the body forces $\boldsymbol{f}_{n+1}$ and surface traction $\boldsymbol{t}_{n+1}$ fields at t_{n+1}, find a kinematically admissible configuration $\varphi_{n+1}\left(\mathcal{B}\right) \in \mathcal{K}_{n+1}$ such that the virtual work equation:

$$\begin{aligned} \int_{\varphi_{n+1}(\mathcal{B})} \boldsymbol{\sigma} : \nabla_x \boldsymbol{\eta}\, dv - \int_{\varphi_{n+1}(\mathcal{B})} \boldsymbol{f}_{n+1} \cdot \boldsymbol{\eta}\, dv \\ + \int_{\varphi_{n+1}(\mathcal{B})} \rho \ddot{\boldsymbol{u}}_{n+1} \cdot \boldsymbol{\eta}\, dv - \int_{\varphi_{n+1}(\partial\mathcal{B}_C)} \boldsymbol{t}_{n+1} \cdot \boldsymbol{\eta}\, da = 0 \end{aligned} \tag{3.15}$$

is satisfied for any $\boldsymbol{\eta} \in \mathcal{V}$, where φ_{n+1} is the deformation map at t_{n+1}. The set $\mathcal{K}_{n+1}$ is defined as:

$$\mathcal{K}_{n+1} = \left\{ \boldsymbol{u} : \mathcal{B} \rightarrow \mathcal{U} \mid \boldsymbol{u} = \bar{\boldsymbol{u}}_{n+1} \text{ on } \partial\mathcal{B}_u \right\} \tag{3.16}$$

where $\bar{\boldsymbol{u}}_{n+1}$ is the prescribed boundary displacement at t_{n+1}." As already stated, the initial boundary value problem will be reduced to a set of incremental boundary value problems, making use of the contemporary configuration at time t_n as the reference configuration for the time step $\left[t_n, t_{n+1}\right]$. This formulation is known as Updated Lagrangian formulation (UL), distinctive from the Total Lagragian formulation (TL) that always refer to the initial (unstressed) configuration as the reference configuration [Klerck 2000].

In the case of the dynamic explicit integration scheme, the resolution of the incremental boundary value problem will be performed at time t_n. So, let us go back to the dynamic discrete system given by Equation (3.8). The objective is, then, to obtain the values of all dynamic quantities at the end of a specific time interval $t_{n+1} = t_n + \Delta t_{n+1}$, exclusively based on values available at time t_n. Written at the nth

time increment, the semi-discrete form of the dynamic equilibrium equation (Equation (3.8)) is given as follows [Saanouni 2007]:

$$\boldsymbol{M}\ddot{\boldsymbol{u}}_n + \mathbf{f}^{\text{int}}\left(\boldsymbol{u}_n\right) = \mathbf{f}_n^{\text{ext}}, \tag{3.17}$$

in which the mass matrix $\boldsymbol{M}$ is generally a symmetric, positive definite, but non-diagonal matrix. The accelerations for all nodes at time t_n are directly obtained as:

$$\ddot{\boldsymbol{u}}_n = \boldsymbol{M}^{-1}\left[\mathbf{f}^{\text{int}}\left(\boldsymbol{u}_n\right) - \mathbf{f}_n^{\text{ext}}\right]. \tag{3.18}$$

It is computationally advantageous to replace the non-diagonal consistent matrix $\boldsymbol{M}$ by a diagonal one, called the lumped mass matrix $\boldsymbol{M}^L$. The use of a lumped mass matrix is justified by the reduced (almost null) computation cost of its inverse calculation and by the straightforward multiplication with the inertial force vector, requiring only n operations, being n the number of degrees of freedom in the model. This nodal mass lumping consists in placing concentrated point masses m_i at nodes i in the directions of assumed displacement DOF's [Saanouni 2007], rendering a diagonal mass matrix. More details of mathematical methods for nodal mass lumping and its consequences for the solution accuracy, the reader is referred to [Zienkiewicz 2000a], among many others.

To obtain the displacement field $\boldsymbol{u}_{n+1}$, at time $t_{n+1} = t_n + \Delta t_{n+1}$, the central difference integration scheme is used and is illustrated in Figure 3.1 [Pires 2005].

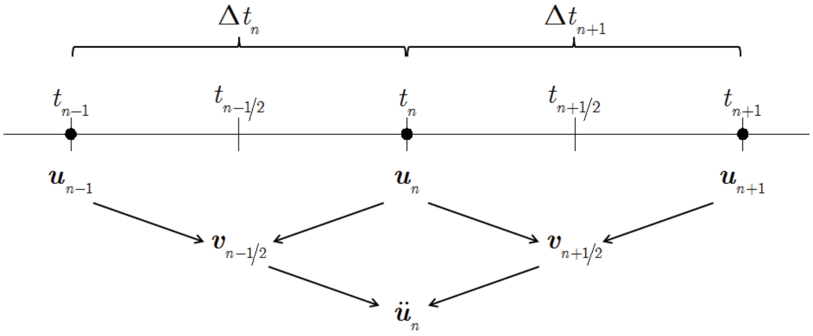

Figure 3.1 Central difference scheme.

The relevant mid-increment velocities are defined as:

$$\boldsymbol{v}_{n-1/2} = \frac{\boldsymbol{u}_n - \boldsymbol{u}_{n-1}}{\Delta t_n} \text{ and } \boldsymbol{v}_{n+1/2} = \frac{\boldsymbol{u}_{n+1} - \boldsymbol{u}_n}{\Delta t_{n+1}}. \tag{3.19}$$

The second order central difference equation for acceleration at time t_n is given by:

$$\ddot{\boldsymbol{u}}_n = \frac{\boldsymbol{v}_{n+1/2} - \boldsymbol{v}_{n-1/2}}{\Delta t_{n+1/2}} \tag{3.20}$$

where $\Delta t_{n+1/2}$ is an average time step, calculated as:

$$\Delta t_{n+1/2} = \frac{\Delta t_n + \Delta t_{n+1}}{2}. \tag{3.21}$$

Using Equations (3.18) and (3.20), the mid-increment velocity $\boldsymbol{v}_{n+1/2}$ can be rewritten as:

$$\boldsymbol{v}_{n+1/2} = \boldsymbol{v}_{n-1/2} + \Delta t_{n+1/2} \boldsymbol{M}^{-1} \left[\mathbf{f}^{\text{int}} \left(\boldsymbol{u}_n \right) - \mathbf{f}_n^{\text{ext}} \right] \tag{3.22}$$

and displacement, at time t_{n+1}, calculated as:

$$\boldsymbol{u}_{n+1} = \boldsymbol{u}_n + \Delta t_{n+1} \boldsymbol{v}_{n+1/2}. \tag{3.23}$$

After the computation of the displacement field, the dynamic explicit solution strategy proceeds with the calculation of internal force vector $\mathbf{f}_{n+1}^{\text{int}} \left(\boldsymbol{u}_{n+1} \right)$ assembled from the individual contributions of the internal force vector for each element:

$$\mathbf{f}_{(e)}^{\text{int}} = \int_{\varphi\left(\mathcal{B}^{(e)}\right)} \mathbf{B}^T \hat{\boldsymbol{\sigma}} \left(\boldsymbol{u}_{n+1}, \boldsymbol{\alpha}_n \right) dv \tag{3.24}$$

where $\hat{\boldsymbol{\sigma}}$ is the vector containing the Cauchy stress components delivered by the constitutive model algorithm. This assembling is made in such way that a global stiffness matrix is not needed to be formed [ABAQUS 2008]. In this stage, it is required to integrate the constitutive equation over the time step Δt_{n+1} and obtain the corresponding updated Cauchy stress. This local integration of the constitutive equations is further explained in Section 3.4. The external force vector $\mathbf{f}_{n+1}^{\text{ext}}$, comprising all forces acting on boundary, including contact forces, is also assembled from the individual contributions of the external force vector for each element:

$$\mathbf{f}_{(e)}^{\text{ext}} = \int_{\varphi\left(\mathcal{B}^{(e)}\right)} \mathbf{N}^T \boldsymbol{f}_{n+1} dv + \int_{\varphi\left(\partial\mathcal{B}^{(e)}\right)} \mathbf{N}^T \boldsymbol{t}_{n+1} da. \tag{3.25}$$

Finally, the velocity field at time t_{n+1} can also be evaluated by using the mid-increment quantity as:

$$\boldsymbol{v}_{n+1} = \boldsymbol{v}_{n+1/2} + \frac{1}{2} \Delta t_{n+1} \ddot{\boldsymbol{u}}_{n+1}. \tag{3.26}$$

The dynamic explicit solution strategy is conveniently summarized in Box 3.1. As seen, no iteration procedure is required for the dynamic explicit scheme as well as the assembling of the tangent stiffness matrix. However, no verification is performed at time t_{n+1} concerning the equilibrium state. Due to the intrinsic conditional stability of the central difference operator [Klerck 2000], this incremental solution procedure is also

Box 3.1 Dynamic Explicit (DE) solution strategy.

i) Lump the mass matrix and set initial conditions:

$$\boldsymbol{M} \rightarrow \boldsymbol{M}^L\,;$$

ii) Estimate the time step Δt_{n+1} by calculating the critical time step:

$$\Delta t_{n+1} = \Delta t_{cr}\,;$$

iii) Update displacements $\boldsymbol{u}_{n+1}$:

$$\boldsymbol{u}_{n+1} = \boldsymbol{u}_n + \Delta t_{n+1} \boldsymbol{v}_{n+1/2}\,,$$

$$\boldsymbol{v}_{n+1/2} = \boldsymbol{v}_{n-1/2} + \frac{\Delta t_n + \Delta t_{n+1}}{2} \ddot{\boldsymbol{u}}_n\,,$$

$$\boldsymbol{v}_{n-1/2} = \frac{\boldsymbol{u}_n - \boldsymbol{u}_{n-1}}{\Delta t_n}\,;$$

iv) Compute the stress $\boldsymbol{\sigma}_{n+1}$ and internal variables $\boldsymbol{\alpha}_{n+1}$ by integrating the full set of constitutive equations (see Section 3.4);

v) Compute the internal forces $\mathbf{f}^{\text{int}}_{n+1}\left(\boldsymbol{u}_{n+1}\right)$ vector:

$$\mathbf{f}^{\text{int}}_{n+1}\left(\boldsymbol{u}_{n+1}\right) = \mathop{\mathbf{A}}_{e=1}^{n_{\text{elem}}} \left(\mathbf{f}^{\text{int}}_{(e)}\right);$$

vi) Compute the external forces $\mathbf{f}^{\text{ext}}_{n+1}$ vector:

$$\mathbf{f}^{\text{ext}}_{n+1} = \mathop{\mathbf{A}}_{e=1}^{n_{\text{elem}}} \left(\mathbf{f}^{\text{ext}}_{(e)}\right);$$

vii) Solve discretized dynamic system for the accelerations:

$$\ddot{\boldsymbol{u}}_{n+1} = \left(\boldsymbol{M}^L\right)^{-1} \left[\mathbf{f}^{\text{int}}_{n+1}\left(\boldsymbol{u}_{n+1}\right) - \mathbf{f}^{\text{ext}}_{n+1}\right];$$

viii) Compute the velocity field:

$$\boldsymbol{v}_{n+1} = \boldsymbol{v}_{n+1/2} + \frac{1}{2}\Delta t_{n+1} \ddot{\boldsymbol{u}}_{n+1}\,;$$

ix) If $t < t_{\max}$ go to (ii), if not STOP.

conditionally stable, being the accuracy of the solution of the IBVP highly dependent on the chosen time step Δt. Therefore, and according to the high nonlinearity of the system (Equation (3.8)), the explicit scheme should be used only with an automatic variation of time increment Δt. So, it is essential to establish some restrictions in such automatic time step control in order to avoid exceeding stability limits and to control solution accuracy. An approximation to the stability limit is often written as the smallest transit time of a dilatational wave across any of the elements in the mesh:

$$\Delta t \leq \min\left(\frac{L^e}{c_d}\right) \tag{3.27}$$

where L^e is the smallest element dimension in the mesh (calculated as the smallest distance between adjacent nodes of the element e) and c_d is the dilatational wave speed of the material, determined by calculating the effective hypoelastic material moduli from the material's constitutive response (for more details see [ABAQUS 2008]).

As the critical time interval calculated by Equation (3.27) can be of order 10^{-7} or lower, the number of required increments for a stamping simulation can easily exceed one million, representing unacceptable calculation times. To reduce the necessary number of increments, some numerical artifices are used to achieve such aimed reduction [Alves 2003], namely the virtual increase of the punch speed comparatively to the real punch speed (and thus reducing the total time $t_{\max}$) and / or the virtual increase of density, reducing the dilatational wave speed of the material, and, according to Equation (3.27), allowing larger time intervals.

3.4 Local integration of constitutive equations

Whatever the solution scheme is chosen, there is a central issue in the incremental solution procedures: the computation of the new stress state $\boldsymbol{\sigma}_{n+1}$ and the updated set of internal variables $\boldsymbol{\alpha}_{n+1}$ based on the incremental displacement $\Delta\boldsymbol{u}$ and the knowledge of the converged values $\boldsymbol{\sigma}_n$ and $\boldsymbol{\alpha}_n$ at time t_n. Using the additive decomposition of the rate of deformation tensor, the objective class of phenomenological constitutive equations can be defined as:

$$\boldsymbol{\sigma}^{\bullet} = \mathbf{E} : \boldsymbol{d}^e = \mathbf{E} : \left(\boldsymbol{d} - \boldsymbol{d}^p\right) \tag{3.28}$$

where $\sigma^{\bullet}$ is an objective stress rate of the spatial Cauchy stress, $\mathbf{E}$ is the objective fourth order linear elastic operator and $\boldsymbol{d}^p$ is the plastic rate of deformation, defined by a flow rule as:

$$\boldsymbol{d}^p = \dot{\gamma}\frac{\partial\Phi}{\partial\boldsymbol{\sigma}} \tag{3.29}$$

where $\dot{\gamma}$ is the plastic consistency parameter and Φ is a plastic potential. To satisfy the objectivity requirement, the original rate constitutive equation is mapped into a rigid motion-insensitive local configuration. This approach is formally known as rotation neutralized description or rotated frame formulation. In this work, the objective Green-Naghdi stress update procedure is adopted. It must be remarked that the elastic response predicted by the rate-form constitutive equation will be dependent on the objective stress rate employed. However, since in metal plasticity elastic strains are small, the inconsistencies associated with these hypoelastic-based models remain almost negligible.

Let us consider a time interval $\Delta t = t_{n+1} - t_n$ and, for this time interval, the midpoint velocity gradient $\boldsymbol{l}_{n+1/2}$ is given by:

$$\boldsymbol{l}_{n+1/2} = \nabla_{n+1/2}\boldsymbol{v}_{n+1/2} \tag{3.30}$$

obtained for the midpoint configuration $\boldsymbol{u}_{n+1/2}$ defined as:

$$\boldsymbol{u}_{n+1/2} = \boldsymbol{u}_n + \frac{1}{2}\Delta\boldsymbol{u} \tag{3.31}$$

by the calculation of the corresponding mid-increment velocity:

$$\boldsymbol{v}_{n+1/2} = \frac{\boldsymbol{u}_{n+1} - \boldsymbol{u}_n}{\Delta t}. \tag{3.32}$$

Using the velocity gradient defined in Equation (3.30), it is possible to define the midpoint stretching tensor:

$$\boldsymbol{d}_{n+1/2} = \operatorname{sym}\left(\boldsymbol{l}_{n+1/2}\right). \tag{3.33}$$

Applying the same midpoint rule, the equivalent rate form, in the local rotated configuration, of the rate constitutive equation defined in Equation (3.28) is given by:

$$\boldsymbol{\Sigma}_{n+1} - \boldsymbol{\Sigma}_n = \Delta t\dot{\boldsymbol{\Sigma}}_{n+1/2} = \mathsf{E} : \Delta t\boldsymbol{D}_{n+1/2} \tag{3.34}$$

where $\boldsymbol{\Sigma}_n$ denotes the rotated Cauchy stress tensor, calculated as:

$$\boldsymbol{\Sigma}_n = \boldsymbol{R}_n^T\boldsymbol{\sigma}_n\boldsymbol{R}_n \tag{3.35}$$

and the midpoint rotated stretching tensor, denoted as $\boldsymbol{D}_{n+1/2}$, is computed as:

$$\boldsymbol{D}_{n+1/2} = \boldsymbol{R}_{n+1/2}^T\boldsymbol{d}_{n+1/2}\boldsymbol{R}_{n+1/2}. \tag{3.36}$$

The midpoint rotation tensor $\boldsymbol{R}_{n+1/2}$ is calculated by the polar decomposition of the deformation gradient at the midpoint configuration:

$$\boldsymbol{F}_{n+1/2} = \boldsymbol{R}_{n+1/2}\boldsymbol{U}_{n+1/2} = \boldsymbol{I} + \frac{1}{2}\nabla_{n+1/2}\left(\Delta\boldsymbol{u}\right). \tag{3.37}$$

In order to achieve second-order accuracy [Klerck 2000], the strain increment is evaluated at the midpoint configuration:

$$\Delta\boldsymbol{\varepsilon} = \boldsymbol{R}_{n+1/2}^{T}\left(\Delta t\boldsymbol{d}_{n+1/2}\right)\boldsymbol{R}_{n+1/2} \tag{3.38}$$

conveniently rotated to the reference configuration. After the computation of all the above quantities, the algorithm proceeds with the computation of the updated rotated stress $\boldsymbol{\Sigma}_{n+1}$ using the standard small strain integration algorithm, here denoted as [Pires 2005]:

$$\boldsymbol{\Sigma}_{n+1} = \hat{\boldsymbol{\Sigma}}\left(\boldsymbol{\Sigma}_{n}, \Delta\boldsymbol{\varepsilon}, \boldsymbol{\alpha}_{n}\right) \tag{3.39}$$

where $\boldsymbol{\alpha}_{n}$ represents a set of internal variables, that should be rotated accordingly if tensorial variables are included.

The standard small strain integration algorithm relies in the operator split methodology that results in an algorithm which consists of two basic steps [Pires 2005]. The first step corresponds to the elastic predictor, where the problem is supposed to be purely elastic between times t_{n} and t_{n+1} and, therefore, no plastic flow neither internal variable evolution is assumed to occur. If this elastic trial state is plastically admissible, then the process is indeed purely elastic and the updated state corresponds to the computed trial state. Otherwise, plastic yielding occurs between times t_{n} and t_{n+1}, then the second step, the plastic corrector, is used in order to restore consistency by “returning” the trial stress to the yield surface. In this step, the elastic trial state is taken as the initial condition in the solution of a discrete system of equations comprising the elasticity law, plastic flow, internal variables evolution and the loading / unloading criterion, written as:

$$\dot{\gamma} \geq 0\,;\ \Phi \leq 0\,;\ \dot{\gamma}\Phi = 0\,. \tag{3.40}$$

Finally, after the computation of the updated rotated stress $\boldsymbol{\Sigma}_{n+1}$, the updated stress $\boldsymbol{\sigma}_{n+1}$ is obtained by rotating the updated rotated quantity back to the spatial configuration:

$$\boldsymbol{\sigma}_{n+1} = \boldsymbol{R}_{n+1}\left(\boldsymbol{\Sigma}_{n+1}\right)\boldsymbol{R}_{n+1}^{T}\,. \tag{3.41}$$

The incrementally objective integration algorithm for a general Green-Naghdi rate-based finite plasticity model is summarized in Box 3.2. It should be mentioned that, throughout this thesis and for the sake of simplicity, all tensorial quantities used in the development of rate-independent plasticity algorithms in subsequent chapters are assumed to be in the rotated configuration, and, so, all subscripts and specific rotated quantities notation will be omitted.

Box 3.2 Objective Green-Nagdhi stress update procedure.

i) Update configuration and compute midpoint configuration:

$$\boldsymbol{u}_{n+1} = \boldsymbol{u}_{n} + \Delta \boldsymbol{u}_{n+1}\,,\ \boldsymbol{u}_{n+1/2} = \boldsymbol{u}_{n} + \frac{1}{2}\Delta \boldsymbol{u}\,;$$

ii) Compute midpoint velocity configuration:

$$\boldsymbol{v}_{n+1/2} = \frac{\boldsymbol{u}_{n+1} - \boldsymbol{u}_{n}}{\Delta t} = \frac{\Delta \boldsymbol{u}}{\Delta t}\,;$$

iii) Compute midpoint velocity gradient and stretching tensors:

$$\boldsymbol{l}_{n+1/2} = \nabla_{n+1/2}\boldsymbol{v}_{n+1/2}\,,\ \boldsymbol{d}_{n+1/2} = \mathrm{sym}\left(\boldsymbol{l}_{n+1/2}\right);$$

ii) Perform polar decomposition to assemble rotation matrices:

$$\boldsymbol{F}_{n} = \boldsymbol{R}_{n}\boldsymbol{U}_{n}\,,\ \boldsymbol{F}_{n+1/2} = \boldsymbol{R}_{n+1/2}\boldsymbol{U}_{n+1/2}\,,\ \boldsymbol{F}_{n+1} = \boldsymbol{R}_{n+1}\boldsymbol{U}_{n+1}\,;$$

iv) Calculate strain increment at midpoint configuration:

$$\Delta\boldsymbol{\varepsilon} = \boldsymbol{R}_{n+1/2}^{T}\left(\Delta t\boldsymbol{d}_{n+1/2}\right)\boldsymbol{R}_{n+1/2}\,;$$

v) Map Cauchy stress from previous configuration (time t) to reference configuration:

$$\boldsymbol{\Sigma}_{n} = \boldsymbol{R}_{n}^{T}\left(\boldsymbol{\sigma}_{n}\right)\boldsymbol{R}_{n}\,;$$

vi) Update rotated stress in reference configuration:

$$\boldsymbol{\Sigma}_{n+1} = \hat{\boldsymbol{\Sigma}}\left(\boldsymbol{\Sigma}_{n}, \Delta\boldsymbol{\varepsilon}, \boldsymbol{\alpha}_{n}\right);$$

vii) Update Cauchy stress in spatial configuration by mapping rotated stress from reference configuration:

$$\boldsymbol{\sigma}_{n+1} = \boldsymbol{R}_{n+1}\left(\boldsymbol{\Sigma}_{n+1}\right)\boldsymbol{R}_{n+1}^{T}\,.$$

3.5 Contact with friction modelling

Since interaction between tool and blank is always present in metal forming processes, the numerical treatment of contact with friction must be taken into account because the frictional behaviour has an important contribution in the equilibrium equations, as a part of the external force vector. The contact with friction modelling introduces additional initial and evolving boundary conditions and adds extra complexity to the boundary value problem due to the non-linear nature of the introduced boundary conditions. Two main subjects must be addressed in the contact-friction modelling: the contact search algorithm and the numerical treatment of the contact occurrences.

Basically, contact is established between two surfaces: a master surface, considered as a reference, and a slave surface, which relative movement to the first one is mapped. Both surfaces can be considered as deformable surfaces, but, usually, in metal forming, the tool surface (master) is considered as a rigid (undeformable) surface while the part surface is defined as a deformable one, being only necessary to satisfy contact-friction equations for this deformable body.

The contact search algorithm allows detecting any kinematic incompatibilities such as the penetration of the slave surface nodes into the master surface. This task can be an extremely time-consuming step in the numerical simulation. An efficient algorithm should use, at first, a global search stage, to detect potential areas where the contact interaction can be introduced, and, then, a local search algorithm, in order to determine the location where the contact is established. This hierarchical global / local search algorithm promotes an increase of algorithm efficiency and a subsequent reduction in the computation time spent in this search task [ABAQUS 2008].

Important in this master / slave strategy is the way the rigid surfaces are defined. Several ways can be considered in the definition of tool surfaces: analytical functions, parametric surfaces, points or rigid elements. A critical assessment of the advantages and disadvantages of these different tool descriptions is provided in [Santos 1993]. The calculation of surface normal, required for the computation of gap distance between tool surface and nodes from deformable body, will be necessarily depending on the type of tool surface description. But, no matter the tool description approach, the impenetrability condition must hold and can be stated by the Signorini conditions:

$$d \geq 0\,;\; F_n \geq 0 \text{ and } dF_n = 0 \tag{3.42}$$

where d and F_n represent the distance and normal component of the contact force, respectively. The solution of these contact conditions can be undertaken by different methods: Lagrange multipliers method, penalty method and augmented Lagrangian method [Alves 2003]. Once contact is established, it is required to calculate contact and friction kinematic variables, by using appropriate frictional constitutive equations.

The friction mechanism is a highly complex phenomenon and depends directly of several factors: contact pressure, sliding speed, material of contacting bodies, surface roughness, lubrication, temperature, etc. Due to the large variety of highly interactive factors, the formulation of the contact-friction models is a very complex task justifying the limit number of available theoretical and numerical methods for the modelling of contact-friction behaviour. Moreover, these available models are considered too simplistic in comparison to the real physical phenomenon [Alves 2003]. The main used contact-friction constitutive law is the classical Coulomb friction model, which is based on a phenomenological approach and follows a formalism similar to the plasticity theory. The basic concept of this model is to relate the maximum allowable frictional (shear) stress across an interface to the contact pressure between the contacting bodies [ABAQUS 2008]. To relate both quantities, a friction yield surface is introduced and a definition of an equivalent tangential stress must be provided. In a 3D contact situation, the equivalent tangential stress, τ_{eq}, is given by:

$$\tau_{eq} = \sqrt{\tau_1^2 + \tau_2^2} \tag{3.43}$$

where τ_1 and τ_2 are the two principal directions of tangential stresses, calculated in the contact interface. Using this equivalent quantity, the Coulomb friction model can be defined as:

$$\begin{cases} \tau_{eq} < \mu P \Rightarrow v_t = 0 & \text{(sticking contact)} \\ \tau_{eq} > \mu P \Rightarrow \left|v_t\right| > 0 & \text{(sliding contact)} \end{cases} \tag{3.44}$$

where P is the contact pressure, v_t is the relative tangential velocity and μ is the friction coefficient. In words, the Coulomb friction model defines a critical shear stress, $\tau_{crit} = \mu P$, at which sliding of the surfaces starts as a fraction of the contact pressure, P, between the surfaces. In this classical model, the friction coefficient is considered to be isotropic (not dependent upon the sliding direction) and assumed constant during all forming operation.

For further discussion about these contact issues and numerical aspects, reader is referred to more specific works as [Santos 1993] [Oliveira 2005] and user’s manual [ABAQUS 2008], among others.

4. ISOTROPIC DAMAGE MECHANICS

This chapter reviews some basic concepts of internal damage in solids. A review on developments in Continuum Damage Mechanics is provided and the original isotropic damage model proposed by Lemaitre [1984] is presented. An enhancement to this model is proposed by the inclusion of plastic anisotropy described by the Hill48 yield criterion. For the numerical implementation, two integration algorithms are presented: partial coupling and full coupling schemes. Based on the simplified partial coupling algorithm, quasi-unilateral effects on damage evolution are introduced in order to model micro-crack closure effect under compressive stress states.

4.1 Introduction

The growing knowledge of the physical mechanisms that promote internal progressive deterioration of the mechanical properties for a high range of materials turned possible the formulation of constitutive models capable of describing the initiation and evolution of such mechanical degradation. This new branch of Continuous Mechanics theory is known as Continuous Damage Mechanics (CDM). The progress in the understanding of physical phenomena, allied with the development of the numerical techniques, allowed that the use of computational tools can perform reliable failure predictions and determine the remaining useful life of structural components, representing, therefore, a viable alternative decision tool in the development of new products and in the determination of current damage state of a component in service.

After more than four decades since its origin, Continuous Damage Mechanics has now reached a development stage that allows solving most of the practical engineering problems. The theory is based on the definition of a continuous variable (damage), which can be related to the density of internal defects, to describe the evolution of mechanical deterioration of the material before the initiation of macro-cracks. This continuous quantity is one of the main aspects that distinguish this theory from other branches such as the Fracture Mechanics framework, which considers the process of initiation and growth of micro-cracks as a discontinuous phenomenon. Especially important for our main area of interest (metal forming processes) is the ductile damage phenomenon, for which is given a particular emphasis in the brief historical review provided in the next paragraphs.

4.2 Physical aspects of internal damage in solids

Damage in materials is the physical process of progressive deterioration that can lead to macroscopic collapse. That degradation is the result of the nucleation, growth and coalescence of micro-cracks and micro-cavities, visible from microscopic observations. The description of this internal degradation, as well as the its scale (microscopic, macroscopic or structural), is strongly dependent on the material, type and rate of loading application, temperature and other environmental factors to which the material is subjected. Therefore, instead of analyzing only the material itself, it is important to consider a combined analysis including also the thermo-mechanical process, in order to study the evolution of material degradation. Although it is nearly impossible to enumerate all damaging processes in the case of metallic materials, the damaging phenomenon can be generally divided in two different types: brittle damage and ductile damage.

Brittle damage occurs mainly in the form of cleavage of crystallographic planes in the presence of negligible inelastic deformations [Souza Neto 2008]. It is associated with cleavage forces that, although small to produce slips, are sufficient to overcome debonding forces. This behaviour is usually observed for many metallic materials at low temperatures, but it can also appear for high temperatures, associated with creep mechanisms. Ductile damage occurs simultaneously with large plastic deformations, larger than a certain threshold [Lemaitre 1996]. It results from the nucleation of cavities due to decohesions between inclusions and the matrix followed by their growth and their coalescence through the phenomenon of plastic instability. Although a distinction can be made between brittle and ductile damage, for most metallic materials, damage behaviour is a combination of brittle and ductile response.

Another type of damage, worth mentioning, is the fatigue damage. It occurs when material is subjected to a large number of loading and / or temperature cycles, at a low stress level, below the macroscopic yield stress limit. Strains remain also very low and are almost negligible. Despite the low meso-scale stress level, micro-cracking nucleates in highly stressed areas near microscopic defects, where localized cycles of plastic deformation occur [Souza Neto 2008]. Fatigue damage is essentially attributed to this micro-cracking caused by this cyclic straining and also to the accumulation of dislocations. Coalescence of these micro-cracks often results in a transgranular crack propagation mode.

In this work, we will limit ourselves to the study of ductile damage. Three important phases occur in the ductile damaging process [Chaboche 2007], as shown in Figure 4.1.

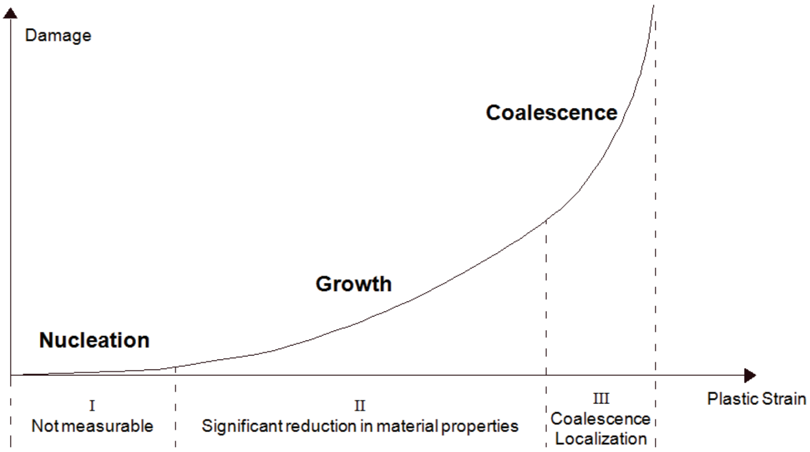

Figure 4.1 Schematic of ductile damage evolution.

The first phase corresponds to a limited apparent deterioration and, although it leads to a reduction in remaining life, its effects on the physical properties of the material can be neglected. In this phase, nucleation of micro-cracks at the boundaries of some favourable inclusions is the main damaging process. During second phase, nucleation still occurs but a significant growth of already nucleated micro-cracks is observed. This growth is associated with particle debonding, rupture of brittle phases, very localized and intense dislocation pilings and deformation accumulations, leading to cavities or micro-cracks. The material properties are highly affected in this phase and damage effect in mechanical properties can be measured. The last phase corresponds to the coalescence of local damage defects due to the proximity between them and the failure of residual ligaments due to high localized plastic deformation. Further coalescence results in the localization into a main defect that can be considered as a major crack [Chaboche 2007]. This last phase corresponds to the limit of validity of CDM approaches, being acceptable to make a macro-crack analysis in order to define its propagation, i.e., the consideration of a Fracture Mechanics-based model.

4.3 Continuous Damage Mechanics developments

4.3.1 Original developments

At microscopic scale, damage can be considered as a discontinuous phenomenon, related with decohesion of interatomic bounds or the plastic magnification of micro-voids. Without a well-defined physical definition, Kachanov [1958] was the first author to propose the definition of a continuous internal variable to reflect the density of such defects and to characterize the observable loss of load-carrying capability. The physical interpretation of damage was later developed by Rabotnov [1963] who proposed the reduction of the cross-sectional area due to the presence of cracks and cavities as the measure for the state of internal damage. In order to define and manipulate this dimensionless variable, it is necessary to enlarge the phenomena to the scale of a representative volume element (RVE) that contains enough and randomly distributed defects so that damage mechanism can be well represented by a mean variable, leading to continuous variable [Voyiadjis 2005]. Let A be a sectional area of a damaged RVE identified by its normal $\boldsymbol{n}$.

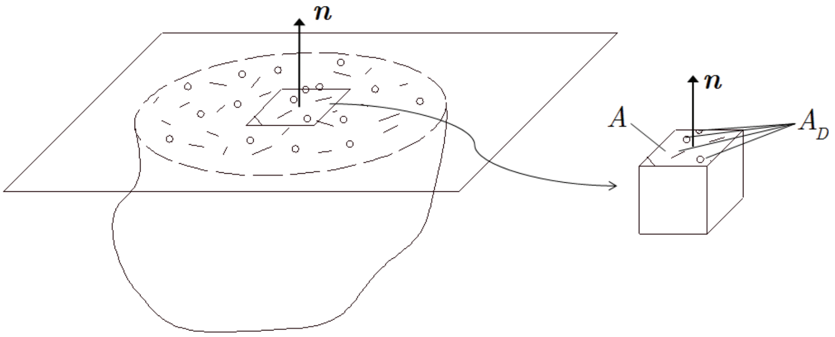

Figure 4.2 Damaged representative volume element.

In this sectional area, micro-cracks and cavities (which constitute damage) assume different shapes and sizes and are randomly distributed. Consider an effective resistant area $\tilde{A}$, lower than the original area A ($\tilde{A} < A$), taking into account the area occupied by those defects, the micro-stress concentrations in the neighbourhood of geometric discontinuities and the interactions between the neighbouring defects [Lemaitre 1984]. The difference between original area A and effective resistant area $\tilde{A}$:

$$A_D = A - \tilde{A} \tag{4.1}$$

gives the total area of defects. Damage is then introduced as:

$$D = \frac{A_D}{A}, \tag{4.2}$$

representing a ratio between the total area of defects A_D and the total sectional area A. From a mathematical point of view, when the total area of defects A_D tends to the total sectional area A, damage D will tend to 1, and thus, damage can assume values from 0 ($A_D = 0$), corresponding to virgin (undamaged) material, up to 1 ($A_D = A$), corresponding to the fully damaged material and the physical separation of the RVE in two parts. So, the physical definition for the damage value can be postulated as the relative (or corrected) area of cracks and cavities, cut by a plane normal to the direction $\boldsymbol{n}$.

The introduction of a damage variable which represents a surface density of discontinuities in the material leads directly to the concept of effective stress, i.e., to the stress calculated over the section which effectively resists the forces [Voyiadjis 2005]. Considering an uniaxial case, if a force F is applied to a RVE with a transverse section A, the stress that satisfies the balance is given by:

$$\sigma = \frac{F}{A}. \tag{4.3}$$

But, in the presence of damage, the resistant area is reduced due to the presence of micro-cracks and force F will act in this reduced or effective area. The effective or corrected area $\tilde{A}$ is obtained from the initial area A by the relation (using Equation (4.1) and (4.2)):

$$\tilde{A} = A - A_D = A\left(1 - D\right). \tag{4.4}$$

This reduction in the resistant area increases stress effects induced by the external force. This magnified or effective stress $\tilde{\sigma}$ is given by the expression:

$$\tilde{\sigma} = \frac{F}{\tilde{A}} = \frac{F}{A\left(1 - D\right)} = \frac{\sigma}{1 - D}. \tag{4.5}$$

In order to describe the strain rate increase that characterizes tertiary creep, Kachanov [1958] has replaced the observed uniaxial stress σ by this effective stress $\tilde{\sigma}$ in the standard Norton's law for creep.

After this pioneering work of Kachanov [1958] and Rabotnov [1963], essentially applied to describe creep failure in metallic materials, several works have followed this starting point of CDM. Using a thermodynamic formalism, the theoretical concepts of CDM were later described by Germain *et al.* [1983] and successfully extended to describe other types of damage: Elastic-brittle [Murakami 1997] [Lubarda 1995] [Murakami 1988], brittle [Krajcinovic 1981] [Krajcinovic 1983], creep [Murakami 1981] [Leckie 1974], fatigue [Chaboche 1988a] [Chaboche 1988b] [Lemaitre 1999] and creep-fatigue damage [Chaboche 1988a] [Chaboche 1988b].

Concerning damage quantification, damage effects are measurable during second phase of damaging process, as already stated in Section 4.2. Different methods can be used for such measurement [Lemaitre 1987]. In a broad sense, they can be divided into direct and non-direct methods. Direct methods are based on the direct assessment of micro-cracks, volume fraction of defects and cavities, present in the material. This is done by the observation of micrographic pictures or by using the decrease of the density, measurable based on the Archimedean principle. In non-directs methods, as the name states, damage is not measured directly but through its effects on mechanical behaviour. The most popular method for damage evaluation is the measurement of its influence on the degradation of elastic moduli by ultrasonic waves propagation methods or micro-hardness techniques [Mkaddem 2006]. A critical assessment of the reliability of the latter indentation-based damage quantification procedures is discussed in [Tasan 2009].

4.3.2 Ductile damage

Ductile fracture in structural metals deformed at room temperature takes place by the nucleation, growth and coalescence of micro-voids. The voids generally nucleate by decohesion of second-phase particles or by particle fracture, and grow by plastic deformation of the surrounding matrix. Due to great difficulties in the modelling of interactivity between micro-cracks and their spatial distribution, at the present, micromechanical analyses are meaningful only under the assumption of dilute micro-cracks. Also, since microscopic-macroscopic homogenization procedures are rather time consuming, the rigor of quantum mechanics is ultimately traded for the computational efficiency needed in engineering design, using phenomenological models [Wu 2008].

An extensive literature concerning damage accumulation in ductile materials has been published. Generally, they can be divided into two main frameworks: micromechanical-based (or physical) damage models and phenomenological damage models. The first framework is related with the original work developed by Gurson [1977], that has formulated a model for the description of material degradation by using an internal variable that represents the volume fraction of spherical voids, f, defined as the ratio between the accumulated volume of individual voids and the total volume of the RVE. In order to establish the coupling between plasticity and damage, Gurson [1977] proposed an approximate macroscopic yield function for a ideally plastic matrix material containing a certain volume of fraction voids, considering the effects of hydrostatic stress. The evolution equation for the volume fraction was obtained as a sum of three rates, representing the three phases of damage mechanism (nucleation, growth and coalescence) being postulated from experimental observations [Gurson 1977]. This model was later developed by Tvergaard [1982] and Tvergaard and Needleman [1984], who have modified Gurson's yield function in order to account for rate sensitivity and necking instabilities in plastically deforming solids and to provide better representation of final void coalescence. The Gurson-Tvergaard-Needleman (GTN) model has shown to be especially suitable for the representation of behaviour of porous materials although it is also used for sheet metals [Brunet 2001] [Chen 2009].

The other framework, called phenomenological approach, is based on the classical CDM theory proposed by Lemaitre *et al.* [1984] [1985a] [1985b], who has described the above discussed three phases of ductile damage by using a purely phenomenological model within the framework of thermodynamics of irreversible processes [Germain 1983] [Lemaitre 2000b]. The original development was made by assuming an isotropic condition, i.e., considering that cracks and voids were equally distributed in all directions, not dependent upon $\boldsymbol{n}$ (see Figure 4.2) and, therefore, the intrinsic damage variable was represented by a scalar D (Chapter 5 deals with higher-order definition of damage variables). Evoking the method of local state [Lemaitre 1996], Lemaitre has postulated the principle of strain equivalence which states that "Every strain behaviour of a damaged material is represented by constitutive equations of the undamaged material in the potential of which the stress is simply replaced by the effective stress", avoiding a micromechanical analysis for each type of defect and each type of mechanism of damage. Using this principle and the effective stress concept, it is possible to establish the uniaxial law of elasticity of a damaged material as:

$$\tilde{\sigma} = E\varepsilon \tag{4.6}$$

or, equivalently, as:

$$\sigma = \tilde{E}\varepsilon \tag{4.7}$$

where E and:

$$\tilde{E} = \left(1 - D\right)E \tag{4.8}$$

are the Young's moduli of virgin (undamaged) and damaged materials, respectively. Hence, the variation of the Young's modulus as ductile damage progresses can be used as the measure of damage itself, redefining it as:

$$D = 1 - \frac{\tilde{E}}{E} \tag{4.9}$$

for a ideally isotropic case, instead of the evaluation of load bearing area by means of micrographic pictures. Another type of equivalence principle was proposed by Cordebois and Sideroff [1982], the energy equivalence principle, which considers an equivalence of elastic strain energy between the effective (undamaged) material and the current damaged configuration. A drawback of this equivalence principle is the significant constraints that are induced on the form of the damaged elastic stiffness (or compliance stiffness) [Chaboche 2007].

The thermodynamically consistent framework developed by Lemaitre *et al.* [1985a] [1996] for the description of elasto-plasticity with damage has been a subject of study and developments over the past three decades. Several alternative formulations have emerged, mainly related with different equivalence assumptions (strain or energy equivalences), with different forms of state coupling (inclusion of damage in the Helmholtz free energy or Gibbs thermodynamic potential) and with different coupling of dissipations (coupling between damage and plasticity mechanisms).

Concerning state coupling, the equivalence principles and the effective stress concept allow to establish a state coupling between elasticity and damage. The initial theoretical format, as proposed by Lemaitre and Chaboche [1978], considers that state coupling remains linked only with the elastic part of the Helmholtz free energy and there is no coupling between damage and hardening. This theory provides an associated thermodynamical force that has the same meaning, no matter if a purely elastic or elasto-plastic case is considered. Later, Cordebois and Sideroff [1982] included an additional term in the free energy, dependent of a new variable β that represents a measure of cumulative damage. Although this theory does not introduce an explicit coupling between damage and hardening, it adds another term in the energy dissipated by damage, corresponding to the product between the new variable and its corresponding thermodynamical force. A stronger state coupling is achieved by considering that damage influences both elastic and plastic terms in the Helmholtz free energy. This approach is followed by Ju [1989] and Saanouni *et al.* [2000]. Obviously, the introduction of this dependence changes the conjugate thermodynamical force, now containing two terms, corresponding to the elastic and plastic-damaged components.

Concerning coupling of dissipative phenomena, Lemaitre's original theory [Lemaitre 1985a] [Lemaitre 1996] assumes that both plasticity and damage are governed by a single mechanism and by a single dissipation potential. This dissipation potential, from which derives the evolution equations, is assumed to be additively decomposed into plastic and damage terms. With this assumption, there is a strong coupling between the two dissipative processes, plasticity and damage, meaning that damage cannot take place without plastic yielding. This can be seen as a strong limitation, especially in the cases where damage occurs without significant plastic flow, as for example, high-cycle fatigue. To overcome this limitation, Lemaitre *et al.* [1999] used a two scale model applied to fatigue deterioration, considering a micro-mechanics based model of a weak micro-inclusion subjected to plasticity and damage embedded in an elastic meso-element. Due to distinct degradation phenomena taking place in plasticity (dislocation along slip planes) and damage (micro-crack nucleation, growth and coalescence), other theories have postulated the existence of several independent dissipation potentials, each one associated with a dissipative process. This is the case of the framework followed by several authors [Cordebois 1982] [Chow 1987] [Zhu 1995] [Al-Rub 2003] [Voyiadjis 2009]. Besides the plastic flow potential, an additional potential is associated with damage mechanism and damage effects are introduced in the plastic flow potential through the effective stress concept. This double-dissipative coupled model allows that damage yielding and plastic yielding can occur independently, letting damage evolution occurrence without plasticity, thus providing a simplified analysis in the case of high-cycle fatigue.

Another question is related with the selection of the plastic yielding surface. The effective stress concept supplies a limited choice for the plastic yield surface selection [Chaboche 2007]. In his original work, Lemaitre [1996] considered that damage only influences Cauchy stress tensor $\boldsymbol{\sigma}$ and no amplification of hardening is considered due to damage growth. This assumption leads to a plastic yield surface not centered in the back-stress tensor $\boldsymbol{X}$. A more standard form of the plastic yield surface is to include damage effects in the kinematic hardening term, as later proposed by Lemaitre and Chaboche [1990], and, therefore, elastic domain remains centered on the effective back-stress tensor $\tilde{\boldsymbol{X}}$ in the stress space. Another possibility was explored by Saanouni *et al.* [2000] [2006] by including the definition of an effective isotropic hardening variable $\tilde{R}$. Although good results were obtained, this approach present some difficulties to generalize for higher-order damage variables and, so, the previous form is usually preferred [Chaboche 2007].

Despite the considered state or dissipation coupling, computational aspects were also subject of different approaches. Two main ways can be taken to numerically simulate damage occurrence: uncoupled and coupled approaches. Uncoupled approach consists in carry out the conventional FEA simulation, evaluating part shape and stress state during a forming operation. Damage evaluation is done by post-processing the finite element solution, performing the time integration of the damage evolution law using the computed thermodynamical fields. Inevitably, this kind of approach neglects stress and strain redistribution caused by damage growth and consequent plastic softening behaviour. Nevertheless, it can be used as a fast procedure for early development phases. For more accurate engineering applications, coupling between elasto-inelastic constitutive equations and damage must be strong and, therefore, the so-called fully coupled approach is required. A more complete review can be found in several works [Lemaitre 2005] [Chaboche 2007] [Voyiadjis 2005].

4.4 Lemaitre's elasto-plastic isotropic damage theory

The description of Lemaitre's ductile damage model [Lemaitre 1985a] [Lemaitre 1996] is presented in the following.

4.4.1 State potential and state relations

The starting point of the theory is the assumption of a state or thermodynamic potential, from which derives the state laws. The Helmholtz free energy is taken as the thermodynamic potential and can be defined as a function of the set $\left\{\boldsymbol{\varepsilon}^e, r, \boldsymbol{\beta}, D\right\}$ of state variables, in the form:

$$\psi = \psi\left(\boldsymbol{\varepsilon}^e, r, \boldsymbol{\beta}, D\right) \tag{4.10}$$

where $\boldsymbol{\varepsilon}^e$ is the elastic strain tensor and r and D are the scalar internal variables associated, respectively, with isotropic hardening and isotropic damage. The second order tensor $\boldsymbol{\beta}$ is the internal variable related to kinematic hardening. Table 4.1 depicts the state variables and the corresponding associated thermodynamical forces.

Table 4.1 State variables for isotropic damage theory.

Mechanism	**Type**	**State Variables**		**Associated**
		Observables	**Internal**	**Variables**
Elasticity	Tensor	$\boldsymbol{\varepsilon}$		$\boldsymbol{\sigma}$
Plasticity	Tensor		$\boldsymbol{\varepsilon}^p$	$-\boldsymbol{\sigma}$
Isotropic Hardening	Scalar		r	R
Kinematic Hardening	Tensor		$\boldsymbol{\beta}$	$\boldsymbol{X}$
Damage	Scalar		D	Y

In this case, it is assumed an isothermal process, so the choice of internal variables depends on the physical phenomena under consideration (elasticity, isotropic and kinematic hardening and damage). Under the hypothesis that damage only affects elasticity, the Helmholtz free energy can be expressed by an additive decomposition of two state potentials corresponding to the elastic-damage and hardening contributions to the free energy, given by the sum:

$$\psi\left(\boldsymbol{\varepsilon}^e, r, \boldsymbol{\beta}, D\right) = \psi^{ed}\left(\boldsymbol{\varepsilon}^e, D\right) + \psi^p\left(r, \boldsymbol{\beta}\right) \tag{4.11}$$

where ψ^{ed} and ψ^p are, respectively, the elastic-damage and plastic terms of the free energy. The elastic-damage state potential is defined as:

$$\bar{\rho}\psi^{ed}\left(\boldsymbol{\varepsilon}^e, D\right) = \frac{1}{2}\boldsymbol{\varepsilon}^e : \tilde{\mathbf{E}} : \boldsymbol{\varepsilon}^e = \frac{1}{2}\boldsymbol{\varepsilon}^e : \left(1 - D\right)\mathbf{E} : \boldsymbol{\varepsilon}^e \tag{4.12}$$

where $\mathbf{E}$ is standard isotropic elasticity tensor. A classical proof [Chaboche 2007] allows to eliminate all the reversible processes from the Clausius-Duhem inequality, and, therefore, state relations are given by:

$$\boldsymbol{\sigma} = \bar{\rho}\,\frac{\partial\psi^{ed}\left(\boldsymbol{\varepsilon}^e, D\right)}{\partial\boldsymbol{\varepsilon}^e} = \left(1 - D\right)\mathbf{E} : \boldsymbol{\varepsilon}^e \tag{4.13}$$

which represents the linear elasticity law or Hooke's law. Equivalently, the above damaged elastic law can be written as:

$$\tilde{\boldsymbol{\sigma}} = \mathbf{E} : \boldsymbol{\varepsilon}^e \tag{4.14}$$

where $\tilde{\boldsymbol{\sigma}}$ is the effective stress tensor, being related with Cauchy stress tensor by the expression:

$$\tilde{\boldsymbol{\sigma}} = \frac{1}{1-D}\boldsymbol{\sigma}. \tag{4.15}$$

The thermodynamical force associated with damage internal variable, Y, also derives from the elastic-damage state potential and can be expressed as:

$$Y = \overline{\rho}\frac{\partial \psi^{ed}\left(\boldsymbol{\varepsilon}^e, D\right)}{\partial D} = -\frac{1}{2}\boldsymbol{\varepsilon}^e : \mathbf{E} : \boldsymbol{\varepsilon}^e \tag{4.16}$$

or, using the inverse of the elastic stress / strain law, as:

$$Y = -\frac{1}{2}\tilde{\boldsymbol{\sigma}} : \mathbf{E}^{-1} : \tilde{\boldsymbol{\sigma}}. \tag{4.17}$$

After some straightforward algebra, it is possible to define Y as a function of the stress triaxiliaty ratio $\left(\sigma_H / \overline{\sigma}\right)$ as [Souza Neto 2008]:

$$Y = -\frac{\overline{\sigma}^2}{2E\left(1-D\right)^2}\left[\frac{2}{3}\left(1+\nu\right) + 3\left(1-2\nu\right)\left(\frac{\sigma_H}{\overline{\sigma}}\right)^2\right] \tag{4.18}$$

where $\overline{\sigma}$ represents the von Mises equivalent stress, ν the Poisson ratio and σ_H the hydrostatic stress. Also, it can be demonstrated that $-Y$ is equal to half the elastic strain energy released by damage evolution at fixed stress [Chaboche 2007]. Starting from the law of elasticity and differentiating, one has:

$$d\boldsymbol{\sigma} = \tilde{\mathbf{E}} : d\boldsymbol{\varepsilon}^e + \frac{\partial \tilde{\mathbf{E}}}{\partial D} : \boldsymbol{\varepsilon}^e dD = \boldsymbol{0}. \tag{4.19}$$

Knowing that $\tilde{\mathbf{E}} = \left(1-D\right)\mathbf{E}$ and rearranging, Equation (4.19) can be written as:

$$d\boldsymbol{\varepsilon}^e = \boldsymbol{\varepsilon}^e \frac{dD}{1-D}. \tag{4.20}$$

Defining the elastic energy variation, at constant stress, as:

$$dW^e = \boldsymbol{\sigma} : d\boldsymbol{\varepsilon}^e \tag{4.21}$$

and using the definition of Equation (4.20), it is sufficient to calculate:

$$\begin{aligned} dW^e &= \boldsymbol{\sigma} : d\boldsymbol{\varepsilon}^e \\ &= \boldsymbol{\sigma} : \boldsymbol{\varepsilon}^e \frac{dD}{1-D} \\ &= \boldsymbol{\varepsilon}^e : \left(1-D\right)\mathbf{E} : \boldsymbol{\varepsilon}^e \frac{dD}{1-D} \\ &= \boldsymbol{\varepsilon}^e : \mathbf{E} : \boldsymbol{\varepsilon}^e dD \end{aligned} \tag{4.22}$$

and, finally, using the definition of Equation (4.16), one may write:

$$-Y = \frac{1}{2}\frac{dW^e}{dD}\bigg|_{\sigma} . \tag{4.23}$$

This last equation allows $-Y$ to be called the strain energy density release rate, equal to one half the variation of the strain energy density corresponding to a variation of damage at constant stress [Lemaitre 1996]. It corresponds to the elastic energy release rate for a crack, J, used in basic Fracture Mechanics theories.

Concerning the plastic state potential $\psi^p\left(r,\boldsymbol{\beta}\right)$, it is considered as the sum of independent contributions of isotropic and kinematic hardenings. Therefore, plastic state potential is given by the sum of terms:

$$\overline{\rho}\psi^p\left(r,\boldsymbol{\beta}\right) = \overline{\rho}\psi^I\left(r\right) + \frac{a}{2}\boldsymbol{\beta} : \boldsymbol{\beta} \tag{4.24}$$

where a is a material constant associated with kinematic hardening and the isotropic hardening contribution, $\psi^I\left(r\right)$, is an arbitrary scalar function of the internal isotropic variable r. So, it is possible to postulate the state relations for the thermodynamical forces associated with isotropic and kinematic hardening, R and $\boldsymbol{X}$, respectively, related with internal variables as:

$$R = \overline{\rho}\frac{\partial\psi^p\left(r,\boldsymbol{\beta}\right)}{\partial r} = \frac{\partial\psi^I\left(r\right)}{\partial r} = R\left(r\right) \tag{4.25}$$

$$\boldsymbol{X} = \overline{\rho}\frac{\partial\psi^p\left(r,\boldsymbol{\beta}\right)}{\partial\boldsymbol{\beta}} = a\boldsymbol{\beta} \tag{4.26}$$

where $\boldsymbol{X}$ is the so-called back-stress tensor.

4.4.2 Dissipation potential and associated evolution equations

Having all the state and corresponding associated variables defined, a second potential will give the kinetic constitutive relations to describe the evolution of the phenomena [Lemaitre 1996]. The existence of a single dissipation potential, Ψ, is assumed from which, using a normality rule, the evolution equations for all internal variables are derived. But, before presenting the explicit expression for the dissipation potential, let us define some restrictions to its formulation. Selecting three physical phenomena, isotropic hardening, kinematic hardening and damage, the intrinsic dissipation must satisfy the Second Principle of Thermodynamics, written as:

$$\boldsymbol{\sigma} : \dot{\boldsymbol{\varepsilon}}^p - \boldsymbol{X} : \dot{\boldsymbol{\beta}} - R\dot{r} - Y\dot{D} \geq 0 \,, \tag{4.27}$$

taking into account the definition of the thermodynamic associated force to each internal variable. One can rewrite the above inequality assuming that it can be decomposed in two terms, namely, plastic dissipation and damage dissipation, respectively, given by:

$$\begin{aligned} \boldsymbol{\sigma} : \dot{\boldsymbol{\varepsilon}}^p - \boldsymbol{X} : \dot{\boldsymbol{\beta}} - R\dot{r} \geq 0 \\ - Y\dot{D} \geq 0 \end{aligned} . \tag{4.28}$$

As shown in Equation (4.28), the inequality should be identically verified for each selected dissipative mechanism. As $-Y$ is a positive quadratic function (see Equation (4.18)), the damage rate $\dot{D}$ must also be a non-negative function. This means that damage variable only takes into account progressive deterioration of materials, not being possible any kind of recovery of strength. In order to satisfy 'a priori' this restriction and the dissipation inequality, it is assumed the existence of a scalar-valued dissipation (pseudo-) potential Ψ^*, function of the rates of change of the internal variables:

$$\Psi^* = \Psi^*\left(\dot{\boldsymbol{\varepsilon}}^p, \dot{r}, \dot{\boldsymbol{\beta}}, \dot{D}; \boldsymbol{\varepsilon}^p, r, \boldsymbol{\beta}, D\right) \tag{4.29}$$

where internal variables as considered as parameters in this potential. Using the Legendre-Fenschel transformation, a complementary equivalent dissipation (pseudo-) potential Ψ can be postulated. It is also a scalar-valued function, continuous, non-negative and convex with respect to each thermodynamical forces:

$$\Psi = \Psi\left(\boldsymbol{\sigma}, R, \boldsymbol{X}, Y; \boldsymbol{\varepsilon}^p, r, \boldsymbol{\beta}, D\right). \tag{4.30}$$

Using a single dissipation potential approach, this complementary dissipation potential is given by an additive decomposition of hardening Ψ^p and damage Ψ^d potentials in the form:

$$\Psi = \Psi^p + \Psi^d = \Phi + \frac{b}{2a}\boldsymbol{X} : \boldsymbol{X} + \frac{S}{\left(1-D\right)\left(s+1\right)}\left(\frac{-Y}{S}\right)^{s+1} \tag{4.31}$$

where a , b , S and s are material constants and Φ is the yield function of von Mises type:

$$\Phi\left(\boldsymbol{\sigma},\boldsymbol{X},R;D\right)=\frac{\sqrt{3J_2\left(\boldsymbol{s}-\boldsymbol{X}\right)}}{1-D}-\left[\sigma_{Y0}+R\left(r\right)\right] \tag{4.32}$$

where σ_{Y0} is the initial yield stress of the material. According to the hypothesis of generalised normality, the plastic flow is given by:

$$\dot{\boldsymbol{\varepsilon}}^p=\dot{\gamma}\frac{\partial\Psi}{\partial\boldsymbol{\sigma}}=\dot{\gamma}\boldsymbol{N} \tag{4.33}$$

where $\boldsymbol{N}$ stands for the flow vector, expressed as:

$$\boldsymbol{N}=\sqrt{\frac{3}{2}}\frac{\left(\boldsymbol{s}-\boldsymbol{X}\right)}{\left(1-D\right)\left\|\boldsymbol{s}-\boldsymbol{X}\right\|}. \tag{4.34}$$

The evolution of internal variables associated with isotropic and kinematic hardening, $\dot{r}$ and $\dot{\boldsymbol{\beta}}$, are:

$$\begin{aligned}\dot{r}&=-\dot{\gamma}\frac{\partial\Psi}{\partial R}=\dot{\gamma}\\ \dot{\boldsymbol{\beta}}&=-\dot{\gamma}\frac{\partial\Psi}{\partial\boldsymbol{X}}=\dot{\gamma}\left(a\boldsymbol{N}-b\boldsymbol{X}\right)\end{aligned} \tag{4.35}$$

and damage evolution law is given by:

$$\dot{D}=-\dot{\gamma}\frac{\partial\Psi}{\partial Y}=\frac{\dot{\gamma}}{1-D}\left(\frac{-Y}{S}\right)^s \tag{4.36}$$

where $\dot{\gamma}$ is the plastic parameter, that must satisfies the standard complementary law of rate-independent plasticity:

$$\dot{\gamma}\geq0;\ \Phi\leq0;\ \dot{\gamma}\Phi=0. \tag{4.37}$$

To complete the formal description of elasto-plasticity coupled with damage, it is important to define the equivalent plastic strain rate $\dot{\bar{\varepsilon}}^p$, which has to be in accordance with the considered yield criterion. For the von Mises criterion and assuming the equivalence of plastic work rate, one has:

$$\dot{W}^p=\boldsymbol{\sigma}:\dot{\boldsymbol{\varepsilon}}^p=\bar{\sigma}\,\dot{\bar{\varepsilon}}^p. \tag{4.38}$$

Using Equation (4.33) and the definition of equivalent stress for a von Mises material:

$$\bar{\sigma}=\sqrt{\frac{3}{2}}\left(\boldsymbol{s}:\boldsymbol{s}\right)^{\frac{1}{2}}, \tag{4.39}$$

equivalent plastic strain rate is calculated from the equivalence in Equation (4.38) as:

$$\dot{\bar{\varepsilon}}^p=\frac{\dot{\gamma}}{1-D}. \tag{4.40}$$

Thus, using Equation (4.36) and (4.40), one can rewrite the evolution equation for damage as:

$$\dot{D} = \dot{\bar{\varepsilon}}^p \left(\frac{-Y}{S} \right)^s . \tag{4.41}$$

4.4.3 Damage threshold

As already stated in Section 4.2, for low values of accumulated plastic strain, a limited apparent deterioration is observed and its effects on physical properties can be neglected. Taking as example the monotonic pure tension case, it is assumed that internal degradation or damage only starts to grow when a certain value of accumulated plastic strain is attained [Lemaitre 1996]. Since damage evolution equation is governed by the equivalent plastic strain rate, it is logical to define this threshold based on the accumulated plastic strain. This critical value is denoted by damage threshold ε_D^p and corresponds to value of equivalent plastic strain below which no damage by micro-cracking occurs. Although this threshold depends upon type of loading and type of damage, it is generally considered a material parameter, identified from a monotonic uniaxial loading. This threshold is introduced in the model by using the Heaviside step function H as:

$$\dot{D} = \dot{\gamma} \frac{\partial \Psi}{\partial Y} = \dot{\bar{\varepsilon}}^p \left(\frac{-Y}{S} \right)^s H\left(\bar{\varepsilon}^p - \varepsilon_D^p \right) \tag{4.42}$$

where H, the Heavyside step function, is defined as:

$$H\left(a\right) = \begin{cases} a \text{ if } a \geq 0 \\ 0 \text{ if } a < 0 \end{cases} . \tag{4.43}$$

4.4.4 Critical damage criterion

Several ways are possible to define localization and meso-crack initiation. The simplest and most practical solution is to use the critical damage criterion, which states that a meso-crack is initiated when damage reaches a critical value [Lemaitre 2005]:

$$D > D_C . \tag{4.44}$$

The term D_C is considered a material constant. Although its value is difficult to obtain, for most materials, critical damage ranges from 0.2 up to 0.5.

Another possible way to identify meso-crack initiation is to use a strain damage localization criterion. The most common approaches are the bifurcation approach and the perturbation analysis theory. The bifurcation approach consists of the analysis of the loss of uniqueness in the rate mechanical problem. The perturbation approach is based on the perturbation of the reference solution and the analysis of the perturbed solution. Instability is assumed if the perturbed solution drifts from the reference solution. The main disadvantages of these criterions are due to their intrinsic difficulty to be handled inside finite element codes, requiring high computation times, and also, to their dependence on the type of material and damage evolution law.

4.4.5 Computational aspects

The numerical integration of Lemaitre's elasto-plastic isotropic damage constitutive equations by means of a return mapping-type scheme has been originally proposed by Benallal *et al.* [1988] and Doghri and Billardon [1995] under small-strain hypothesis and later explored by several authors within finite strains context [Souza Neto 1994] [Souza Neto 1998] [Saanouni 2000]. Original integration algorithm leads to a non-linear system of 15 scalar equations for a general 3D case, solved iteratively according to the Newton-Rapshon scheme. Exploiting standard return mapping procedures [Simo 1998], the return mapping stage can be reduced to the solution of 2 non-linear equations in the case of fully isotropic case [Saanouni 2007]. Further simplification to the solution of a single scalar non-linear equation was proposed by Souza Neto [2002] for a version of Lemaitre's ductile damage model that disregards kinematic hardening. The proposed integration algorithm has proven to be particularly efficient, but requires the knowledge 'a priori' of the evolution of internal variable r, not possible to obtain directly from a stress-strain curve obtained from a standard tensile test.

4.5 Elasto-plastic isotropic damage model with anisotropic flow

The constitutive model proposed in this section, to describe the mechanism of internal damaging, was inspired in the model described in Section 4.4. In this improved model, plastic anisotropy, which generally characterizes thin sheet behaviour, is introduced.

While for bulk metal forming, the assumption of initial isotropy is admissible, in the case of sheet metal forming, the previous history of thermo-mechanical processing of sheet material induces preferred directions for plastic deformation, which generally has an orthotropic character. In such cases, the isotropy assumption may lead to a poor representation of the actual mechanical behaviour and the formulation and the use of appropriate anisotropic plasticity models becomes crucial to ensure reasonable accuracy in finite element predictions. Also, during forming operation, additional anisotropy can be introduced by the evolution of the microstructure and may even be responsible for the destruction of orthotropic plastic behaviour. However, this deformation-induced anisotropy is usually considered very small in comparison with the anisotropy imposed during hot and cold rolling. This consideration is well accepted and widely adopted in the analysis of sheet metal forming processes. So, for the modelling of initial anisotropy, the quadratic Hill48 [Hill 1948] criterion was selected.

This criterion represents a generalization of the isotropic quadratic criterion proposed by von Mises [von Mises 1913], capable to describe orthotropic behaviour found in rolled sheets. With σ_{ij} denoting the components of the stress tensor in the orthogonal reference system $\left\{e_1, e_2, e_3\right\}$, which vectors coincide with principle axes of plastic orthotropy, yield function for this criterion is given by:

$$\Phi = \sqrt{F\left(\sigma_{22}-\sigma_{33}\right)^2 + G\left(\sigma_{33}-\sigma_{11}\right)^2 + H\left(\sigma_{11}-\sigma_{22}\right)^2 + 2L\sigma_{23}^2 + 2M\sigma_{31}^2 + 2N\sigma_{12}^2} - \sigma_Y \tag{4.45}$$

where F, G, H, L, M and N are the Hill's anisotropic parameters that define material anisotropy and σ_Y is the updated yield stress that describes the hardening state of the material. Hill's parameters are calculated from the Lankford coefficients r_0, r_{45} and r_{90}, determined from uniaxial tensile testings at 3 different directions 0°, 45° and 90° from rolling direction, through the expressions:

$$\begin{aligned} &F = \frac{H}{r_{90}} = \frac{r_0 G}{r_{90}} = \frac{r_0}{r_{90}\left(1+r_0\right)};\ G = \frac{1}{1+r_0};\ H = r_0 G = \frac{r_0}{1+r_0} \\ &L = M = \frac{3}{2};\ N = \frac{1}{2}\frac{\left(r_0+r_{90}\right)\left(2r_{45}+1\right)}{r_{90}\left(r_0+1\right)} \end{aligned} . \tag{4.46}$$

One important feature of this criterion is the fact that fully recovers the von Mises isotropic criterion when anisotropic coefficients r_0, r_{45} and r_{90} are considered equal to 1. Also, like the isotropic criterion, it is "pressure insensitive", which reflects the independence of the criterion of the hydrostatic pressure, allowing to express its yield function in terms of the components of the stress deviator, $\boldsymbol{s}$. This criterion has been widely used in the numerical modelling of sheet metal forming processes over the past years. Besides being well accepted theoretically and proven to properly describe sheet metal initial anisotropy, it can be applied to a generic stress state and leads to linear relations between stress and incremental plastic strains.

4.5.1 Constitutive model

Including initial plastic anisotropy, the main difference to the previous explained damage model is the replacement of the isotropic yield function in the dissipation potential by an anisotropic one. In this case, one has for the flow potential Ψ:

$$\Psi = \Psi^p + \Psi^d = \Phi + \frac{b}{2a}\boldsymbol{X} : \boldsymbol{X} + \frac{S}{\left(1-D\right)\left(s+1\right)}\left(\frac{-Y}{S}\right)^{s+1} \tag{4.47}$$

where S and s are damage-related material constants and Φ is the yield function of Hill48 criterion [Hill 1948]:

$$\Phi\left(\boldsymbol{\sigma}, R, \boldsymbol{X}, D\right) = \frac{\sqrt{\left(\boldsymbol{\sigma} - \boldsymbol{X}\right) : \mathbf{M} : \left(\boldsymbol{\sigma} - \boldsymbol{X}\right)}}{1 - D} - \left[\sigma_{Y0} + R\left(r\right)\right]. \tag{4.48}$$

$\mathbf{M}$ is the Hill fourth order operator, function of the Hill's anisotropic parameters. It is important to remark that, as in Lemaitre's formulation, damage affects both stress $\boldsymbol{\sigma}$ and back-stress $\boldsymbol{X}$ tensors, keeping the elastic domain centered on $\boldsymbol{X}$ in the stress space as damage increases. Considering the standard hypothesis of generalised normality, the evolution law for the plastic flow is given by:

$$\dot{\boldsymbol{\varepsilon}}^p = \dot{\gamma} \frac{\partial \Psi}{\partial \boldsymbol{\sigma}} = \dot{\gamma} \frac{\partial \Phi}{\partial \boldsymbol{\sigma}} = \dot{\gamma} \boldsymbol{N} \tag{4.49}$$

where $\boldsymbol{N}$ is the flow vector, which takes the following form for the Hill48 criterion:

$$\boldsymbol{N} = \frac{\partial \Phi}{\partial \boldsymbol{\sigma}} = \frac{\mathbf{M} : \left(\boldsymbol{\sigma} - \boldsymbol{X}\right)}{\left(1 - D\right)\sqrt{\left(\boldsymbol{\sigma} - \boldsymbol{X}\right) : \mathbf{M} : \left(\boldsymbol{\sigma} - \boldsymbol{X}\right)}}. \tag{4.50}$$

The evolution laws for the isotropic and kinematic hardening internal variables are respectively given by:

$$\dot{r} = -\dot{\gamma} \frac{\partial \Psi}{\partial R} = \dot{\gamma} \tag{4.51}$$

$$\dot{\boldsymbol{\beta}} = -\dot{\gamma} \frac{\partial \Psi}{\partial \boldsymbol{X}} = \dot{\gamma}\left(a\boldsymbol{N} - b\boldsymbol{X}\right) \tag{4.52}$$

and the damage evolution law written as:

$$\dot{D} = -\dot{\gamma} \frac{\partial \Psi}{\partial Y} = \frac{\dot{\gamma}}{1 - D}\left(\frac{-Y}{S}\right)^s. \tag{4.53}$$

By the equivalence of plastic work rate, equivalent plastic strain rate is calculated as:

$$\dot{\bar{\varepsilon}}^p = \frac{\dot{\gamma}}{1 - D} \tag{4.54}$$

and the damage evolution law can be rewritten as:

$$\dot{D} = -\dot{\gamma} \frac{\partial \Psi}{\partial Y} = \dot{\bar{\varepsilon}}^p \left(\frac{-Y}{S}\right)^s. \tag{4.55}$$

The plastic multiplier $\dot{\gamma}$ satisfies the plastic loading / unloading rules (Kuhn-Tucker condition):

$$\dot{\gamma} \geq 0\,;\ \Phi \leq 0\,;\ \dot{\gamma}\Phi = 0\,. \tag{4.56}$$

The constitutive equations of the overall elasto-plastic isotropic damage model with anisotropic flow are summarized in Box 4.1.

Box 4.1 Lemaitre's ductile isotropic damage model with anisotropic flow.

i) Elasto-plastic split of the strain tensor

$$\boldsymbol{\varepsilon} = \boldsymbol{\varepsilon}^e + \boldsymbol{\varepsilon}^p$$

ii) Elastic law (coupled with damage)

$$\boldsymbol{\sigma} = \left(1 - D\right)\mathbf{E} : \boldsymbol{\varepsilon}^e$$

iii) Yield function

$$\Phi = \frac{\sqrt{\left(\boldsymbol{\sigma} - \boldsymbol{X}\right) : \mathbf{M} : \left(\boldsymbol{\sigma} - \boldsymbol{X}\right)}}{1 - D} - \left[\sigma_{Y0} + R\left(r\right)\right]$$

iv) Plastic flow and evolution equations

$$\dot{\boldsymbol{\varepsilon}}^p = \dot{\gamma}\frac{\mathbf{M} : \left(\boldsymbol{\sigma} - \boldsymbol{X}\right)}{\left(1 - D\right)\sqrt{\left(\boldsymbol{\sigma} - \boldsymbol{X}\right) : \mathbf{M} : \left(\boldsymbol{\sigma} - \boldsymbol{X}\right)}}$$

$$\dot{\bar{\varepsilon}}^p = \frac{\dot{\gamma}}{1 - D}$$

$$\dot{\boldsymbol{\beta}} = \dot{\gamma}\left(a\boldsymbol{N} - b\boldsymbol{X}\right)$$

$$\dot{D} = \dot{\bar{\varepsilon}}^p\left(\frac{-Y}{S}\right)^s$$

with Y given by:

$$Y = -\frac{1}{2\left(1 - D\right)^2}\boldsymbol{\sigma} : \mathbf{E}^{-1} : \boldsymbol{\sigma}$$

v) Loading / unloading criterion

$$\dot{\gamma} \geq 0\,;\ \Phi \leq 0\,;\ \dot{\gamma}\Phi = 0$$

4.5.2 Integration algorithm

The integration algorithm of the equations of elasto-plasticity coupled with Lemaitre's ductile damage model is a special case of the implicit scheme known as elastic predictor / plastic corrector [Simo 1987]. Here we shall focus in the exact linearisation of the field equations which provides the basis of the standard Newton-Raphson iterative scheme for solution of the associated nonlinear boundary value problem. Other authors have also focused the numerical implementation of ductile damage model for orthotropic sheet metal forming processes [Saanouni 2006] [Khelifa 2007]. In these implementations, the return mapping procedure involves the solution of a system of two (or three) non-linear equations, where at least one of the equations is a tensorial one. In this work and in order to obtain a simpler form for numerical implementation, kinematic hardening is excluded from the constitutive model. The use of such simplified theory can be justified whenever the effects of kinematic hardening are not relevant, i.e., in any process where reverse plastic loading does not occur or has little influence on the overall evolution of damage and plastic flow [Souza Neto 2008].

Disregarding kinematic hardening, the return mapping stage can be reduced to the solution of a system of two scalar non-linear equations. In order to achieve such more efficient algorithm, it is important to define Hill48 yield criterion in a quadratic form as:

$$\Phi = \boldsymbol{\sigma} : \mathbf{M} : \boldsymbol{\sigma} - \sigma_Y^2 . \tag{4.57}$$

This is a valid hypothesis since:

$$\begin{aligned} &\boldsymbol{\sigma} : \mathbf{M} : \boldsymbol{\sigma} - \sigma_Y^2 = 0 \\ &\Leftrightarrow \left(\sqrt{\boldsymbol{\sigma} : \mathbf{M} : \boldsymbol{\sigma}} - \sigma_Y\right)\left(\sqrt{\boldsymbol{\sigma} : \mathbf{M} : \boldsymbol{\sigma}} + \sigma_Y\right) = 0 \\ &\Leftrightarrow \sqrt{\boldsymbol{\sigma} : \mathbf{M} : \boldsymbol{\sigma}} - \sigma_Y = 0 \ \vee \ \sqrt{\boldsymbol{\sigma} : \mathbf{M} : \boldsymbol{\sigma}} + \sigma_Y = 0 \end{aligned} \tag{4.58}$$

and the condition $\sqrt{\boldsymbol{\sigma} : \mathbf{M} : \boldsymbol{\sigma}} + \sigma_Y = 0$ is unattainable. So, it is feasible to define yield criterion in such form, allowing the definition of updated stress $\boldsymbol{\sigma}_{n+1}$ only as a function of incremental plastic multiplier $\Delta\gamma$, as we will see later.

In the context of finite element analysis, the problem to be addressed in the integration algorithm is the updating of variables $\boldsymbol{\sigma}_n$, $\boldsymbol{\varepsilon}_n^e$, $\boldsymbol{\varepsilon}_n^p$, $\bar{\varepsilon}_n^p$ and D_n, converged in the previous increment t_n, into their corresponding values $\boldsymbol{\sigma}_{n+1}$, $\boldsymbol{\varepsilon}_{n+1}^e$, $\boldsymbol{\varepsilon}_{n+1}^p$, $\bar{\varepsilon}_{n+1}^p$ e D_{n+1} in the updated configuration, at time t_{n+1}. Given a strain increment $\Delta\boldsymbol{\varepsilon}$ corresponding to the pseudo-time interval $\left[t_n, t_{n+1}\right]$, the fully coupled damage-plasticity integration algorithm follows the evaluation of an elastic trial stress state, and, if the consistency condition is infringed, the return mapping process is applied. So, the algorithm starts with the computation of the elastic trial stress state $\boldsymbol{\sigma}^{trial}$:

$$\boldsymbol{\sigma}^{trial} = \boldsymbol{\sigma}_n + \omega_n \mathbf{E} : \Delta\boldsymbol{\varepsilon} = \omega_n \tilde{\boldsymbol{\sigma}}^{trial} \tag{4.59}$$

where $\tilde{\boldsymbol{\sigma}}^{trial}$ is the effective trial stress tensor and ω_n is the material integrity defined as:

$$\omega_n = 1 - D_n , \tag{4.60}$$

introduced in the algorithm, instead of variable D_n, for computational convenience. Considering that all internal variables are "frozen" at time t_n, yield function is evaluated for the computed trial stress:

$$\Phi^{trial} = \tilde{\boldsymbol{\sigma}}^{trial} : \mathbf{M} : \tilde{\boldsymbol{\sigma}}^{trial} - \sigma_Y^2\left(\bar{\varepsilon}_n^p\right) = \frac{\boldsymbol{\sigma}^{trial} : \mathbf{M} : \boldsymbol{\sigma}^{trial}}{\omega_n^2} - \sigma_Y^2\left(\bar{\varepsilon}_n^p\right). \tag{4.61}$$

If the condition $\Phi^{trial} \leq 0$ verifies, then all strain increment $\Delta\boldsymbol{\varepsilon}$ is purely elastic and there is no evolution of internal variables. Therefore, the trial state corresponds to updated state for $t = t_{n+1}$ and updated variables $\boldsymbol{\sigma}_{n+1}$, $\boldsymbol{\varepsilon}^{e}_{n+1}$, $\boldsymbol{\varepsilon}^{p}_{n+1}$, $\bar{\varepsilon}^{p}_{n+1}$ e D_{n+1} are given by:

$$\begin{aligned}
\boldsymbol{\sigma}_{n+1} &= \boldsymbol{\sigma}^{trial} = \boldsymbol{\sigma}_{n} + \omega_{n} \mathbf{E} : \Delta\boldsymbol{\varepsilon} \\
\boldsymbol{\varepsilon}^{e}_{n+1} &= \boldsymbol{\varepsilon}^{e}_{n} + \Delta\boldsymbol{\varepsilon} \\
\boldsymbol{\varepsilon}^{p}_{n+1} &= \boldsymbol{\varepsilon}^{p}_{n} \\
\bar{\varepsilon}^{p}_{n+1} &= \bar{\varepsilon}^{p}_{n} \\
D_{n+1} &= D_{n}.
\end{aligned} \tag{4.62}$$

In the other hand, if $\Phi^{trial} > 0$, then one must apply the plastic corrector algorithm to ensure the consistency condition. It is now important to define the updated stress tensor $\boldsymbol{\sigma}_{n+1}$ as a function of the incremental consistent plastic parameter $\Delta\gamma$, and, additionally, as a function of the material integrity, ω_{n+1}.

Starting from the definition of the elastic trial strain tensor $\boldsymbol{\varepsilon}^{e\ trial}$ and assuming additive strain decomposition, one may write that:

$$\boldsymbol{\varepsilon}^{e}_{n+1} = \boldsymbol{\varepsilon}^{e\ trial} - \Delta\boldsymbol{\varepsilon}^{p}. \tag{4.63}$$

Considering an associative flow rule, plastic flow is given by:

$$\dot{\boldsymbol{\varepsilon}}^{p} = \dot{\gamma} \frac{\partial \Phi}{\partial \boldsymbol{\sigma}} \tag{4.64}$$

which, for Hill48 criterion with isotropic damage written in a quadratic form, is equal to:

$$\dot{\boldsymbol{\varepsilon}}^{p} = \dot{\gamma} \frac{2}{\omega^{2}} \mathbf{M} : \boldsymbol{\sigma} \tag{4.65}$$

and, therefore:

$$\boldsymbol{\varepsilon}^{e}_{n+1} = \boldsymbol{\varepsilon}^{e\ trial} - \frac{2\Delta\gamma}{\omega^{2}_{n+1}} \mathbf{M} : \boldsymbol{\sigma}_{n+1}. \tag{4.66}$$

Introducing in the above equation the trivial definitions:

$$\begin{aligned}
\boldsymbol{\sigma}_{n+1} &= \omega_{n+1} \mathbf{E} : \boldsymbol{\varepsilon}^{e}_{n+1} \\
\boldsymbol{\sigma}^{trial} &= \omega_{n} \mathbf{E} : \boldsymbol{\varepsilon}^{e\ trial} \\
\tilde{\boldsymbol{\sigma}}^{trial} &= \mathbf{E} : \boldsymbol{\varepsilon}^{e\ trial} \\
\mathbf{E} : \mathbf{M} &= 2G\,\mathbf{M}
\end{aligned} \tag{4.67}$$

and, after a straightforward algebraic manipulation, one obtains the following expression for the updated stress $\boldsymbol{\sigma}_{n+1}$:

$$\boldsymbol{\sigma}_{n+1} = \omega_{n+1}\left(\mathbf{I} + \frac{4\Delta\gamma G}{\omega_{n+1}}\mathbf{M}\right)^{-1} : \tilde{\boldsymbol{\sigma}}^{trial} \tag{4.68}$$

where $\mathbf{I}$ is the fourth order identity tensor and G is the bulk modulus. Furthermore, it is also possible to deduce explicitly the expression for the equivalent plastic strain increment $\Delta\bar{\varepsilon}^{p}$, function of the incremental consistent plastic parameter $\Delta\gamma$ and material integrity ω_{n+1}. Using the definition of incremental plastic work ΔW^{p} and equality between effective and equivalent stress and strain states, the increment of equivalent plastic strain can be computed from the relation:

$$\Delta\bar{\varepsilon}^{p} = \frac{\tilde{\boldsymbol{\sigma}}_{n+1} : \Delta\boldsymbol{\varepsilon}^{p}}{\tilde{\bar{\sigma}}_{n+1}} \tag{4.69}$$

where $\tilde{\bar{\sigma}}_{n+1}$ is the effective equivalent stress given by:

$$\tilde{\bar{\sigma}}_{n+1} = \sqrt{\tilde{\boldsymbol{\sigma}}_{n+1} : \mathbf{M} : \tilde{\boldsymbol{\sigma}}_{n+1}} = \frac{\sqrt{\boldsymbol{\sigma}_{n+1} : \mathbf{M} : \boldsymbol{\sigma}_{n+1}}}{\omega_{n+1}} = \frac{\bar{\sigma}_{n+1}}{\omega_{n+1}} = \frac{\bar{\sigma}_{n+1}}{1 - D_{n+1}}\,. \tag{4.70}$$

So, equivalent plastic strain increment can be expressed as:

$$\Delta\bar{\varepsilon}^{p} = \frac{2\Delta\gamma}{\omega_{n+1}^{2}}\sqrt{\boldsymbol{\sigma}_{n+1} : \mathbf{M} : \boldsymbol{\sigma}_{n+1}}\,. \tag{4.71}$$

Therefore, the return mapping algorithm for the fully coupled integration of plasticity and damage can be reduced to the solution of a system of two non-linear scalar equations, function of the incremental consistent plastic multiplier $\Delta\gamma$ and material integrity ω_{n+1}:

$$\begin{cases} \dfrac{\boldsymbol{\sigma}_{n+1} : \mathbf{M} : \boldsymbol{\sigma}_{n+1}}{\omega_{n+1}^{2}} - \sigma_{Y}^{2}\left(\bar{\varepsilon}_{n+1}^{p}\right) = 0 \\ \omega_{n+1} - \omega_{n} + \Delta\bar{\varepsilon}_{n+1}^{p}\left(\dfrac{-Y_{n+1}}{S}\right)^{s} H\left(\bar{\varepsilon}_{n+1}^{p} - \varepsilon_{D}^{p}\right) = 0 \end{cases} \tag{4.72}$$

where the first equation represents yield function and the second one the damage evolution law expressed by the material integrity ω_{n+1}. Variables $\boldsymbol{\sigma}_{n+1}$, $\Delta\bar{\varepsilon}_{n+1}^{p}$, $\bar{\varepsilon}_{n+1}^{p}$ e Y_{n+1} are defined as:

$$\begin{aligned}
\boldsymbol{\sigma}_{n+1} &= \omega_{n+1}\left(\mathbf{I}+\frac{4\Delta\gamma G}{\omega_{n+1}}\mathbf{M}\right)^{-1} : \tilde{\boldsymbol{\sigma}}^{trial} \\
\Delta\bar{\varepsilon}^{p} &= \frac{2\Delta\gamma}{\omega_{n+1}^{2}}\sqrt{\boldsymbol{\sigma}_{n+1} : \mathbf{M} : \boldsymbol{\sigma}_{n+1}} \\
\bar{\varepsilon}^{p}_{n+1} &= \bar{\varepsilon}^{p}_{n} + \frac{2\Delta\gamma}{\omega_{n+1}^{2}}\sqrt{\boldsymbol{\sigma}_{n+1} : \mathbf{M} : \boldsymbol{\sigma}_{n+1}} \\
Y_{n+1} &= \frac{-1}{2\omega_{n+1}^{2}}\boldsymbol{\sigma}_{n+1} : \mathbf{E}^{-1} : \boldsymbol{\sigma}_{n+1}
\end{aligned} \quad . \tag{4.73}$$

The resulting implicit elastic predictor / plastic corrector procedure is summarized in Box 4.2 within an incremental time integration scheme. The solution of the system is undertaken by the Newton-Raphson iterative scheme, conveniently summarized in Box 4.3. The partial derivatives used in the iterative scheme are given by:

$$\begin{aligned}
\frac{\partial r_{\gamma}}{\partial\Delta\gamma} = &-\frac{4\sigma_{Y}H'}{\omega_{n+1}^{2}}\sqrt{\boldsymbol{\sigma}_{n+1} : \mathbf{M} : \boldsymbol{\sigma}_{n+1}} \\
&-\frac{8G}{\omega_{n+1}^{3}}\left(1-\frac{2\Delta\gamma\sigma_{Y}H'}{\sqrt{\boldsymbol{\sigma}_{n+1} : \mathbf{M} : \boldsymbol{\sigma}_{n+1}}}\right)\boldsymbol{\sigma}_{n+1} : \mathbf{M} : \left(\mathbf{I}+\frac{4\Delta\gamma G}{\omega_{n+1}}\mathbf{M}\right)^{-1} : \mathbf{M} : \boldsymbol{\sigma}_{n+1}
\end{aligned} \tag{4.74}$$

$$\frac{\partial r_{\gamma}}{\partial\omega_{n+1}} = -\frac{\Delta\gamma}{\omega_{n+1}}\frac{\partial r_{\gamma}}{\partial\Delta\gamma} \tag{4.75}$$

$$\begin{aligned}
\frac{\partial r_{\omega}}{\partial\Delta\gamma} = &\frac{2}{\omega_{n+1}^{2}}\left(\frac{-Y_{n+1}}{S}\right)^{s} H\left(\bar{\varepsilon}^{p}_{n+1}-\varepsilon^{p}_{D}\right)\sqrt{\boldsymbol{\sigma}_{n+1} : \mathbf{M} : \boldsymbol{\sigma}_{n+1}} \\
&-\frac{4Gs\Delta\bar{\varepsilon}^{p}}{S\omega_{n+1}^{3}}\left(\frac{-Y_{n+1}}{S}\right)^{s-1} H\left(\bar{\varepsilon}^{p}_{n+1}-\varepsilon^{p}_{D}\right)\boldsymbol{\sigma}_{n+1} : \mathbf{E}^{-1} : \left(\mathbf{I}+\frac{4\Delta\gamma G}{\omega_{n+1}}\mathbf{M}\right)^{-1} : \mathbf{M} : \boldsymbol{\sigma}_{n+1} \\
&-\frac{8G\Delta\gamma}{\omega_{n+1}^{3}\sqrt{\boldsymbol{\sigma}_{n+1} : \mathbf{M} : \boldsymbol{\sigma}_{n+1}}}\left(\frac{-Y_{n+1}}{S}\right)^{s} H\left(\bar{\varepsilon}^{p}_{n+1}-\varepsilon^{p}_{D}\right)\boldsymbol{\sigma}_{n+1} : \mathbf{M} : \left(\mathbf{I}+\frac{4\Delta\gamma G}{\omega_{n+1}}\mathbf{M}\right)^{-1} : \mathbf{M} : \boldsymbol{\sigma}_{n+1}
\end{aligned} \tag{4.76}$$

$$\frac{\partial r_{\omega}}{\partial\omega_{n+1}} = 1-\frac{\Delta\gamma}{\omega_{n+1}}\frac{\partial r_{\gamma}}{\partial\Delta\gamma} \tag{4.77}$$

where H' is the tangent modulus to the hardening curve. As local integration of the fully coupled constitutive equations will be undertaken in a dynamic explicit solution procedure, the computation of the consistent tangent operator with the described above integration scheme for the assembly of the tangent stiffness matrix is not required and it is not, therefore, addressed in this work.

Box 4.2 State update procedure for fully coupled Lemaitre's ductile isotropic damage model.

i) Elastic predictor

Given an elastic trial strain $\boldsymbol{\varepsilon}^{e\ trial} = \boldsymbol{\varepsilon}_n^e + \Delta\boldsymbol{\varepsilon}$, evaluate elastic trial stress:

$$\boldsymbol{\sigma}^{trial} = \boldsymbol{\sigma}_n + \omega_n \mathbf{E} : \Delta\boldsymbol{\varepsilon}$$

Check plastic consistency:

$$\text{IF } \Phi^{trial} = \frac{\boldsymbol{\sigma}^{trial} : \mathbf{M} : \boldsymbol{\sigma}^{trial}}{\omega_n^2} - \sigma_Y^2\left(\overline{\varepsilon}_n^p\right) \leq 0 \text{ THEN}$$

$$\text{Set } \left(.\right)_{n+1} = \left(.\right)^{trial} \text{ and RETURN}$$

ELSE go to (ii)

(ii) Plastic corrector (solve the system for the unknowns $\Delta\gamma$ and ω_{n+1})

$$\begin{cases} \dfrac{\boldsymbol{\sigma}_{n+1} : \mathbf{M} : \boldsymbol{\sigma}_{n+1}}{\omega_{n+1}^2} - \sigma_Y^2\left(\overline{\varepsilon}_{n+1}^p\right) = 0 \\ \omega_{n+1} - \omega_n + \Delta\overline{\varepsilon}^p \left(\dfrac{-Y_{n+1}}{S}\right)^s H\left(\overline{\varepsilon}_{n+1}^p - \varepsilon_D^p\right) = 0 \end{cases}$$

where:

$$\boldsymbol{\sigma}_{n+1} = \omega_{n+1}\left(\mathbf{I} + \frac{4\Delta\gamma G}{\omega_{n+1}}\mathbf{M}\right)^{-1} : \tilde{\boldsymbol{\sigma}}^{trial}$$

$$\Delta\overline{\varepsilon}^p = \frac{2\Delta\gamma}{\omega_{n+1}^2}\sqrt{\boldsymbol{\sigma}_{n+1} : \mathbf{M} : \boldsymbol{\sigma}_{n+1}}$$

$$Y_{n+1} = \frac{-1}{2\omega_{n+1}^2}\boldsymbol{\sigma}_{n+1} : \mathbf{E}^{-1} : \boldsymbol{\sigma}_{n+1}$$

(iii) Update $\overline{\varepsilon}_{n+1}^p$

$$\overline{\varepsilon}_{n+1}^p = \overline{\varepsilon}_n^p + \frac{2\Delta\gamma}{\omega_{n+1}^2}\sqrt{\boldsymbol{\sigma}_{n+1} : \mathbf{M} : \boldsymbol{\sigma}_{n+1}}$$

(iv) RETURN

Box 4.3 Newton-Raphson algorithm for return mapping system of equations for integration of fully coupled Lemaitre's ductile isotropic damage model.

i) Initialize Newton-Raphson method. Set initial guess $\Delta\gamma^{(0)} = 0$ and $\omega_{n+1}^{(0)} = \omega_n$ and compute residuals r_γ and r_ω

$$\begin{cases} r_\gamma = \dfrac{\boldsymbol{\sigma}_{n+1} : \mathbf{M} : \boldsymbol{\sigma}_{n+1}}{\omega_{n+1}^2} - \sigma_Y^2\left(\bar{\varepsilon}_{n+1}^p\right) \\ r_\omega = \omega_{n+1} - \omega_n + \Delta\bar{\varepsilon}^p \left(\dfrac{-Y_{n+1}}{S}\right)^s H\left(\bar{\varepsilon}^p - \varepsilon_D^p\right) \end{cases}$$

with:

$$\boldsymbol{\sigma}_{n+1} = \omega_{n+1}\left(\mathbf{I} + \frac{4\Delta\gamma G}{\omega_{n+1}}\mathbf{M}\right)^{-1} : \tilde{\boldsymbol{\sigma}}^{trial}$$

$$\Delta\bar{\varepsilon}^p = \frac{2\Delta\gamma}{\omega_{n+1}^2}\sqrt{\boldsymbol{\sigma}_{n+1} : \mathbf{M} : \boldsymbol{\sigma}_{n+1}}\ ;\ Y_{n+1} = \frac{-1}{2\omega_{n+1}^2}\boldsymbol{\sigma}_{n+1} : \mathbf{E}^{-1} : \boldsymbol{\sigma}_{n+1}$$

ii) Perform Newton-Raphson iteration

$$\begin{bmatrix} \dfrac{\partial r_\gamma}{\partial \Delta\gamma} & \dfrac{\partial r_\gamma}{\partial \omega_{n+1}} \\ \dfrac{\partial r_\omega}{\partial \Delta\gamma} & \dfrac{\partial r_\omega}{\partial \omega_{n+1}} \end{bmatrix}^{(k-1)} \begin{bmatrix} \delta\Delta\gamma \\ \delta\omega \end{bmatrix}^{(k)} = -\begin{bmatrix} r_\gamma\left(\Delta\gamma, \omega_{n+1}\right) \\ r_\omega\left(\Delta\gamma, \omega_{n+1}\right) \end{bmatrix}^{(k-1)}$$

New guess for $\Delta\gamma$ and ω_{n+1}:

$$\Delta\gamma^{(k)} = \Delta\gamma^{(k-1)} + \delta\Delta\gamma^{(k)}\ ;\ \omega_{n+1}^{(k)} = \omega_{n+1}^{(k-1)} + \delta\omega^{(k)}$$

Update stress, equivalent plastic strain and energy release rate:

$$\boldsymbol{\sigma}_{n+1} = \omega_{n+1}\left(\mathbf{I} + \frac{4\Delta\gamma G}{\omega_{n+1}}\mathbf{M}\right)^{-1} : \tilde{\boldsymbol{\sigma}}^{trial}$$

$$\Delta\bar{\varepsilon}^p = \frac{2\Delta\gamma}{\omega_{n+1}^2}\sqrt{\boldsymbol{\sigma}_{n+1} : \mathbf{M} : \boldsymbol{\sigma}_{n+1}}\ ;\ Y_{n+1} = \frac{-1}{2\omega_{n+1}^2}\boldsymbol{\sigma}_{n+1} : \mathbf{E}^{-1} : \boldsymbol{\sigma}_{n+1}$$

iii) Compute new residuals $\left(r_\gamma, r_\omega\right)$ and check for convergence

IF $\left\| r_\gamma \right\| \le tolerance$ AND $\left\| r_\omega \right\| \le tolerance$ THEN RETURN

iv) Go to (ii)

4.6 Simplified elasto-plastic isotropic damage model with crack closure

The efficiency of the numerical integration schemes has a direct impact on the overall efficiency of the finite element framework. In the case of dynamic explicit solution strategy, the computational cost of an analysis depends decisively on the CPU time spent in Gauss point calculations. The use of more complex constitutive models, such the Barlat family criteria [Barlat 1991] [Barlat 2005] or recent criteria for HCP metals [Cazacu 2006] [Plunkett 2008], can potentially incur in a dramatic increase in analysis time, if a fully coupled damage model is adopted. Moreover, an extra degree of complexity is introduced in the theoretical formulation and in the exact linearization of the field equations for the implementation in a finite element code.

Having in mind a dynamic explicit implementation, a possible way to reduce the computational cost and to have a fast integration algorithm is to consider a decoupling between stress and damage update algorithms, but with damage variable, converged in the previous time increment, affecting hardening law in the current stress update procedure. The main advantage of this approach is to provide a fast method to include damage evaluation in an already implemented constitutive model with minor changes in the code. Another characteristic is concerned with plastic softening behaviour and constant change in stress distribution and triaxiality information along component caused by damage growth. This problem associated with fully uncoupled approaches does not arise in this partial coupling strategy that enables the estimation of continuous degradation of the physical properties, as occurs in fully coupled approaches. Also, this simplified damage inclusion allows that further improvements to the original damage model can be included without the risk of increasing analysis time in a remarkable way or add extra difficulties in numerical implementation.

An important refinement that can be included in the model is the micro-crack closure effect, particularly relevant for bulk metal forming processes where material is subjected to high compressive forces and extreme straining. Original Lemaitre's model presents an important feature, typical of damage functions [Atkins 1996], which is related to the fact that damage evolution depends on the stress triaxiality:

$$\dot{D} = \frac{\dot{\gamma}}{1-D}\left(\frac{-Y}{S}\right)^{s} \tag{4.78}$$

where Y, the strain energy density release rate, is given by:

$$Y = -\frac{\bar{\sigma}^2}{2E\left(1-D\right)^2}\left[\frac{2}{3}\left(1+\nu\right)+3\left(1-2\nu\right)\left(\frac{\sigma_H}{\bar{\sigma}}\right)^2\right] \tag{4.79}$$

where $\bar{\sigma}$ is the equivalent von Mises stress, σ_H the hydrostatic stress and E and ν are the Young's modulus and Poisson's ratio. But, since the dependence is done in a quadratic way, no distinction is made in terms of damage growth rates for identical stress triaxiality with opposite signs. As stated by Pires [2005], a clear distinction must be performed between both states due to the fact that, under a compressive state, micro-cracks may partially close and, therefore, there is an increase of loading bearing area, promoting a decrease in the damage growth rate. This important feature was studied and implemented by several authors [Pires 2003] [Pires 2005] [Desmorat 2008]. The basic idea is to introduce an additional parameter h_C that enables the modelling of such micro-crack closure effect.

Based on the work of Pires [2005], this section presents the simplified damage coupling strategy with the inclusion of unilateral effects in damage evolution.

4.6.1 Crack closure effect definition

Under compressive stresses, micro-defects may partially close, increasing the area that effectively carries the compression load. In this case, material stiffness may be partially or, depending on the conditions, fully recovered. It is known that some materials may present different values for the effective Young's modulus for tension and compression. This phenomenon is usually referred as unilateral conditions, standing for partial (or fully) recovery of initial undamaged elasticity under compression [Lemaitre 2005]. Being a thermodynamical state, damage is represented by the same value in both states but its influence is dissimilar in tension and compression. To introduce this dissimilarity, let us consider the uniaxial stress case. In accordance with Lemaitre's theory, for a material already damaged in tension, the effective Young's modulus $\tilde{E}$ is given by:

$$\tilde{E} = \left(1 - D\right) E \, . \tag{4.80}$$

Using the hypothesis of strain equivalence and the effective stress concept, the uniaxial elastic damaged law is given by:

$$\sigma = \left(1 - D\right) E \varepsilon \tag{4.81}$$

and damage D can be defined as:

$$D = 1 - \frac{\tilde{E}}{E} \, . \tag{4.82}$$

When a compressive force is applied, perpendicular to the damaged section area, micro-cracks will partially close, thus effective load bearing area increases. In this case, damage will act in a less pronounced mode in the stress. To model this lower damage influence, an extra parameter is introduced in the uniaxial elastic damaged law. Therefore, in compression, the uniaxial stress-strain law is assumed to take the form:

$$\sigma = \left(1 - h_C D\right) E\varepsilon \tag{4.83}$$

where h_C is the micro-crack closure parameter. This parameter can be determined experimentally and assumes values ranging from 0 up to 1. $h_C = 1$ reports a similar behaviour in tension and compression, without any closure action, while $h_C = 0$ describes the full closure effect in compression, fully recovering the undamaged elastic behaviour.

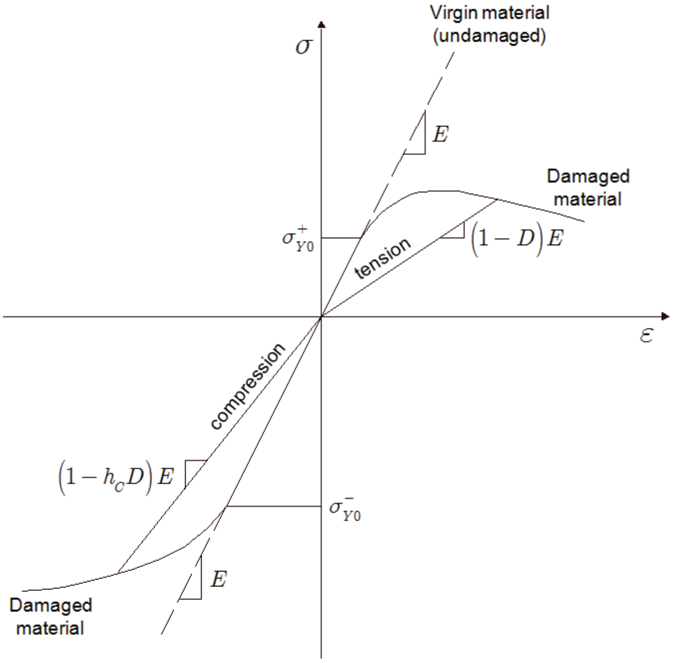

Figure 4.3 Uniaxial elastic model with damage and partial crack closure effect.

Considering distinctive effective Young's modulus for tension and compression as $\tilde{E}^{+}$ and $\tilde{E}^{-}$, respectively, h_C can be calculated as:

$$h_C = \frac{E - \tilde{E}^{-}}{E - \tilde{E}^{+}}. \tag{4.84}$$

A typical value of 0.2 for h_C is observed in experiments [Lemaitre 1996] and it is assumed to be a material parameter, neglecting any effect of damage itself on the closure phenomenon and, consequently, in the variation of h_C. Figure 4.3 [Pires 2005] depicts the above described distinctive behaviour for an uniaxial stress state.

4.6.2 Tensile / compressive split of stress tensor

As seen, for the uniaxial case, it is relatively easy to establish a distinction between compressive and tensile states. However, the same model extension to a generic three-dimensional situation is not trivial. In model proposed by Pires [2005], such distinction is performed on the basis of a tensile / compressive split of the stress tensor.

Representing a three-dimensional stress tensor $\boldsymbol{\sigma}$ using their principal components, one can write that:

$$\boldsymbol{\sigma} = \sum_{i=1}^{3} \sigma_i \, \boldsymbol{e}_i \otimes \boldsymbol{e}_i \tag{4.85}$$

where σ_i are the principal stresses and $\left\{ \boldsymbol{e}_1, \boldsymbol{e}_2, \boldsymbol{e}_3 \right\}$ is the orthonormal basis vectors along the principal directions. In this representation, stress tensor can be additively decomposed into positive and negative components as:

$$\boldsymbol{\sigma} = \boldsymbol{\sigma}^+ + \boldsymbol{\sigma}^- \tag{4.86}$$

where $\boldsymbol{\sigma}^+$ and $\boldsymbol{\sigma}^-$ are, respectively, the tensile and compressive components of $\boldsymbol{\sigma}$, defined as:

$$\boldsymbol{\sigma}^+ = \sum_{i=1}^{3} \left\langle \sigma_i \right\rangle \boldsymbol{e}_i \otimes \boldsymbol{e}_i \tag{4.87}$$

$$\boldsymbol{\sigma}^- = -\sum_{i=1}^{3} \left\langle -\sigma_i \right\rangle \boldsymbol{e}_i \otimes \boldsymbol{e}_i \, . \tag{4.88}$$

The symbol $\left\langle \; \right\rangle$ represents the Macauley bracket function, that for a scalar a, delivers:

$$\left\langle a \right\rangle = \begin{cases} a & \mathit{if} \;\; a \geq 0 \\ 0 & \mathit{if} \;\; a < 0 \end{cases} . \tag{4.89}$$

This simple methodology will allows us to clearly establish a differentiation on damage growth in opposite stress states as we will see in the next section.

4.6.3 Crack closure effect on damage evolution

If a fully coupled analysis is considered, the inclusion of the above crack closure effect behaviour leads to a rather complex integration algorithm since the damaged elasticity law casted in the original Lemaitre's model given by:

$$\begin{aligned} \boldsymbol{\varepsilon} &= \frac{1}{1-D} \mathbf{E} : \boldsymbol{\sigma} \\ &= \frac{1}{1-D} \left[\frac{1+\nu}{2E} \boldsymbol{\sigma} - \frac{\nu}{2E} \operatorname{tr}\left(\boldsymbol{\sigma} \right) \boldsymbol{I} \right] \end{aligned} \tag{4.90}$$

for a multi-dimensional damaged elastic material needs to be changed in order to contemplate the tensile / compressive split of the stress tensor as follows:

$$\boldsymbol{\varepsilon} = \frac{1+\nu}{2E}\left(\frac{\boldsymbol{\sigma}^{+}}{1-D} + \frac{\boldsymbol{\sigma}^{-}}{1-h_C D}\right) - \frac{\nu}{2E}\left(\frac{\langle \mathrm{tr}\,\boldsymbol{\sigma}\rangle}{1-D} + \frac{\langle -\mathrm{tr}\,\boldsymbol{\sigma}\rangle}{1-h_C D}\right)\boldsymbol{I}. \tag{4.91}$$

As can be seen, this new stress-strain relation, although remaining isotropic, is no longer linear and its computation must be performed by means of a Newton-Raphson procedure. The computational implementation of the above damaged elasticity law, without any damage evolution, was treated by Souza Neto *et al.* [2008] within an implicit finite element environment.

Assuming that elastic strains remain almost infinitesimal for the class of materials and processes addressed in this thesis, as supposed by Pires [2005], it is possible to justify the decoupling between elasticity and damage, avoiding the non-linear damaged elasticity law, and to take into account the closure effect only in the damage evolution law. This alternative description is provided by the damage evolution law proposed by Ladevèze and Lemaitre [1984] (described in more detail in [Lemaitre 1996]). In their approach, the inclusion of the crack closure effect is achieved by modifying the strain energy density release rate Y, given in the original model as:

$$Y = \frac{-1}{2E(1-D)^2}\left[(1+\nu)\boldsymbol{\sigma}:\boldsymbol{\sigma} - \nu(\mathrm{tr}\boldsymbol{\sigma})^2\right] \tag{4.92}$$

by the definition:

$$\begin{aligned} Y = & \frac{-1}{2E(1-D)^2}\left[(1+\nu)\boldsymbol{\sigma}^{+}:\boldsymbol{\sigma}^{+} - \nu\langle \mathrm{tr}\boldsymbol{\sigma}\rangle^2\right] \\ & - \frac{h_C}{2E(1-h_C D)^2}\left[(1+\nu)\boldsymbol{\sigma}^{-}:\boldsymbol{\sigma}^{-} - \nu\langle -\mathrm{tr}\boldsymbol{\sigma}\rangle^2\right] \end{aligned} \tag{4.93}$$

where the tensile / compressive split of stress tensor is carried out according to Equation (4.86), keeping the damage evolution law unchanged:

$$\dot{D} = \frac{\dot{\gamma}}{1-D}\left(\frac{-Y}{S}\right)^{s}. \tag{4.94}$$

4.6.4 Simplified integration algorithm

In this section, the derivation of the simplified integration algorithm is done for the elasto-plastic damage constitutive model with quasi-unilateral effects as described in previous sections. As already done for the fully coupled analysis, let us consider what happens at a typical integration point of finite element mesh in a pseudo-time interval $[t_n, t_{n+1}]$. Having variables $\boldsymbol{\sigma}_n$, $\boldsymbol{\varepsilon}^e_n$, $\boldsymbol{\varepsilon}^p_n$, $\bar{\varepsilon}^p_n$ and D_n defined in the beginning of interval, t_n, and given a strain increment $\Delta\boldsymbol{\varepsilon}$ corresponding to the time interval

$\left[t_n, t_{n+1}\right]$, the numerical integration algorithm should supply the updated values $\boldsymbol{\sigma}_{n+1}$, $\boldsymbol{\varepsilon}^e_{n+1}$, $\boldsymbol{\varepsilon}^p_{n+1}$, $\bar{\varepsilon}^p_{n+1}$ and D_{n+1} for the end of interval, t_{n+1}, in a consistent manner with the constitutive equations of the model. For the sake of completeness, the main steps leading to the numerical implementation are repeated here.

4.6.4.1 Elastic predictor

The first step is to evaluate the elastic trial stress, assuming that increment is purely elastic, without any evolution of internal variables. Therefore, the elastic trial stress $\boldsymbol{\sigma}^{trial}$ is calculated by using the linear isotropic elasticity law given by:

$$\boldsymbol{\sigma}^{trial} = \boldsymbol{\sigma}_n + \mathbf{E} : \Delta\boldsymbol{\varepsilon} \tag{4.95}$$

where $\mathbf{E}$ is the linear elastic operator. The yield function is then evaluated for the stress state defined in the elastic trial:

$$\Phi^{trial} = \boldsymbol{\sigma}^{trial} : \mathbf{M} : \boldsymbol{\sigma}^{trial} - \left(1 - D_n\right)^2 \sigma_Y^2\left(\bar{\varepsilon}^p_n\right). \tag{4.96}$$

Note that damage value D_n converged in previous increment affects the hardening rule. If $\Phi^{trial} \leq 0$, the process is indeed elastic within the interval $\left[t_n, t_{n+1}\right]$ and the elastic trial state coincides with the updated state at time $t = t_{n+1}$. In other words, there is no plastic flow or damage evolution within the interval and:

$$\begin{aligned}
\boldsymbol{\sigma}_{n+1} &= \boldsymbol{\sigma}^{trial} \\
\boldsymbol{\varepsilon}^e_{n+1} &= \boldsymbol{\varepsilon}^e_n + \Delta\boldsymbol{\varepsilon} \\
\boldsymbol{\varepsilon}^p_{n+1} &= \boldsymbol{\varepsilon}^p_n \qquad . \\
\bar{\varepsilon}^p_{n+1} &= \bar{\varepsilon}^p_n \\
D_{n+1} &= D_n
\end{aligned} \tag{4.97}$$

If the consistency condition $\Phi^{trial} \leq 0$ is violated, one needs to apply the plastic corrector procedure and, additionally, the damage state update procedure, whose step-by-step derivation is described in the following paragraphs.

4.6.4.2 Plastic corrector

Using the special features obtained for the updated stress tensor $\boldsymbol{\sigma}_{n+1}$ and equivalent plastic strain $\bar{\varepsilon}^p_{n+1}$ by using the Hill48 criterion in a quadratic form (see Section 4.5.2), it is possible to reduce the plastic return algorithm to the solution of the non-linear equation in $\Delta\gamma$:

$$\Phi\left(\Delta\gamma\right) = \boldsymbol{\sigma}_{n+1} : \mathbf{M} : \boldsymbol{\sigma}_{n+1} - \left(1 - D_n\right)^2 \sigma_Y^2\left(\bar{\varepsilon}^p_{n+1}\right) \tag{4.98}$$

where σ_Y is the current yield stress, given by a hardening rule function of the equivalent plastic strain $\bar{\varepsilon}^p_{n+1}$, and $\boldsymbol{\sigma}_{n+1}$ e $\bar{\varepsilon}^p_{n+1}$ are defined as a function of the incremental consistency plastic multiplier, $\Delta\gamma$:

$$\boldsymbol{\sigma}_{n+1} = \left(\mathbf{I} + 4\Delta\gamma G \mathbf{M}\right)^{-1} : \boldsymbol{\sigma}^{trial} \tag{4.99}$$

$$\bar{\varepsilon}^p_{n+1} = \bar{\varepsilon}^p_n + 2\Delta\gamma\sqrt{\boldsymbol{\sigma}_{n+1} : \mathbf{M} : \boldsymbol{\sigma}_{n+1}}\,. \tag{4.100}$$

The solution of the system is undertaken by the Newton-Raphson iterative scheme. The term for the linearization of the iterative method is given by:

$$\begin{aligned}\frac{d\Phi}{d\Delta\gamma} &= -4\sigma_Y H'\sqrt{\boldsymbol{\sigma}_{n+1} : \mathbf{M} : \boldsymbol{\sigma}_{n+1}} \\ &\quad - 4G\left(2 - \frac{4\sigma_Y H'\Delta\gamma}{\sqrt{\boldsymbol{\sigma}_{n+1} : \mathbf{M} : \boldsymbol{\sigma}_{n+1}}}\right)\boldsymbol{\sigma}_{n+1} : \mathbf{M} : \left(\mathbf{I} + 4\Delta\gamma G\mathbf{M}\right)^{-1} : \mathbf{M} : \boldsymbol{\sigma}_{n+1}\end{aligned} \tag{4.101}$$

where H' denotes the updated slope to the hardening curve at t_{n+1}:

$$H' = \left.\frac{d\sigma_Y}{d\bar{\varepsilon}^p}\right|_{\bar{\varepsilon}^p_{n+1}}. \tag{4.102}$$

4.6.4.3 Damage state update

After the computation of the new stress state $\boldsymbol{\sigma}_{n+1}$, algorithm proceeds with the update of damage variable, D_{n+1}. The calculation of the new damage state is made by solving the non-linear equation for the updated damage D_{n+1}:

$$D_{n+1} - D_n - \frac{\Delta\gamma}{1 - D_{n+1}}\left(\frac{-Y_{n+1}}{S}\right)^s H\left(\bar{\varepsilon}^p_{n+1} - \varepsilon^p_D\right) = 0 \tag{4.103}$$

where $\Delta\gamma$ the incremental consistency plastic multiplier and Y_{n+1} is the strain energy density release rate given by the expression:

$$\begin{aligned}Y_{n+1} &= \frac{-1}{2E\left(1 - D_{n+1}\right)^2}\left[\left(1+\nu\right)\boldsymbol{\sigma}^+_{n+1} : \boldsymbol{\sigma}^+_{n+1} - \nu\left\langle \mathrm{tr}\boldsymbol{\sigma}_{n+1}\right\rangle^2\right] \\ &\quad - \frac{h_C}{2E\left(1 - h_C D_{n+1}\right)^2}\left[\left(1+\nu\right)\boldsymbol{\sigma}^-_{n+1} : \boldsymbol{\sigma}^-_{n+1} - \nu\left\langle -\mathrm{tr}\boldsymbol{\sigma}_{n+1}\right\rangle^2\right]\end{aligned} \tag{4.104}$$

accounting for micro-cracking closure effect.

The solution of Equation (4.103) is also undertaken by the Newton-Raphson iterative scheme and the corresponding term for the linearization of the method is given by:

$$\begin{aligned}\frac{dr}{dD_{n+1}} = 1 - &\frac{\Delta\gamma}{\left(1-D_{n+1}\right)^2}\left(\frac{-Y_{n+1}}{S}\right)^s H\left(\bar{\varepsilon}^p_{n+1} - \varepsilon^p_D\right) \\ &- \frac{s\Delta\gamma}{\left(1-D_{n+1}\right)S}\left(\frac{-Y_{n+1}}{S}\right)^{s-1}\frac{d\left(-Y_{n+1}\right)}{dD_{n+1}} H\left(\bar{\varepsilon}^p_{n+1} - \varepsilon^p_D\right)\end{aligned} \tag{4.105}$$

where derivative $d\left(-Y_{n+1}\right)/dD_{n+1}$ is calculated as:

$$\begin{aligned}\frac{d\left(-Y_{n+1}\right)}{dD_{n+1}} = &\frac{1}{E\left(1-D_{n+1}\right)^3}\left[\left(1+\nu\right)\boldsymbol{\sigma}^+_{n+1} : \boldsymbol{\sigma}^+_{n+1} - \nu\left\langle \mathrm{tr}\boldsymbol{\sigma}_{n+1}\right\rangle^2\right] \\ &+ \frac{h_C^2}{E\left(1-h_C D_{n+1}\right)^3}\left[\left(1+\nu\right)\boldsymbol{\sigma}^-_{n+1} : \boldsymbol{\sigma}^-_{n+1} - \nu\left\langle -\mathrm{tr}\boldsymbol{\sigma}_{n+1}\right\rangle^2\right]\end{aligned} . \tag{4.106}$$

The partial coupling state update algorithm can be summarized as presented in Box 4.4. Obviously, using this simplified decoupled implementation, damage growth indirectly affects the plasticity evolution law, causing plastic softening and allowing stress redistribution and triaxiality change due to damage. Thus, there is no need to recalibrate the material parameters, identified using a fully coupled implementation, for this simplified strategy. However, this integration algorithm has the disadvantage of being largely dependent on the considered time increment, Δt. If the time increment becomes too large, this partially coupled integration algorithm may not guarantee that the yield condition is satisfied on $t = t_{n+1}$, incurring in small errors, and, as a result, it is possible that the solution drifts away from the updated yield surface. But, since a dynamic explicit finite element environment is used, this is not a concern because stable time increment is usually sufficiently small to overcome this disadvantage and provide good accuracy.

Box 4.4 State update procedure for partially coupled Lemaitre's ductile isotropic damage model.

```
i) Elastic predictor
    Given an elastic trial strain $\boldsymbol{\varepsilon}^{e\ trial} = \boldsymbol{\varepsilon}^{e}_{n} + \Delta\boldsymbol{\varepsilon}$, evaluate elastic trial stress:
        $\boldsymbol{\sigma}^{trial} = \boldsymbol{\sigma}_{n} + \mathbf{E} : \Delta\boldsymbol{\varepsilon}$
    Check plastic consistency:
        IF $\Phi^{trial} = \boldsymbol{\sigma}^{trial} : \mathbf{M} : \boldsymbol{\sigma}^{trial} - \left(1 - D_{n}\right)^{2} \sigma_{Y}^{2}\left(\bar{\varepsilon}^{p}_{n}\right) \leq 0$ THEN
            Set $\left(.\right)_{n+1} = \left(.\right)^{trial}$ and RETURN
        ELSE go to (ii)

ii) Plastic corrector (solve the non–linear equation for the unknown $\Delta\gamma$)
    $\Phi\left(\Delta\gamma\right) = \boldsymbol{\sigma}_{n+1} : \mathbf{M} : \boldsymbol{\sigma}_{n+1} - \left(1 - D_{n}\right)^{2} \sigma_{Y}^{2} = 0$
    where:
    $\boldsymbol{\sigma}_{n+1} = \left(\mathbf{I} + 4\Delta\gamma G \mathbf{M}\right)^{-1} : \boldsymbol{\sigma}^{trial}$
    $\Delta\bar{\varepsilon}^{p} = 2\Delta\gamma\sqrt{\boldsymbol{\sigma}_{n+1} : \mathbf{M} : \boldsymbol{\sigma}_{n+1}}$

iii) Update $\bar{\varepsilon}^{p}_{n+1}$
    $\bar{\varepsilon}^{p}_{n+1} = \bar{\varepsilon}^{p}_{n} + 2\Delta\gamma\sqrt{\boldsymbol{\sigma}_{n+1} : \mathbf{M} : \boldsymbol{\sigma}_{n+1}}$

iv) Damage state update (solve the non–linear equation for the new damage state $D_{n+1}$)
    $D_{n+1} - D_{n} - \dfrac{\Delta\gamma}{1 - D_{n+1}}\left(\dfrac{-Y_{n+1}}{S}\right)^{s} H\left(\bar{\varepsilon}^{p}_{n+1} - \varepsilon^{p}_{D}\right) = 0$
    where:
    $Y_{n+1} = \dfrac{-1}{2E\left(1 - D_{n+1}\right)^{2}}\left[\left(1 + \nu\right)\boldsymbol{\sigma}_{+} : \boldsymbol{\sigma}_{+} - \nu\left\langle \mathrm{tr}\boldsymbol{\sigma}\right\rangle^{2}\right]$
        $- \dfrac{h_{C}}{2E\left(1 - h_{C} D_{n+1}\right)^{2}}\left[\left(1 + \nu\right)\boldsymbol{\sigma}_{-} : \boldsymbol{\sigma}_{-} - \nu\left\langle -\mathrm{tr}\boldsymbol{\sigma}\right\rangle^{2}\right]$

v) RETURN
```

4.7 Remarks on non-local formulations

The classical theories of plasticity and damage, based on the use of internal variables and their evolution, are local continuum theories, meaning that material behaviour is assumed to be independent of influences of surroundings material points. With this assumption, the introduction of damage evolution in large deformation problems may result in numerical stability problems, namely a pathological effect of discretization dependence, either in size either in orientation. This is particularly relevant when the characteristic dimension of the plastic deformation or damage is of the same order as the material intrinsic length scale, as can occur in the neighbourhood of localized strain area. These length scale effects can be described by micromechanics theories and, although multi-scale modelling is an ongoing and promising research field, its implementation and application is still computationally expensive and phenomenological models are still favoured.

To remedy and / or attenuate the pathological mesh dependence at a macroscopic scale, several authors supply an internal length scale to the continuum model, aiming to mimic length scale effects due to microstructure heterogeneity. In these so-called non-local formulations, the local constitutive internal quantity associated with the dissipative process is simply replaced by its non-local counterpart in order to alleviate the discretization dependence. To define this non-local field, two main approaches can be considered: integral and gradient formulations. In integral models, the non-local damage field $\bar{D}$ is defined from a weighted average of the local damage field D as:

$$\bar{D}\left(\boldsymbol{x}\right)=\int_V w\left(\boldsymbol{x},\boldsymbol{p}\right)D\left(\boldsymbol{p}\right)dV \tag{4.107}$$

where $w\left(\boldsymbol{x},\boldsymbol{p}\right)$ is a chosen non-local weight function, establishing the influence of the local damage at point $\boldsymbol{p}$ to the non-local damage field at point $\boldsymbol{x}$.

In the case of gradient models, the non-local variable for damage $\bar{D}$ is defined as an average of the local variable field D, conditioned by the length scale value l, which acts as a diffusivity term, and by the difference between the local and non-local fields, which acts as a source term:

$$\left[D\left(\boldsymbol{x}\right)-\bar{D}\left(\boldsymbol{x}\right)\right]+\frac{1}{2}l^2\nabla^2\bar{D}\left(\boldsymbol{x}\right)=0. \tag{4.108}$$

The length parameter determines the size of the volume, which effectively contributes to the non-local quantity and is related to the scale of the microstructure.

In the literature, further details of these models are addressed in several works as the ones developed by [Peerlings 1996] [Bazant 2002] [Al-Rub 2004] [César de Sá 2006] [Mediavilla 2006], for instance.

5. ANISOTROPIC DAMAGE MECHANICS

This chapter reviews higher order definitions for the damage variable, introduced in order to model the directional nature of damaging process. The physical interpretation of a second order representation is presented and the thermodynamically consistent damage model proposed by Lemaitre *et al.* [2000a], based on this definition, is described. The corresponding computational anisotropic damage model is developed and implemented using an updated Lagrangian finite element formulation for the numerical solution of the problem. Finally, a sensitivity analysis of the implemented model regarding the influence of several parameters is also presented.

5.1 Introduction. Higher-order nature of damage variables

The scalar definition is obviously the simplest representation that can be considered to define the damage variable [Chaboche 2007]. Its simplicity is very attractive for numerical implementation and, in the case of proportional loadings, the adoption of a scalar value for damage is sufficient to provide an acceptable prediction of load carrying capability to withstand additional loadings, number of cycles or useful life until failure of structural components.

However, in situations of non-proportional loading and complex cases of anisotropy, the consideration of a scalar value to characterize damage can be simplistic. It is therefore imperative to define a variable of higher order to be able to capture the directional nature of nucleation and growth of micro-cracks, which are inevitably dependent on the direction of loading and plastic flow and, therefore, are essentially anisotropic. Different types of damage variables were introduced in order to describe the oriented features of damaging effects [Chaboche 2007]. The most simple theory was proposed by Ladevèze [Lemaitre 1996] which employs a double scalar damage definition for attempting to describe anisotropic damage behaviour, affecting one variable to the deviatoric stress components and the other to the hydrostatic stress. Other theories introduce several scalar variables, each one associated with predefined material directions in order to describe directional nature of damage and / or several damage mechanisms present in the structure. This kind of approach is more used for composite structures, where micro-cracks are often oriented by the structure and direction of the constituents (plies, reinforcements, fibers) [Gasser 1998]. One-rank tensor damage variable was also proposed by Krajcinovic and Fonseka [1981] within the framework of the general thermodynamics theory. The original model assumed a vector-based damage variable to account for the progressive deterioration of brittle materials emphasizing a multitude of flat, penny-shaped planar micro-defects. A drawback of these vectorial damage variable models is related to the fact that they are not able to degenerate onto their isotropic versions. Only second or higher even-order tensors can be adopted as damage variables to properly describe damage-induced anisotropy [Wu 2008]. Fourth-order tensors are the lowest order tensors capable to completely describe the damage-induced anisotropy, regardless of the initial isotropic or anisotropic damage state of the material. First consideration of this damage definition was made by Chaboche [Chaboche 2007] using directly the concept of effective stress associated with the principle of strain equivalence for linear elasticity. Others authors also pursuit this definition for the anisotropic damage behaviour [Ortiz 1985] [Ju 1989]. Although higher-rank tensors contain more information and can provide a more accurate representation of the behaviour of material degradation, drawbacks to the application of these tensors are often associated with the difficulty of measuring all the required material parameters, with inefficient numerical analysis and difficulties in postulating appropriate evolution laws [Wu 2008]. Thus, second-order tensor representation is preferred in the modelling of damage-induced anisotropy and corresponds to the most frequently used variable nature for the description of damage-induced anisotropy. This approach has been widely used by several authors [Cordebois 1982] [Chow 1987] [Murakami 1988] [Lemaitre 2000a] [Al-Rub 2003] [Brunig 2003] and stands as the minimum complexity of an anisotropic damage theory. The physical meaning of this variable can be related with the decrease of load-carrying effective area caused by the development of microscopic cracks and cavities [Murakami 1988], as in the isotropic damage definition, but this second order representation is limited to the description of orthotropic damage behaviour of initially isotropic materials. On the contrary of the fourth-order damage theory that directly provides the fourth-order operator for the effective stress definition, the second-rank damage variable introduces difficulties in the effective stress definition, since it is necessary to state how the second-rank tensor acts on the fourth-rank operator characterizing the elastic-damaged behaviour [Murakami 1988] [Chaboche 2007]. Nevertheless, due to its clear physical meaning and the thermodynamical consistent theory developed by Lemaitre *et al.* [2000a], the second-order tensor damage variable is adopted in this work to express the elastic or plastic behaviours of anisotropic damaged materials.

5.2 Physical interpretation of a second order damage variable

In order to establish the physical interpretation of the second order damage variable, let us first define the concept of fictitious (or equivalent) undamaged state for the simplest case, the uniaxial case. Consider a bar, undeformed, with an initial sectional area A_0, in an undamaged state, $D = 0$, as shown in Figure 5.1a.

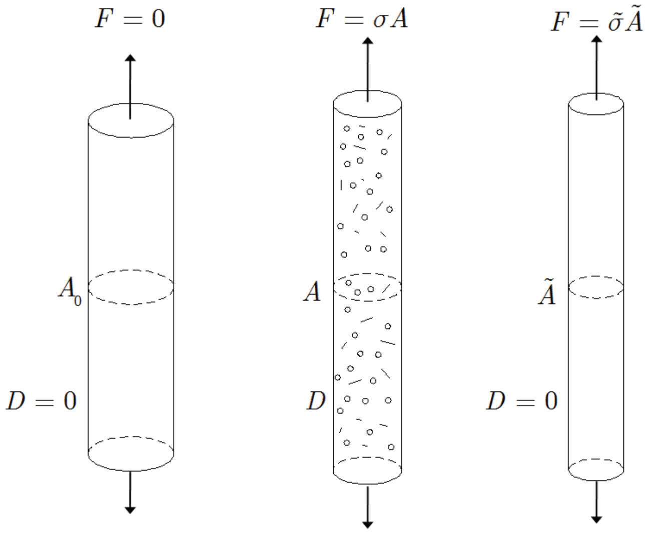

Figure 5.1 Damage of a bar under uniaxial tension; a) Initial undeformed and undamaged state; b) Current damaged state; c) Equivalent (fictitious) undamaged state.

Applying a force F to both ends, the bar will deform plastically and, due to nucleation, growth and coalescence of micro-voids, damage will occur and the so-called current damaged state is attained, Figure 5.1b. In this state, the total area is represented by the variable A and the stress that acts in this area can be written as:

$$\sigma = \frac{F}{A}. \tag{5.1}$$

But, due to damage, the load-carrying net area will be reduced and force F will act in such reduced or effective area $\tilde{A}$, magnifying the effects of stress. Damage can be related with this reduced area as:

$$1 - D = \frac{\tilde{A}}{A}. \tag{5.2}$$

It is then possible to assume the existence of a mechanically equivalent bar, Figure 5.1c, undamaged, where the cross-sectional area is reduced due to damage to an effective area $\tilde{A}$ and the stress is substituted by the amplified effective stress $\tilde{\sigma}$, subjected to an equivalent force F:

$$F = \tilde{\sigma}\tilde{A}. \tag{5.3}$$

Thus, damage D can be seen as the relation between the areas A and $\tilde{A}$ corresponding to the two mechanically equivalent states, current damaged state and fictitious undamaged state, expressed by the relation in Equation (5.2). This uniaxial concept of fictitious (or equivalent) undamaged state, taking into account the load-carrying net area reduction due to damage, can also be extended to characterize damage state in a general tridimensional case [Murakami 1988].

To this end, let us define an area element PQR, arbitrarily oriented in a three-dimensional body $\mathcal{B}$, as shown in Figure 5.2b. This element is represented by the line elements PQ and PR and the area PQR is defined by vectors $d\boldsymbol{x}$, $d\boldsymbol{y}$ and $\boldsymbol{v}dA$. Consider, also, the existence of an initial state $\mathcal{B}_0$, undeformed, and the representation of the corresponding area element in this state, defined by line elements P_0Q_0 and P_0R_0 and vectors $d\boldsymbol{x}_0$, $d\boldsymbol{y}_0$ and $\boldsymbol{v}_0 dA_0$. Additionally, consider that the deformation gradient that transforms the initial state into the deformed and damaged state is represented by $\boldsymbol{F}$.

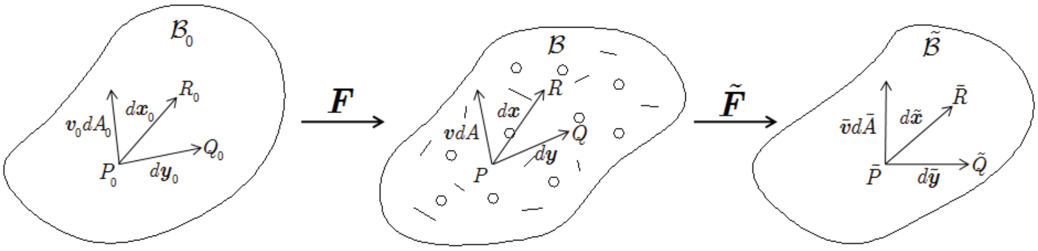

Figure 5.2 Definition of a tridimensional damage state; a) Initial undamaged configuration; b) Current damaged configuration; c) Equivalent (fictitious) undamaged configuration.

Considering the occurrence of tridimensional damage and its effects in reducing the area PQR, it is possible, as in the uniaxial case, to postulate the existence of a fictitious undamaged state $\tilde{\mathcal{B}}$, where the element PQR in the current damaged configuration is equivalent to the surface element $\tilde{P}\tilde{Q}\tilde{R}$ in this fictitious configuration, defined by the vectors $d\tilde{\boldsymbol{x}}$, $d\tilde{\boldsymbol{y}}$ and $\tilde{\boldsymbol{v}}d\tilde{A}$. The fictitious deformation gradient that transforms $\mathcal{B}$ to $\tilde{\mathcal{B}}$ is represented by $\tilde{\boldsymbol{F}}$. Therefore, vectors $d\tilde{\boldsymbol{x}}$ and $d\tilde{\boldsymbol{y}}$ are given as:

$$d\tilde{\boldsymbol{x}} = \tilde{\boldsymbol{F}}d\boldsymbol{x} \text{ and } d\tilde{\boldsymbol{y}} = \tilde{\boldsymbol{F}}d\boldsymbol{y} \tag{5.4}$$

and the area vector $\tilde{\boldsymbol{v}}d\tilde{A}$ is related with $\boldsymbol{v}dA$ in $\mathcal{B}$ as [Murakami 1988]:

$$\tilde{\boldsymbol{\upsilon}} d\tilde{A} = \frac{1}{2} d\tilde{\boldsymbol{x}} \times d\tilde{\boldsymbol{y}} = \tilde{J}\left(\tilde{\boldsymbol{F}}^{-1}\right)^{T} \boldsymbol{\upsilon} dA \tag{5.5}$$

where $\tilde{J}$ is the determinant of the deformation gradient $\tilde{\boldsymbol{F}}$:

$$\tilde{J} = \det\left(\tilde{\boldsymbol{F}}\right). \tag{5.6}$$

Bearing in mind the relationship established between the areas of the damaged and fictitious configurations for the uniaxial case in Equation (5.2), it is also possible to define the same relation for a general damage state based on the transformation between area vectors $\boldsymbol{\upsilon} dA$ and $\tilde{\boldsymbol{\upsilon}} d\tilde{A}$. Thus, one has that:

$$\tilde{J}\left(\tilde{\boldsymbol{F}}^{-1}\right)^{T} = \boldsymbol{I} - \boldsymbol{D} \tag{5.7}$$

where $\boldsymbol{I}$ is the second-order identity tensor and the second-order tensor $\boldsymbol{D}$ is, therefore, the damage variable that represents the general damage state of the material in the current damaged configuration. Some mathematical restrictions can be placed to this tensor [Murakami 1988]: positivity of tensor $\left(\boldsymbol{I} - \boldsymbol{D}\right)$, proved by the positivity of scalar product between both area vectors $\boldsymbol{\upsilon} dA$ and $\tilde{\boldsymbol{\upsilon}} d\tilde{A}$:

$$\left(\tilde{\boldsymbol{\upsilon}} d\tilde{A}\right) \cdot \left(\boldsymbol{\upsilon} dA\right) > 0 \tag{5.8}$$

and the assumption of a symmetric damage tensor $\boldsymbol{D}$, proved by the null contribution of the antisymmetric part of $\left(\boldsymbol{I} - \boldsymbol{D}\right)$ in the transformation of $\boldsymbol{\upsilon} dA$ into $\tilde{\boldsymbol{\upsilon}} d\tilde{A}$. This latter symmetry condition allows to state that the second order damage variable $\boldsymbol{D}$ possesses three orthogonal principal directions $\boldsymbol{n}_i$ and, therefore, the tensor can be expressed in the canonical form:

$$\boldsymbol{D} = D_i \boldsymbol{n}_i \otimes \boldsymbol{n}_i \tag{5.9}$$

where D_i corresponds to the three principal damage values. To get a physical insight of the damage tensor, one can construct two tetrahedra in the principal coordinate system $Ox_1x_2x_3$ which vertices are the points P, Q and R for the current damage configuration and points $\tilde{P}$, $\tilde{Q}$ and $\tilde{R}$ for the fictitious undamaged configuration, consisting in the area elements PQR and $\tilde{P}\tilde{Q}\tilde{R}$, respectively, as can be seen in Figure 5.3. Substituting Equation (5.9) into Equation (5.5) and considering Equation (5.7) gives:

$$\tilde{\boldsymbol{\upsilon}} d\tilde{A} = \sum_{i=1}^{3} \left(1 - D_i\right) dA_i \boldsymbol{n}_i = \boldsymbol{n}_1 d\tilde{A}_1 + \boldsymbol{n}_2 d\tilde{A}_2 + \boldsymbol{n}_3 d\tilde{A}_3 \tag{5.10}$$

with:

$$d\tilde{A}_i = \left(1 - D_i\right) dA_i \ (i = 1,2,3). \tag{5.11}$$

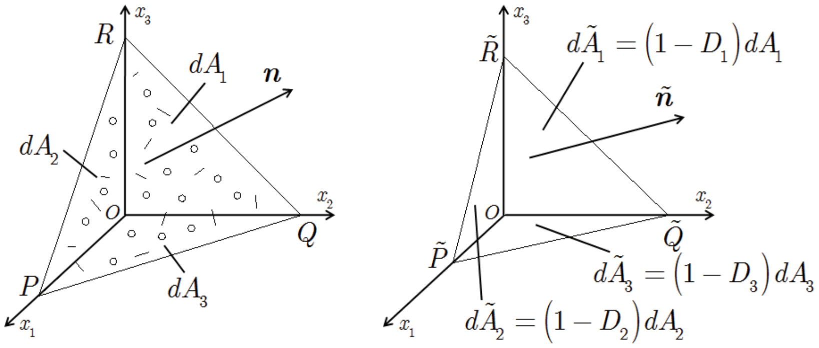

Figure 5.3 Interpretation of damage tensor; a) Current damaged configuration; b) Equivalent (fictitious) undamaged configuration.

According to Equation (5.10) and representation in Figure 5.3, the principal values of the damage tensor can be interpreted as the load-carrying net area reduction that occurs on the three principal planes of $\boldsymbol{D}$. This interpretation reinforces the assumption of the positivity of tensor $(\boldsymbol{I} - \boldsymbol{D})$ since the area reduction cannot be larger than the area itself. Furthermore, a direct conclusion of the canonical expression presented in Equation (5.9) is that this second order representation for the damage variable cannot describe damage states more complicated than orthotropic behaviour [Murakami 1988].

5.3 Coupled elasto-plastic anisotropic damage theory

The formulation of anisotropic damage theory still remains a largely open question and at the leading edge of material modelling science. Using the physically related second-order damage variable $\boldsymbol{D}$, a problem arises in the definition of the effective stress tensor, to ensure the coupling between elasticity and damage. The direct extrapolation of the isotropic case, where effective stress is obtained by affecting the Cauchy stress tensor by $1/(1-D)$, does not yield a symmetric effective stress tensor in the anisotropic case, as required by constitutive relations for metals. Thus, some symmetrisation procedure should be adopted. Possible symmetrisation methods were proposed by Murakami [1988] by adopting:

$$\tilde{\boldsymbol{\sigma}} = \frac{1}{2}\left[(\boldsymbol{I} - \boldsymbol{D})^{-1}\boldsymbol{\sigma} + \boldsymbol{\sigma}(\boldsymbol{I} - \boldsymbol{D})^{-1}\right], \tag{5.12}$$

or, the symmetrisation technique suggested by Cordebois and Sideroff [1982], by considering effective stress equals to:

$$\tilde{\boldsymbol{\sigma}} = (\boldsymbol{I} - \boldsymbol{D})^{-1/2}\boldsymbol{\sigma}(\boldsymbol{I} - \boldsymbol{D})^{-1/2}. \tag{5.13}$$

Despite these two methods, a particularly relevant symmetrisation procedure was proposed by Lemaitre *et al.* [2000a] that besides satisfying the restrictive principles of thermodynamics, also keeps effective stress independent of the strain behaviour. Lemaitre *et al.* [2000a] proposed an effective stress definition for the second order damage tensor representation, within the principle of strain equivalence, as an approximation of the exact effective stress deduced from the general representation of the damage by the fourth order tensor, as we will see bellow.

5.3.1 The constitutive model

The description of the anisotropic damage constitutive model is presented in the following.

5.3.1.1 State variables

The Helmholtz free energy, the thermodynamic potential from which the state laws are derived, can be defined as a function of the set $\left\{\boldsymbol{\varepsilon}^{e}, r, \boldsymbol{D}\right\}$ of state variables, in the form:

$$\psi = \psi\left(\boldsymbol{\varepsilon}^{e}, r, \boldsymbol{D}\right) \tag{5.14}$$

where $\boldsymbol{\varepsilon}^{e}$ is the elastic strain tensor, r is the internal variable associated isotropic hardening and $\boldsymbol{D}$ is the second-order damage variable. In this formulation, kinematic hardening is excluded. Table 5.1 depicts the state variables and the respective associated thermodynamical forces.

Table 5.1 State variables for anisotropic damage theory.

Mechanism	**Type**	**State Variables**		**Associated**
		Observables	**Internal**	**Variables**
Elasticity	Tensor	$\boldsymbol{\varepsilon}$		$\boldsymbol{\sigma}$
Plasticity	Tensor		$\boldsymbol{\varepsilon}^{p}$	$-\boldsymbol{\sigma}$
Isotropic Hardening	Scalar		r	R
Damage	Tensor		$\boldsymbol{D}$	$\boldsymbol{Y}$

5.3.1.2 Elastic-damage state potential

Using the hypothesis of decoupling between elastic-damage and plastic hardening, the specific free energy is given by the sum:

$$\psi = \psi\left(\boldsymbol{\varepsilon}^{e}, r, \boldsymbol{D}\right) = \psi^{ed}\left(\boldsymbol{\varepsilon}^{e}, \boldsymbol{D}\right) + \psi^{p}\left(r\right) \tag{5.15}$$

where ψ^{ed} and ψ^{p} are, respectively, the elastic-damage and plastic contributions for the free energy. The elastic-damage potential is postulated in the form:

$$\overline{\rho}\psi^{ed}\left(\boldsymbol{\varepsilon}^{e},\boldsymbol{D}\right)=\frac{1}{2}\boldsymbol{\varepsilon}^{e}:\tilde{\mathbf{E}}:\boldsymbol{\varepsilon}^{e} \tag{5.16}$$

where $\tilde{\mathbf{E}}$ is the effective isotropic elasticity operator. As in the isotropic case, damage modifies the elastic properties of the material and an effective stiffness tensor $\tilde{\mathbf{E}}$ can be introduced by the composition:

$$\tilde{\mathbf{E}}=\mathbf{L}^{-1}:\mathbf{E} \tag{5.17}$$

where $\mathbf{L}$ is the fourth-rank damage effect operator, function of the damage tensor $\boldsymbol{D}$, generalizing the isotropic case where $\tilde{\mathbf{E}}$ is defined as:

$$\tilde{\mathbf{E}}=\left(1-D\right)\mathbf{E}. \tag{5.18}$$

In the scalar damage definition, operator $\mathbf{L}$ is given by:

$$\mathbf{L}=\frac{1}{1-D}\mathbf{I}$$

being $\mathbf{I}$ the fourth order identity tensor. Under the hypothesis of strain equivalence, the same fourth-rank damage effect operator $\mathbf{L}$ is used to define the effective stress $\tilde{\boldsymbol{\sigma}}$ as:

$$\tilde{\boldsymbol{\sigma}}=\mathbf{L}:\boldsymbol{\sigma}=\mathbf{E}:\boldsymbol{\varepsilon}^{e}. \tag{5.19}$$

The question is how to define the fourth order tensor $\mathbf{L}$ from the second order tensor $\boldsymbol{D}$, keeping a compatibility between physics and thermodynamics, maintaining the independence of the effective stress tensor upon the elasticity parameters and supplying a symmetric effective stress tensor suitable for elasto-plastic constitutive relations for metals. To solve this question, Lemaitre *et al.* [2000a] introduced two damage quantities corresponding to two mechanisms: the variation of the deviatoric elastic constitutive behaviour and the variation of Poisson's ratio due to damage. By convenience and using a partial Legendre-Fenschel transformation on the elastic strain $\boldsymbol{\varepsilon}^{e}$, the dual equivalent potential from the Helmholtz free energy, the Gibbs specific free enthalpy ψ^{*}, is postulated as:

$$\overline{\rho}\psi^{ed*}\left(\sigma_{ij},D_{ij}\right)=\frac{1+\nu}{2E}H_{ij}s_{jk}H_{kl}s_{li}+\frac{3\left(1-2\nu\right)}{2E}\frac{\sigma_{H}^{2}}{1-d_{H}} \tag{5.20}$$

accounting for linear and initially isotropic elasticity and anisotropic damage, where E and ν are, respectively, the Young's modulus and Poisson ratio of the undamaged material, $\boldsymbol{s}$ the deviatoric stress tensor and σ_{H} the hydrostatic stress. The Gibbs elastic potential is, therefore, divided into a deviatoric part affected by a tensorial damage quantity $\boldsymbol{H}$ and a hydrostatic part affected by another (scalar) damage quantity d_H. $\boldsymbol{H}$ is the so-called second order damage effect tensor and can be written as:

$$\boldsymbol{H}^2 = \left(\boldsymbol{I} - \boldsymbol{D}\right)^{-1} \tag{5.21}$$

where $\boldsymbol{I}$ represents the second order identity tensor. The scalar value d_H that affects hydrostatic stress is a function of the hydrostatic damage and a good approximation for this function consists in taking [Lemaitre 2000a]:

$$d_H = \eta D_H \tag{5.22}$$

with D_H, the hydrostatic damage, given as:

$$D_H = \frac{1}{3}\operatorname{tr}\left(\boldsymbol{D}\right). \tag{5.23}$$

The material parameter η is required for a correct representation of experiments concerning the variation in the Poisson's ratio with damage and characterizes material sensitivity to hydrostatic stress. This parameter is considered independent upon damage evolution and, for metals, has a value ranging from 2 to 3 [Desmorat 2008].

Following thermodynamics of internal variables, the elasticity law for this particular potential is given by:

$$\boldsymbol{\varepsilon}^e = \overline{\rho}\,\frac{\partial \psi^{ed*}\left(\boldsymbol{\sigma}, \boldsymbol{D}\right)}{\partial \boldsymbol{\sigma}} = \mathbf{E}^{-1} : \tilde{\boldsymbol{\sigma}} \tag{5.24}$$

where $\tilde{\boldsymbol{\sigma}}$ is the effective stress tensor, related with the Cauchy stress tensor by the expression:

$$\tilde{\boldsymbol{\sigma}} = \operatorname{dev}\left(\boldsymbol{HsH}\right) + \frac{\sigma_H}{1 - \eta D_H}\boldsymbol{I} \tag{5.25}$$

where $\operatorname{dev}\left(\bullet\right)$ represents that only the deviatoric part of the tensor is taken. This relation introduces a symmetric effective stress tensor that will be used for the coupling with plasticity. The fourth order damage effect operator $\mathbf{L}$ that transforms Cauchy stress into effective stress, as expressed in Equation (5.19), can be written as a function of the second order damage effect tensor $\boldsymbol{H}$ as:

$$\begin{aligned}\mathbf{L} = \boldsymbol{H} \underline{\otimes} \boldsymbol{H} - \frac{1}{3}\left[\boldsymbol{H}^2 \otimes \boldsymbol{I} + \boldsymbol{I} \otimes \boldsymbol{H}^2\right] \\ + \frac{1}{9}\left(\operatorname{tr}\left(\boldsymbol{H}^2\right)\right)\boldsymbol{I} \otimes \boldsymbol{I} + \frac{1}{3\left(1 - \eta D_H\right)}\boldsymbol{I} \otimes \boldsymbol{I}\end{aligned}. \tag{5.26}$$

The special tensorial operation $\underline{\otimes}$ introduced in Equation (5.26) is calculated as:

$$\left(\boldsymbol{H} \underline{\otimes} \boldsymbol{H}\right)_{ijkl} = H_{ik} H_{lj}. \tag{5.27}$$

When the Helmholtz free energy is used for the state potential, the damage conjugate force $\boldsymbol{Y}$ is given as a function of the elastic strains. In this case, using the Gibbs equivalent potential, the conjugate thermodynamical force $\boldsymbol{Y}$ to the damage variable $\boldsymbol{D}$ is expressed as a function of the stress tensor as [Lemaitre 2000a]:

$$Y_{ij} = \bar{\rho}\frac{\partial \psi^{ed*}}{\partial D_{ij}} = \frac{1+\nu}{E} s_{kp} H_{pq} s_{ql} A^{-1}_{klmn} H^{2}_{mi} H^{2}_{jn} + \frac{\eta\left(1-2\nu\right)}{2E}\frac{\sigma_{H}^{2}}{\left(1-\eta D_{H}\right)^{2}}\delta_{ij} \tag{5.28}$$

where tensor $\mathbf{A}$ is defined as:

$$A_{ijkl} = \frac{1}{2}\left(H_{ik}\delta_{jl} + H_{jl}\delta_{ik} + H_{il}\delta_{jk} + H_{jk}\delta_{il}\right). \tag{5.29}$$

Analogously to the isotropic case, a scalar quantity can be defined, the effective elastic energy density $\bar{Y}$, related to the strain energy density release rate, as:

$$\bar{Y} = \frac{1}{2}\tilde{\sigma}_{ij}\varepsilon^{e}_{ij} \tag{5.30}$$

or, by using the effective stress definition, as:

$$\bar{Y} = \frac{1}{2}E^{-1}_{ijkl}\tilde{\sigma}_{ij}\tilde{\sigma}_{kl}. \tag{5.31}$$

A straightforward algebra leads to a definition of effective elastic energy density as an effective triaxiality function:

$$\bar{Y} = \frac{\tilde{\bar{\sigma}}^{2}}{2E}\left[\frac{2}{3}\left(1+\nu\right) + 3\left(1-2\nu\right)\left(\frac{\tilde{\sigma}_{H}}{\tilde{\bar{\sigma}}}\right)^{2}\right] \tag{5.32}$$

where $\tilde{\bar{\sigma}}$ and $\tilde{\sigma}_{H}$ are the effective von Mises equivalent stress and the effective hydrostatic stress, respectively. This scalar quantity will be used for the definition of the anisotropic damage evolution law, as we will see later, instead of tensor $\boldsymbol{Y}$.

As in the isotropic damage model, the isotropic hardening contribution is left as an arbitrary scalar function of the internal isotropic variable r. The thermodynamic force associated with isotropic hardening R is calculated as:

$$R = \bar{\rho}\frac{\partial \psi^{p}\left(r\right)}{\partial r} = \frac{\partial \psi^{I}\left(r\right)}{\partial r} = R\left(r\right). \tag{5.33}$$

5.3.1.3 Flow potential. Evolution of internal variables

According to the thermodynamics framework, the evolution law of internal variables derives from a dissipation potential Ψ, assumed to be additively decomposed into plastic Ψ^{p} and damage Ψ^{d} components, written as:

$$\Psi = \Psi^p + \Psi^d . \tag{5.34}$$

The plastic component of the dissipation potential is considered to be equal to the yield function Φ. Instead of using the isotropic von Mises yield function as in the original Lemaitre's formulation [Lemaitre 2000a], here we introduce again the anisotropic plastic behaviour by using the Hill48 yield function, writing the yield function in the following form:

$$\Phi\left(\boldsymbol{\sigma}, R, \boldsymbol{D}\right) = \sqrt{\tilde{\boldsymbol{\sigma}} : \mathbf{M} : \tilde{\boldsymbol{\sigma}}} - \left[\sigma_{Y0} + R\left(r\right)\right]. \tag{5.35}$$

According to the standard associative plasticity theory, the evolution law for the plastic flow of a damaged material is given by:

$$\dot{\boldsymbol{\varepsilon}}^p = \dot{\gamma} \frac{\partial \Psi}{\partial \boldsymbol{\sigma}} = \dot{\gamma} \boldsymbol{N} . \tag{5.36}$$

The flow vector $\boldsymbol{N}$ is obtained by the derivative chain rule as:

$$\boldsymbol{N} = \frac{\partial \Phi}{\partial \boldsymbol{\sigma}} = \frac{\partial \Phi}{\partial \tilde{\boldsymbol{\sigma}}} : \frac{\partial \tilde{\boldsymbol{\sigma}}}{\partial \boldsymbol{\sigma}} \tag{5.37}$$

where the partial derivatives are expressed as:

$$\begin{aligned} \frac{\partial \Phi}{\partial \tilde{\boldsymbol{\sigma}}} &= \frac{1}{\sqrt{\tilde{\boldsymbol{\sigma}} : \mathbf{M} : \tilde{\boldsymbol{\sigma}}}} \mathbf{M} : \tilde{\boldsymbol{\sigma}} \\ \frac{\partial \tilde{\boldsymbol{\sigma}}}{\partial \boldsymbol{\sigma}} &= \mathbf{L} \end{aligned} . \tag{5.38}$$

The evolution law of the internal variable associated with isotropic hardening, $\dot{r}$, is also expressed by the normality rule as:

$$\dot{r} = -\dot{\gamma} \frac{\partial \Psi}{\partial R} = \dot{\gamma} . \tag{5.39}$$

For the damage dissipation potential component, Ψ^d, Lemaitre *et al.* [2000a] proposed a "simple" extension of the isotropic case, providing a damage potential given by the expression:

$$\Psi^d = \left(\frac{\overline{Y}}{S}\right)^s \boldsymbol{Y} : \left|\frac{d\boldsymbol{\varepsilon}^p}{dr}\right|^{ii} \tag{5.40}$$

where operation $\left|\bullet\right|^{ii}$ performed to a tensor stands for the absolute value of the tensor components when represented in his principal components. Thus, considering the normality rule, the anisotropic damage evolution law is finally given by:

$$\dot{\boldsymbol{D}} = \dot{\gamma} \frac{\partial \Psi}{\partial \boldsymbol{Y}} = \left(\frac{\overline{Y}}{S}\right)^s \left|\dot{\boldsymbol{\varepsilon}}^p\right|^{ii} \tag{5.41}$$

with S and s being material and temperature dependent parameters. This evolution law generalizes the isotropic (scalar) damage law to account for anisotropic damage induced by plasticity. According to Equation (5.41), the principal directions of the damage rate coincide with those of the plastic strain rate.

To complete the formal description of the elasto-plastic anisotropic damage model, it is important to define the equivalent plastic strain rate $\dot{\bar{\varepsilon}}^p$, which has to be in accordance with the considered yield criterion. Using the equivalent plastic work approach defined in terms of effective stresses, one has the equivalence:

$$\tilde{\bar{\sigma}}\,\dot{\bar{\varepsilon}}^p = \tilde{\boldsymbol{\sigma}} : \dot{\boldsymbol{\varepsilon}}^p \tag{5.42}$$

which results in an equivalent plastic strain rate equal to:

$$\dot{\bar{\varepsilon}}^p = \dot{\gamma}\frac{\tilde{\boldsymbol{\sigma}} : \left(\mathbf{M} : \tilde{\boldsymbol{\sigma}} : \mathbf{L}\right)}{\tilde{\boldsymbol{\sigma}} : \mathbf{M} : \tilde{\boldsymbol{\sigma}}}\,. \tag{5.43}$$

The consistent plastic parameter $\dot{\gamma}$ that appears in the evolution laws is calculated by asserting the well-known plasticity loading / unloading conditions:

$$\dot{\gamma} \geq 0\,;\ \Phi \leq 0\,;\ \dot{\gamma}\Phi = 0\,. \tag{5.44}$$

The constitutive equations of anisotropic ductile damage model are conveniently grouped in Box 5.1.

One important aspect that any anisotropic damage theory should cover is the capability to degenerate into its isotropic damage definition. Considering the hydrostatic parameter η equal to 1 and considering that damage tensor $\boldsymbol{D}$ is equal to:

$$\boldsymbol{D} = D\boldsymbol{I}\,, \tag{5.45}$$

the corresponding second order damage effect tensor is represented by:

$$\boldsymbol{H} = \frac{1}{\sqrt{1-D}}\boldsymbol{I}\,. \tag{5.46}$$

and function d_H becomes equal to:

$$d_H = \eta D_H = \frac{1}{3}\left(D + D + D\right) = D\,. \tag{5.47}$$

Using the effective stress definition of Equation (5.25), one has:

$$\begin{aligned}\tilde{\boldsymbol{\sigma}} &= \operatorname{dev}\left(\boldsymbol{H}\boldsymbol{s}\boldsymbol{H}\right) + \frac{\sigma_H}{1-d_H}\boldsymbol{I}\\ &= \frac{\boldsymbol{s}}{1-D} + \frac{\sigma_H}{1-D}\boldsymbol{I}\\ &= \frac{\boldsymbol{\sigma}}{1-D}\end{aligned} \tag{5.48}$$

Box 5.1 Lemaitre's ductile anisotropic damage model with anisotropic flow.

i) Elasto-plastic split of the strain tensor

$$\boldsymbol{\varepsilon} = \boldsymbol{\varepsilon}^e + \boldsymbol{\varepsilon}^p$$

ii) Elastic law (coupled with damage)

$$\tilde{\boldsymbol{\sigma}} = \mathbf{E} : \boldsymbol{\varepsilon}^e$$

with $\tilde{\boldsymbol{\sigma}}$ given by:

$$\tilde{\boldsymbol{\sigma}} = \operatorname{dev}\left(\boldsymbol{HsH}\right) + \frac{\sigma_H}{1-\eta D_H}\boldsymbol{I}$$

$$\sigma_H = \frac{1}{3}\operatorname{tr}\left(\boldsymbol{\sigma}\right)$$

$$D_H = \frac{1}{3}\operatorname{tr}\left(\boldsymbol{D}\right)$$

iii) Yield function

$$\Phi = \sqrt{\tilde{\boldsymbol{\sigma}} : \mathbf{M} : \tilde{\boldsymbol{\sigma}}} - \left[\sigma_{Y0} + R\left(r\right)\right]$$

iv) Plastic flow and evolution equations

$$\dot{\boldsymbol{\varepsilon}}^p = \frac{\dot{\gamma}}{\sqrt{\tilde{\boldsymbol{\sigma}} : \mathbf{M} : \tilde{\boldsymbol{\sigma}}}} \mathbf{M} : \tilde{\boldsymbol{\sigma}} : \mathbf{L}$$

$$\dot{r} = \dot{\gamma}$$

$$\dot{\bar{\varepsilon}}^p = \dot{\gamma}\frac{\tilde{\boldsymbol{\sigma}} : \left(\mathbf{M} : \tilde{\boldsymbol{\sigma}} : \mathbf{L}\right)}{\tilde{\boldsymbol{\sigma}} : \mathbf{M} : \tilde{\boldsymbol{\sigma}}}$$

$$\dot{\boldsymbol{D}} = \left(\frac{\bar{Y}}{S}\right)^s \left|\dot{\boldsymbol{\varepsilon}}^p\right|^{ii}$$

with $\bar{Y}$ given by:

$$\bar{Y} = \frac{1}{2}\tilde{\boldsymbol{\sigma}} : \mathbf{E}^{-1} : \tilde{\boldsymbol{\sigma}}$$

v) Loading / unloading criterion

$$\dot{\gamma} \geq 0\,;\ \Phi \leq 0\,;\ \dot{\gamma}\Phi = 0$$

recovering, therefore, the isotropic definition for the effective stress. The same degeneration to the isotropic model can also be demonstrated for the anisotropic damage evolution law, presented in Equation (5.41). Naturally, due to different nature of the variables, different damage potentials are formulated as the starting point for the derivation of the damage evolution law. Nevertheless, an equivalence between effective elastic energy density $\bar{Y}$ (anisotropic case) and the strain energy release rate $-Y$ (isotropic case) is observed:

$$-Y = \bar{Y}\,. \tag{5.49}$$

Using the effective stress definition from the isotropic law in Equation (5.36), one has for the plastic strain rate tensor:

$$\dot{\boldsymbol{\varepsilon}}^p = \dot{\gamma}\boldsymbol{N} = \frac{\dot{\gamma}}{\left(1-D\right)\sqrt{\boldsymbol{\sigma} : \mathbf{M} : \boldsymbol{\sigma}}}\mathbf{M} : \boldsymbol{\sigma} \tag{5.50}$$

and for the equivalent plastic strain rate:

$$\dot{\bar{\varepsilon}}^p = \dot{\gamma}\frac{\tilde{\boldsymbol{\sigma}} : \left(\mathbf{M} : \tilde{\boldsymbol{\sigma}} : \mathbf{L}\right)}{\tilde{\boldsymbol{\sigma}} : \mathbf{M} : \tilde{\boldsymbol{\sigma}}} = \frac{\dot{\gamma}}{1-D} \tag{5.51}$$

recovering, therefore, their isotropic definitions. Assuming that damage evolution law is given by $\dot{\boldsymbol{D}} = \dot{D}\boldsymbol{I}$ and using Equations (5.49) and (5.51), the anisotropic damage evolution law reduces to the isotropic one:

$$\dot{\boldsymbol{D}} = \dot{D}\boldsymbol{I} = \frac{\dot{\gamma}}{1-D}\left(\frac{-Y}{S}\right)^s \boldsymbol{I}\,. \tag{5.52}$$

5.3.1.4 Damage threshold

As for the isotropic model, it is assumed that damage effects on physical properties only starts to be significant after a certain amount of plastic strain. This threshold value is evaluated in terms of equivalent plastic strain, ε_D^p, and its inclusion in the constitutive model is done by switching off damage evolution before plastic strain threshold is attained:

$$\dot{\boldsymbol{D}} = \begin{cases} \left(\dfrac{\bar{Y}}{S}\right)^s \left|\dot{\boldsymbol{\varepsilon}}^p\right|^{ii} & \text{if} \quad \bar{\varepsilon}^p > \varepsilon_D^p \\ \boldsymbol{0} & \text{if} \quad \bar{\varepsilon}^p < \varepsilon_D^p \end{cases}. \tag{5.53}$$

5.3.1.5 Critical damage criterion

In the isotropic model, the macro-crack initiation was attained when the damage reaches a critical value D_C, which is assumed to be independent of loading conditions and damage evolution, and, therefore, considered as a material parameter. For metals, this critical value ranges between 0.2 and 0.5 [Lemaitre 1996]. For anisotropic damage, a critical damage criterion is also used, but, in this case, calculation of critical damage is done by evaluating damage intensity acting in one plane, with normal n_j. The condition for macro-crack initiation is achieved when micro-crack density, defined as the norm of the damage vector $D_{ij}n_j$, reaches the critical damage. A simple way to determine the larger micro-crack density and the corresponding plane is to perform the evaluation in the principal directions of the damage tensor, i.e., evaluating the principal damage components. The critical damage criterion for the anisotropic damage model can then be written as [Lemaitre 2005]:

$$\max\left(D_I\right) > D_C \tag{5.54}$$

where $\max\left(D_I\right)$ represents the maximum value of principal damage components, D_1, D_2 or D_3. Additionally to this critical damage criterion, a purely mathematical stop criterion can also be defined in the function d_H. When d_H equal to 1, an undefined result emerges in the hydrostatic part of the effective stress, Equation (5.25). Therefore, using the definition of Equation (5.22) for function d_H, one should also define the following stop criterion for damage evolution:

$$\eta D_H \approx 1. \tag{5.55}$$

5.3.2 Integration algorithm

Let us consider what happens in a typical integration point of the finite element mesh in a pseudo time interval $\left[t_n, t_{n+1}\right]$. Given an incremental strain $\Delta\boldsymbol{\varepsilon}$, the algorithm integrates constitutive relations in a typical Gauss point, starting from the knowledge of the last equilibrium state, at time $t = t_n$, provided by variables $\boldsymbol{\sigma}_n$, $\boldsymbol{\varepsilon}^e_n$, $\boldsymbol{\varepsilon}^p_n$, $\overline{\varepsilon}^p_n$ and $\boldsymbol{D}_n$, and achieving a new equilibrium state in time $t = t_{n+1}$ and corresponding updated variables $\boldsymbol{\sigma}_{n+1}$, $\boldsymbol{\varepsilon}^e_{n+1}$, $\boldsymbol{\varepsilon}^p_{n+1}$, $\overline{\varepsilon}^p_{n+1}$ and $\boldsymbol{D}_{n+1}$. The integration algorithm based on Hill48 criterion coupled with the tensorial definition for damage is also a variation of the classical scheme elastic predictor / plastic corrector.

5.3.2.1 Elastic Predictor

The algorithm starts with the computation of the elastic trial stress. In this case, where damage is defined as a second order tensor, $\boldsymbol{D}$, and, for the sake of simplicity, inside the state update subroutine, calculations are made using the effective stress concept, $\tilde{\boldsymbol{\sigma}}$, and the computation of the corresponding Cauchy stress tensor $\boldsymbol{\sigma}$ is only performed at the end of algorithm, in order be returned to the finite element program. Since we adopted an explicit time integration scheme, the elastic predictor stage requires the following straightforward modification in the computation of the elastic trial stress tensor, $\tilde{\boldsymbol{\sigma}}^{trial}$:

$$\tilde{\boldsymbol{\sigma}}^{trial} = \mathbf{L}_n : \boldsymbol{\sigma}_n + \mathbf{E} : \Delta\boldsymbol{\varepsilon} \tag{5.56}$$

where $\mathbf{L}_n$ is the fourth order damage effect tensor, function of the converged damage tensor $\boldsymbol{D}_n$ at time $t = t_n$, defined as:

$$\begin{aligned}\mathsf{\mathbf{L}}_n = \boldsymbol{H}_n \underline{\otimes} \boldsymbol{H}_n - \frac{1}{3}\left[\boldsymbol{H}_n^2 \otimes \boldsymbol{I} + \boldsymbol{I} \otimes \boldsymbol{H}_n^2\right] \\ + \frac{1}{9}\left(\mathrm{tr}\left(\boldsymbol{H}_n^2\right)\right)\boldsymbol{I} \otimes \boldsymbol{I} + \frac{1}{3\left(1-\eta D_H^n\right)}\boldsymbol{I} \otimes \boldsymbol{I}\end{aligned} \tag{5.57}$$

with $\boldsymbol{H}_n$, the second order damage effect tensor, computed as:

$$\boldsymbol{H}_n^2 = \left(\boldsymbol{I} - \boldsymbol{D}_n\right)^{-1} \tag{5.58}$$

and D_H^n, the hydrostatic damage, computed as:

$$D_H^n = \frac{1}{3}\mathrm{tr}\left(\boldsymbol{D}_n\right). \tag{5.59}$$

Defined the elastic trial state $\tilde{\boldsymbol{\sigma}}^{trial}$, the yield function is evaluated in a quadratic way (as done for the isotropic model, see section 4.5.2):

$$\Phi^{trial} = \tilde{\boldsymbol{\sigma}}^{trial} : \mathsf{\mathbf{M}} : \tilde{\boldsymbol{\sigma}}^{trial} - \sigma_Y^2\left(\bar{\varepsilon}_n^p\right). \tag{5.60}$$

If the imposed strain increment in time interval $\left[t_n, t_{n+1}\right]$ corresponds to an elastic state, i.e., inequality $\Phi^{trial} \leq 0$ verifies, no evolution of internal variables occurs and updated variables will be equal to the computed values converged in the previous time increment. The updated stress tensor $\boldsymbol{\sigma}_{n+1}$ is calculated from the effective elastic trial stress tensor $\tilde{\boldsymbol{\sigma}}^{trial}$, using the damage tensor $\boldsymbol{D}_n$ to define the fourth order damage effect tensor $\mathsf{\mathbf{L}}_n$. Hence, updated variables $\boldsymbol{\sigma}_{n+1}$, $\boldsymbol{\varepsilon}_{n+1}^e$, $\boldsymbol{\varepsilon}_{n+1}^p$, $\bar{\varepsilon}_{n+1}^p$ and $\boldsymbol{D}_{n+1}$ are computed as:

$$\begin{aligned}\boldsymbol{\sigma}_{n+1} &= \boldsymbol{\sigma}^{\mathrm{tr}ial} = \mathsf{\mathbf{L}}_n^{-1} : \tilde{\boldsymbol{\sigma}}^{\mathrm{tr}ial} \\ \boldsymbol{\varepsilon}_{n+1}^e &= \boldsymbol{\varepsilon}_n^e + \Delta\boldsymbol{\varepsilon} \\ \boldsymbol{\varepsilon}_{n+1}^p &= \boldsymbol{\varepsilon}_n^p \qquad . \\ \bar{\varepsilon}_{n+1}^p &= \bar{\varepsilon}_n^p \\ \boldsymbol{D}_{n+1} &= \boldsymbol{D}_n\end{aligned} \tag{5.61}$$

If yielding occurs with the imposed strain increment $\Delta\boldsymbol{\varepsilon}$, i.e., $\Phi^{trial} > 0$ verifies, an iterative procedure is required until condition $\Phi_{n+1} = 0$ is reached.

5.3.2.2 Plastic Corrector / Return Mapping

The return mapping procedure in the case of tensorial damage definition is by far more complex than in the case of isotropic damage and requires the solution of a non-linear system of three equations, two of which are tensorial equations. The objective is to determine unknowns $\tilde{\boldsymbol{\sigma}}_{n+1}$, $\boldsymbol{D}_{n+1}$ and $\Delta\gamma$, in order to satisfy the consistency condition $\Phi_{n+1} = 0$ over the actual time step. The calculation of the new stress and damage states represent, in the most general case, the solution of a non-linear system of equations for a total of 13 unknowns. So, additional equations must be solved along with the consistency condition in order to determine all the variables that fully characterize the new incremental plastic state. Therefore, considering the independent variables $\tilde{\boldsymbol{\sigma}}_{n+1}$, $\boldsymbol{D}_{n+1}$ and $\Delta\gamma$, the system of equations to be linearized and solved iteratively by the Newton-Raphson scheme can be written in the form:

$$\begin{cases} \tilde{\boldsymbol{\sigma}}_{n+1} : \mathbf{M} : \tilde{\boldsymbol{\sigma}}_{n+1} - \sigma_Y^2\left(\bar{\varepsilon}^p_{n+1}\right) = 0 \\ \mathbf{E}^{-1} : \left(\tilde{\boldsymbol{\sigma}}_{n+1} - \tilde{\boldsymbol{\sigma}}^{\mathrm{trial}}\right) + \Delta\gamma \boldsymbol{N}_{n+1} = \boldsymbol{0} \\ \boldsymbol{D}_{n+1} - \boldsymbol{D}_n - \left|\Delta\boldsymbol{\varepsilon}^p\right|^{ii} \left(\dfrac{\overline{Y}_{n+1}}{S}\right)^s H\left(\bar{\varepsilon}^p_{n+1} - \varepsilon^p_D\right) = \boldsymbol{0} \end{cases} \tag{5.62}$$

where the first equation represents the yield function, the second one the additive decomposition of strain increment $\Delta\boldsymbol{\varepsilon}$ and the third equation represents the anisotropic damage evolution law. In order to apply the iterative Newton-Raphson method, it is imperative to define all the variables as a function of the independent variables, $\tilde{\boldsymbol{\sigma}}_{n+1}$, $\boldsymbol{D}_{n+1}$ and $\Delta\gamma$. Using the quadratic formulation for the yield criterion, new relations for the plastic strain increment tensor $\Delta\boldsymbol{\varepsilon}^p$ and for the equivalent plastic strain increment $\Delta\bar{\varepsilon}^p$ should be explicitly defined. The definition of these two quantities is, again, based on the associative plastic flow rule and on the incremental plastic work definition, respectively. In this way, using the associative flow rule, plastic strain increment tensor $\Delta\boldsymbol{\varepsilon}^p$ is given by:

$$\Delta\boldsymbol{\varepsilon}^p = \Delta\gamma \boldsymbol{N}_{n+1} \tag{5.63}$$

where $\boldsymbol{N}_{n+1}$ is now equal to:

$$\boldsymbol{N}_{n+1} = \operatorname{dev}\left(\boldsymbol{H}_{n+1}\tilde{\boldsymbol{N}}_{n+1}\boldsymbol{H}_{n+1}\right) \tag{5.64}$$

where operation $\operatorname{dev}(\bullet)$ represents that only the deviatoric part is taken into account and $\tilde{\boldsymbol{N}}_{n+1}$ stands for the effective flow vector given as:

$$\tilde{\boldsymbol{N}}_{n+1} = \frac{\partial\Phi}{\partial\tilde{\boldsymbol{\sigma}}_{n+1}} = 2\mathbf{M} : \tilde{\boldsymbol{\sigma}}_{n+1}. \tag{5.65}$$

Using the above definitions, plastic strain increment tensor can be rewritten as:

$$\begin{aligned} &\Delta\boldsymbol{\varepsilon}^p = \Delta\gamma \operatorname{dev}\left(\boldsymbol{H}_{n+1}\tilde{\boldsymbol{N}}_{n+1}\boldsymbol{H}_{n+1}\right) \\ &\Leftrightarrow \Delta\boldsymbol{\varepsilon}^p = 2\Delta\gamma \operatorname{dev}\left[\boldsymbol{H}_{n+1}\left(\mathbf{M} : \boldsymbol{\sigma}_{n+1}\right)\boldsymbol{H}_{n+1}\right] \end{aligned} \tag{5.66}$$

or, equivalently, as:

$$\Delta\boldsymbol{\varepsilon}^p = 2\Delta\gamma \,\mathbf{Q}_{n+1} : \tilde{\boldsymbol{N}}_{n+1} \tag{5.67}$$

where $\mathbf{Q}_{n+1}$ represents a fourth order tensor operator, function of damage tensor $\boldsymbol{D}_{n+1}$, given by the expression:

$$\mathbf{Q}_{n+1} = \boldsymbol{H}_{n+1} \underline{\otimes} \boldsymbol{H}_{n+1} - \frac{1}{3} \boldsymbol{I} \otimes \boldsymbol{H}^2_{n+1}. \tag{5.68}$$

The definition of the equivalent plastic strain increment is obtained from the incremental plastic work definition as:

$$\begin{aligned} \Delta\bar{\varepsilon}^p &= \frac{\tilde{\boldsymbol{\sigma}}_{n+1} : \Delta\boldsymbol{\varepsilon}^p}{\bar{\tilde{\sigma}}_{n+1}} \\ \Leftrightarrow \Delta\bar{\varepsilon}^p &= \frac{2\Delta\gamma}{\sqrt{\tilde{\boldsymbol{\sigma}}_{n+1} : \mathbf{M} : \tilde{\boldsymbol{\sigma}}_{n+1}}} \tilde{\boldsymbol{\sigma}}_{n+1} : \left[\mathbf{Q}_{n+1} : \left(\mathbf{M} : \tilde{\boldsymbol{\sigma}}_{n+1} \right) \right] \end{aligned}. \tag{5.69}$$

The state update procedure for the anisotropic damage model is presented in Box 5.2. As already mentioned, the solution of the system is undertaken by using the Newton-Raphson iterative scheme, conveniently summarized in Box 5.3. Partial derivatives of each equation with respect to variables $\tilde{\boldsymbol{\sigma}}_{n+1}$, $\boldsymbol{D}_{n+1}$ e $\Delta\gamma$ that define the Jacobian matrix to be used in the Newton-Rapshon iterative procedure are given by:

$$\begin{aligned} \frac{\partial r_\gamma}{\partial \Delta\gamma} &= -4\sigma_Y H' \frac{\tilde{\boldsymbol{\sigma}}_{n+1} : \left(\mathbf{Q}_{n+1} : \mathbf{M} : \tilde{\boldsymbol{\sigma}}_{n+1} \right)}{\sqrt{\tilde{\boldsymbol{\sigma}}_{n+1} : \mathbf{M} : \tilde{\boldsymbol{\sigma}}_{n+1}}} \\ \frac{\partial \boldsymbol{r}_\sigma}{\partial \Delta\gamma} &= \boldsymbol{N}_{n+1} \\ \frac{\partial \boldsymbol{r}_D}{\partial \Delta\gamma} &= -\left(\frac{\bar{Y}_{n+1}}{S} \right)^s \left| \boldsymbol{N}_{n+1} \right|^{ii} \end{aligned} \tag{5.70}$$

$$\begin{aligned} \frac{\partial r_\gamma}{\partial \tilde{\boldsymbol{\sigma}}_{n+1}} &= \left[2\left(1 + \frac{\sigma_Y H' \Delta\bar{\varepsilon}^p}{\tilde{\boldsymbol{\sigma}}_{n+1} : \mathbf{M} : \tilde{\boldsymbol{\sigma}}_{n+1}} \right) \mathbf{I} - \frac{8\sigma_Y H' \Delta\gamma}{\sqrt{\tilde{\boldsymbol{\sigma}}_{n+1} : \mathbf{M} : \tilde{\boldsymbol{\sigma}}_{n+1}}} \mathbf{Q}_{n+1} \right] : \mathbf{M} : \tilde{\boldsymbol{\sigma}}_{n+1} \\ \frac{\partial \boldsymbol{r}_\sigma}{\partial \tilde{\boldsymbol{\sigma}}_{n+1}} &= \mathbf{E}^{-1} + 2\Delta\gamma \mathbf{Q}_{n+1} : \mathbf{M} \\ \frac{\partial \boldsymbol{r}_D}{\partial \tilde{\boldsymbol{\sigma}}_{n+1}} &= -\Delta\gamma \left(\frac{\bar{Y}_{n+1}}{S} \right)^s \frac{\partial \left| \boldsymbol{N}_{n+1} \right|^{ii}}{\partial \tilde{\boldsymbol{\sigma}}_{n+1}} - \frac{s\Delta\gamma}{S} \left(\frac{\bar{Y}_{n+1}}{S} \right)^{s-1} \left| \boldsymbol{N}_{n+1} \right|^{ii} \otimes \left(\mathbf{E}^{-1} : \tilde{\boldsymbol{\sigma}}_{n+1} \right) \end{aligned} \tag{5.71}$$

$$\begin{aligned} \frac{\partial r_\gamma}{\partial \boldsymbol{D}_{n+1}} &= 2\sigma_Y H' \frac{\Delta\gamma}{\sqrt{\tilde{\boldsymbol{\sigma}}_{n+1} : \mathbf{M} : \tilde{\boldsymbol{\sigma}}_{n+1}}} \tilde{\boldsymbol{\sigma}}_{n+1} : \frac{\partial \boldsymbol{N}_{n+1}}{\partial \boldsymbol{D}_{n+1}} \\ \frac{\partial \boldsymbol{r}_\sigma}{\partial \boldsymbol{D}_{n+1}} &= \Delta\gamma \frac{\partial \boldsymbol{N}_{n+1}}{\partial \boldsymbol{D}_{n+1}} \\ \frac{\partial \boldsymbol{r}_D}{\partial \boldsymbol{D}_{n+1}} &= \mathbf{I} - \Delta\gamma \left(\frac{\bar{Y}_{n+1}}{S} \right)^s \frac{\partial \left| \boldsymbol{N}_{n+1} \right|^{ii}}{\partial \boldsymbol{D}_{n+1}} \end{aligned}. \tag{5.72}$$

The derivative of the flow vector $\boldsymbol{N}$ with respect to damage tensor $\boldsymbol{D}$ is obtained from the definition of the flow vector (for notation convenience the scripts are omitted):

$$\boldsymbol{N} = \operatorname{dev}\left(\boldsymbol{H}\tilde{\boldsymbol{N}}\boldsymbol{H}\right) = \boldsymbol{H}\tilde{\boldsymbol{N}}\boldsymbol{H} - \frac{1}{3}\boldsymbol{I} : \left(\boldsymbol{H}\tilde{\boldsymbol{N}}\boldsymbol{H}\right). \tag{5.73}$$

Applying the chain derivative rule, one obtains:

$$\frac{\partial \boldsymbol{N}}{\partial \boldsymbol{D}} = \frac{\partial\left(\boldsymbol{H}\tilde{\boldsymbol{N}}\boldsymbol{H}\right)}{\partial \boldsymbol{H}} : \frac{\partial \boldsymbol{H}}{\partial \boldsymbol{D}} - \frac{1}{3}\boldsymbol{I} \otimes \tilde{\boldsymbol{N}} : \left(\boldsymbol{H}^2 \underline{\otimes} \boldsymbol{H}^2\right) \tag{5.74}$$

where the displayed partial derivatives are respectively given by:

$$\frac{\partial\left(\boldsymbol{H}\tilde{\boldsymbol{N}}\boldsymbol{H}\right)}{\partial \boldsymbol{H}} = \boldsymbol{I} \underline{\otimes} \left(\boldsymbol{H}\tilde{\boldsymbol{N}}\right) + \left(\boldsymbol{H}\tilde{\boldsymbol{N}}\right) \underline{\otimes} \boldsymbol{I} \tag{5.75}$$

and:

$$\frac{\partial \boldsymbol{H}}{\partial \boldsymbol{D}} = \left(\boldsymbol{H} \underline{\otimes} \boldsymbol{I} + \boldsymbol{I} \underline{\otimes} \boldsymbol{H}\right)^{-1} : \left(\boldsymbol{H}^2 \underline{\otimes} \boldsymbol{H}^2\right). \tag{5.76}$$

In order to avoid the calculation of “time-expensive” derivatives, $\partial \boldsymbol{r}_D \big/ \partial \tilde{\boldsymbol{\sigma}}_{n+1}$ and $\partial \boldsymbol{r}_D \big/ \partial \boldsymbol{D}_{n+1}$ are simplified by eliminating the terms where derivative of the tensorial operation $\left|\bullet\right|^{ii}$ is required and, therefore, derivatives assume an approximated form given by:

$$\begin{aligned} &\frac{\partial \boldsymbol{r}_D}{\partial \tilde{\boldsymbol{\sigma}}_{n+1}} \approx -\frac{s\Delta\gamma}{S}\left(\frac{\bar{Y}_{n+1}}{S}\right)^{s-1} \left|\boldsymbol{N}_{n+1}\right|^{ii} \otimes \left(\boldsymbol{\mathsf{E}}^{-1} : \tilde{\boldsymbol{\sigma}}_{n+1}\right) \\ &\frac{\partial \boldsymbol{r}_D}{\partial \boldsymbol{D}_{n+1}} \approx \boldsymbol{\mathsf{I}} \end{aligned}. \tag{5.77}$$

This approximation leads to an incomplete linearization of the Newton-Raphson method and, consequently, the quadratic convergence rate, typical of this iterative method, may not be achieved. Nevertheless, using the approximations of Equation (5.77), the quadratic convergence rate is traded by a less time consuming derivative calculation. Finally, as local integration of the fully coupled constitutive equations will be undertaken in a dynamic explicit solution procedure, the computation of the consistent tangent operator with the described above integration scheme for the assembly of the tangent stiffness matrix is not required and it is not addressed in this work.

Box 5.2 State update procedure for fully coupled Lemaitre's ductile anisotropic damage model.

i) Elastic predictor

Given an elastic trial strain $\boldsymbol{\varepsilon}^{e\ trial} = \boldsymbol{\varepsilon}_n^e + \Delta\boldsymbol{\varepsilon}$, evaluate elastic trial stress:

$$\tilde{\boldsymbol{\sigma}}^{trial} = \mathbf{L}_n : \boldsymbol{\sigma}_n + \mathbf{E} : \Delta\boldsymbol{\varepsilon}$$

with:

$$\mathbf{L}_n = \boldsymbol{H}_n \underline{\otimes} \boldsymbol{H}_n - \frac{1}{3}\left[\boldsymbol{H}_n^2 \otimes \boldsymbol{I} + \boldsymbol{I} \otimes \boldsymbol{H}_n^2\right] + \frac{1}{9}\left(\operatorname{tr}\left(\boldsymbol{H}_n^2\right)\right)\boldsymbol{I} \otimes \boldsymbol{I} + \frac{1}{3\left(1 - \eta D_n^H\right)}\boldsymbol{I} \otimes \boldsymbol{I}$$

$$\boldsymbol{H}_n^2 = \left(\boldsymbol{I} - \boldsymbol{D}_n\right)^{-1}; \qquad D_n^H = \frac{1}{3}\operatorname{tr}\left(\boldsymbol{D}_n\right)$$

Check plastic consistency:

IF $\Phi^{trial} = \tilde{\boldsymbol{\sigma}}^{trial} : \mathbf{M} : \tilde{\boldsymbol{\sigma}}^{trial} - \sigma_Y^2\left(\bar{\varepsilon}_n^p\right) \leq 0$ THEN

Set $\boldsymbol{\sigma}_{n+1} = \boldsymbol{\sigma}^{trial} = \mathbf{L}_n^{-1} : \tilde{\sigma}^{trial}$ and $\left(.\right)_{n+1} = \left(.\right)^{trial}$ and RETURN

ELSE go to (ii)

ii) Plastic corrector (solve the system for the unknowns $\Delta\gamma$, $\tilde{\boldsymbol{\sigma}}_{n+1}$ and $\boldsymbol{D}_{n+1}$)

$$\left\{\begin{matrix} \tilde{\boldsymbol{\sigma}}_{n+1} : \mathbf{M} : \tilde{\boldsymbol{\sigma}}_{n+1} - \sigma_Y^2\left(\bar{\varepsilon}_{n+1}^p\right) \\ \mathbf{E}^{-1} : \left(\tilde{\boldsymbol{\sigma}}_{n+1} - \tilde{\boldsymbol{\sigma}}^{trial}\right) + \Delta\gamma\boldsymbol{N}_{n+1} \\ \boldsymbol{D}_{n+1} - \boldsymbol{D}_n - \Delta\gamma\left|\boldsymbol{N}_{n+1}\right|^{ii}\left(\bar{Y}_{n+1}/S\right)^s H\left(\bar{\varepsilon}_{n+1}^p - \varepsilon_D^p\right) \end{matrix}\right\} = \left\{\begin{matrix} 0 \\ \boldsymbol{0} \\ \boldsymbol{0} \end{matrix}\right\}$$

where:

$$\boldsymbol{H}_{n+1}^2 = \left(\boldsymbol{I} - \boldsymbol{D}_{n+1}\right)^{-1}; \qquad \boldsymbol{N}_{n+1} = 2\mathbf{Q}_{n+1} : \mathbf{M} : \tilde{\boldsymbol{\sigma}}_{n+1}$$

$$\Delta\bar{\varepsilon}^p = \Delta\gamma\frac{\tilde{\boldsymbol{\sigma}}_{n+1} : \boldsymbol{N}_{n+1}}{\sqrt{\tilde{\boldsymbol{\sigma}}_{n+1} : \mathbf{M} : \tilde{\boldsymbol{\sigma}}_{n+1}}}; \qquad \bar{Y}_{n+1} = \frac{1}{2}\tilde{\boldsymbol{\sigma}}_{n+1} : \mathbf{E}^{-1} : \tilde{\boldsymbol{\sigma}}_{n+1}$$

iii) Update $\bar{\varepsilon}_{n+1}^p$:

$$\bar{\varepsilon}_{n+1}^p = \bar{\varepsilon}_n^p + \Delta\gamma\frac{\tilde{\boldsymbol{\sigma}}_{n+1} : \boldsymbol{N}_{n+1}}{\sqrt{\tilde{\boldsymbol{\sigma}}_{n+1} : \mathbf{M} : \tilde{\boldsymbol{\sigma}}_{n+1}}}$$

iv) RETURN

Box 5.3 Newton-Raphson algorithm for return mapping system of equations for integration of fully coupled Lemaitre's ductile anisotropic damage model.

i) Initialize Newton-Raphson method. Set initial guess $\Delta\gamma^{(0)} = 0$, $\tilde{\boldsymbol{\sigma}}_{n+1}^{(0)} = \tilde{\boldsymbol{\sigma}}^{trial}$ and $\boldsymbol{D}_{n+1}^{(0)} = \boldsymbol{D}_n$ and compute residuals r_γ, $\boldsymbol{r}_\sigma$ and $\boldsymbol{r}_D$

$$\begin{cases} r_\gamma = \tilde{\boldsymbol{\sigma}}_{n+1} : \mathbf{M} : \tilde{\boldsymbol{\sigma}}_{n+1} - \sigma_Y^2\left(\bar{\varepsilon}_{n+1}^p\right) \\ \boldsymbol{r}_\sigma = \mathbf{E}^{-1} : \left(\tilde{\boldsymbol{\sigma}}_{n+1} - \tilde{\boldsymbol{\sigma}}^{\mathrm{tr}ial}\right) + \Delta\gamma \boldsymbol{N}_{n+1} \\ \boldsymbol{r}_D = \boldsymbol{D}_{n+1} - \boldsymbol{D}_n - \left|\Delta\boldsymbol{\varepsilon}^p\right|^{ii} \left(\dfrac{\bar{Y}_{n+1}}{S}\right)^s H\left(\bar{\varepsilon}_{n+1}^p - \varepsilon_D^p\right) \end{cases}$$

ii) Perform Newton-Raphson iteration

$$\begin{bmatrix} \dfrac{\partial r_\gamma}{\partial \Delta\gamma} & \dfrac{\partial r_\gamma}{\partial \tilde{\boldsymbol{\sigma}}_{n+1}} & \dfrac{\partial r_\gamma}{\partial \boldsymbol{D}_{n+1}} \\ \dfrac{\partial \boldsymbol{r}_\sigma}{\partial \Delta\gamma} & \dfrac{\partial \boldsymbol{r}_\sigma}{\partial \tilde{\boldsymbol{\sigma}}_{n+1}} & \dfrac{\partial \boldsymbol{r}_\sigma}{\partial \boldsymbol{D}_{n+1}} \\ \dfrac{\partial \boldsymbol{r}_D}{\partial \Delta\gamma} & \dfrac{\partial \boldsymbol{r}_D}{\partial \tilde{\boldsymbol{\sigma}}_{n+1}} & \dfrac{\partial \boldsymbol{r}_D}{\partial \boldsymbol{D}_{n+1}} \end{bmatrix}^{(k-1)} \begin{bmatrix} \delta\Delta\gamma \\ \delta\tilde{\boldsymbol{\sigma}} \\ \delta\boldsymbol{D} \end{bmatrix}^{(k)} = -\begin{bmatrix} r_\gamma\left(\Delta\gamma, \tilde{\boldsymbol{\sigma}}_{n+1}, \boldsymbol{D}_{n+1}\right) \\ \boldsymbol{r}_\sigma\left(\Delta\gamma, \tilde{\boldsymbol{\sigma}}_{n+1}, \boldsymbol{D}_{n+1}\right) \\ \boldsymbol{r}_D\left(\Delta\gamma, \tilde{\boldsymbol{\sigma}}_{n+1}, \boldsymbol{D}_{n+1}\right) \end{bmatrix}^{(k-1)}$$

New guess for $\Delta\gamma$, $\tilde{\boldsymbol{\sigma}}_{n+1}$ and $\boldsymbol{D}_{n+1}$:

$$\Delta\gamma = \Delta\gamma^{(k-1)} + \delta\Delta\gamma^{(k)};\ \tilde{\boldsymbol{\sigma}}_{n+1}^{(k)} = \tilde{\boldsymbol{\sigma}}_{n+1}^{(k-1)} + \delta\tilde{\boldsymbol{\sigma}}^{(k)};\ \boldsymbol{D}_{n+1}^{(k)} = \boldsymbol{D}_{n+1}^{(k-1)} + \delta\boldsymbol{D}^{(k)}$$

Update plastic strain, equivalent plastic strain and effective elastic density:

$$\Delta\boldsymbol{\varepsilon}^p = \Delta\gamma \boldsymbol{N}_{n+1}$$

$$\bar{\varepsilon}_{n+1}^p = \bar{\varepsilon}_n^p + \Delta\gamma \frac{\tilde{\boldsymbol{\sigma}}_{n+1} : \boldsymbol{N}_{n+1}}{\sqrt{\tilde{\boldsymbol{\sigma}}_{n+1} : \mathbf{M} : \tilde{\boldsymbol{\sigma}}_{n+1}}}$$

$$\boldsymbol{N}_{n+1} = 2\mathbf{Q}_{n+1} : \mathbf{M} : \tilde{\boldsymbol{\sigma}}_{n+1}$$

$$\bar{Y}_{n+1} = \frac{1}{2}\tilde{\boldsymbol{\sigma}}_{n+1} : \mathbf{E} : \tilde{\boldsymbol{\sigma}}_{n+1}$$

iii) Compute new residuals (r_γ, $\boldsymbol{r}_\sigma$, $\boldsymbol{r}_D$) and check for convergence

IF $\left\|r_\gamma\right\| \leq tolerance$ AND $\left\|\boldsymbol{r}_\sigma\right\| \leq tolerance$ AND $\left\|\boldsymbol{r}_D\right\| \leq tolerance$ THEN RETURN

iv) Go to (ii)

5.4 Sensitivity analysis of anisotropic damage model

In this section, a sensitivity analysis of the implemented anisotropic damage model is performed taking into account the variation of damage parameters, stress triaxiality ratio, hardening behaviour and anisotropic coefficients in order to quantify its effects on mechanical properties degradation. A fictitious material has been considered and corresponding material properties are presented in Table 5.2.

Table 5.2 Initial material properties.

Property	**Symbol**	**Value**
Young modulus [GPa]	E	70
Poisson coefficient	ν	0.3
Initial yield stress [MPa]	σ_{Y0}	137
Yield stress [MPa]	σ_Y	$570\left(\bar{\varepsilon}^p\right)^{0.35}$
r-values	r_0, r_{45}, r_{90}	1.0, 1.0, 1.0
Damage denominator [MPa]	S	1.0
Damage exponent	s	1.0
Damage threshold	ε_D^p	0.0
Damage hydrostatic parameter	η	3.0

5.4.1 Influence of damage evolution law parameters

For the sake of completeness, the anisotropic damage evolution law is repeated in this section. The law is formulated as:

$$\dot{\boldsymbol{D}} = \left(\frac{\bar{Y}}{S}\right)^s \left|\dot{\boldsymbol{\varepsilon}}^p\right|^{ii} \tag{5.78}$$

where S and s are characteristic material parameters and the effective elastic energy density $\bar{Y}$ is given by:

$$\bar{Y} = \frac{\tilde{\bar{\sigma}}^2}{2E}\left[\frac{2}{3}\left(1+\nu\right) + 3\left(1-2\nu\right)\left(\frac{\tilde{\sigma}_H}{\tilde{\bar{\sigma}}}\right)^2\right]. \tag{5.79}$$

The tensor $\left|\dot{\boldsymbol{\varepsilon}}^p\right|^{ii}$, which represents the positive values of the plastic strain rate tensor, along with the effective elastic energy density $\bar{Y}$, imply that damage is governed by the elastic energy and the plastic strain rate, as shown by many experimental observations [Lemaitre 1998]. There are, at least, two parameters that have a direct influence in the evolution law, the denominator S and exponent s damage parameters.

Concerning damage denominator parameter S influence, it can be seen in Figure 5.4b that, as higher values are considered for this parameter, damage rate will be considerably lower, traduced into a delay of the degradation of mechanical properties of the material, Figure 5.4a, and, hence, in a postponement of failure criterion achievement, Figure 5.4b. Although not shown, the behaviour of all components of the damage tensor follow the same trend presented for the hydrostatic damage in Figure 5.4b.

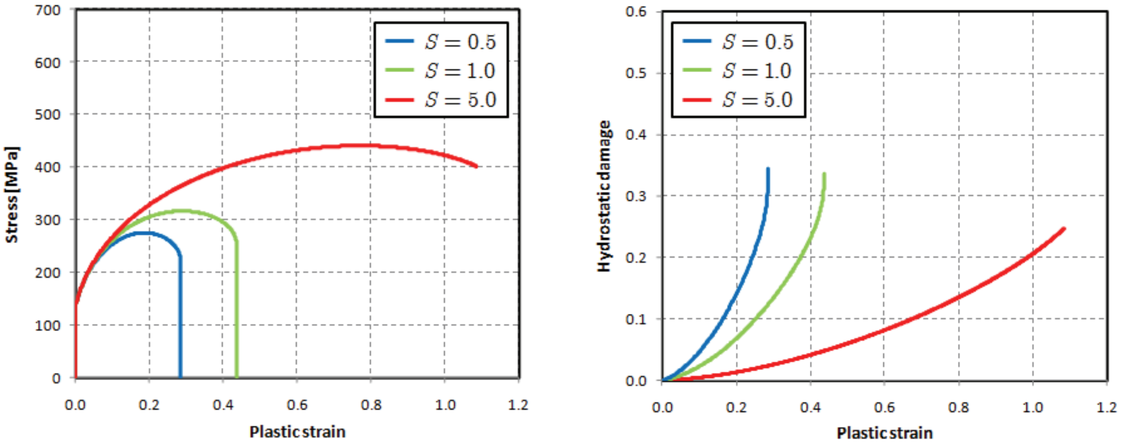

Figure 5.4 Influence of damage denominator parameter on stress and hydrostatic damage evolutions.

Regarding the influence of the damage exponent parameter s, it is important to distinguish two different cases, directly related with the value calculated in the ratio $\bar{Y} / S$.

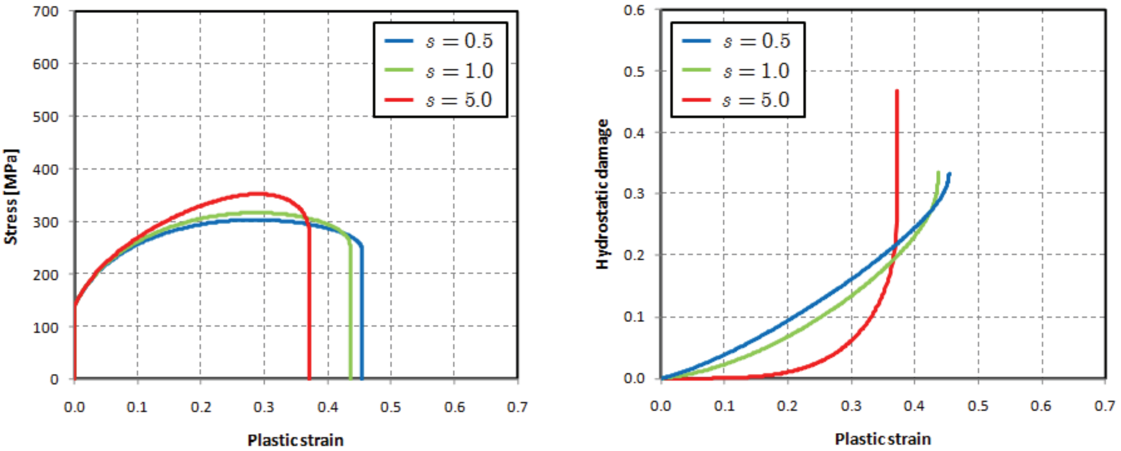

Figure 5.5 Influence of damage exponent parameter on stress and hydrostatic damage evolutions.

When the ratio $\bar{Y} / S$ is lower than unity, a higher value of the exponent leads to a slower damage evolution for all damage components, but, once the computed ratio $\bar{Y} / S$ reaches a value greater than one, damage growth will be exponentially proportional to the considered exponent value and, therefore, critical damage will be rapidly reached. This behaviour is valid for exponent values greater than one. However, there is the possibility of exponent values lower than 1 to be considered for some materials [Lemaitre 2005]. In this case, the behaviour of damage evolution rate is exactly opposite to that presented for values where $s \geq 1$. The evolution becomes less noticeable when ratio $\bar{Y} / S$ attains a value greater than unity, as shown in the Figure 5.5b. Naturally, this influence in the damage rate has a corresponding effect in mechanical properties degradation, anticipating or delaying failure occurrence, as seen in Figure 5.5a.

Another parameter, the hydrostatic parameter η, introduced in the effective stress definition (see Equation (5.25)), also shows to have a huge influence in the stress evolution and in the plastic strain value calculated for the occurrence of rupture. However, its influence is only noticeable for high values of damage, evidenced by the superposition of the damage evolution curves for hydrostatic damages values below 0.3, Figure 5.6b. The introduction of this parameter in the definition of effective stress is justified by the need for a proper modelling of the experimental values, in order to reflect the variation of Poisson's ratio with the plastic deformation [Lemaitre 2000a].

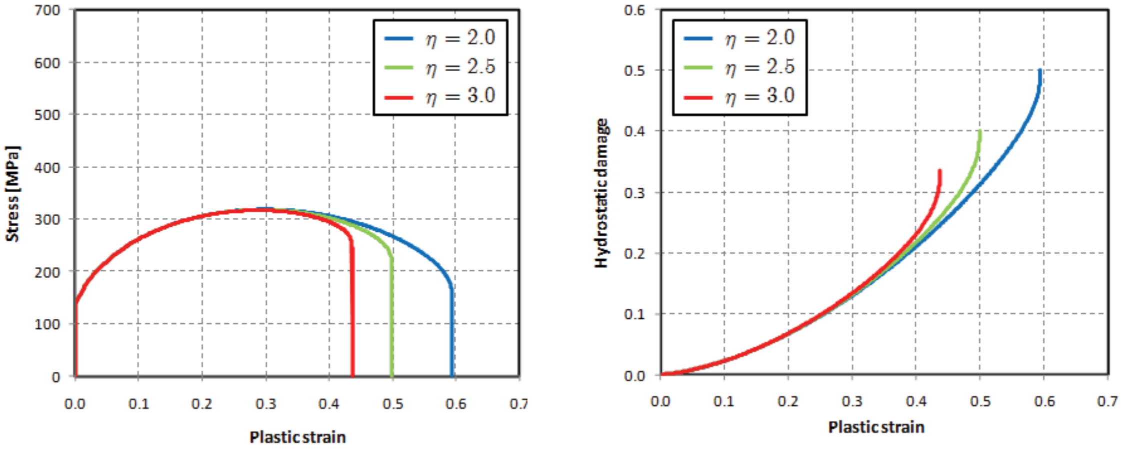

Figure 5.6 Influence of damage hydrostatic parameter on stress and hydrostatic damage evolutions.

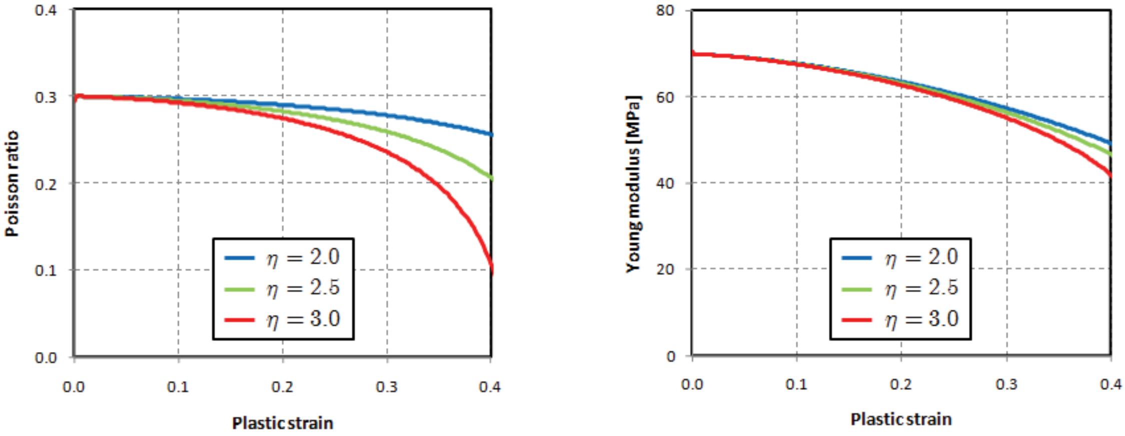

Figure 5.7 Influence of damage hydrostatic parameter on Poisson ratio and Young modulus evolutions.

As seen in Figure 5.7a, the consideration of a higher value for this parameter leads to a faster degradation of the Poisson ratio, even when smaller damage values are computed. The influence of this parameter in the elastic modulus only becomes important for higher damage values, as shown in Figure 5.7b, similar to the influence observed for the equivalent stress evolution.

Another important influence is related with stress triaxiality ratio $\tilde{\sigma}_H / \tilde{\bar{\sigma}}$, introduced in the evolution law through the effective elastic strain energy $\overline{Y}$. In order to study the influence of this ratio in the stress and damage evolutions, three loading cases have been considered: uniaxial tension (UT), plane strain (PS) and equibiaxial stretching (BS) corresponding to stress triaxiality ratios of $1/3$, $1/\sqrt{3}$ and $2/3$, respectively (for a isotropic material and monotonic loadings). The influence of the stress triaxiality ratio is shown in Figure 5.8.

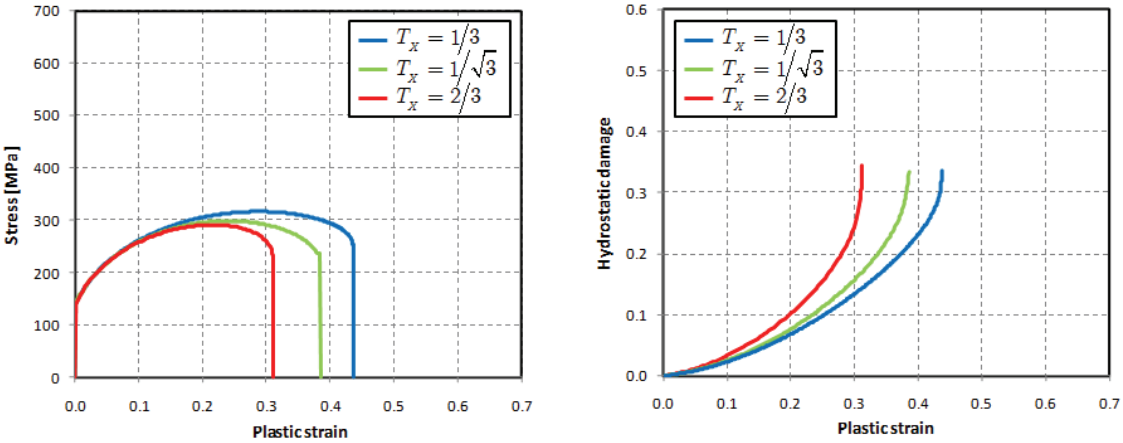

Figure 5.8 Influence of stress triaxiality on stress and hydrostatic damage evolutions.

According to Equations (5.78) and (5.79) and as expected, damage will grow more rapidly under higher stress triaxiality ratios, as the evolution of hydrostatic damage presented in Figure 5.8 depicts.

5.4.2 Influence of hardening parameters

To study the hardening effect in the evolution of damage and in the mechanical properties degradation of the material, three distinct values were considered for the hardening coefficient K (300, 570 and 700 MPa) and for the hardening exponent n (0.1, 0.35 and 0.5). The considered hardening law is the power law given by the expression:

$$\sigma_Y = K\left(\bar{\varepsilon}^p\right)^n . \tag{5.80}$$

The stress-strain curves corresponding to the variations of the two hardening parameters are presented in Figure 5.9.

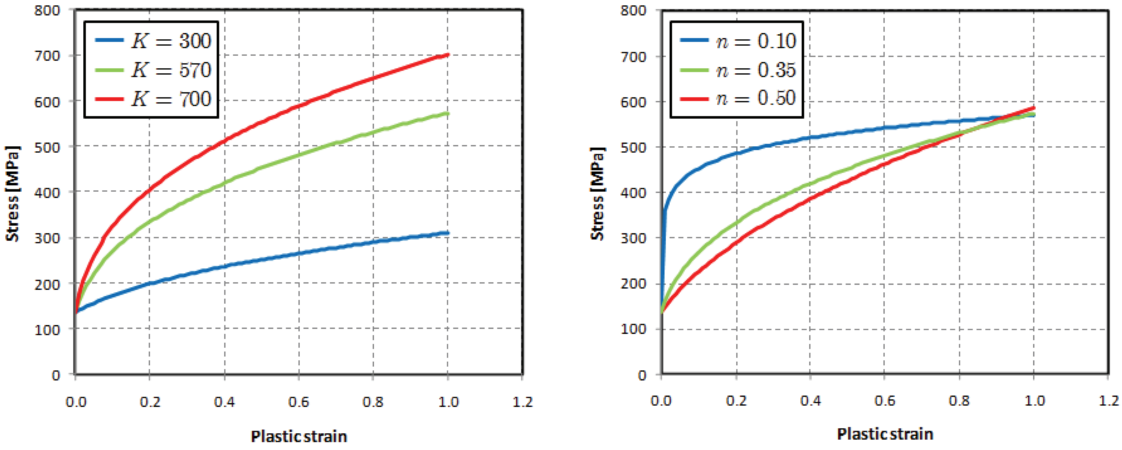

Figure 5.9 Stress-strain curves for different hardening coefficients and hardening exponents.

The influence of the hardening strength K on stress and hydrostatic damage evolutions is shown in Figure 5.10.

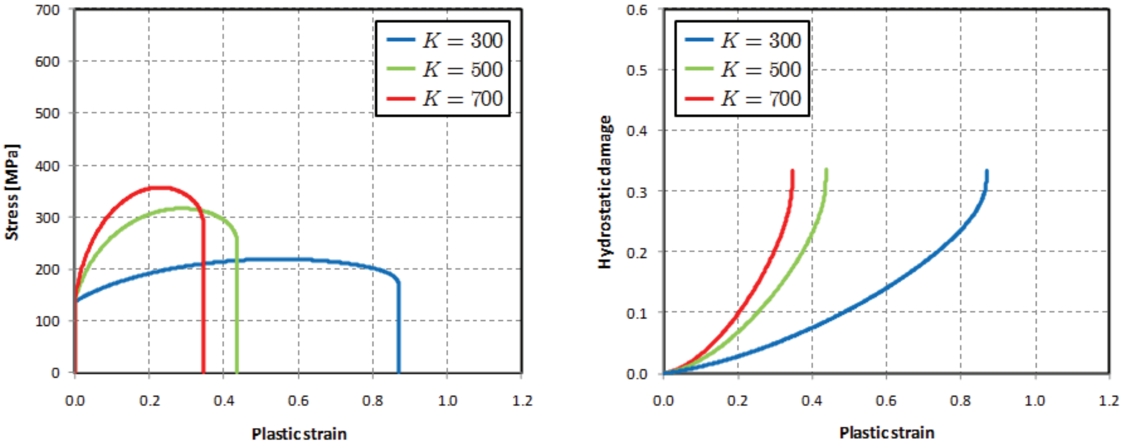

Figure 5.10 Influence of hardening strength on stress and hydrostatic damage evolutions.

As can be seen in Figure 5.10, higher values of the hardening coefficient lead to higher damage growth rates and, consequently, to a faster degradation of mechanical properties. This behaviour is in agreement with the damage evolution law presented in Equation (5.78). The consideration of a higher value for the hardening coefficient drives to more important yield stress values for the same plastic strain, Figure 5.9a. Assuming that the triaxiality ratio remains constant (monotonic loading), these more important yield stress values lead to a higher computed value for the effective elastic energy density $\overline{Y}$ that, maintaining the same denominator S in the damage law, promotes a higher damage growth rate.

A similar effect in the damage evolution is rendered by the variation of exponent parameter n of the hardening law, as seen in Figure 5.11.

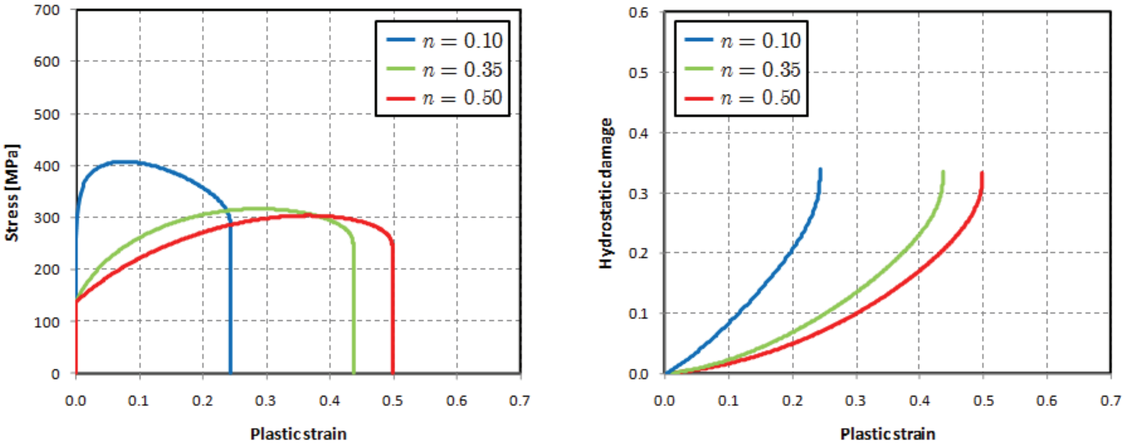

Figure 5.11 Influence of hardening exponent on stress and hydrostatic damage evolutions.

Keeping the same value for the hardening coefficient, a lower value of the hardening exponent n leads to higher yield stress values, Figure 5.9b. In this way, the ratio $\bar{Y} / S$ becomes higher for lower values of plastic strain and, consequently, leads to a faster evolution of the damage, in accordance with the damage evolution law. Therefore, the damage growth rate will be smaller for higher values of the exponent parameter considered in the hardening law.

5.4.3 Influence of normal anisotropy

Before addressing the influence of normal anisotropy, it is important to define this measure. The normal anisotropy parameter $\bar{r}$ is the average value of the r-values obtained for different directions in the plane of sheet metal, calculated as:

$$\bar{r} = \frac{r_0 + 2r_{45} + r_{90}}{4} \tag{5.81}$$

where r_0, r_{45} and r_{90} represents the anisotropic or Lankford coefficients determined for 0°, 45° and 90° directions from rolling direction. Another important measure is the so-called planar anisotropy parameter Δr:

$$\Delta r = \frac{r_0 + r_{90} - 2r_{45}}{4} \tag{5.82}$$

which represents the measure of the variation of normal anisotropy with the angle to the rolling direction [Banabic 2000]. In this study, one has consider $\Delta r = 0$ and, so:

$$r_0 = r_{45} = r_{90}, \tag{5.83}$$

and three different values for the normal anisotropy $\overline{r}$: 0.5, 1.0 and 2.0. The influence of the normal anisotropy coefficient on principal damage values evolutions is presented in Figure 5.12, under uniaxial tension loading applied along 1-direction.

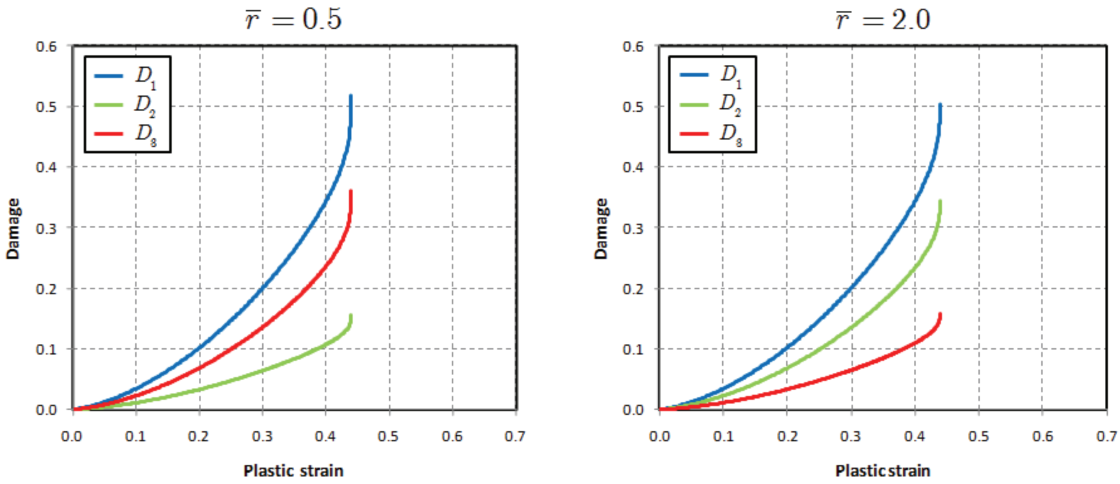

Figure 5.12 Influence of normal anisotropy on damage evolutions under uniaxial tension.

A change in damage evolutions for D_2 and D_3 is observed when one considers normal anisotropy coefficients lower and higher than one. To understand this change, let us consider again the anisotropic damage evolution law (Equation (5.78)). Principal damage values are given as:

$$\begin{bmatrix} \dot{D}_1 & 0 & 0 \\ 0 & \dot{D}_2 & 0 \\ 0 & 0 & \dot{D}_3 \end{bmatrix} = \left(\frac{\overline{Y}}{S}\right)^s \begin{bmatrix} \left|\dot{\varepsilon}_1^p\right| & 0 & 0 \\ 0 & \left|\dot{\varepsilon}_2^p\right| & 0 \\ 0 & 0 & \left|\dot{\varepsilon}_3^p\right| \end{bmatrix}. \tag{5.84}$$

Assuming a monotonic tensile loading and integrating the differential equation using $D_1 = D_2 = D_3 = 0$ for a equivalent plastic strain lower than ε_D^p (which is considered equal to zero, Table 5.2), one reach:

$$\begin{aligned} D_1 &= \left(\frac{\overline{Y}}{S}\right)^s \left|\varepsilon_1^p\right| \\ D_2 &= \left(\frac{\overline{Y}}{S}\right)^s \left|\varepsilon_2^p\right|. \\ D_3 &= \left(\frac{\overline{Y}}{S}\right)^s \left|\varepsilon_3^p\right| \end{aligned} \tag{5.85}$$

By definition, anisotropic coefficient is given by the ratio:

$$r = \frac{\varepsilon_2^p}{\varepsilon_3^p} \tag{5.86}$$

where ε_2^p and ε_3^p are the plastic strains in the transverse and thickness directions. Substituting in Equation (5.86) the relation obtained in Equation (5.85), anisotropic parameter can be rewritten as:

$$r = \frac{D_2}{D_3}\,. \tag{5.87}$$

Therefore, under uniaxial tensile loading, the magnitude of the damage evolution in width and thickness direction will be dependent on the considered normal anisotropic coefficient. When $\overline{r} < 1$, damage in thickness direction will assume a more important position in the failure calculation.

6. APPLICATION OF DAMAGE TO FAILURE PREDICTION

Numerical tests were carried out and compared to corresponding experimental testings in order to evaluate the performance and accuracy of the proposed damage models in the failure prediction in sheet metal forming processes. A wide-range of benchmark studies are conducted including classical testings for material characterization and complex applications involving plastic anisotropy and contact. Intrinsically, the adopted (and implemented) damage models are tested and a qualitative characterization of the capabilities of the proposed models is achieved.

6.1 Tensile test

The classical uniaxial tensile test was chosen to illustrate damage model features. This example corresponds to the simulation of a tensile test performed on a plate specimen subjected to monotonic axial stretching. The selected material is the aluminium alloy 5182, in O temper state. This aluminium wrought material is largely used in automotive industry to produce internal and structural body parts.

According to [LPMTM 2001], this aluminium alloy has a nearly isotropic behaviour in flow stress evolution and exhibits a pronounced saturation of the flow stress during monotonic loading. Also, the observed Bauschinger effect was rather small during reversed deformation of Bauschinger tests, thus a saturated isotropic hardening behaviour can be assumed for this material. In order to describe this behaviour, the most adequate hardening law is the Voce law given by the expression:

$$\sigma_Y = \sigma_{Y0} + R_{sat}\left[1 - \exp\left(-C_R \bar{\varepsilon}^p\right)\right] \tag{6.1}$$

where σ_{Y0} is the initial yield stress and R_{sat} and C_R are material parameters, determined from a single tensile test. This law is adequate to describe the behaviour of materials which exhibit a saturated isotropic hardening, with a weak or negligible kinematic hardening. Concerning anisotropic flow behaviour, although variation of anisotropy coefficients is not very large [LPMTM 2001], better results were achieved in the identification of the elastoplastic models using Hill48 criterion, when compared with the von Mises criterion. Therefore, it was concluded that the behaviour of this material can be satisfactorily described by using an isotropic hardening with saturation given by the Voce law, combined with Hill48 criterion. The material parameters are presented in Table 6.1 [LPMTM 2001] and the true stress – true strain curves at 0, 45 and 90 degrees from rolling direction are depicted in Figure 6.1.

Table 6.1 Material parameters of AA 5182-O.

Property	**Symbol**	**Value**
Young modulus [GPa]	E	70
Poisson coefficient	ν	0.3
Initial yield stress [MPa]	σ_{Y0}	149
Voce law parameter[MPa]	R_{sat}	208.7
Voce law parameter	C_R	12.1
r-values	r_0, r_{45}, r_{90}	0.79, 0.851, 0.7

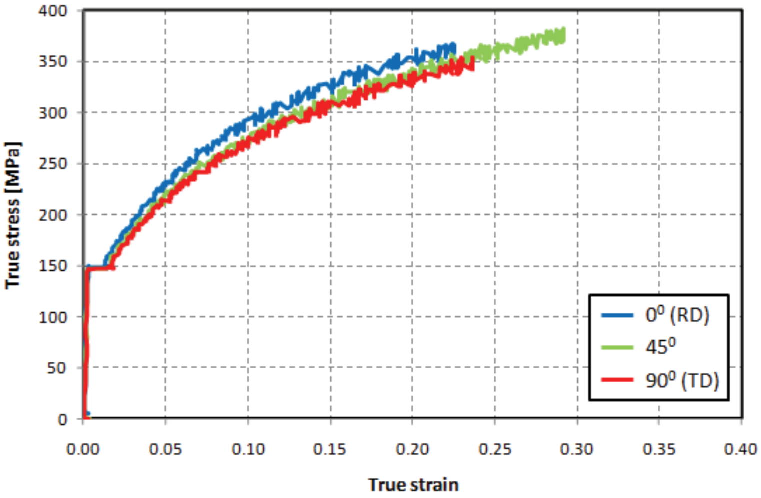

Figure 6.1 Uniaxial true stress – true strain curves of AA 5182-O.

Concerning damage model parameters, a partial identification procedure, similar to the procedure proposed by Lemaitre *et al.* [2005], was used to determine parameters from available tensile test data. During a monotonic tensile loading, isotropic damage evolution law can be written as:

$$\dot{D} = \left(\frac{\tilde{\sigma}^2}{2ES} \right)^s \dot{\varepsilon}^p \tag{6.2}$$

where $\tilde{\sigma}$ is the effective stress. Integrating the differential equation using $D = 0$ for a equivalent plastic strain lower than ε_D^p, one has:

$$D = \left(\frac{\tilde{\sigma}^2}{2ES} \right)^s \left(\varepsilon^p - \varepsilon_D^p \right). \tag{6.3}$$

Therefore, isotropic damage model needs the identification of 4 parameters: damage exponent s, damage threshold ε_D^p, critical damage D_C and damage denominator S.

Concerning damage exponent, it can be considered equal to 1 since multi-experiments have shown that $s \approx 1$ [Lemaitre 1985b]. Plastic strain at damage threshold ε_D^p can be defined as the value of plastic strain for which diffuse necking starts, corresponding to the true plastic strain attained when the maximum value in the engineering stress-strain curve is reached. Therefore:

$$\varepsilon_D^p \approx \varepsilon_U . \tag{6.4}$$

Before addressing the partial identification procedure of the other two parameters, let us first define some concepts and establish some hypothesis. During the course of a tensile test, a ductile material becomes unstable and necks down before rupture. The local plastic strain attained in the necking zone corresponds to the equivalent plastic strain at rupture, ε_R^p, for which critical damage D_C is attained. Usually, this local plastic strain at rupture in the neck is not available from the tensile test data. To estimate this value, one can use the plastic incompressibility condition in the necked region and the standard definition of true strain. True strain can be continuously given by the relation:

$$\varepsilon = \ln\left(\frac{L}{L_0} \right). \tag{6.5}$$

Once the neck is formed, plastic strain will be localized in the neck and the use of the above equation is not easy since values for the initial length and current length of the neck are difficult to obtain. But, assuming volume constancy, one can define an equivalence between initial and final volumes as:

$$A_0 L_0 = A_R L_R \tag{6.6}$$

where A_R and L_R are the area and length of the neck at rupture. Using this correspondence, it is possible to write:

$$\frac{A_0}{A_R} = \frac{L_R}{L_0}, \tag{6.7}$$

from which it is possible to define the true plastic strain attained in the neck by the expression:

$$\varepsilon_R^p = \ln\left(\frac{A_0}{A_R}\right), \tag{6.8}$$

or, in terms of the necking parameter Z, as:

$$\varepsilon_R^p = \ln\left(\frac{1}{1-Z}\right) \tag{6.9}$$

with:

$$Z = \frac{A_0 - A_R}{A_0}. \tag{6.10}$$

This parameter ε_R^p represents the maximum true strain that the material can withstand before fracture and is related to the total strain to fracture of the engineering stress-strain curve. Using this local plastic strain, it is possible to calculate the corresponding effective (undamaged) stress at rupture, $\tilde{\sigma}_R$, reached in the failure site, using the identified hardening law:

$$\tilde{\sigma}_R = f\left(\varepsilon_R^p\right). \tag{6.11}$$

To evaluate the damage denominator parameter S, it will be assumed that maximum damaged stress σ is obtained when the local neck is formed. This assumption is justified by the fact that when diffuse necking is achieved, for a maximum engineering stress in the engineering stress-strain curve, and further deformation leads to the appearance of a local neck, there is a change in the stress and strain states from a uniaxial state to a state near plane strain path, and, thus, there is a change to a higher stress triaxiality. Another reason is related with the plastic strain rate when localized necking occurs. Once localization of plastic flow is verified, all plastic straining will be restrained to the necking region and a high plastic strain rate is reached in such region. Both these occurrences have a direct impact in the damage growth rate leading to a more accentuated decrease in the material stiffness in the necking region. To determine the starting point of the local necking, the condition postulated by Hill [1952] is used. In his criterion, necking is supposed to start when major tension reaches a maximum (see Section 7.2.1 for more details). After some straightforward algebra, Hill's criterion for localized necking can be written as:

$$\frac{d\sigma_1}{d\varepsilon_1} = \left(1 + \beta\right)\sigma_1 \tag{6.12}$$

where σ_1 and ε_1 are the major principal in-plane stress and strain, respectively, and β represents the strain ratio, defined as the relation between the major and minor principal in-plane strains:

$$\beta = \frac{d\varepsilon_2}{d\varepsilon_1}. \tag{6.13}$$

Using this criterion, it is possible to determine the attained plastic strain when localized necking starts, ε^p_{neck}, and, by using the identified hardening law, the corresponding effective stress, $\tilde{\sigma}_{neck}$. This point in the effective stress-strain curve will correspond to the maximum of damaged stress σ in the damaged stress-strain curve, thus:

$$\left.\frac{d\sigma}{d\varepsilon^p}\right|_{\varepsilon^p = \varepsilon^p_{neck}} = 0. \tag{6.14}$$

By means of the effective stress concept, Equation (6.14) can be rewritten as:

$$\left.\frac{d}{d\varepsilon^p}\left[\left(1 - D\right)\tilde{\sigma}\right]\right|_{\varepsilon^p = \varepsilon^p_{neck}} = 0. \tag{6.15}$$

A straightforward algebra leads to an expression for damage attained at beginning of localized necking:

$$D_{neck} = 1 - \frac{\tilde{\sigma}_{neck}}{H'_{neck}} \left.\frac{dD}{d\varepsilon^p}\right|_{\varepsilon^p = \varepsilon^p_{neck}} \tag{6.16}$$

where H'_{neck} is the hardening modulus calculated for the plastic strain ε^p_{neck}:

$$H'_{neck} = \left.\frac{d\tilde{\sigma}}{d\varepsilon^p}\right|_{\varepsilon^p = \varepsilon^p_{neck}} \tag{6.17}$$

and derivative $dD/d\varepsilon^p$ is computed from the damage evolution law (Equation(6.3)) as:

$$\left.\frac{dD}{d\varepsilon^p}\right|_{\varepsilon^p = \varepsilon^p_{neck}} = \frac{s\tilde{\sigma}_{neck} H'_{neck}}{ES}\left(\frac{\tilde{\sigma}^2_{neck}}{2ES}\right)^{s-1}\left(\varepsilon^p_{neck} - \varepsilon^p_D\right) + \left(\frac{\tilde{\sigma}^2_{neck}}{2ES}\right)^{s}. \tag{6.18}$$

Using Equations (6.3) and (6.16) and the assumption of a unitary damage exponent, $s = 1$, damage denominator parameter S is given by:

$$S = \frac{\tilde{\sigma}^2_{neck}}{E}\left[\frac{3}{2}\left(\varepsilon^p_{neck} - \varepsilon^p_D\right) + \frac{\tilde{\sigma}_{neck}}{2H'_{neck}}\right], \tag{6.19}$$

which, for a material that has isotropic hardening behaviour with saturation given by the Voce law, may be written as:

$$S = \frac{\tilde{\sigma}_{neck}^2}{E}\left[\frac{3}{2}\left(\varepsilon_{neck}^p - \varepsilon_D^p\right) + \frac{\tilde{\sigma}_{neck}}{2R_{sat}C_R \exp\left(-C_R \varepsilon_{neck}^p\right)}\right]. \tag{6.20}$$

Finally, critical damage D_C is then evaluated by the rupture stress $\tilde{\sigma}_R$ and strain ε_R^p values. In order to take into account the plane strain condition inside the neck, a correction to the stress is performed by introducing the notion of damage equivalent stress σ^* [Lemaitre 1985a] obtained as:

$$\sigma^* = \bar{\sigma} R_v^{1/2} \tag{6.21}$$

where R_v is the triaxiality function given by:

$$R_v = \frac{2}{3}\left(1+\nu\right) + 3\left(1-2\nu\right)\left(\frac{\sigma_H}{\bar{\sigma}}\right)^2. \tag{6.22}$$

For a uniaxial case $R_v = 1$ but, for the plane strain case, the triaxiality function will be given by:

$$R_\nu = \frac{5-4\nu}{3}. \tag{6.23}$$

Thus, critical damage D_C is calculated as:

$$D_C = \left(\frac{\tilde{\sigma}_R^2 R_\nu}{2ES}\right)^s \left(\varepsilon_R^p - \varepsilon_D^p\right). \tag{6.24}$$

For the selected aluminium alloy 5182-O, the mechanical properties are summarized in Table 6.2 [Wouters 2002], measured in a set of standard ISO 20x80 tensile specimens.

Table 6.2 Mechanical characteristics of AA 5182-O.

Direction from RD	$R_{p0,2}$ [MPa]	R_m [MPa]	R_e/R_m [%]	A_g [%]	A_{80} [%]	n
0°	149.5	283.8	52.7	20.7	24.4	0.335
45°	148.2	279.4	53.1	20.6	28	0.307
90°	151.6	280.3	54.1	24.5	26.2	0.365

The ultimate engineering strain in the rolling direction is attained for 20.7 %. The corresponding ultimate true strain ε_U of:

$$\varepsilon_U = \ln\left(1 + A_g\right) = 0.188\,, \tag{6.25}$$

and, so, plastic strain to damage threshold is set to 0.188. Since the necking parameter Z is difficult to obtain in a sheet specimen, the typical value for aluminium alloys will be used, which is near 35 % [DIN EN 10002 2001]. Therefore, inside the neck, true strain at rupture ε_R^p is given by:

$$\varepsilon_R^p = \ln\left(\frac{1}{1 - 0.35}\right) \approx 0.43\,. \tag{6.26}$$

which corresponds to an effective stress at rupture:

$$\tilde{\sigma}_R = \sigma_{Y0} + R_{sat}\left[1 - \exp\left(-C_R \varepsilon_R^p\right)\right] = 356.6\,MPa\,. \tag{6.27}$$

Using Hill's necking criterion, localized necking starts at a plastic strain of:

$$\varepsilon_{neck}^p = 0.214\,. \tag{6.28}$$

At this plastic strain level, the effective stress $\tilde{\sigma}_{neck}$, given by the Voce law, is equal to:

$$\tilde{\sigma}_{neck} = \sigma_{Y0} + R_{sat}\left[1 - \exp\left(-C_R \varepsilon_{neck}^p\right)\right] = 342.0\,MPa\,. \tag{6.29}$$

Using Equation (6.20), one gets for the damage denominator parameter S:

$$S = \frac{\tilde{\sigma}_{neck}^2}{E}\left[\frac{3}{2}\left(\varepsilon_{neck}^p - \varepsilon_D^p\right) + \frac{\tilde{\sigma}_{neck}}{2R_{sat}C_R \exp\left(-C_R \varepsilon_{neck}^p\right)}\right] = 1.57\,MPa\,. \tag{6.30}$$

Critical damage D_C is then obtained from the values at rupture. Therefore, using values from Equations (6.26), (6.27) and (6.30) in Equation (6.24), critical damage is equal to:

$$D_C = \left(\frac{\tilde{\sigma}_R^2 R_\nu}{2ES}\right)^s \left(\varepsilon_R^p - \varepsilon_D^p\right) \approx 0.18\,. \tag{6.31}$$

The parameters identified by this partial identification procedure are summarized in Table 6.3.

Table 6.3 Isotropic damage model parameters for AA 5182-O.

Parameter	**Symbol**	**Value**
Damage denominator [MPa]	S	1.57
Damage exponent	s	1.0
Damage threshold	ε_D^p	0.188
Critical damage value	D_C	0.18

As already stated in Section 4.3.1, quantification of damage may be deduced from a set of experimental data using the elasticity modulus change. Using this data, further effort in the formulation of an identification procedure is required in order to identify the set of material parameters for the constitutive model which gives the best representation of a maximum volume of experimental data and information on a given material. Unfortunately, these experimental data are not commonly available. The described method allows obtaining material damage parameters for a specific material using typical properties derived from a unique or few tensile tests. It must be remarked that the rate of damage accumulation depends on the stress state in the process, and, therefore, tensile data may not be indicative of damage in other stress states. Nevertheless, obtained parameters can be seen as a good starting point for a precise identification procedure.

6.1.1 Numerical modelling

A mesh with a single layer of 900 eight-noded solid elements (C3D8R from the ABAQUS library [ABAQUS 2008]) was used in the specimen discretization. Due to symmetry, only one quarter of the problem was modelled and appropriate boundary conditions were imposed. The relevant process parameters are listed in Table 6.4 and specimen dimensions are presented in Figure 6.2. Tensile simulation was performed by applying a prescribed displacement on the specimen edge. Rolling direction is assumed to be along loading direction (Figure 6.3).

Table 6.4 Tensile test numerical conditions.

Blank	
Element type	Reduced integration solid (8-noded)
Element size [mm]	1.0x1.0x1.0 (gauge area)
Number of layers	1
Number of elements	900
Process parameters	
Crosshead velocity [m/s]	1

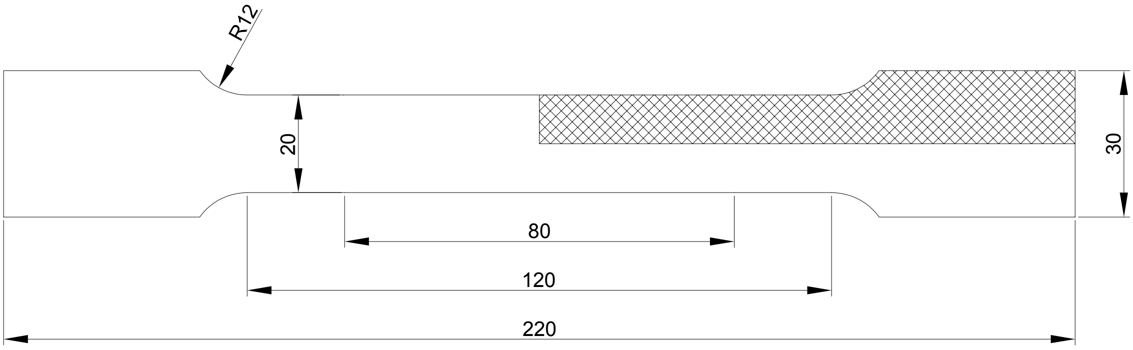

Figure 6.2 Sheet tensile test specimen dimensions (in mm).

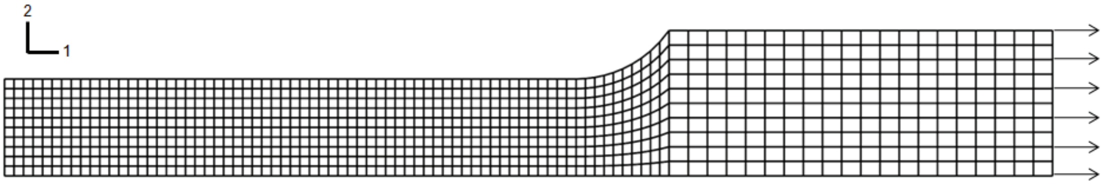

Figure 6.3 Adopted numerical mesh for tensile test.

6.1.2 Results and discussion

The main purpose of this example is to show the predictive capabilities of the proposed damage methodology on a simple case for which plastic localization mode and failure location is known. Additionally, a critical assessment of the reliability of the partial identification procedure of the damage material parameters is also performed. Applying a monotonic loading, plastic strain is initially uniformly distributed along the gauge area, reaching a uniform plastic strain of 0.188. This point corresponds to the diffuse necking initiation and it is attained for a cross-head displacement of 12.8 mm. It is possible to infer this critical cross-head displacement by the visible change in the stress triaxiality evolution, which corresponds to the initiation of diffuse necking [Lee 2005], Figure 6.4.

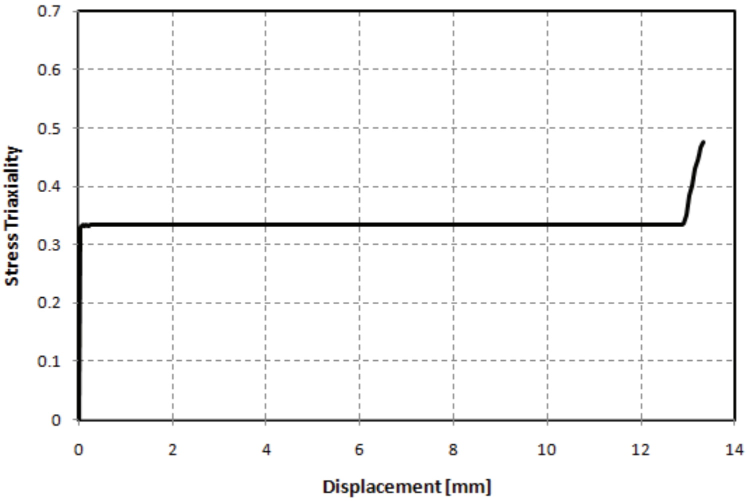

Figure 6.4 Evolution of stress triaxiality.

Further displacement leads to the localization of plastic strain which, for the case of the uniaxial tensile, takes the form of a shear band. As can be seen in Figure 6.5, the damage coupled simulation gives a realistic localization mode, at an angle near 45 degrees, where also high values of plastic strain are observed, Figure 6.6.

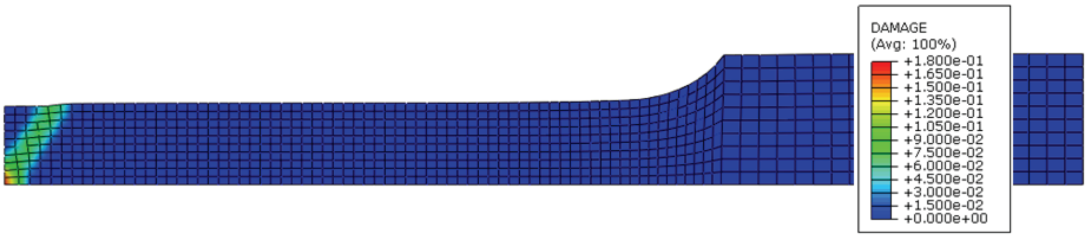
DAMAGE
(Avg: 100%)
+1.800e-01
+1.650e-01
+1.500e-01
+1.350e-01
+1.200e-01
+1.050e-01
+9.000e-02
+7.500e-02
+6.000e-02
+4.500e-02
+3.000e-02
+1.500e-02
+0.000e+00

Figure 6.5 Tensile test damage contour.

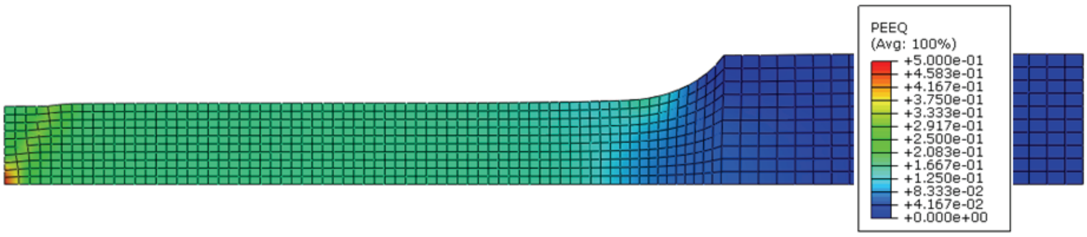
PEEQ
(Avg: 100%)
+5.000e-01
+4.583e-01
+4.167e-01
+3.750e-01
+3.333e-01
+2.917e-01
+2.500e-01
+2.083e-01
+1.667e-01
+1.250e-01
+8.333e-02
+4.167e-02
+0.000e+00

Figure 6.6 Tensile test equivalent plastic strain contour.

For the element located in the center of the specimen, where meso-crack starts, the corresponding damaged and undamaged curves are presented in Figure 6.7.

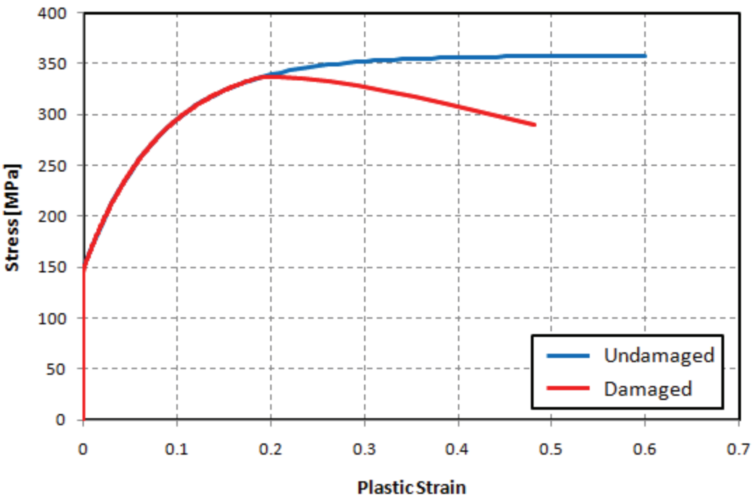

Figure 6.7 Stress-strain curves for tensile test.

A decrease in the flow stress is observed after damage threshold is attained, i.e., at 0.188 plastic strain. Failure is assumed to occur when damage reaches the critical value of 0.18, which, for the element located in the necked region, is attained for a plastic strain of 0.48. A discrepancy exits between the value determined by numerical simulation, 0.48, and the value assumed as the true strain at rupture, 0.43, Equation (6.26). This difference can be related with the assumption made in the partial identification procedure of the critical damage parameter. As seen in Figure 6.4, stress triaxiality evolves almost linearly from the uniaxial tension up to the plane strain condition, resulting in a lower damage growth when compared to the assumed drastic change in the deformation path after necking occurrence in the partial identification procedure. Naturally, this lower damage evolution postpones the critical damage achievement, allowing more straining until failure. Nevertheless, the obtained engineering stress - engineering strain curve for the tensile specimen is presented in Figure 6.8.

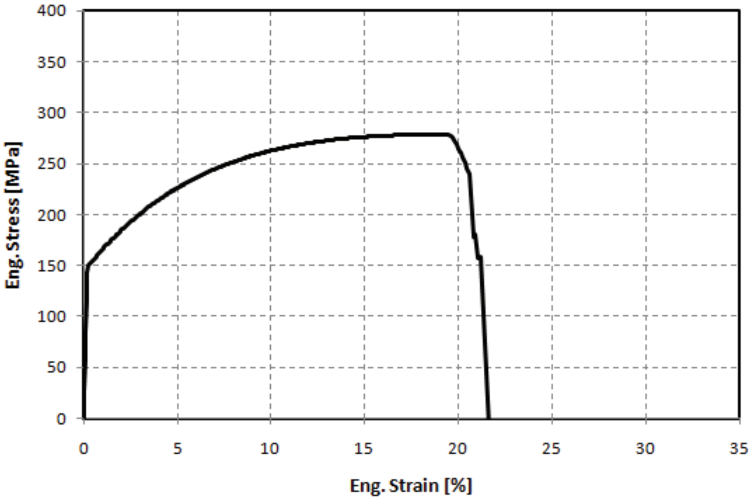

Figure 6.8 Engineering stress- strain curve.

An interesting observation in this example is concerned with the stress value in the failure zone, i.e., in the fully damaged zone. While for the simulation with damage consideration the stress value is zero in this location, Figure 6.9, the same numerical model, with no damage evolution and plastic softening taken into account, computes the maximum stress value in the damaged zone, Figure 6.10. This unrealistic situation provided by an uncoupled analysis reinforces the need of damage coupled formulations, that can lead to improved and more realistic modelling of the failure initiation phenomenon.

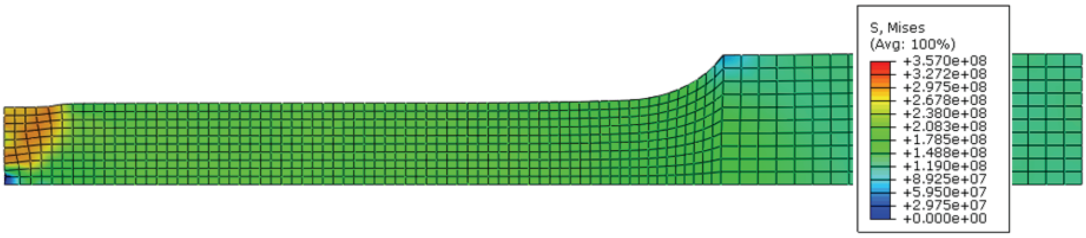
S, Mises
(Avg: 100%)
+3.570e+08
+3.272e+08
+2.975e+08
+2.678e+08
+2.380e+08
+2.083e+08
+1.785e+08
+1.488e+08
+1.190e+08
+8.925e+07
+5.950e+07
+2.975e+07
+0.000e+00

Figure 6.9 Tensile test equivalent stress contour (coupled analysis).

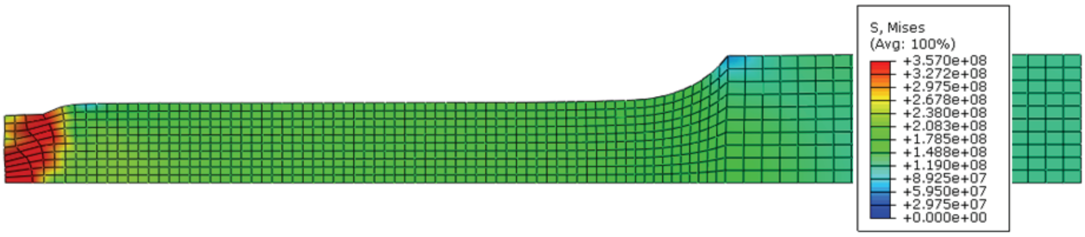
S, Mises
(Avg: 100%)
+3.570e+08
+3.272e+08
+2.975e+08
+2.678e+08
+2.380e+08
+2.083e+08
+1.785e+08
+1.488e+08
+1.190e+08
+8.925e+07
+5.950e+07
+2.975e+07
+0.000e+00

Figure 6.10 Tensile equivalent stress contour (uncoupled analysis).

6.2 Bulge test

The standard uniaxial tensile test is a widely accepted method to obtain relevant properties of sheet metal materials. These fundamental parameters can be used in numerical modelling of sheet metal forming operations to predict and assess formability and to perform failure analysis. However, the range of strain obtained from tensile test is limited and, therefore, if one needs further information on material behaviour, extrapolation of tensile data is performed. The bulge test is an alternative method to obtain such deformation ranges, higher than the ones obtained in tensile test, thus being possible to obtain more realistic, non-extrapolated data for material behaviour. In this test, a sheet metal specimen is subjected to a hydraulic pressure that bulges the specimen up to failure. Final geometry of the bulged test specimen is defined by the geometry of the bulge die. Changing die geometry, one can impose different strain paths to the sheet metal, and, in this way, determine different points in the forming limit diagram. Besides the possibility to obtain higher strains, another advantage can be pointed out to this test when compared to similar tests, as for example, Nakajima test. There is no contact between the specimen and any active tool part in the sampling region and, thus, friction effect is eliminated from the material's plastic behaviour assessment.

In this example, a comparison between the isotropic and anisotropic damage models is performed. The cross-identification isotropic / anisotropic damage models procedure proposed by Desmorat and Otin [2008a] has been used to estimate the anisotropic damage parameters for the AA 5182-O. Considering that, for the monotonic uniaxial tension case, stress and damage tensor are given by:

$$\boldsymbol{\sigma} = \begin{bmatrix} \sigma & 0 & 0 \\ 0 & 0 & 0 \\ 0 & 0 & 0 \end{bmatrix} \text{ and } \boldsymbol{D} = D \begin{bmatrix} 1 & 0 & 0 \\ 0 & 1/2 & 0 \\ 0 & 0 & 1/2 \end{bmatrix}, \tag{6.32}$$

the triaxiality function R_ν, explicitly given as:

$$R_\nu = \frac{2}{3}\left(1+\nu\right) + 3\left(1-2\nu\right)\left(\frac{\tilde{\sigma}_H}{\tilde{\tilde{\sigma}}}\right)^2 \tag{6.33}$$

is different from one, unlike in the isotropic damage case. The effective hydrostatic stress $\tilde{\sigma}_H$ and the effective von Mises stress $\tilde{\tilde{\sigma}}$ are calculated for the anisotropic damage as:

$$\tilde{\sigma}_H = \frac{\sigma_H}{1-\eta D_H} = \frac{\sigma}{3-2\eta D} \tag{6.34}$$

$$\tilde{\tilde{\sigma}} = \left[\frac{3}{2}\operatorname{dev}\left(\boldsymbol{HsH}\right) : \operatorname{dev}\left(\boldsymbol{HsH}\right)\right]^{\frac{1}{2}} = \frac{2}{3}\frac{\sigma}{1-D} + \frac{1}{3}\frac{\sigma}{1-\dfrac{D}{2}}, \tag{6.35}$$

and the triaxiality function becomes dependent on damage values. Under uniaxial tension, this function is computed for the anisotropic damage model as:

$$R_\nu = \frac{2}{3}\left(1+\nu\right) + 3\left(1-2\nu\right)\left[\left(1-\frac{2\eta}{3}D\right)\left(\frac{2}{1-D} + \frac{1}{1-D/2}\right)\right]^{-2}. \tag{6.36}$$

The anisotropic damage evolution law can then be reduced to the differential equation:

$$\dot{D} = \left(\frac{\sigma^2 R_\nu}{2ES}\right)^s \dot{\varepsilon}^p. \tag{6.37}$$

Recommendations for this cross-identification procedure [Lemaitre 2005] is to keep the same damage exponent parameter s (as identified for the isotropic model) and to assume a damage hydrostatic parameter η equal to 3. Concerning the damage denominator S and the critical damage D_C, it is required a re-identification of these parameters by using the monotonic tensile curve. Several simulations were performed varying the damage denominator. The best fit with the isotropic damage model was achieved for a damage denominator of 1.41 MPa. The corresponding damaged stress-strain curves for both isotropic and anisotropic models are shown in Figure 6.11.

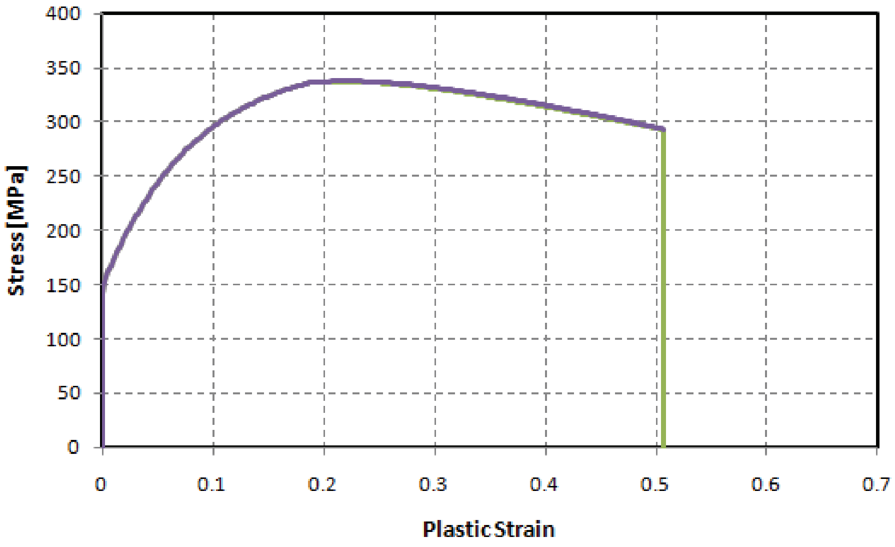

Figure 6.11 Stress-strain curves for isotropic and anisotropic damage models.

Using the anisotropic damage model, the same stress value decrease was obtained for a critical damage of 0.21. The cross-identified parameters for the anisotropic damage model are summarized in Table 6.5.

Table 6.5 Anisotropic damage model parameters for AA 5182-O.

Parameter	**Symbol**	**Value**
Damage denominator [MPa]	S	1.41
Damage exponent	s	1.0
Damage threshold	ε_D^p	0.188
Critical damage value	D_C	0.21
Damage hydrostatic parameter	η	3

6.2.1 Numerical modelling

The problem consists of a circular sheet subjected to internal pressure. The sheet lies on a rigid cylindrical die and its edge is assumed clamped. The geometry and the adopted finite element mesh are shown in Figure 6.12 and Figure 6.13, respectively.

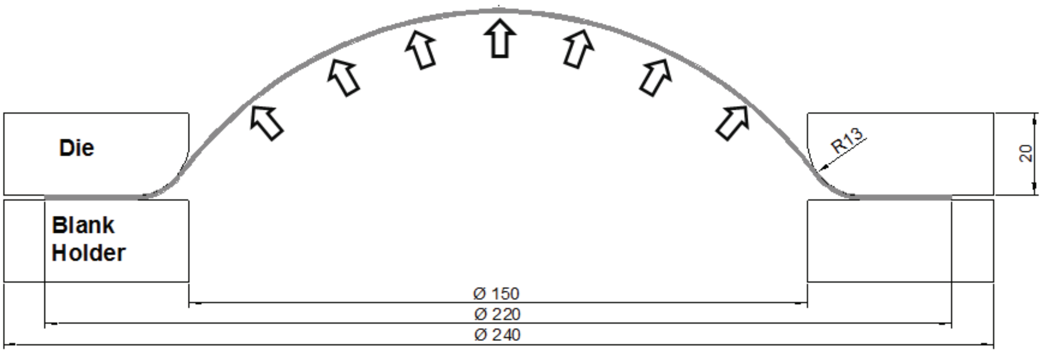

Figure 6.12 Bulge test dimensions (in mm).

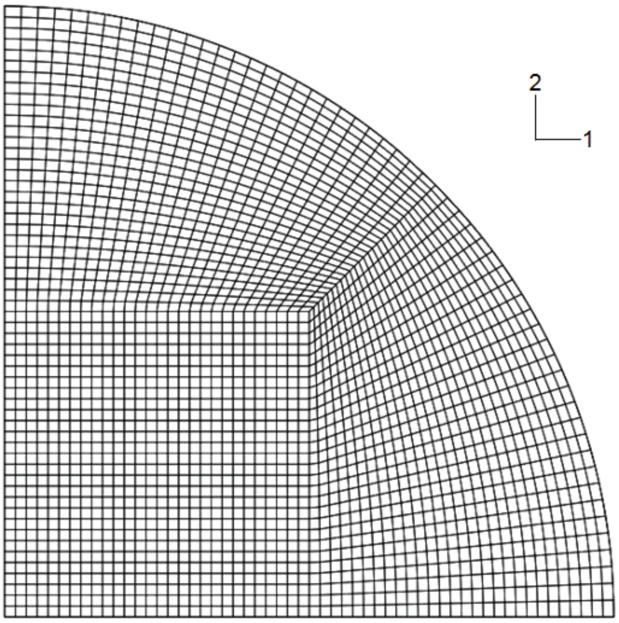

Figure 6.13 Adopted numerical mesh for bulge test.

Due to the symmetry of the problem, only one quarter of the domain is considered in the finite element simulation. A mesh with a double layer of 4704 eight-noded solid elements is used in the discretization of the sheet metal specimen. The surface of the circular die is discretized by three-noded rigid triangular elements and no friction has been considered. Loading consists in a prescribed increasing pressure, defined by a linear ramped evolution until a value of 7.0 MPa is attained. The main process parameters are listed in Table 6.6. Rolling direction is assumed to be along 1-axis, Figure 6.13. The material properties employed in the numerical simulation are listed in Table 6.1 and damage parameters for the isotropic damage model are presented in Table 6.3. Parameters for the anisotropic damage model are listed in Table 6.5.

Table 6.6 Bulge test numerical conditions.

Blank	
Element type	Reduced integration solid (8-noded)
Element size [mm]	1.96x1.96x0.5
Number of layers	2
Number of elements	4704
Tools	
Tool type	Rigid elements
Elements in radii	16
Friction coefficient	0.0
Process parameters	
Pressure evolution	Ramped (Max. value 7.0 MPa)

6.2.2 Results and discussion

Regardless of the die geometry, be it circular or elliptical, a biaxial stretching state is always imposed to the sheet during a bulge test experiment. In this example, a circular die is considered and, consequently, an equibiaxial state is enforced to the sheet during the application of a continuously increased hydraulic pressure. This pressure will force the specimen to freely deform into a nearly spherical form. In the formed bulge center, i.e., in the dome pole, plastic strain reaches the highest value in experiments and this area will be prominent for failure occurrence. Numerical simulation using the isotropic damage model also follows such experimental trend. Isotropic model delivers the maximum value of plastic strain in bulge center, Figure 6.15, where also calculates the maximum damage value, Figure 6.14, and predicts the meso-crack initiation.

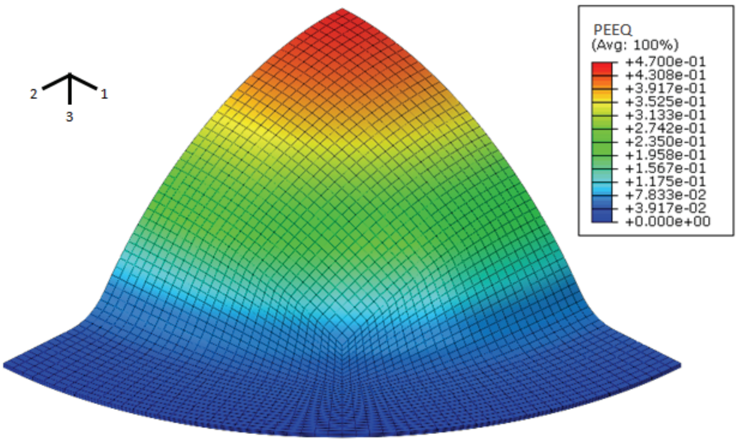
2
1
3
PEEQ
(Avg: 100%)
+4.700e-01
+4.308e-01
+3.917e-01
+3.525e-01
+3.133e-01
+2.742e-01
+2.350e-01
+1.958e-01
+1.567e-01
+1.175e-01
+7.833e-02
+3.917e-02
+0.000e+00

Figure 6.14 Bulge test equivalent plastic strain contour (isotropic damage model).

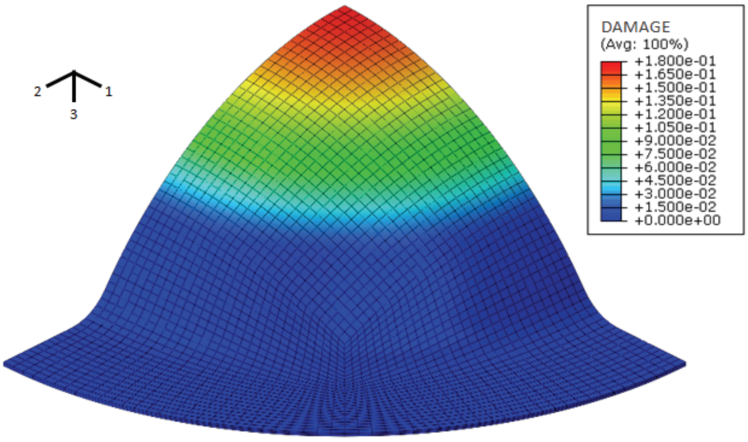
2
1
3
DAMAGE
(Avg: 100%)
+1.800e-01
+1.650e-01
+1.500e-01
+1.350e-01
+1.200e-01
+1.050e-01
+9.000e-02
+7.500e-02
+6.000e-02
+4.500e-02
+3.000e-02
+1.500e-02
+0.000e+00

Figure 6.15 Bulge test damage contour (isotropic damage model).

In this test, damage localization is mainly dependent on the plastic strain rate, as seen by the similarity between damage and equivalent plastic strain distributions. Moreover, the effect of stress triaxiality on damage localization site is negligible since such stress ratio remains almost constant during the application of hydraulic pressure and has the same value in the whole bulge area, as presented in Figure 6.16.

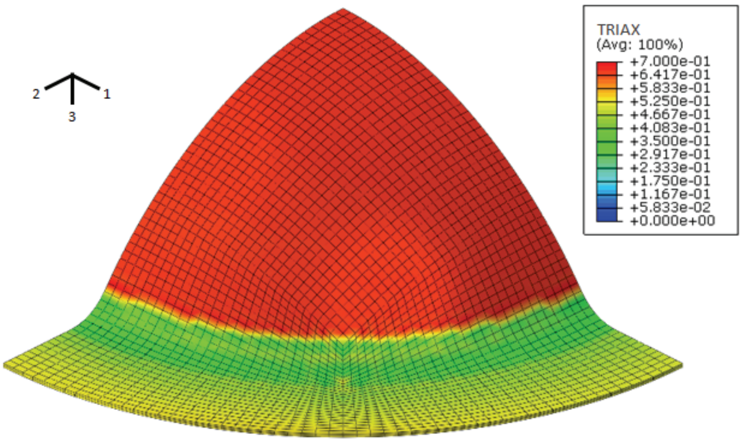
2
1
3
TRIAX
(Avg: 100%)
+7.000e-01
+6.417e-01
+5.833e-01
+5.250e-01
+4.667e-01
+4.083e-01
+3.500e-01
+2.917e-01
+2.333e-01
+1.750e-01
+1.167e-01
+5.833e-02
+0.000e+00

Figure 6.16 Bulge test stress triaxiality contour (isotropic damage model).

Due to damage growth, a decrease in equivalent stress value is observed in the bulge center, Figure 6.17. This reduction in the flow stress, reflecting material strength degradation, endorses the localization of more plastic deformation in this weakened area. Higher plastic strain rate leads to a higher damage growth and corresponding decrease in flow stress. This is in straight contradiction with the plastic straining consequence which leads to a hardened behaviour in metallic materials, but in straight agreement with the concurrent effect between damage growth and hardening.

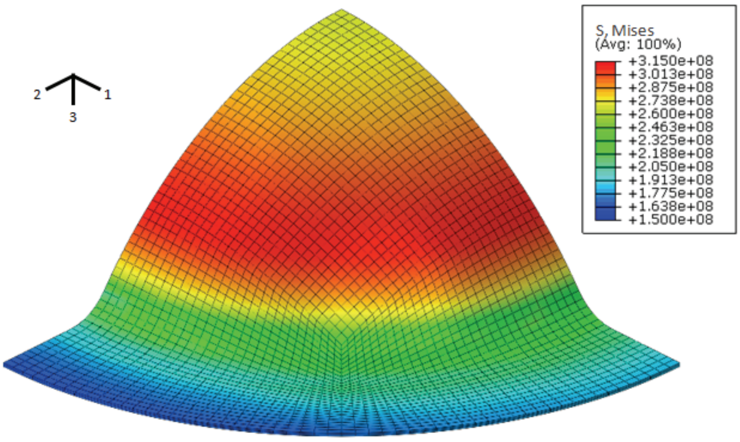

Figure 6.17 Bulge test equivalent stress contour (isotropic damage model).

A comparison of damage evolution with equivalent plastic strain between tensile and bulge test, for the element located in the center of the specimens that fails during loading, is presented in Figure 6.18.

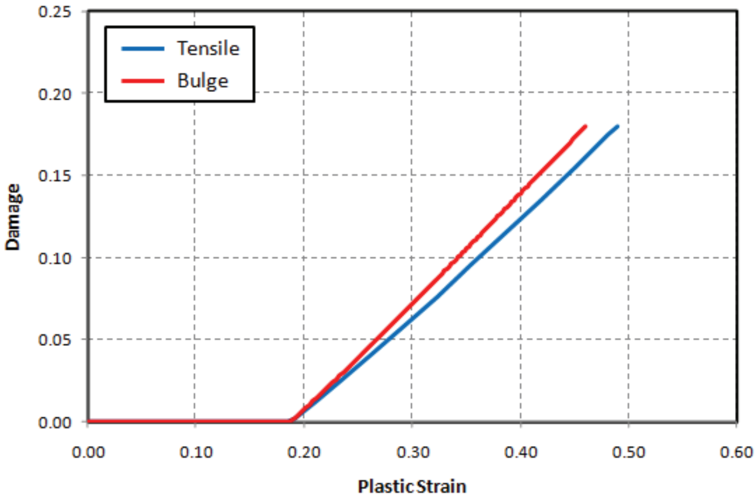

Figure 6.18 Damage evolution comparison between tensile and bulge tests (isotropic damage model).

As can be seen, a higher damage growth is noticed for the bulge test case. The reason is intimately related with the higher stress triaxiality attained by the imposed biaxial strain state that has a direct effect on damage growth and its localization. Under such loading condition, material fails for a lower equivalent plastic strain value than the one predicted for a uniaxial tensile case. This difference reinforces the idea that a failure criterion based only in a critical plastic strain value may be unsuccessful to deliver valid failure predictions and that stress triaxiality effect must be included in material failure calculations.

The same numerical model was used to perform a simulation with the consideration of a distinctive damage evolution, i.e., using the anisotropic damage model. It can be seen in Figure 6.19 that anisotropic damage model also calculates maximum equivalent plastic strain in bulge pole, in accordance with experimental observations.

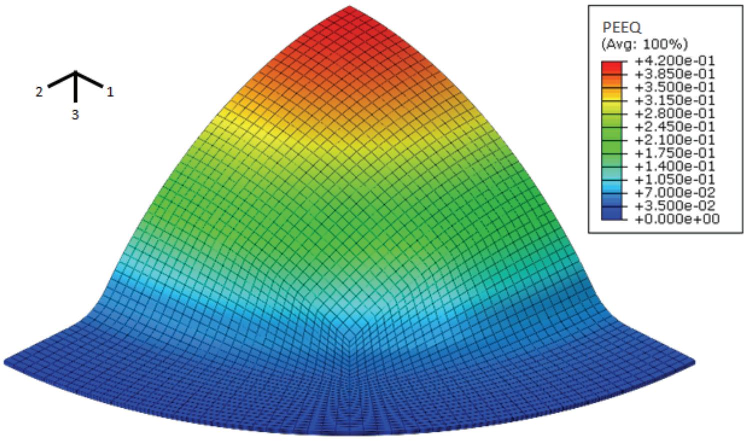

Figure 6.19 Bulge test equivalent plastic strain contour (anisotropic damage model).

For the case of anisotropic damage evolution, failure is assumed to occur when the critical damage value (defined for the anisotropic model) is reached by the maximum value attained in principal damage directions. The obtained damage distributions prior to failure are presented in Figure 6.20. For the bulge test case, damage component along thickness direction is the responsible component for the activation of the failure criterion. During bulging, a biaxial strain state is established on the sheet and a significant reduction in thickness direction is observed. The plastic strain rate achieved in this direction is, therefore, higher than the equivalent rates attained in sheet plane directions, which, according to anisotropic damage evolution law, leads to a damage growth rate also higher in the thickness direction. This damage rate difference is especially important in the case of aluminium alloys due to the fact that they usually present anisotropy coefficients lower than one, which means that forming mainly occurs through a reduction of sheet thickness, and, therefore, a higher deformation rate will be imposed in the thickness direction during biaxial stretching.

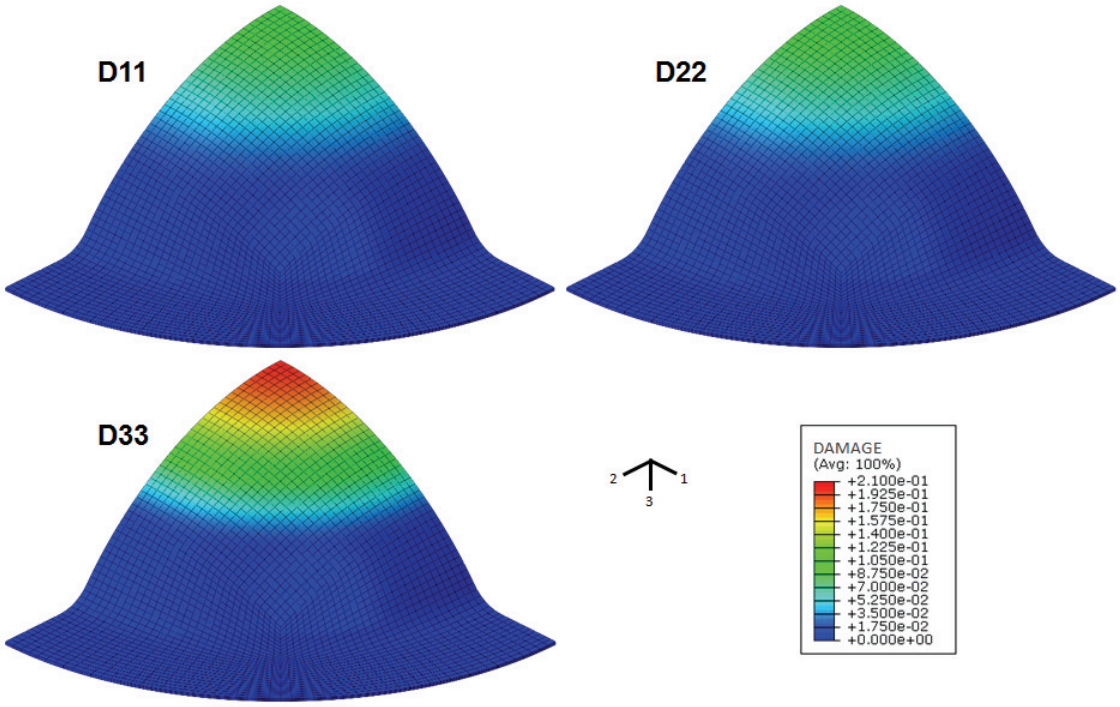
D11
D22
D33
2
1
3
DAMAGE
(Avg: 100%)
+2.100e-01
+1.925e-01
+1.750e-01
+1.575e-01
+1.400e-01
+1.225e-01
+1.050e-01
+8.750e-02
+7.000e-02
+5.250e-02
+3.500e-02
+1.750e-02
+0.000e+00

Figure 6.20 Bulge test damage contour (anisotropic damage model).

The difference between damage components evolution in the anisotropic damage model and a comparison with isotropic damage evolution is provided in Figure 6.21.

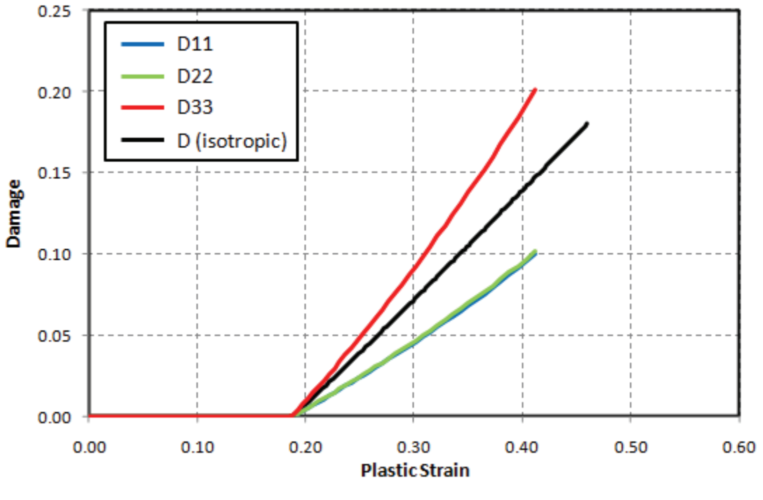

Figure 6.21 Bulge test damage evolution comparison between isotropic and anisotropic damage models.

It is clear from Figure 6.21 that the damage component along thickness direction D_{33} has the most evident evolution and early reaches critical damage for an equivalent plastic strain of 0.42. Concerning in-plane damage values, D_{11} and D_{22}, no significant difference in damage growth is seen, which is in accordance with the small variation of anisotropic coefficients observed for this alloy [LPMTM 2001]. But, despite the same triaxiality level attained by the isotropic and anisotropic damage implementations in the bulged area, failure is detected earlier for the case with the consideration of a distinct evolution of damage in different directions. The explanation is clear in Figure 6.21. A more accentuated damage growth of the critical damage component D_{33} is observed when compared to the isotropic damage value growth due to the fact that anisotropic coefficients lower than one promote deformation in thickness direction.

6.3 U shape geometry

This benchmark corresponds to one of eight selected benchmarks used in a research work, part of the international project 3DS, Digital Die Design System [Col 2002]. One of the goals of the project was the improvement and validation of the ability of numerical codes to predict sheet metal forming behaviour as well as the final stamped geometry after springback. This particular benchmark is prone to develop 2D springback due to the bending / unbending over die radius that promotes a stress differential along thickness direction. Although failure behaviour was not planned for any benchmark, some coupling of experimental conditions and material were producing components with breakage.

6.3.1 Experimental failure

Experimental failure in this component is observed for a punch displacement of 36.4 mm, with an applied initial blank holder force of 300 kN, using the aluminium alloy 5182-O. However, in a total set of 5 experimental testings, failure did not occur for one of the components, as can be observed in Figure 6.22a. This indicates that this holding condition may represent the upper limit for the maximum applicable blank holder force for this material and geometry.

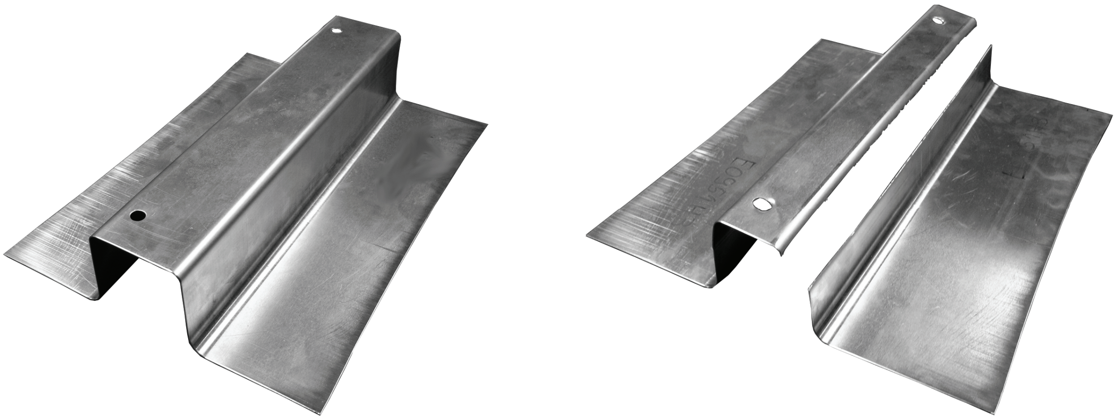

Figure 6.22 Experimental part without rupture (left) and failed part (right) (AA 5182-O, initial blank holder force 300kN).

6.3.2 Numerical modelling

Blank was modelled with a double layer of eight-noded solid elements. Due to symmetry and its intrinsic bidimensional characteristic, a reduced model was considered in order to reduce calculation time. The blank mesh was reduced to a single strip of elements along the perpendicular direction to the U channel. Naturally, appropriate boundary conditions were applied and holding force was adjusted to the reduced sheet surface. Concerning tools, rigid analytical surfaces were considered to model the active tool surfaces and interaction between sheet and tools has been performed with friction. A constant friction coefficient was adopted for all the surfaces of the different tool active parts, namely for the blank holder and die surfaces, die radius and punch. Regarding the blank holder force evolution with punch displacement, it was assumed a linear evolution up to a total punch displacement of 60 mm given by the relation:

$$F_{60} = 1.32 F_{IBHF} \tag{6.38}$$

where F_{60} is the blank holder force attained for 60 mm punch displacement and F_{IBHF} is the imposed initial blank holder force. Main numerical conditions are summarized in Table 6.7. Material properties are given in Table 6.1 and damage law parameters in Table 6.3. Rolling direction was considered to be along the U channel direction.

Table 6.7 U shape geometry numerical conditions.

Blank	
Element type	Reduced integration solid (8-noded)
Element size [mm]	1.67x5.0x0.5
Number of layers	2
Number of elements	178
Tools	
Tool type	Rigid analytical surface
Friction coefficient	0.1 / 0.18
Process parameters	
Punch travel [mm]	60
Punch speed [m/s]	5
Initial blank holder force [kN]	90 / 300

6.3.3 Results and discussion

In order to validate the applied numerical conditions and by the fact that only experimental results for a initial blank holder force of 90 kN are available, additional simulations were performed using this lower initial blank holder force. For this condition, a springback calculation stage was also considered. Tools were removed and nodes were restrained to inhibit rigid body motion. In this stage, an implicit finite element solution strategy has been used (ABAQUS/Standard). Results show that applied numerical conditions during stamping stage and implicit calculation of springback allow an accurate modelling of the process, demonstrated by the similarity between the obtained experimental and numerical shapes, Figure 6.23. A comparison between experimental and numerical section profiles is also presented in Figure 6.24.

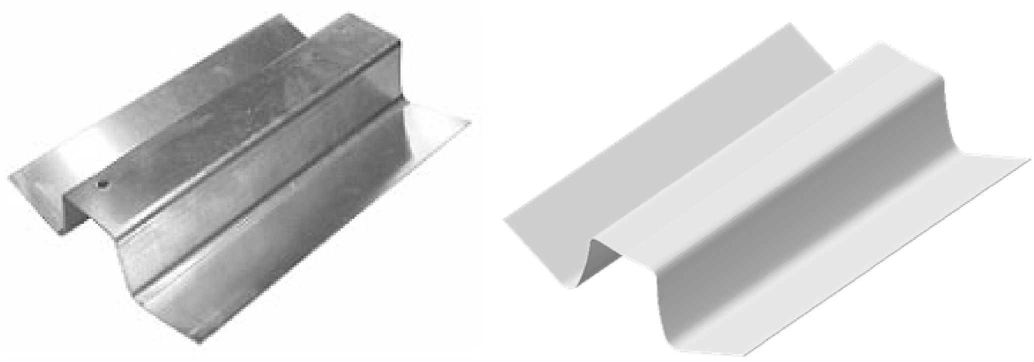

Figure 6.23 U shape geometry experimental and numerical shapes (initial blank holder force 90 kN).

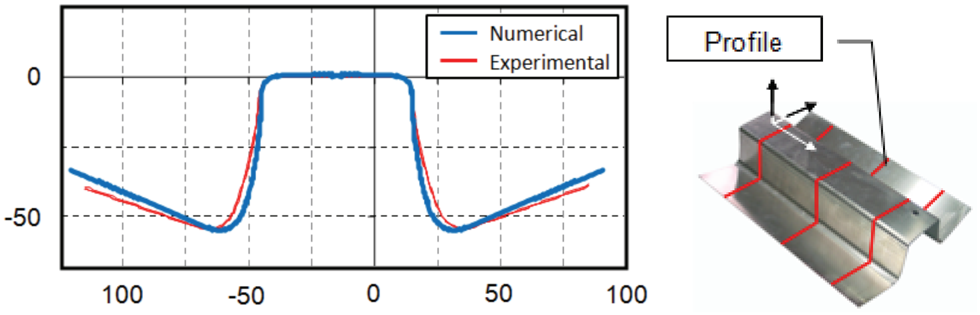

Figure 6.24 U shape geometry experimental and numerical profiles (initial blank holder force 90 kN).

For the 90 kN blank holder force condition, no damage evolution is observed in the part since equivalent plastic strain remains very low, Figure 6.25, bellow damage threshold value ε_D^p. It is important to understand the location of the maximum value of plastic strain. During forming under this lower blank holder force condition, deformation will be restricted to the vertical wall. Almost no deformation occurs in the top and flange areas of the part. Before bending / unbending, flange material does not experiences any previous straining during sliding between blank holder and die surfaces since the lower blank holder force allows the sheet to slide without any stretching. At the beginning of punch movement, material located near punch radius undergoes a bending over a 5 mm radius and material near die radius suffers a bending over a 10 mm radius. This initial bending over the smaller radius of the punch is sufficient to promote material hardening up to 0.1 plastic strain. During forming, this hardened area is the principal location where the punch interacts with blank and will support all the force required for the bending over die radius and unbending during sliding in the vertical wall of the flange material.

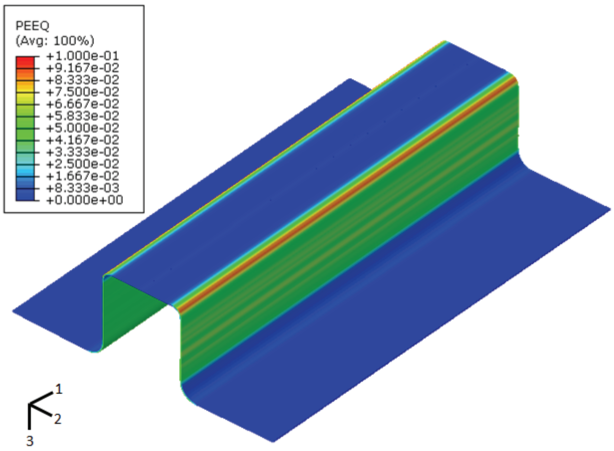
PEEQ
(Avg: 100%)
+1.000e-01
+9.167e-02
+8.333e-02
+7.500e-02
+6.667e-02
+5.833e-02
+5.000e-02
+4.167e-02
+3.333e-02
+2.500e-02
+1.667e-02
+8.333e-03
+0.000e+00
1
2
3

Figure 6.25 U shape geometry equivalent plastic strain contour (initial blank holder force 90 kN).

Another observation is concerned with deformation paths followed by the points that belong to the internal and external fibres. Internal and external points initially follow opposite directions. The internal point undergoes a positive deformation during bending in die radius and suffers a negative deformation during unbending and sliding in the vertical wall. The external point, being subjected to a compressive stress state in the die radius, initially undergoes a negative deformation during bending changing to a positive one during unbending, always following a strain path near plane strain condition. Although final equivalent plastic strain is very close for both points, the difference in the deformation history leads to a dissimilar stress state, Figure 6.26, responsible for the verified springback behaviour.

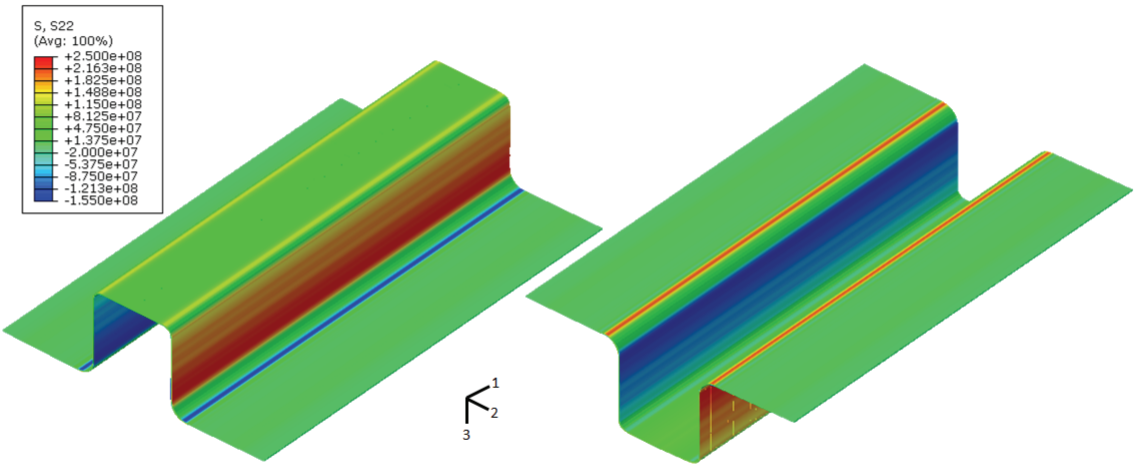
S, S22
(Avg: 100%)
+2.500e+08
+2.163e+08
+1.825e+08
+1.488e+08
+1.150e+08
+8.125e+07
+4.750e+07
+1.375e+07
-2.000e+07
-5.375e+07
-8.750e+07
-1.213e+08
-1.550e+08
1
2
3

Figure 6.26 U shape geometry stress contour (initial blank holder force 90 kN).

For the higher holding condition (300 kN), there is a similarity in the evolution of deformation path followed by internal and external points. The higher initial blank holder force promotes the deformation of the sheet material even during sliding between the die and blank holder surfaces, by applying a plane strain state to sheet to all section points along thickness direction. This effect is visible by measuring the final flange length of the part. Experimentally, there is an increase of about 10 mm in the flange length for the 300 kN holding force (final length for 90 kN is about 58 mm). This experimental result is also verified numerically, existing a closeness with experimental values. The bending / unbending over die radius and vertical wall does not change the previous deformation path and internal and external points reach almost the same point in the principal strain space. This equality in deformation history leads to an similar final stress state, Figure 6.27, justifying the almost non-existent springback in this rail, Figure 6.22a, under this holding condition.

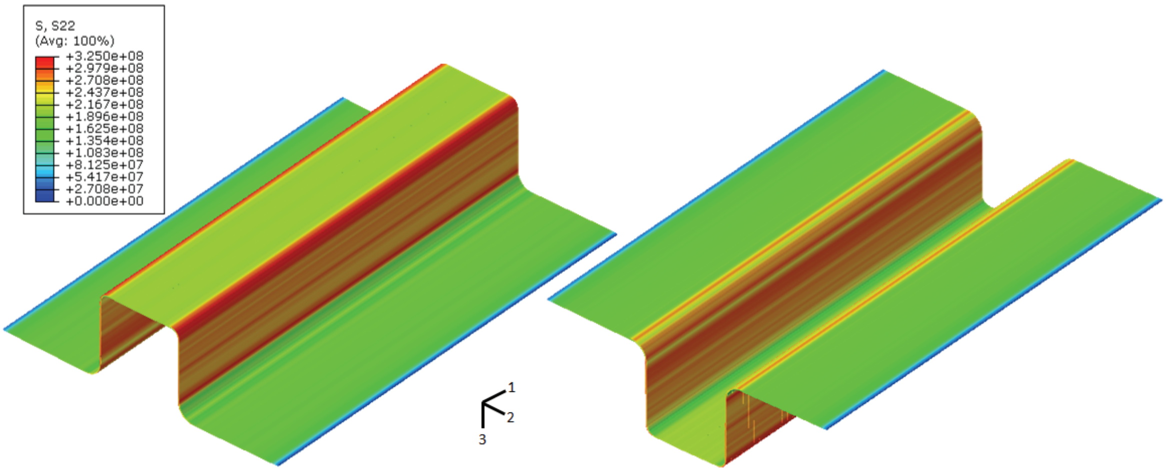
S, S22
(Avg: 100%)
+3.250e+08
+2.979e+08
+2.708e+08
+2.437e+08
+2.167e+08
+1.896e+08
+1.625e+08
+1.354e+08
+1.083e+08
+8.125e+07
+5.417e+07
+2.708e+07
+0.000e+00
1
2
3

Figure 6.27 U shape geometry stress contour (initial blank holder force 300 kN).

Under this higher blank holder force, a high plastic strain rate is reached near the punch radius, Figure 6.28.

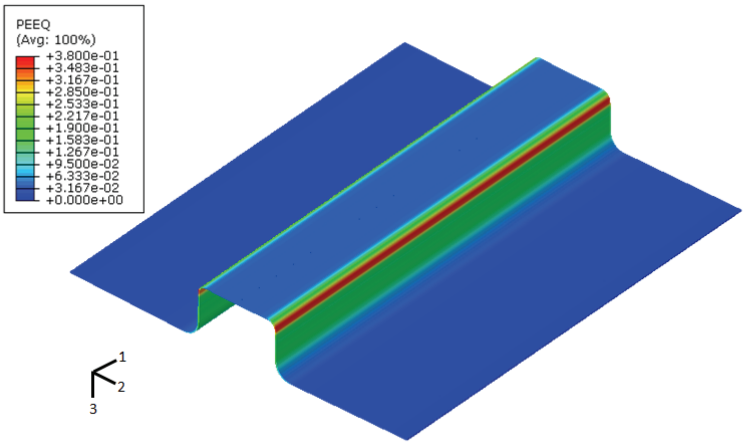
PEEQ
(Avg: 100%)
+3.800e-01
+3.483e-01
+3.167e-01
+2.850e-01
+2.533e-01
+2.217e-01
+1.900e-01
+1.583e-01
+1.267e-01
+9.500e-02
+6.333e-02
+3.167e-02
+0.000e+00
1
2
3

Figure 6.28 U shape geometry equivalent plastic strain contour (initial blank holder force 300 kN).

Without damage evolution, this high plastic strain would lead to an increased strength of the material, moving straining to other regions in the vertical wall. But, due to the concurrent effects of damage and hardening, this area will be softened by the increase of damage and prone to have more deformation due to the decrease in material strength. As a consequence of this plastic localization, damage will grow faster in this weakened zone, rapidly achieving the critical damage value and failure, Figure 6.29. Failure is estimated for a critical punch displacement of 37.5 mm, which is very close to the experimental value (36.4 mm).

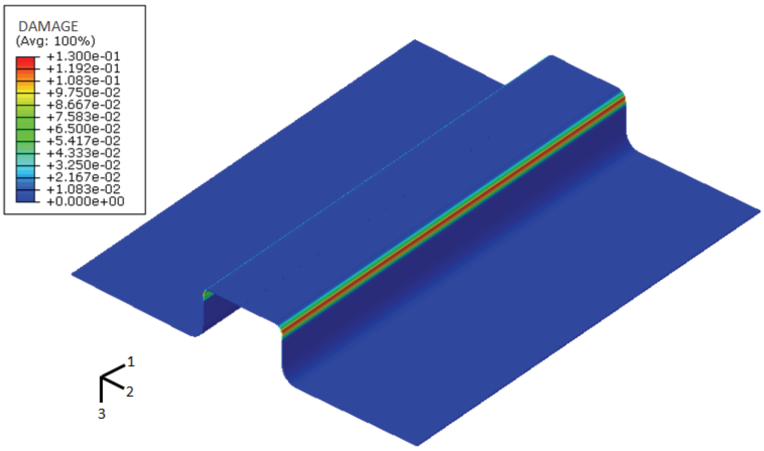

Figure 6.29 U shape geometry damage contour (initial blank holder force 300 kN).

Failure calculation in this 2D bending is extremely dependent on the establish lubrication condition between sheet and blank holder and die surfaces. The reported experimental part that did not fail despite the severe imposed experimental conditions in terms of blank holder force may be related with a more efficient established lubrication condition. To assess and understand this occurrence, a numerical study was performed concerning the variation of the friction coefficient, in order to simulate different lubrication conditions. Corresponding predicted critical punch displacements to failure are presented in Figure 6.30.

It is possible to verify that friction coefficient has a huge influence on the predicted punch displacement to failure. For friction values lower than 0.16, damage model does not provide any failure occurrence. The equivalent plastic strain reached in the critical area is lower than the required one to initiate damage phenomenon, ε_D^p. Sheet movement during sliding is assisted by the low friction and flange material easily flows into die cavity. The required punch force is small, being only needed a sufficient load to bend the material over die radius. For a friction coefficient value greater or equal to 0.2, failure is predicted for a premature punch displacement near 20 mm. This punch stroke corresponds to the beginning of unbending process of the already bended material, near die radius. These high friction coefficients restrain the sheet movement and higher punch forces are required to overcome such restraint. Since material has difficulty and / or does not flow into the die, deformation remains limited to the critical location (near punch radius) and damage threshold is quickly reached, leading to a fast material degradation and consequent failure. Between these two levels, intermediate values for critical punch displacement are predicted. The most similar critical displacement is obtained for a friction coefficient of 0.18 for which isotropic damage model delivers a critical punch displacement of 37.5 mm.

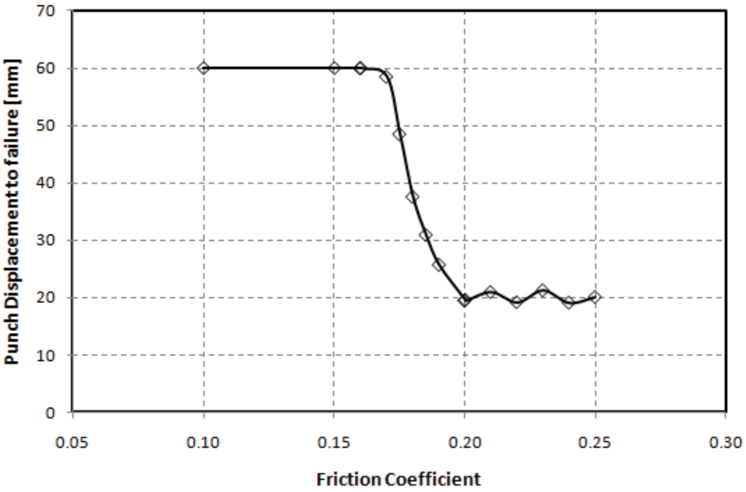

Figure 6.30 Influence of friction coefficient in predicted punch displacement to failure.

Finally, it should be remarked that the consideration of the partial crack closure effect in this component does not lead to significant differences in results, since stamping with a blank holder force of 300 kN is mainly dominated by tensile stresses.

6.4 Warping geometry

This geometry, also studied in the 3DS research project [Col 2002], is prone to develop large wrinkles in the top surface (‘wrinkling’ defect) due to the curvature along the longitudinal direction that promote the appearance of compressive forces responsible for the wrinkling behaviour. Also, 2D springback defect can be obtained in this part due to the bending / unbending over die radius that creates a stress state differential along thickness in the vertical wall and thus flange region assumes a non-planar shape. As for the U channel, the main purpose of this part was to model the above-mentioned typical forming defects. But, some couplings experimental conditions / material have produced failed components.

6.4.1 Experimental failure

In this geometry, failure was experimentally experienced for a premature punch displacement of 15 mm using the aluminium alloy 5182-O, with the application of a blank holder force of 200 kN. However, using a holding force of 152 kN, the component was successfully stamped [Kazama 2001], achieving the predefined draw depth of 60 mm, as can be observed in Figure 6.31a. It is interesting to observe that the wrinkle in the top almost vanish when a blank holder force of 152 kN is used.

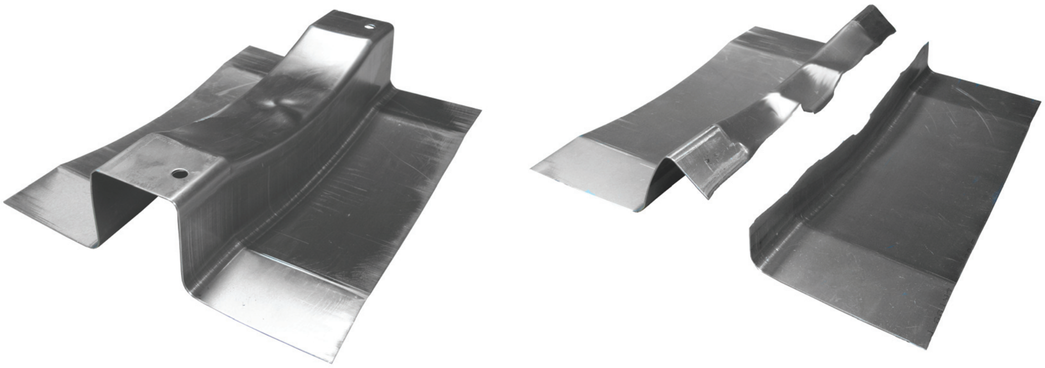

Figure 6.31 Experimental part with 152 kN holding force (left) and failed part with a holding force of 200 kN (right), AA5182-O.

6.4.2 Numerical modelling

Blank was modelled with a structured mesh using a double layer of eight-noded solid elements, Figure 6.32. Due to symmetry over two axes, only one quarter of the geometry was considered and appropriate symmetry boundary conditions were applied in the relevant edges. A total number of 5000 reduced integration linear brick elements were used in the discretization of the blank amounting to a total of 7803 nodes. Concerning tools, rigid elements were considered to model the active tool surfaces and interaction between sheet and tools has been performed with friction. A constant friction coefficient of 0.1 was used for the 90 kN holding force and a coefficient of 0.18 was considered for the 200 kN blank holder force. The blank holder force evolution was considered to be given by Equation (6.38). Parameters adopted in the numerical analysis are listed in Table 6.8. Rolling direction is assumed to be along the channel direction (1-axis in Figure 6.32).

6.4.3 Results and discussion

As for the U shape geometry, an initial blank holder force of 90 kN was also considered to validate applied numerical conditions. Using this holding force, a large wrinkle develops in the top of the part due to the compressive stress state in the center of the curved section, Figure 6.33. A comparison between experimental and numerical profiles for a longitudinal section is presented in Figure 6.34. A similar shape for the wrinkle is obtained by the numerical simulation which confirms the adequacy of applied numerical conditions.

Table 6.8 Warping geometry numerical conditions.

Blank	
Element type	Reduced integration solid (8-noded)
Element size [mm]	3x3x0.5
Number of layers	2
Number of elements	5000
Tools	
Element type	Rigid elements
Elements in radii	12
Friction coefficient	0.1 / 0.18
Process parameters	
Punch travel [mm]	60
Punch speed [m/s]	5
Initial blank holder force [kN]	90 / 200

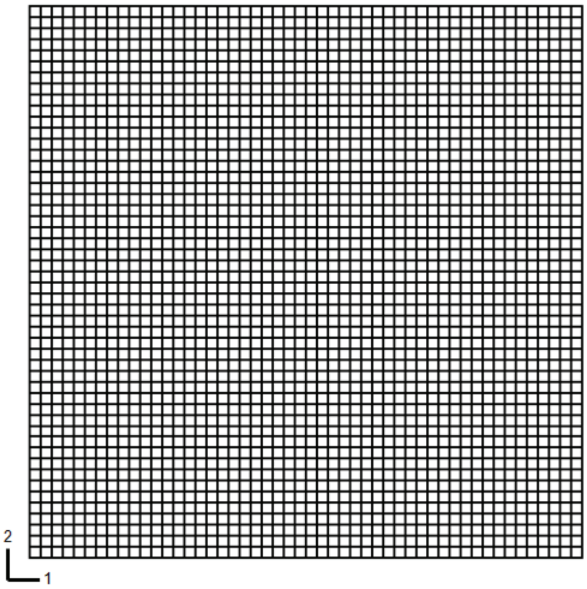

Figure 6.32 Adopted numerical mesh for warping geometry.

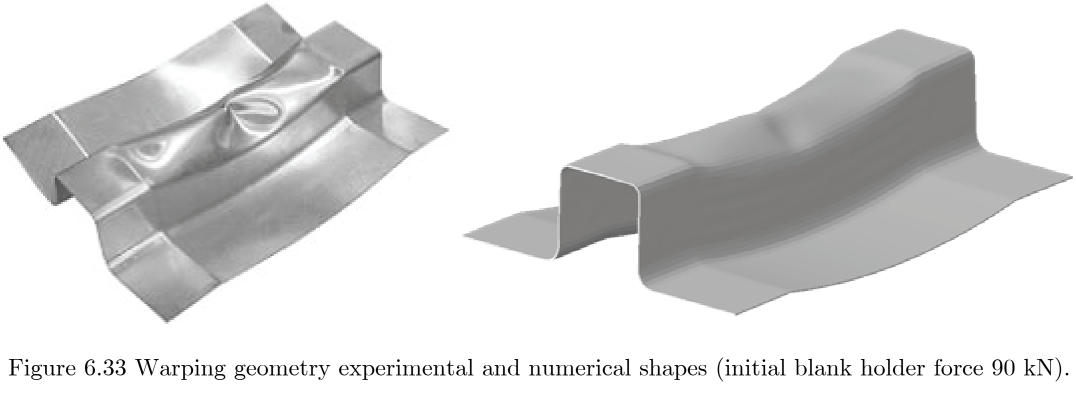

Figure 6.33 Warping geometry experimental and numerical shapes (initial blank holder force 90 kN).

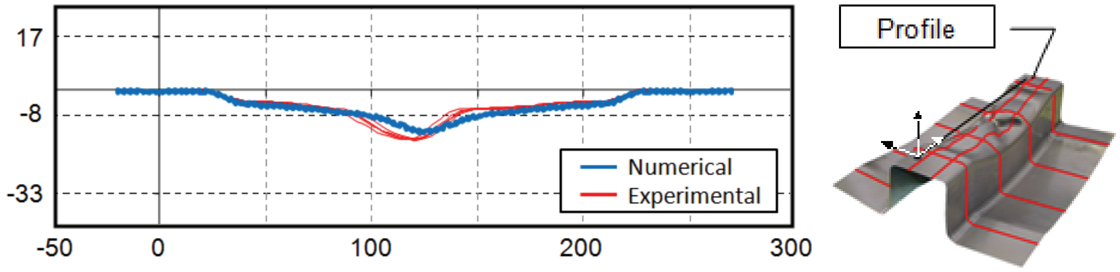

Figure 6.34 Warping geometry experimental and numerical longitudinal profiles (initial blank holder force 90 kN).

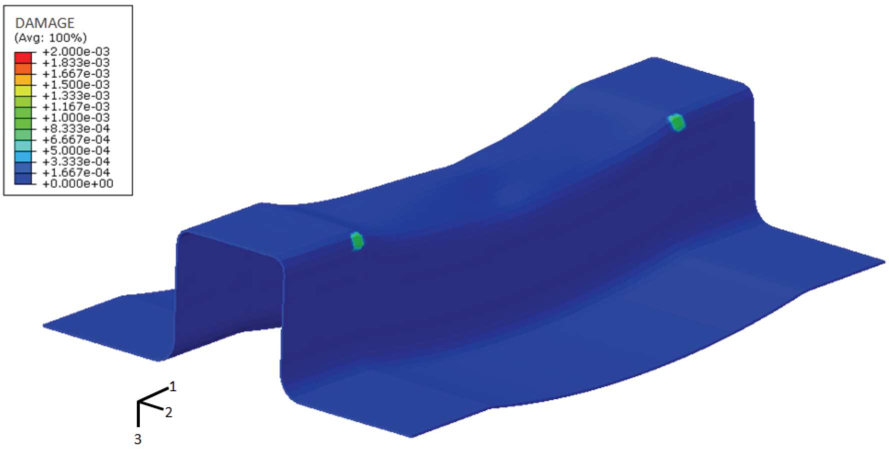
DAMAGE
(Avg: 100%)
+2.000e-03
+1.833e-03
+1.667e-03
+1.500e-03
+1.333e-03
+1.167e-03
+1.000e-03
+8.333e-04
+6.667e-04
+5.000e-04
+3.333e-04
+1.667e-04
+0.000e+00
1
2
3

Figure 6.35 Warping geometry damage contour (initial blank holder force 90 kN).

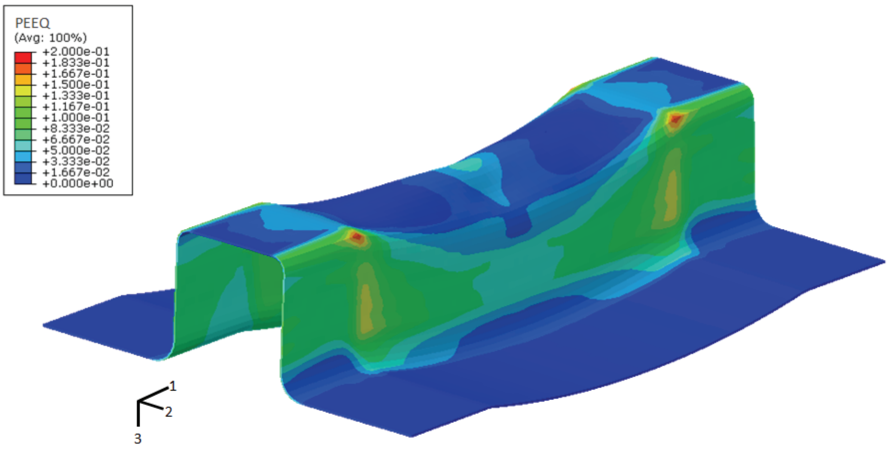
PEEQ
(Avg: 100%)
+2.000e-01
+1.833e-01
+1.667e-01
+1.500e-01
+1.333e-01
+1.167e-01
+1.000e-01
+8.333e-02
+6.667e-02
+5.000e-02
+3.333e-02
+1.667e-02
+0.000e+00
1
2
3

Figure 6.36 Warping geometry equivalent plastic strain contour (initial blank holder force 90 kN).

Despite the experimental successful stampings, a residual damage evolution is also calculated for this lower holding force (90kN). It is limited to punch radius region, near the fillet radius between the top and the curved section. In this area, equivalent plastic strain attains a value greater than damage threshold, Figure 6.36, and, therefore, damage starts to evolve. But, due to its small value, the calculated damage is not sufficient to have an impact in the mechanical properties degradation.

Using the initial blank holder force for which experimentally failure is experienced, i.e., 200 kN, damage model predicts rupture in the same area where the residual damage evolution is observed for the lower holding force condition, at a punch displacement of 17.67 mm. At this point, it is important to understand the strain path followed by the critical element where macro-crack initiation is predicted. During the holding stage, only the material located near the fillet radius between the flat and curved surfaces of the die suffers plastic straining. After this stage, punch starts to move towards the blank, already with a curved shape given by the blank holder and die curved surfaces, and the first contact between the punch and blank is establish in the critical area, where failure is predicted. The outer surface of this region is submitted to biaxial stretching along the two principal in-plane axes: a stretching due to the bending over fillet radius and another stretching due to bending over punch radius. Due to an uneven stretching, the material point of this region initially follows a strain path in the stretching zone, different from the equibiaxial stretching. After this initial bending, punch moves forward and the unbending effect of the bended material in the die radius starts to occur. Since the high blank holder force restrains sheet movement in the flange area, a high stress is reached in the initial contact zone along the perpendicular direction to the channel. In the longitudinal direction, a smaller stress is attained since this stress is the result of the effect of perpendicular stretching force due to punch geometry. This change on the stress state also changes the strain path initially followed by the critical element. During this second phase, the material point changes from biaxial stretching to a strain path as shown in Figure 6.37, where the minor in-plane plastic strain component, although remaining positive, is continuously decreasing. This reflects the high tensile force in the perpendicular direction to the channel in order to force sheet sliding.

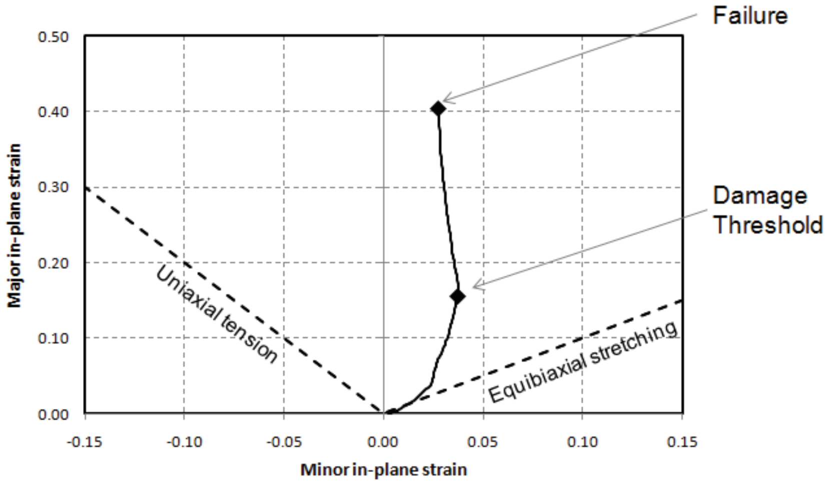

Figure 6.37 Strain path evolution of critical element.

This strain path change undergone by the critical material has almost no effect on damage evolution since it occurs at the same time as damage threshold value is reached. Following the second strain path, plastic strain increases and localizes in the critical zone, with damage also evolving under this deformation path. Due to localization of plastic deformation, critical damage value is rapidly attained and failure is predicted.

Although overcoming the limit of validity of CDM approaches, in this case, the macro-crack propagation is successfully determined by the implemented damage model. As material fails in the punch radius, near the fillet radius between the top and the curved section, elements in this area are eroded from the numerical mesh and failure is gradually predicted for the elements in the punch radius area, propagating the macro-crack towards blank edge, Figure 6.38.

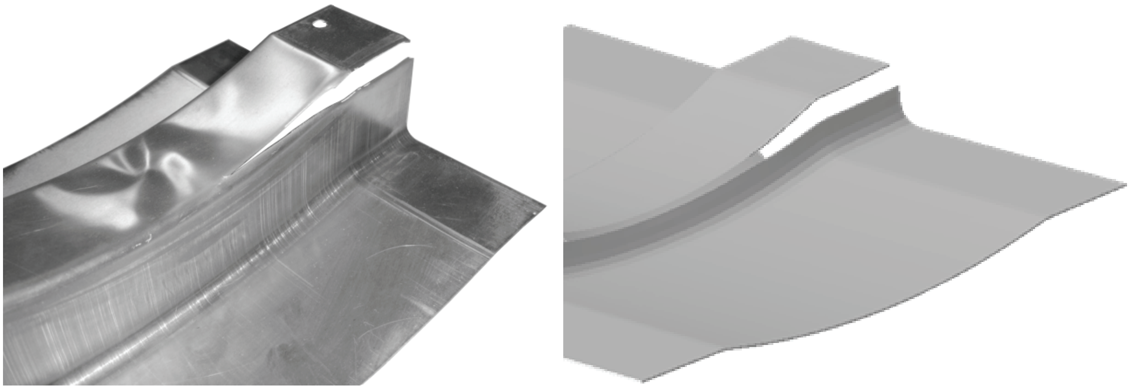

Figure 6.38 Warping geometry numerical and experimental crack evolution.

This numerical behaviour is in accordance with the experimental result. Experimentally, failure also starts in the same critical area as in the numerical simulations and the crack evolves to blank edge along punch radius. After achieving the edge, the crack propagates in the opposite direction, towards the center of the part, as the penny-shaped crack visible in Figure 6.38a shows.

6.5 Axisymmetric cup

This geometry corresponds to an experimental test used to study the anisotropic behaviour of laminated sheets. The tool presented in Figure 6.39 is composed by three main parts, namely a die (diameter 62.5 mm and radius 10 mm), a flat blank holder and a cylindrical punch (diameter 60 mm and radius 5 mm). The blank is circular and has a central hole of 14 mm diameter, used to clamp the blank in the punch ensuring a perfect centering and avoiding any sheet sliding during stamping. Clamping device includes a drawbead in the top of the punch, positioned at 22 mm diameter. Additionally, in the experiments, a circular ring is used between the blank holder and die surfaces, made of the same material as the blank, to limit the blank holder movement in the final phase of the stamping, avoiding the appearance of defects in the blank edge due to the concentration of the blank holder force in this area.

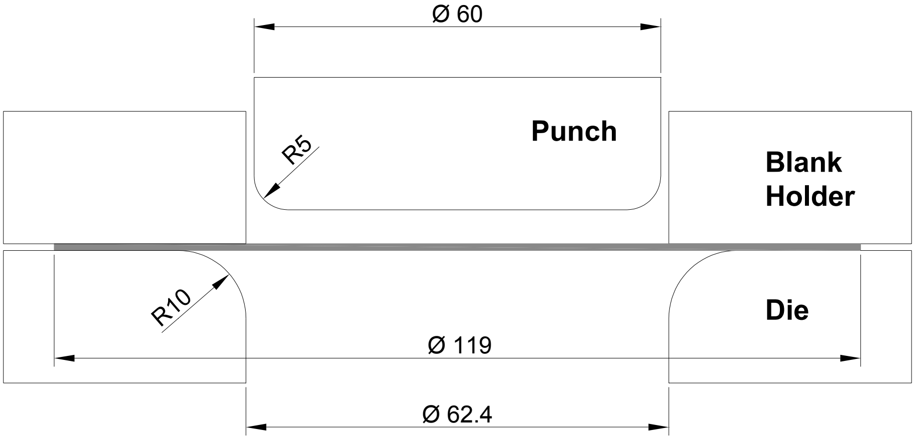

Figure 6.39 Axisymmetric cup tool geometry (in mm).

6.5.1 Experimental failure

Experimental tests [Duarte 2002] have shown that successful stampings are obtained with an initial blank size of 114 mm diameter for the aluminium alloy 5182-O. Using a larger blank (119 mm diameter), successful drawing was only obtained when a high lubrication condition is established, Figure 6.40a. When a poor lubrication is applied to blank, failure occurs in the sidewall, near punch radius, as shown in Figure 6.40b.

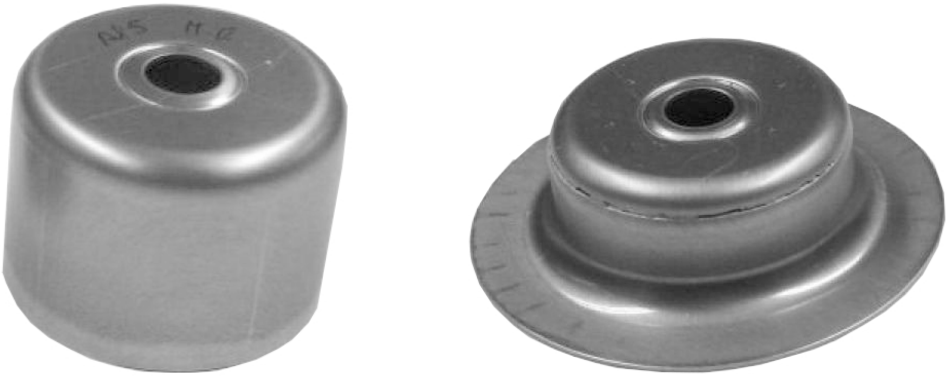

Figure 6.40 Experimental geometry: fully drawn and failure.

6.5.2 Numerical modelling

Due to orthotropic symmetry, only a quarter of the blank domain was modelled by using a double layer of eight-noded elements, in a total of 1500 elements. Tool surfaces were considered completely rigid and were modelled by triangular rigid elements. A constant blank holder force of 40 kN was set and a constant fiction coefficient was also considered to model tribological conditions established between blank and tool active parts. The low lubrication and high lubrication conditions were modelled by applying a low (0.05) and a high friction coefficient (0.2), respectively. Concerning material modelling, hardening and anisotropy parameters are presented in Table 6.1 and isotropic damage model parameters are presented in Table 6.3. Main applied numerical conditions are presented in Table 6.9. Rolling direction is assumed to be along 1-axis, Figure 6.41.

Table 6.9 Axisymmetric cup numerical conditions.

Blank	
Element type	Reduced integration solid (8-noded)
Element size [mm]	3.0x2.0x0.5 (max)
Number of layers	2
Number of elements	1500
Tools	
Element type	Rigid elements
Elements in radii	12
Friction coefficient	0.05 / 0.2
Process parameters	
Punch travel [mm]	60
Punch speed [m/s]	5
Blank holder force [kN]	40

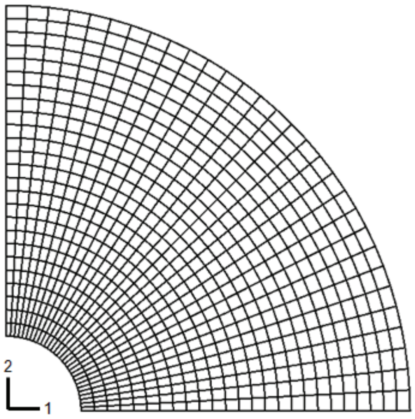

Figure 6.41 Adopted mesh for axisymmetric cup.

6.5.3 Results and discussion

Deformation in this geometry is mainly restricted to the flange area of the blank. No deformation is supposed to occur in the bottom of the cup. But, since a clamping device is used, a negligible deformation can be calculated in the bottom of the cup. During forming, material is bended over die radius and the flange material is subjected to two loadings: a stretching in the radial direction and a compression in the tangential direction. The effect of these large compressive forces is to promote thickness increase and resulting wrinkle development in the flange area. This wrinkling behaviour is prevented if a sufficient blank holder force is used. After bending in die radius, material is straightened during sidewall sliding. This straightening action requires a high punch force to unbend the already hardened material due to the bending over die radius. If material does not flow from the flange into die cavity due to high blank holder force and / or reduced sliding, a higher punch force is achieved and rupture occurs. In this case, the sidewall zone, near punch radius, is going to be the most stressed region since contact with blank is preferentially made in this area. As a result, an excessive thinning occurs in this zone and failure takes place.

Numerical simulations of the high lubrication condition were carried out using the partially coupled isotropic damage model. Three different crack closure parameters were used in order to study its influence on failure predictions: $h_C = 0$ corresponding to a full closure effect, $h_C = 0.2$ corresponding to a partial closure effect using the typical value observed in experiments [Lemaitre 1996] and $h_C = 1$ corresponding to the case where no closure effect is considered. Additionally, the same numerical model was also simulated with the fully coupled algorithm in order to compare its results with the ones obtained by the partially coupled algorithm, with $h_C = 1$.

In experiments, the cup was completely drawn for the high lubrication condition, numerically modelled by applying a low friction coefficient. In this case, a drawing ratio of almost 2 was reached. But, although in experiments no failure has occurred in this condition, failure was numerically detected when using the fully coupled algorithm and the partially coupled algorithm with no closure effect consideration. In both these cases, material located in blank edge, in the neighbourhood of rolling direction, failed during bending over die radius, for a punch displacement of about 37mm. A comparison between the equivalent plastic strains obtained by the four approaches at a punch displacement of 37 mm is presented in Figure 6.42.

As can be noticed, no difference is found in the calculated plastic strain field when comparing different approaches. In all cases, plastic flow does not follow an axisymmetric distribution due to the privileged directions imposed by the orthotropic plasticity. Major plastic strain value is attained in the area located near the cup ear. This material in this area is located far from the center of the cup and is subjected to a larger tangential compressive stress during sliding between die and blank holder surfaces and, therefore, an increase of thickness is observed, Figure 6.43a.

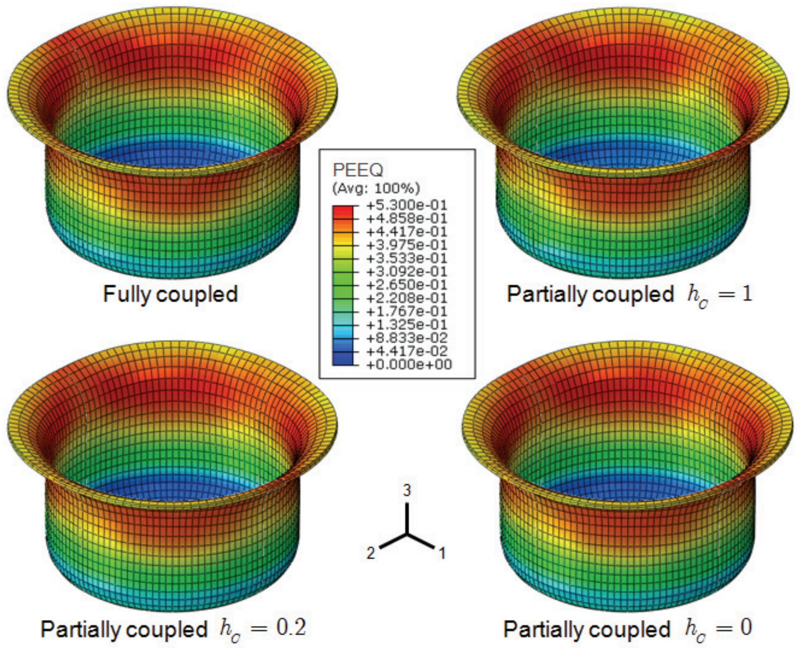
Fully coupled
PEEQ
(Avg: 100%)
+5.300e-01
+4.858e-01
+4.417e-01
+3.975e-01
+3.533e-01
+3.092e-01
+2.650e-01
+2.208e-01
+1.767e-01
+1.325e-01
+8.833e-02
+4.417e-02
+0.000e+00
Partially coupled $h_c = 1$
3
2
1
Partially coupled $h_c = 0.2$
Partially coupled $h_c = 0$

Figure 6.42 Axisymmetric cup equivalent plastic strain contour (high lubrication condition).

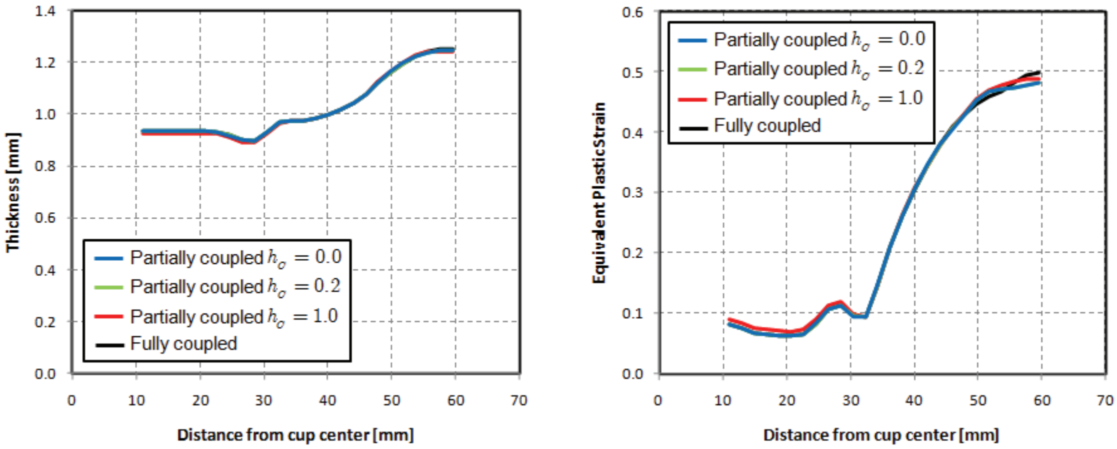

Figure 6.43 Thickness and equivalent plastic strain vs. initial distance from cup center for rolling direction section (high lubrication condition).

The upper limit of this thickness increase is restricted by the gap between punch and die. As can be seen in Figure 6.43a, a plateau at 1.25 mm is observed in the thickness value for the elements originally located near the outer diameter of the blank. This indicates that ironing of cup borders occurs during deep drawing.

Although a similar behaviour is observed for equivalent plastic strain distribution, a distinctive trend is seen for the damage value distribution. The corresponding comparison between the four approaches is presented in Figure 6.44.

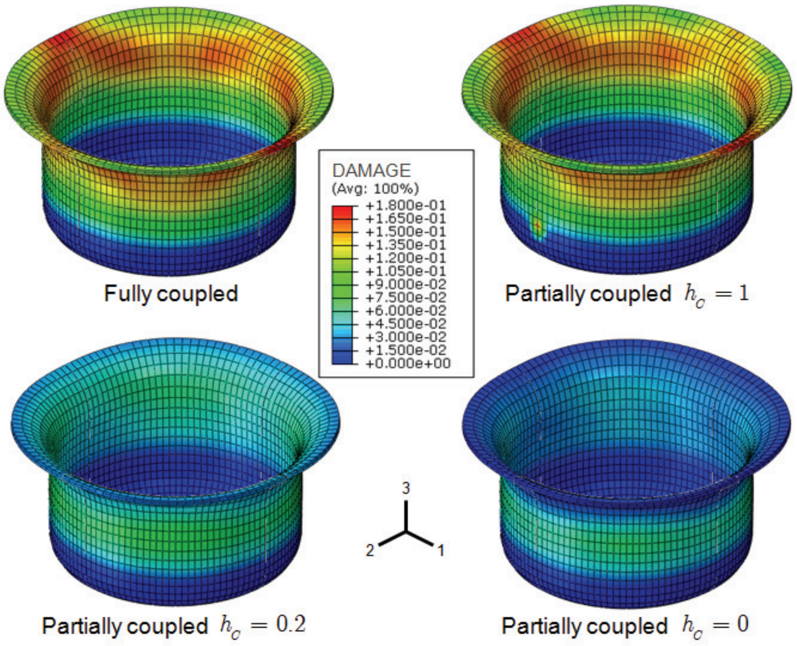
DAMAGE
(Avg: 100%)
+1.800e-01
+1.650e-01
+1.500e-01
+1.350e-01
+1.200e-01
+1.050e-01
+9.000e-02
+7.500e-02
+6.000e-02
+4.500e-02
+3.000e-02
+1.500e-02
+0.000e+00
Fully coupled
Partially coupled $h_c = 1$
Partially coupled $h_c = 0.2$
Partially coupled $h_c = 0$
3
2
1

Figure 6.44 Axisymmetric cup damage contours (high lubrication condition).

For the fully coupled and partially coupled (no tension / compression distinction, $h_C = 1$) algorithms, damage distribution follows the equivalent plastic strain distribution trend. Maximum value of damage variable is also attained in the cup borders and a similar non axisymmetric distribution is calculated. In both cases, damage distribution is mainly dominated by the calculated plastic strain ratio distribution. When unilateral effects are considered, either a full ($h_C = 0$) or a partial closure effect ($h_C = 0.2$), a different distribution of damage values are obtained. Higher values are attained in the middle of the vertical wall of the cup, as shown in Figure 6.45. Despite the same maximum value location, these two algorithms deliver different calculated damage values. Necessarily, this difference is related to the fact that, in the case of the algorithm with full crack closure, no damage growth is calculated during sliding and beginning of bending over die radius due to the negative triaxiality state. However, with a partial closure effect ($h_C = 0.2$), damage grows even during this phase of the deep drawing process, although in a slower mode, in accordance with the adopted crack closure parameter. This difference in damage growth during this phase is visible in Figure 6.45. At a punch displacement of 37 mm, material located at blank edge is undergoing bending over die radius and a null damage value is obtained when a full closure effect is considered.

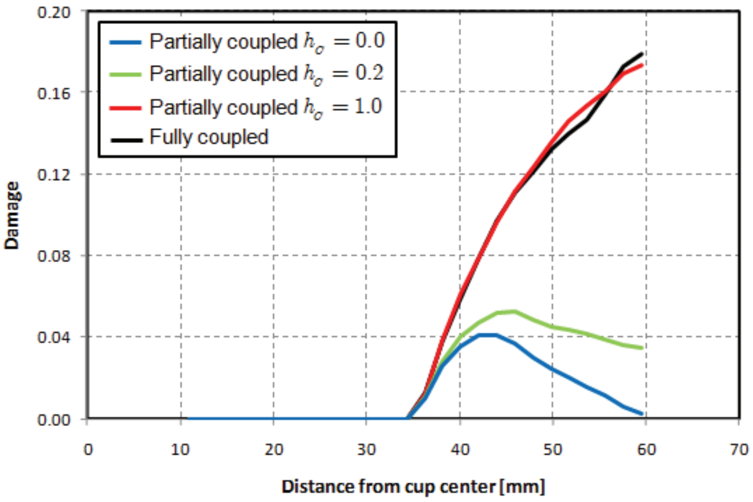

Figure 6.45 Damage vs. initial distance from cup center for rolling direction section (high lubrication condition).

It is also important to note that damage has higher values on the outer surface of the cylindrical cup for models where $0 \leq h_C < 1$, Figure 6.44. During bending over die radius, material in the outer surface is subjected to a compressive stress state that is transferred to positive stress values during unbending in the vertical wall. Once it reaches a positive triaxiality ratio, damage grows without a remarkable influence of the crack closure parameter. In turn, material that will form the inner surface of the cup also suffers a stress state characterized by a negative triaxiality ratio during sliding over blank holder surface that only becomes positive during bending over die radius. During unbending in vertical wall, material presents again a negative triaxiality ratio. Therefore, damage state in the inner surface will be highly dependent on adopted micro-crack closure parameter h_C. If a low or zero value is taken for this parameter, a reduced or no damage growth is calculated during unbending and major contribution to damage state will be given by damage growth calculated during bending over die radius.

The low lubrication condition has also been performed by using the partial closure effect with the three distinct crack closure parameters. A higher friction coefficient was used to model the more severe contact condition. As in experiments, failure is expected to occur near punch shoulder. Equivalent plastic strain contours prior to failure for the four models are presented in Figure 6.46.

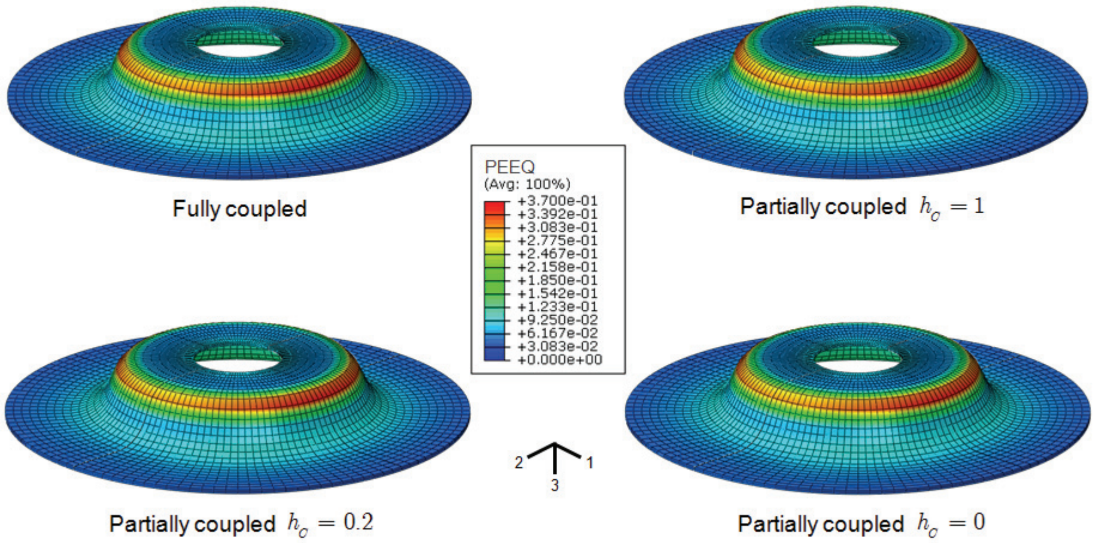
Fully coupled
PEEQ
(Avg: 100%)
+3.700e-01
+3.392e-01
+3.083e-01
+2.775e-01
+2.467e-01
+2.158e-01
+1.850e-01
+1.542e-01
+1.233e-01
+9.250e-02
+6.167e-02
+3.083e-02
+0.000e+00
Partially coupled $h_c = 1$
Partially coupled $h_c = 0.2$
2
1
3
Partially coupled $h_c = 0$

Figure 6.46 Axisymmetric cup equivalent plastic strain contours (low lubrication condition).

As for the high lubrication condition, no remarkable difference is found in the calculated equivalent plastic strain value when comparing different approaches. A non axisymmetric distribution is again obtained and maximum value calculated for the rolling direction (1-direction). For this direction, an excessive thickening is calculated for a distance of 28.5 mm from cup center, Figure 6.47a, and, at the same location, a high value of plastic strain is reached, Figure 6.47b, overcoming damage threshold value.

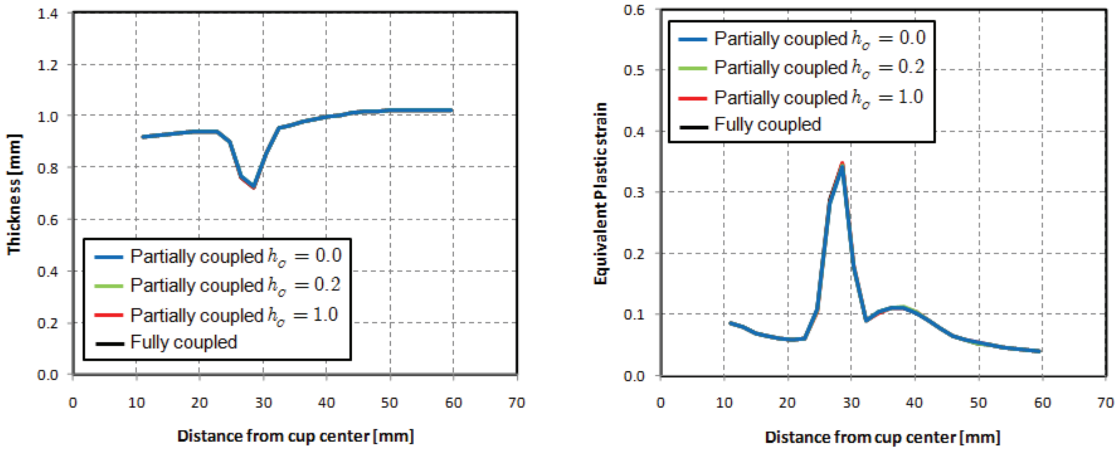

Figure 6.47 Thickness and equivalent plastic strain vs. initial distance from cup center for rolling direction section (low lubrication condition).

But, unlike the high lubrication condition, damage distribution in low lubrication is not affected by the crack closure parameter. Using a higher friction coefficient, all damage algorithms predict failure in the same location as in the experimental setting and similar critical punch displacements up to failure are calculated. Failure is detected for all approaches in the vertical wall, near the bottom of the cup, at a punch displacement of 14 mm, with a deviation of ± 0.02 mm between algorithms. A comparison between damage distributions obtained for the four approaches is presented in Figure 6.48.

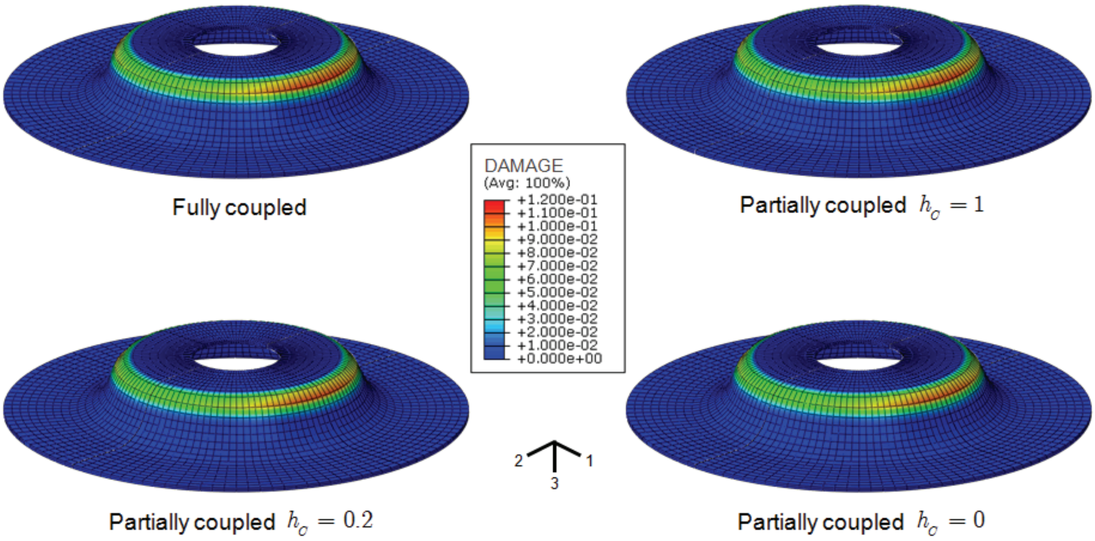
DAMAGE
(Avg: 100%)
+1.200e-01
+1.100e-01
+1.000e-01
+9.000e-02
+8.000e-02
+7.000e-02
+6.000e-02
+5.000e-02
+4.000e-02
+3.000e-02
+2.000e-02
+1.000e-02
+0.000e+00
2
1
3

Fully coupled

Partially coupled $h_c = 1$

Partially coupled $h_c = 0.2$

Partially coupled $h_c = 0$

Figure 6.48 Axisymmetric cup damage contours (low lubrication condition).

It is also noticeable in Figure 6.48 that damage presents a non axisymmetric distribution, influenced by the asymmetric distribution of the equivalent plastic strain variable. All approaches predict that damage starts to localize in rolling direction (1-direction) and macro-crack evolves towards transverse direction, following the same radial position. The explanation for the nonexistent effect of the crack closure parameter is related to the fact that only positive principal stress are found in failure area, and, only this area reaches a equivalent plastic strain value greater than damage threshold.

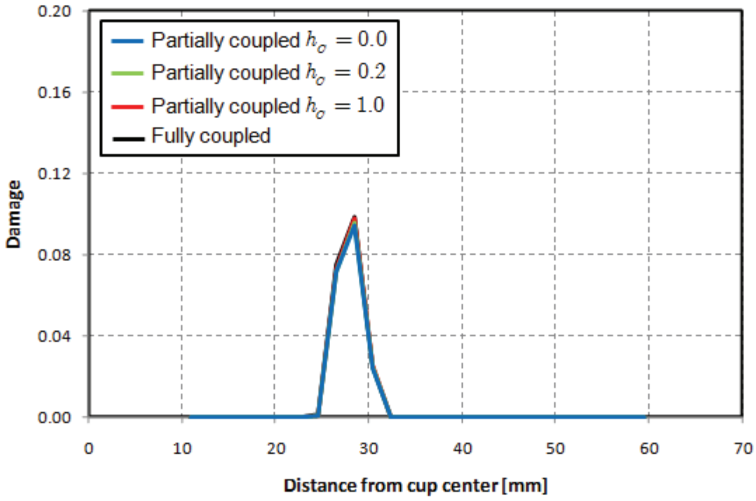

Figure 6.49 Damage vs. initial distance from cup center for rolling direction section (low lubrication condition).

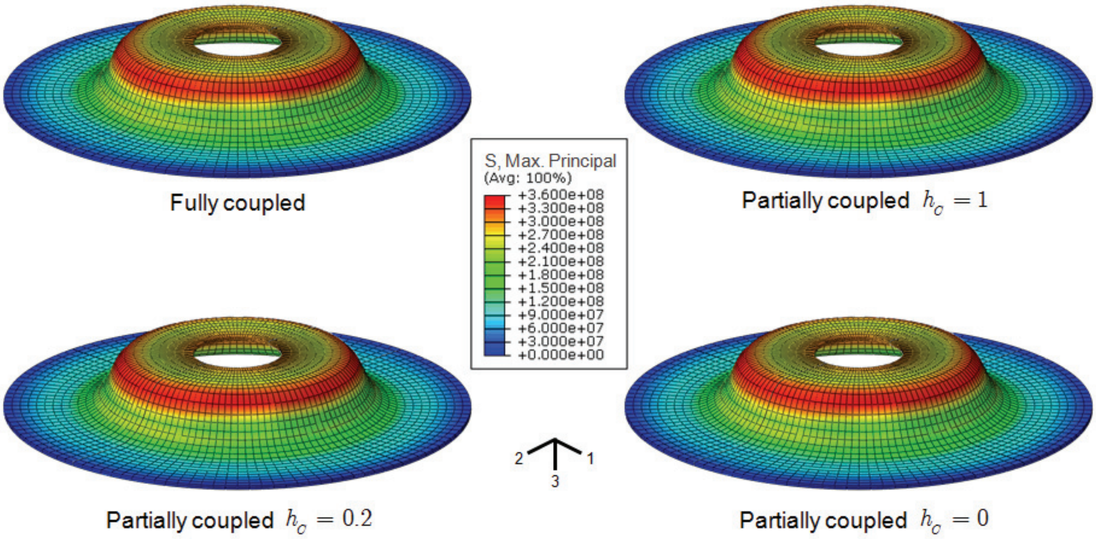
Fully coupled
S, Max. Principal
(Avg: 100%)
+3.600e+08
+3.300e+08
+3.000e+08
+2.700e+08
+2.400e+08
+2.100e+08
+1.800e+08
+1.500e+08
+1.200e+08
+9.000e+07
+6.000e+07
+3.000e+07
+0.000e+00
Partially coupled h_c = 1
2
1
3
Partially coupled h_c = 0.2
Partially coupled h_c = 0

Figure 6.50 Axisymmetric cup major principal stress component (low lubrication condition).

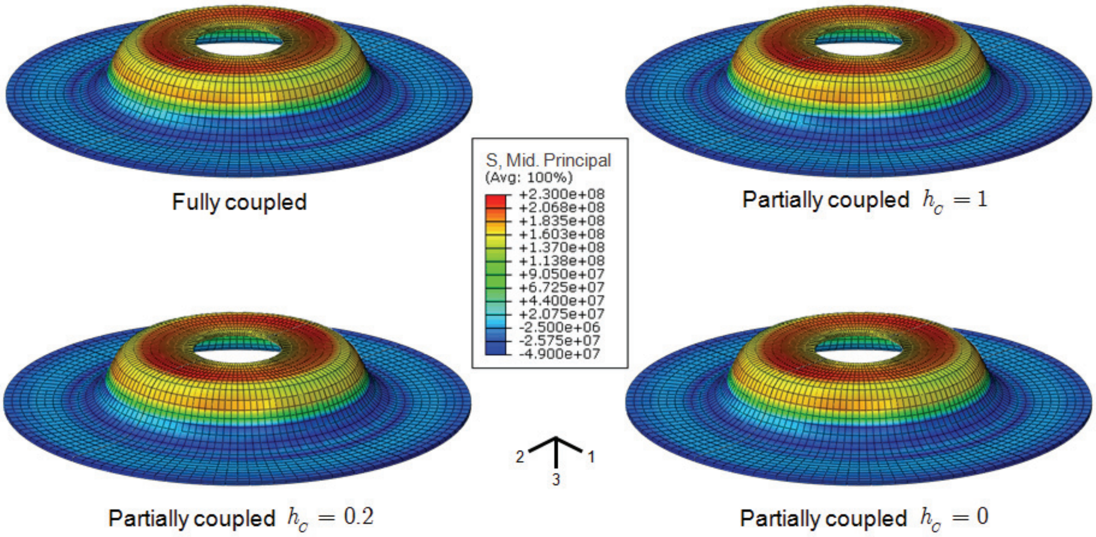
Fully coupled
S, Mid. Principal
(Avg: 100%)
+2.300e+08
+2.068e+08
+1.835e+08
+1.603e+08
+1.370e+08
+1.138e+08
+9.050e+07
+6.725e+07
+4.400e+07
+2.075e+07
-2.500e+06
-2.575e+07
-4.900e+07
Partially coupled h_c = 1
2
1
3
Partially coupled h_c = 0.2
Partially coupled h_c = 0

Figure 6.51 Axisymmetric cup middle principal stress component (low lubrication condition).

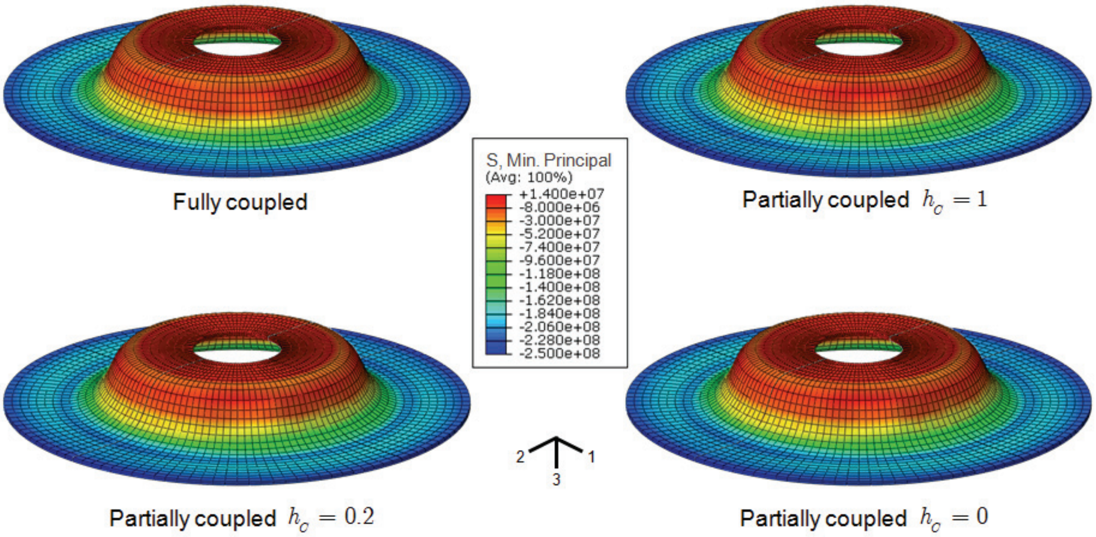
Fully coupled
S, Min. Principal
(Avg: 100%)
+1.400e+07
-8.000e+06
-3.000e+07
-5.200e+07
-7.400e+07
-9.600e+07
-1.180e+08
-1.400e+08
-1.620e+08
-1.840e+08
-2.060e+08
-2.280e+08
-2.500e+08
Partially coupled h_c = 1
2
1
3
Partially coupled h_c = 0.2
Partially coupled h_c = 0

Figure 6.52 Axisymmetric cup minor principal stress component (low lubrication condition).

Therefore, for this severe contact condition between die, holder and blank, crack closure parameter h_C has no influence in the stress distribution, Figure 6.50, Figure 6.51 and Figure 6.52, neither in damage distribution and evolution, as shown in Figure 6.48 and Figure 6.49.

To complete the study of this benchmark, a numerical study concerning the variation of the friction coefficient was also performed. The evolution of predicted critical punch displacement with considered friction coefficient is shown in Figure 6.53.

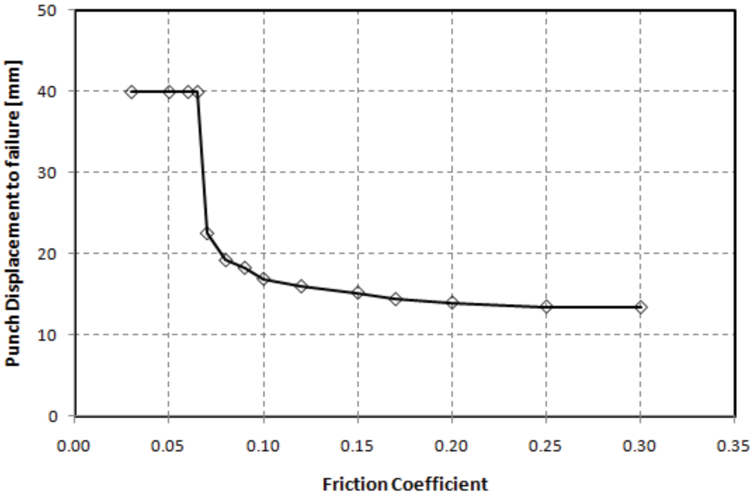

Figure 6.53 Influence of friction coefficient in predicted punch displacement to failure.

For low friction values, up to 0.06, no failure indication is detected using the above damage models. The only exception is in the case of fully coupled algorithm and partially coupled algorithm with no tension / compression distinction that detect failure in cup borders, for a punch displacement near target punch stroke. For values of friction coefficient above 0.07, failure is early detected in vertical wall, near punch radius. The value of the critical punch displacement gradually decreases as one considers higher values for the friction coefficient. However, the change in critical punch displacement values is very small, being the difference between the predicted value between 0.08 and the severe condition of 0.3 of only 5.8 mm.

As conclusion, no significant difference was found between the two algorithms, fully coupled and partially coupled with $h_C = 1$, in terms of failure prediction. So, the usage of explicit time integration codes allows that the partially coupled solution can be adopted without a considerable loss in precision in the evolution of progressive plastic softening during metal forming operations. Moreover, the adoption of the implemented partially coupled solution enables the usage of unilateral conditions, which, in this geometry, represents an important effect to take into account since stress condition in flange area is mainly dominated by a compressive stress state.

6.6 Cross shape geometry

This example corresponds to a complex sheet metal part used in a research project which aimed the development of a tooling decision support system able to estimate an optimal selection of tool material and its optimal fabrication route according to a specific product, required lead time and expected production [Pinto 2008]. One of the tasks in the specific objectives of the project was the investigation of selected alternative tooling materials concerning their manufacturability and its service behaviour. For this task, a tool geometry representing the most severe conditions for production of parts, a cross shape geometry, as presented in Figure 6.54, was selected and a deep drawing quality steel, a mild steel DC04, 1 mm thickness, was used for the blank material, intending to represent the most usual production of sheet metal parts. Under the specified experimental conditions, the part was successfully drawn up to 56 mm punch stroke with the selected mild steel. However, using the AA 5182-O material, a premature failure was experienced.

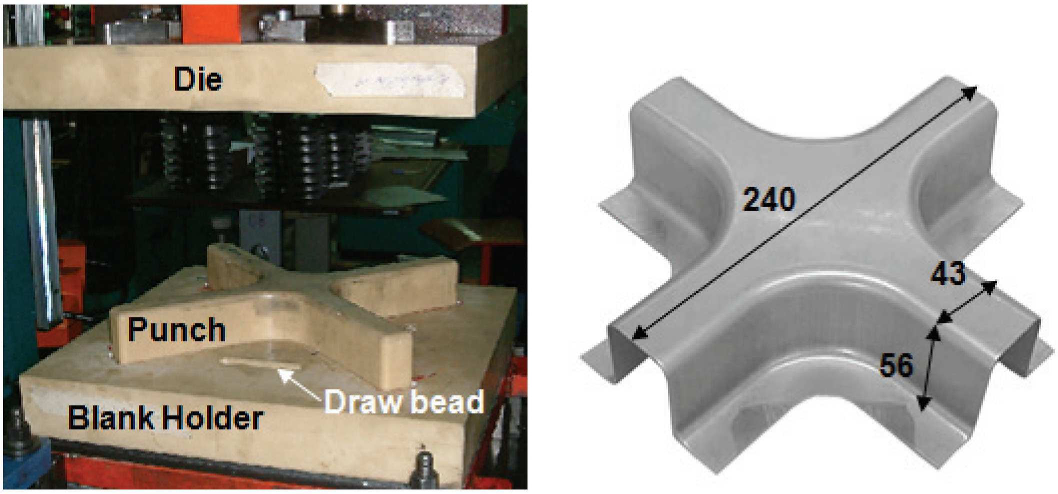

Figure 6.54 Cross shape geometry tool and part dimensions (in mm).

6.6.1 Experimental failure

In order to avoid the effect of existent draw beads positioned in the four quadrants of the cross (Figure 6.54), a corner-cut was made to the initial 270 mm×270 mm square blank for the AA5182-O material. Using different corner-cut lengths, distinctive failure locations were experimentally observed. For a corner-cut length of 85 mm, experimental failure occurs in punch shoulder, near the edges of the cross, Figure 6.55a. For higher corner-cuts, failure is detected in the die radius, near the cross center, as presented in Figure 6.55b.

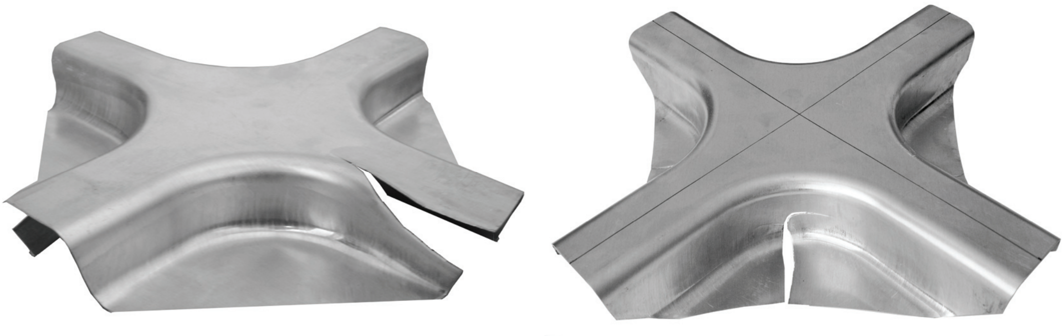

Figure 6.55 Experimental failures: corner-cut of 85 mm and 105 mm.

6.6.2 Numerical modelling

Only a quarter of the domain was considered in the numerical simulation. The total number of elements depends on the considered corner-cut length, Figure 6.56.

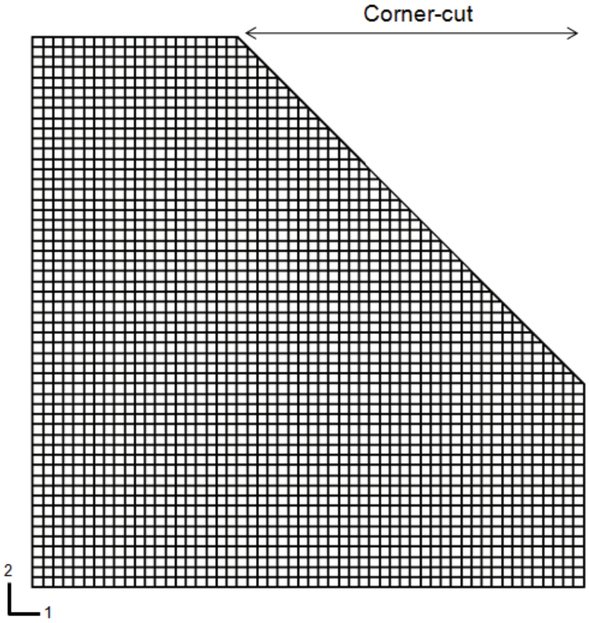

Figure 6.56 Adopted numerical mesh for cross shape geometry.

For the lowest corner-cut length, 85mm, blank mesh is composed by 4710 reduced integration solid elements, distributed in a double layer. For the higher corner-cut length (115mm), the total number of elements is reduced to 3762. Tools were considered rigid and a constant blank holder force of 100 kN was applied. An additional tool active part, a counter-pad, was also used in the simulation, which applies a constant force of 60 kN against punch top surface, preventing blank sliding over punch. Due to some uncertainty concerning tooling status, several friction coefficients were considered, ranging from 0.1 to 0.3, to model the tribological conditions established between blank and tool surfaces. A prescribed velocity of 5 m/s was set to punch and a target punch displacement of 56 mm was defined, corresponding to the part height. The applied numerical conditions are summarized in Table 6.10 and material hardening and damage parameters are presented in Table 6.1, Table 6.3 and Table 6.5, respectively. The adopted mesh is presented in Figure 6.56. Rolling direction was assumed to be along 1-axis.

Table 6.10 Cross shape geometry numerical conditions.

Blank	
Element type	Reduced integration solid (8- and 6-noded)
Element size [mm]	2.5x2.5x0.5
Number of layers	2
Number of elements	4710 / 4426 / 4110 / 3762
Tools	
Element type	Rigid elements
Elements in radii	12
Friction coefficient	0.1~0.3
Process parameters	
Punch travel [mm]	56
Punch speed [m/s]	5
Blank holder force [kN]	100

6.6.3 Results and discussion

In order to study the effect of friction and corner-cut length, numerical models regarding the variation of friction coefficient and corner-cut length were performed by using both isotropic and anisotropic damage models. In Figure 6.57, it is presented the calculated critical punch displacement for a corner-cut of 85 and 105 mm using the isotropic and anisotropic damage models for several friction coefficients, ranging from 0.1 up to 0.3. Concerning damage model influence, no major differences were found in the critical punch displacement predictions given by the isotropic and anisotropic damage models for both corner-cut lengths, Figure 6.57.

Concerning friction coefficient influence, a distinct behaviour is observed in the calculated punch displacement to failure for the two considered corner-cuts, 85 and 105 mm. For the lower corner-cut (85 mm), no remarkable difference is found between a 0.1 and a 0.15 friction coefficient value. For higher values, there is a nearly linear decrease of the predicted critical displacement, from 21.0 mm to 15.2 mm, as a higher friction coefficient value is considered. At this punch displacement and using this corner-cut length, there is still some material located on the edge of the cross between the blank holder and die surfaces, and the high blank holder force blocks the material to slide into die cavity. This sliding resistance given by the blank holder force is potentiated by the use of a larger friction coefficient, and, thus, failure initiation is detected for lower values of punch displacement when higher friction coefficients are used. But, regardless of the considered friction coefficient value, failure always occurs in punch radius region, in the cross edge, for this corner-cut length, where either isotropic and anisotropic damage values localize, as seen in Figure 6.58, for the isotropic damage model case.

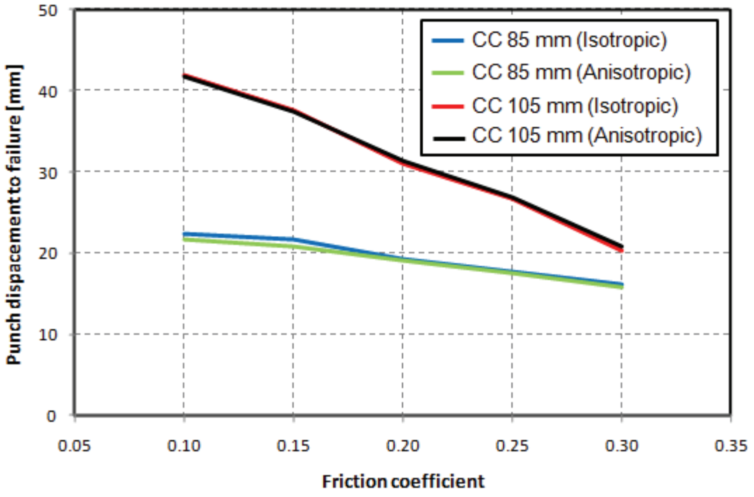

Figure 6.57 Influence of friction coefficient in predicted critical punch displacement (corner-cuts 85 mm and 105 mm).

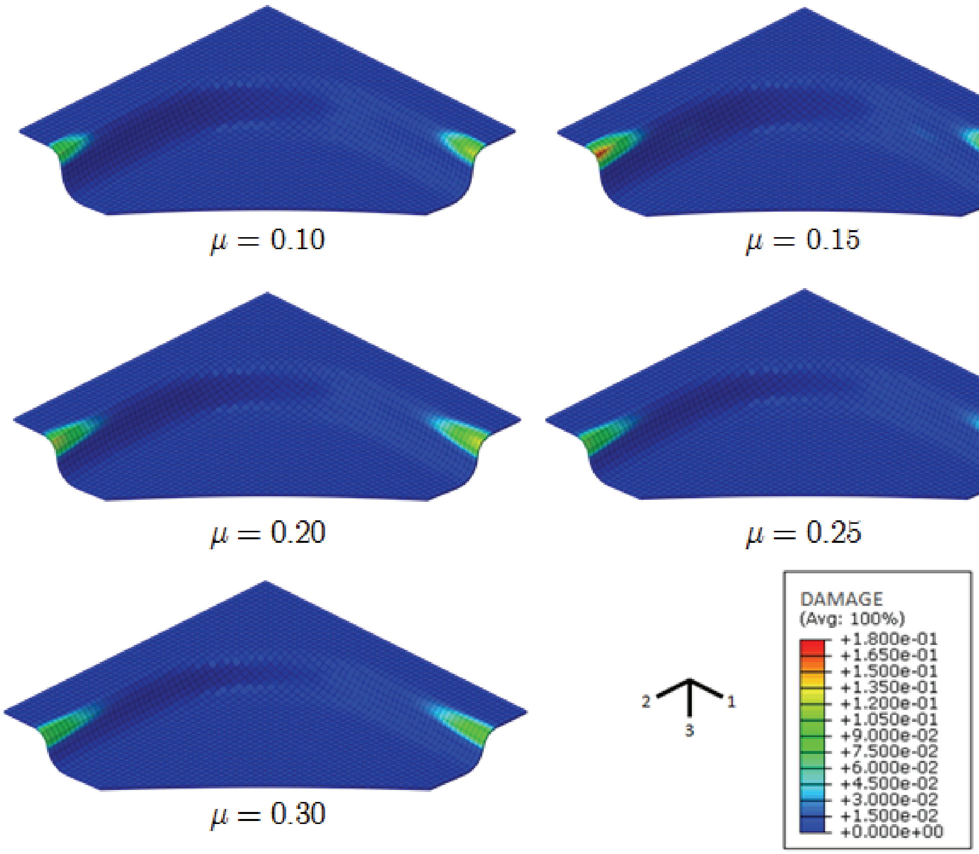
$\mu = 0.10$ $\mu = 0.15$

$\mu = 0.20$ $\mu = 0.25$

$\mu = 0.30$

DAMAGE
(Avg: 100%)
+1.800e-01
+1.650e-01
+1.500e-01
+1.350e-01
+1.200e-01
+1.050e-01
+9.000e-02
+7.500e-02
+6.000e-02
+4.500e-02
+3.000e-02
+1.500e-02
+0.000e+00
2
1
3

Figure 6.58 Cross shape geometry damage contours prior to failure for different friction coefficient values (corner-cut 85mm, isotropic damage model).

In the case of a corner-cut of 105 mm, a higher influence of the friction coefficient is noticed. The critical punch displacement suffers almost a decrease of 50% when values of 0.1 and 0.3 for the friction coefficient are considered, Figure 6.57. In the most severe contact situation, the displacement reached by the punch before failure is 21.0 mm while for the 0.1 friction coefficient value, punch reaches a stroke of 40.6 mm. So, a clear influence of the contact condition in predicted critical punch displacement is experienced for this corner-cut length. However, the friction value influence is not only restricted to the critical punch displacement prediction. The contact condition also influences failure initiation site. For the lower friction value, failure is detected in the die radius, near the blank edge, in the cross segment aligned with rolling direction. As a higher friction coefficient is used, the area where the macro-crack is firstly detected gradually shifts from the cross edge towards the cross center, and from the die radius region to the vertical wall area, as can be seen in Figure 6.59.

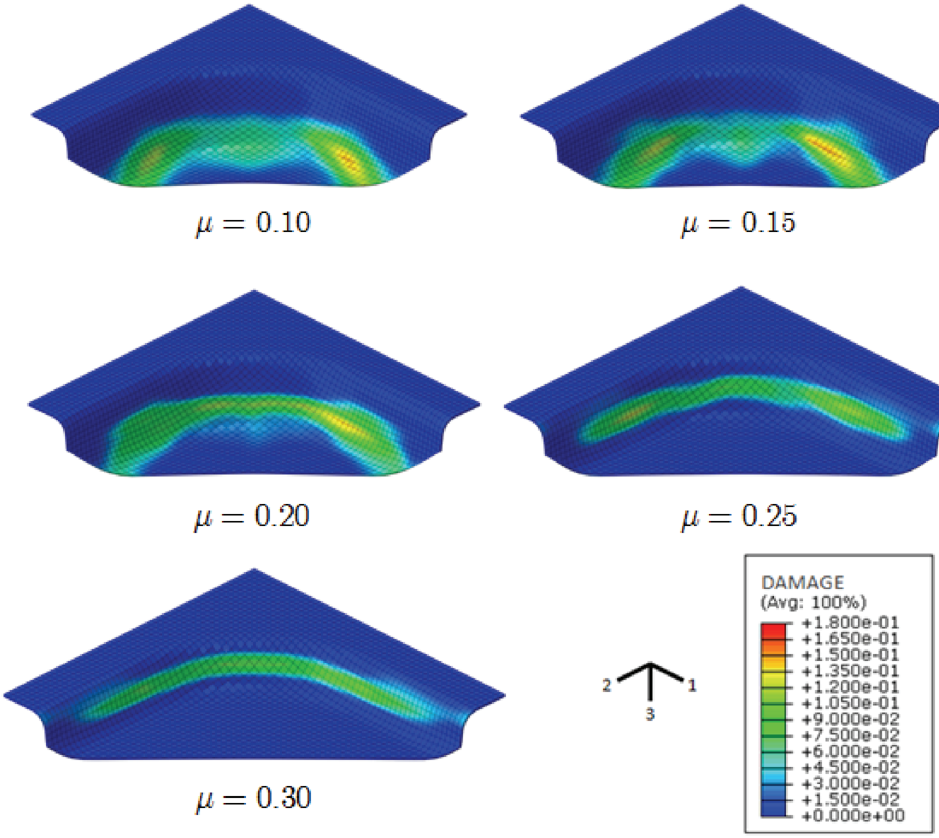

$\mu = 0.10$ $\mu = 0.15$

$\mu = 0.20$ $\mu = 0.25$

$\mu = 0.30$

Figure 6.59 Cross shape geometry damage contours prior to failure for different friction coefficient values (corner-cut 105 mm, isotropic damage model).

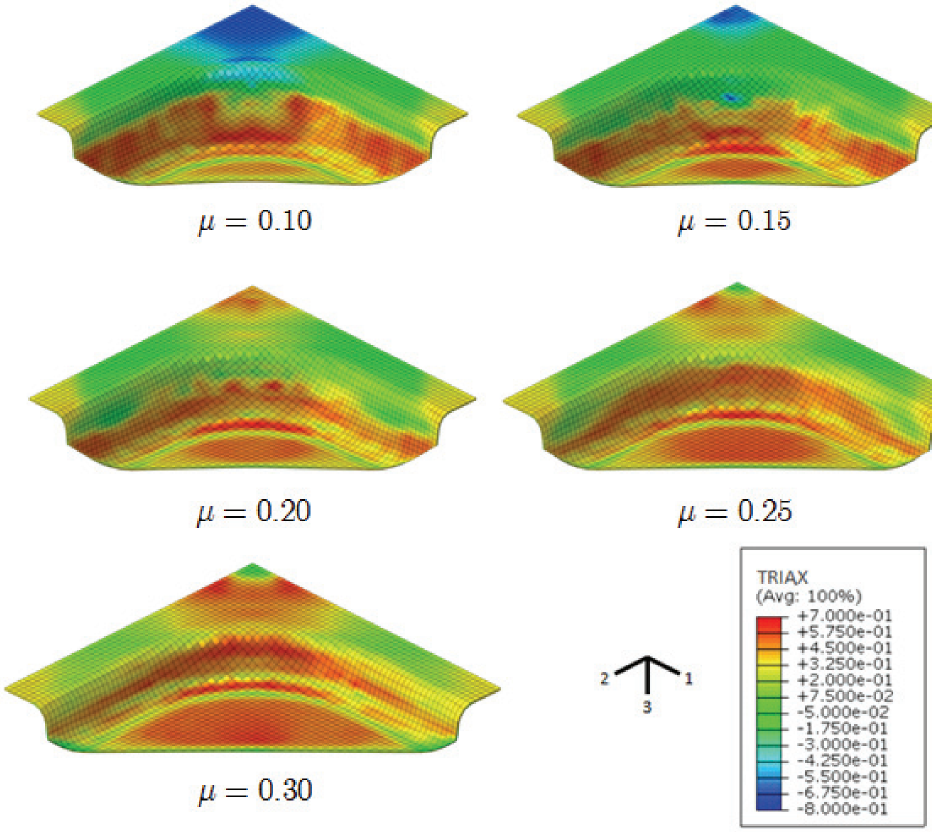

$\mu = 0.10$ $\mu = 0.15$

$\mu = 0.20$ $\mu = 0.25$

$\mu = 0.30$

Figure 6.60 Cross shape geometry stress triaxiality ratio contours prior to failure for different friction coefficient values (corner-cut 105 mm, isotropic damage model).

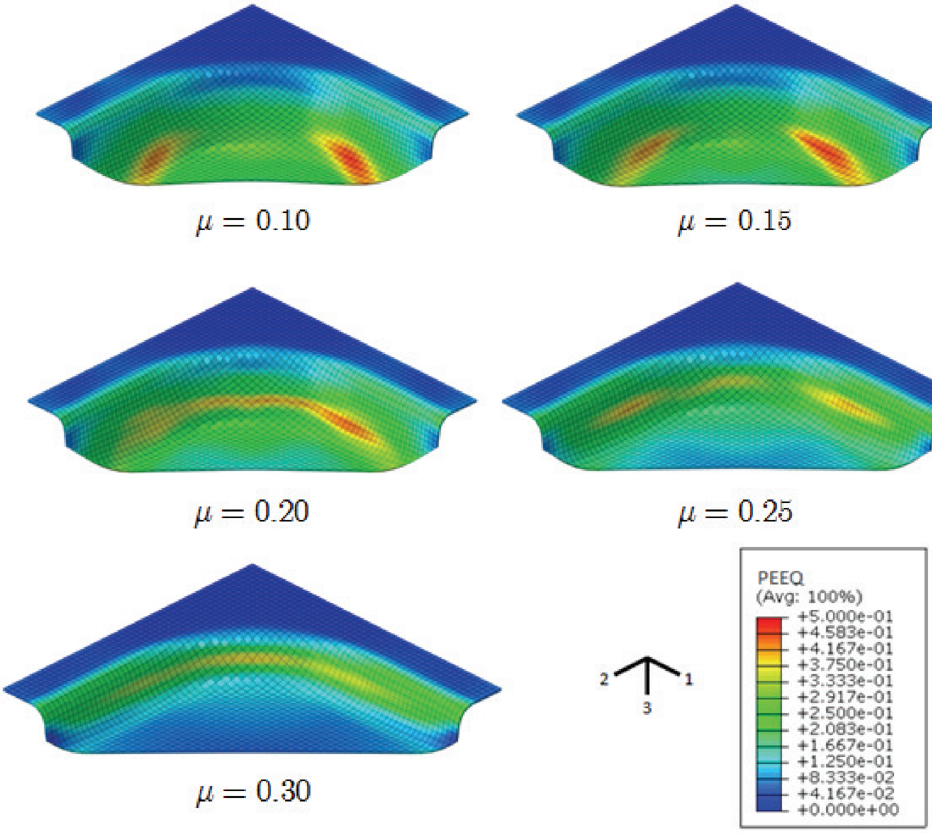

$\mu = 0.10$ $\mu = 0.15$

$\mu = 0.20$ $\mu = 0.25$

$\mu = 0.30$

Figure 6.61 Cross shape geometry equivalent plastic strain contours prior to failure for different friction coefficient values (corner-cut 105 mm, isotropic damage model).

This change in failure location is intimately related with stress triaxiality and equivalent plastic strain distributions attained in the part, as can be seen in Figure 6.60 and Figure 6.61.

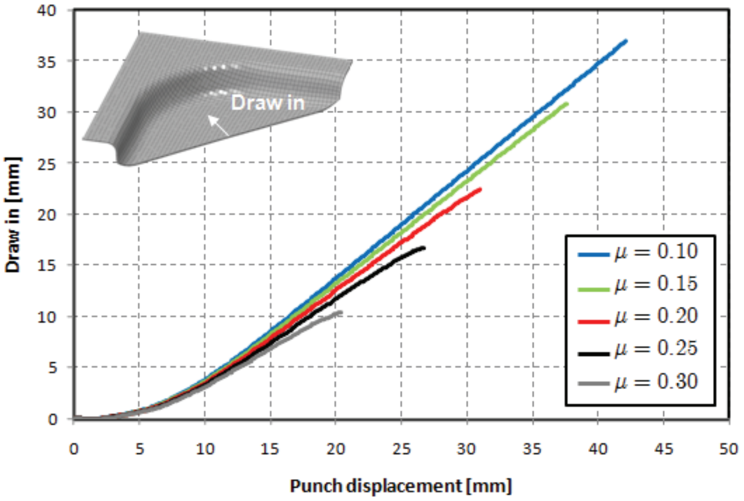

Figure 6.62 Draw-in evolution for different friction coefficients (corner-cut 105 mm, isotropic damage model).

To understand this change in failure location, it is important to observe the evolution of the displacement of a node located at the edge of the plate, in the center of the quadrant of the cross, for several friction coefficients, presented in Figure 6.62. As the considered friction coefficient increases, there is a progressive decrease in the attained node displacement for the same punch stroke. This reduction in the draw-in value promotes the occurrence of higher deformations in the blank and, hence, there is a tendency for the development of increasingly important tension stress states, as shown by the inversion in the stress triaxiality sign in the center of the part, Figure 6.60. For this corner-cut length (105 mm), it is also important to note that the material located near the edge of the cross undergoes bending over die radius in a very early stage of punch displacement, and early losses its status of critical area, being the critical zone for the strain localization transferred to the die radius region. For the lowest friction coefficient, the critical area will be located near the blank edge, in the cross segment aligned with rolling direction, Figure 6.59. But, increasing the force needed to slide the blank along the surface of the blank holder, the material located on the vertical wall will undergo important tension efforts due the restricted material that flows into die cavity from the blank edge. These important tension efforts experienced in the vertical wall tend to lead to strain localization in this area, instead of die radius region. The localization of deformation will also force damage to localize in the vertical wall, and, due to its dependence on triaxiality ratio, will develop more rapidly in the center of the cross where stress triaxiality ratio is higher (Figure 6.60), being this location prone to failure. Finally, it is also interesting to see the influence of the corner-cut length in the predicted punch displacement to rupture, expressed in Figure 6.63.

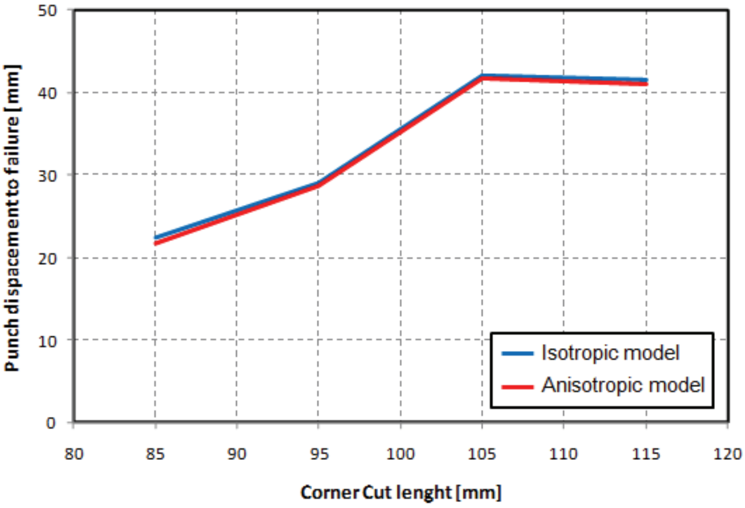

Figure 6.63 Influence of corner-cut length in predicted critical punch displacement (friction coefficient 0.10).

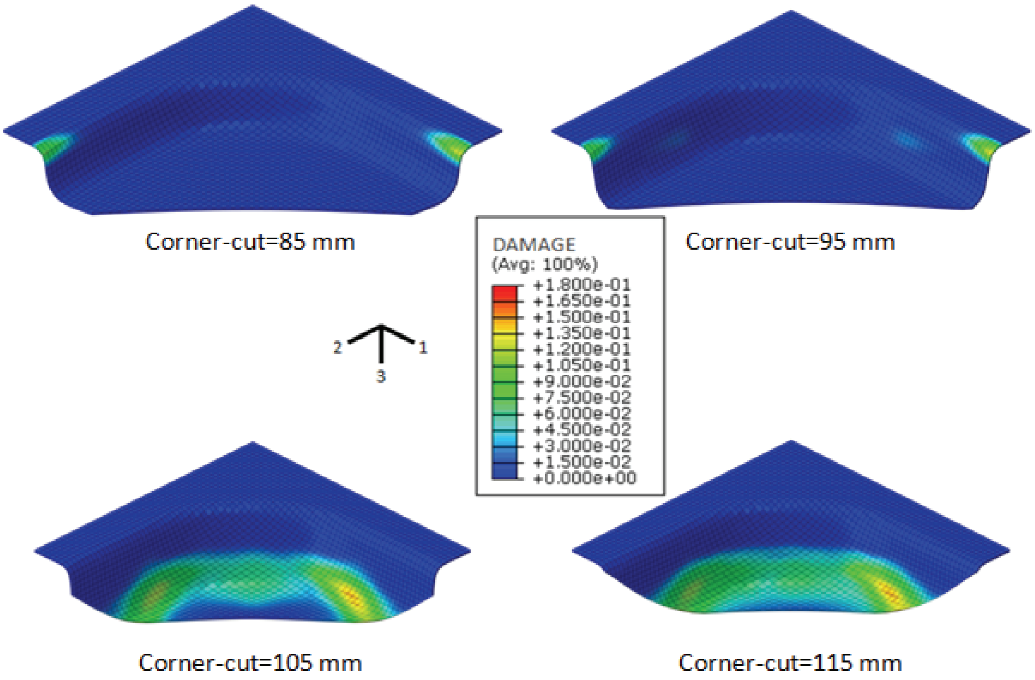
Corner-cut=85 mm
Corner-cut=95 mm
DAMAGE
(Avg: 100%)
+1.800e-01
+1.650e-01
+1.500e-01
+1.350e-01
+1.200e-01
+1.050e-01
+9.000e-02
+7.500e-02
+6.000e-02
+4.500e-02
+3.000e-02
+1.500e-02
+0.000e+00
2
1
3
Corner-cut=105 mm
Corner-cut=115 mm

Figure 6.64 Cross shape geometry damage contours prior to failure for different corner-cut lengths (friction coefficient 0.1, isotropic damage model).

As for the friction coefficient influence, a similar performance is observed by the isotropic and anisotropic damage models concerning critical displacement predictions obtained for several corner-cut lengths. Globally, higher punch displacements to failure are attained for higher corner-cut lengths. However, the influence of this variable is more evident for cut length values below 105 mm. For the larger corner-cut length (115 mm), the predicted punch displacement to failure is very close to the one obtained for a cut of 105 mm. Bellow this value, namely for 95 mm and 85 mm, rupture is detected for values of punch displacement that decrease as a smaller corner-cut length is considered. It is also possible to notice that there is a dissimilar influence of the corner-cut length between the ranges 85 to 95 mm and 105 to 115. This different outcome may be explained by the different predicted location for failure initiation. While for the two upper corner-cut lengths, 105 to 115mm, failure starts at die radius region, along blank edge, in the case of the lower corner-cut lengths, failure is initially predicted at punch radius, in the cross edge, as seen by the damage distribution prior to failure for several corner-cut lengths presented in Figure 6.64.

6.7 Concluding remarks

Numerical tests were carried out and compared with corresponding experimental testings in order to evaluate the performance and accuracy of the proposed damage models in the failure prediction in sheet metal forming processes.

As a first remark, it is important to emphasize that if purely elasto-plastic models without damage consideration are used and the critical value of accumulated plastic strain is taken as the fracture criterion, crack initiation can be predicted in erroneous places. The axisymmetric notched bar tensile example [Pires 2003] is representative of this importance. Although maximum value of accumulated plastic strain is attained in the root of the notch, fracture initiation is predicted in the center of the specimen, in accordance with experiments, where stress triaxiality ratio has his highest value. This occurrence demonstrates the experimentally observed marked decrease in ductility as stress triaxiality increases for ductile materials. The use of damage models, introducing such effect in the damage growth and in the development of strain localization and consequent failure, promoting a constant stress and triaxiality redistribution, is, therefore, crucial in order to provide reliable and useful insights on failure analysis.

But, although stress triaxiality value is particularly important in damage development, its sign can also have a tremendous effect in calculated failure predictions. In some geometries, especially those where high compressive stress states are achieved, the consideration of unilateral conditions in damage development is fundamental to achieve failure predictions in accordance with experiments. The presented simulation of the axisymmetric cup is representative of this importance. For a high lubrication condition, failure was detected in the cup borders under a compressive stress state when using a damage model without a distinction between tensile / compressive stress states, in disagreement with experiments that present a fully drawn cup for such lubrication condition. The inclusion of the distinctive damage evolution behaviour by using the partial coupling strategy was able to capture the experimentally observed behaviour and, additionally, it was shown that decoupling stress and damage update algorithms do not influences significantly damage calculation when comparing with a fully coupled analysis.

Another important issue revealed by numerical results is related with the modelling of tribological conditions established between blank and tool surfaces. Numerical results have shown that a small change in the friction coefficient can have a huge effect in failure predictions, not only in the predicted punch displacement up to failure but also in the crack initiation site. Therefore, the friction-contact situation is of a paramount importance in failure analysis since predictions are highly affected by the modelling of this phenomenon. Also, one can remark that the uncertainty of the tribological conditions together with a simplistic assumption of a constant friction coefficient, disregarding its dependence on several parameters (relative sliding speed, local surface pressure, temperature, etc. [Roll 2008]), can lead to significant changes in contact and frictional forces, imposing important changes in the stress state and affecting decisively failure predictions delivered by the implemented damage models.

A remark can also be made to failure calculations provided by the isotropic and anisotropic damage models. No significant differences were found in the predicted punch displacements to failure given by the two models for the considered material and examples. Due to the fact that a weak anisotropic flow behaviour is observed in the material and no complex cases of non-proportional loadings were achieved in the simulated parts, it is decisive to conclude that, under these conditions, the consideration of a scalar representation to characterize damage is sufficient to provide a satisfactory prediction of failure occurrence in sheet metal forming. Despite this conclusion, the importance of a high-order damage representation will be shown in the next chapter that deals with necking occurrence prediction.

Finally, some comments concerning the pathological effect of discretization dependence in local continuum theories, as the ones considered in this work. Even if not shown and highlighted in the presented numerical results, the discretization dependence is also experienced in these benchmarks. The most representative example is shown in Figure 6.65 concerning mesh refinement in the cross shape geometry.

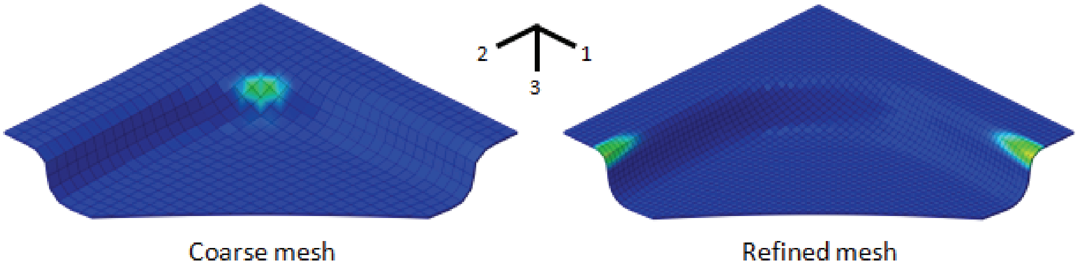

Figure 6.65 Mesh dependence in the cross shape geometry.

As seen in Figure 6.65, the adoption of a larger mesh size leads to a strain localization in the cross center while a more refined mesh predicts damage localization in the cross borders, using the same numerical conditions. The fact that the material behaviour is assumed to be independent of the influence of surroundings points can introduce such numerical stability problems. The adoption of a non-local theory will be studied in order to attenuate the discretization dependence by averaging the internal variable (damage) associated with the dissipative process.

Nevertheless, despite the marked influence of tribological conditions, prediction of rupture occurrence using the implemented damage models are qualitatively in agreement with experimental results and it may be concluded that the use of these constitutive models can provide reliable failure predictions in metal forming processes, representing, therefore, an important decision tool in the development of new stamped products.

7. APPLICATION OF DAMAGE TO NECKING OCCURENCE

This chapter proposes a new criterion for forming limits prediction based on an integrated approach between the anisotropic damage model described in Chapter 5 and the necking criterion proposed by Hora *et al.* [1996], combining the determination of the onset of the two last phases of plastic deformation: necking and failure. A review on forming limit diagrams modelling is provided and most important criterions are presented. The importance of the proposed coupled approach is highlighted since, in addition to providing an improved prediction of necking occurrence, it also allows to determine which phenomenon is the most restrictive event in sheet metal forming, particularly important in materials where fracture can occur before required conditions for necking are achieved.

7.1 Introduction

Formability is, by definition, the capability of the material to undergo plastic deformation to a given shape without defects. Failure, the most severe defect, is usually preceded by strain localization (necking) that causes a reduction of the part's strength, worsens its appearance and is one of the major reasons for rejecting it. Thus, the occurrence of unstable, non-uniform deformation, which mainly takes the form of localized necking, defines the upper limit of the amount of useful plastic deformation that can be imposed on a part during a forming operation. These upper limits can be represented in the principal in-plane strains space for different strain paths, obtaining the so-called forming limit diagram. This forming limit diagram (FLD) concept was firstly introduced by Keeler and Backofen [1963] and Goodwin [1968], and stands as the first safety criterion in deep drawing operations and still a conventional approach to assess formability. Although this concept is very simple and well understood for proportional and non-proportional complex loading paths, its experimental determination is rather complex, demanding a wide range of sheet forming tests. Moreover, forming limits of sheet metal are influenced by several physical factors (strain path history, hardening behaviour, anisotropy, etc.), thus, making its experimental determination tedious, expensive and, in some circumstances, impossible [Barata da Rocha 2009]. Therefore, an extensive effort has been devoted to the development of mathematical models capable of accurately determining the plastic flow occurrence in sheet metal forming. A large number of theories have been proposed, which can be differentiated in two broad theoretical frameworks: the necking theory in homogeneous sheets, based on the original work developed by Hill [1952] and Swift [1952], and the theory of sheet non-homogeneity proposed by Marciniak and Kuczynski [1967]. Since these theoretical models are based on plasticity analyses of instability, thus requiring a profound knowledge of continuum mechanics and mathematics, another brand of models, semi-empirical ones, based on experimental evidence, were also developed in recent years [Banabic 2000].

Usually, the appearance of necking is a limiting criterion in sheet metal forming. However, in some materials, particularly in advanced high strength steels (AHSS), fracture can occur before or after necking, depending on material's ductility. This new generation of steels have caught the attention of industry due to its outstanding mechanical properties but its widespread use is still hampered by difficulties in predicting their forming behaviour through numerical simulations. AHSS steels are characterized by a relatively large hardening exponent, which raises the limiting major strain for necking, allowing more stretch under positive strain conditions. As a result, there is a high probability that increased limiting strains for necking rise above critical strains for fracture and, therefore, fracture will occur before necking [Shi 2006]. Those critical strains at fracture can also be represented in the principal in-plane strains space, originating the so-called fracture forming limit diagram (FFLD).

Fracture usually occurs at larger strains than does localized necking so the fracture curve is usually well above the instability curve and decreases continuously with increasing triaxiality. When fracture occurs before necking, this means that the fracture forming limit diagram (FFLD) will intersect the theoretical FLD, which is defined for localized necking. An example of this case is presented in Figure 7.1, where experimental fracture has occurred without a typical localized neck for large positive and large negative minor strains [Keeler 1989].

This phenomenon is not only observed in these new-generation steels. Also, in aluminium alloys, this behaviour is experienced especially in the biaxial tension region.

This is illustrated in Figure 7.2 from LeRoy and Embury [1978] experiments, which shows that in equibiaxial stretching, fracture occurs before plane-strain necking, and, in this case, limit strains are governed by fracture rather than by local necking and a truncation must be performed to the forming limit curve as a result of its intersection with the fracture forming limit curve. This occurrence makes the entire forming predictive capabilities based only on necking analysis models not reliable enough. Therefore, a proper description of forming limits should include not only the localized necking appearance or the final fracture occurrence alone, but should address the determination of the onset of these two last phases of the plastic deformation, in order to verify which phenomenon is the most restrictive event in sheet metal forming.

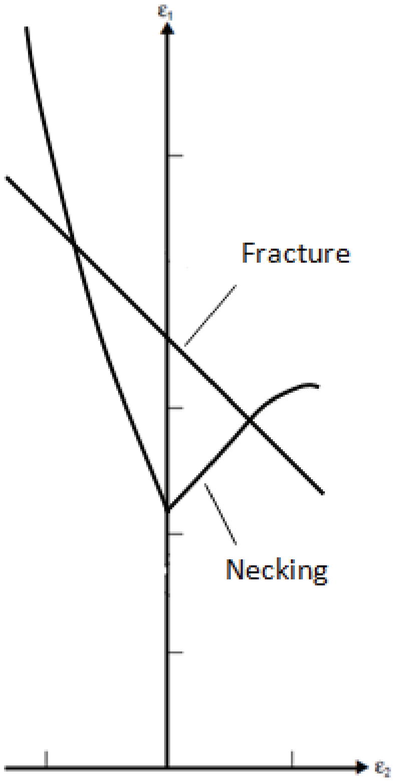

Figure 7.1 A high strength steel with a large number of inclusions can have a FFLD which will intersect the FLD [Keeler 1989].

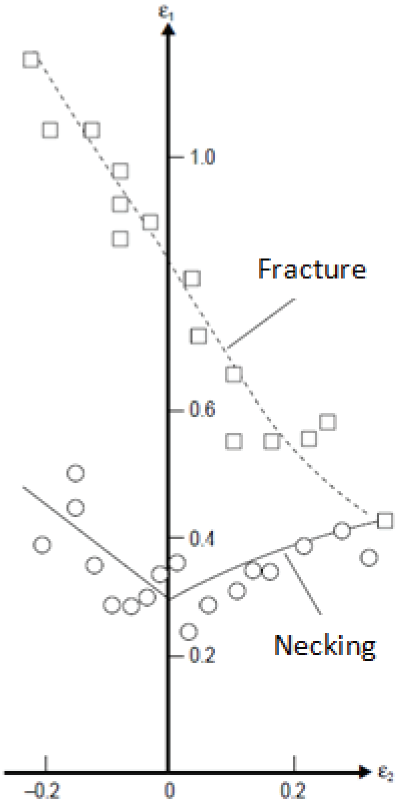

Figure 7.2 Fracture and local necking strains in aluminium alloy 5154-O. Under equibiaxial stretching, failure occurs by fracture before local necking [LeRoy 1978].

Concerning fracture initiation modelling, theories that consider material inhomogeneities are usually employed, namely, theories that describe the mechanism of internal damaging in ductile materials, conveniently coupled with plasticity theory, either by using a micromechanics-based formulation [Gurson 1977] or a Continuous Damage Mechanics (CDM) approach, popularized by Lemaitre [1985a] through the thermodynamics of irreversible processes. Both frameworks have already proven to be efficient for determination of ductile failures in sheet metal forming [Lemaitre 1985b] [Murakami 1988] [Doege 1995] [Pires 2003] [Al-Rub 2003] [Saanouni 2006] [Teixeira 2006], but, for the analysis of onset of necking using these models, some difficulties arise since a unique critical damage value for all strain paths evolutions cannot be easily defined, as it is made for fracture. An alternative approach for strain localization condition modelling, using continuous damage mechanics, is to introduce into the analysis an instability criterion, responsible for the necking prediction. The coupled approach between plastic softening evolution and instability criteria can lead to more reliable and more accurate predictions of localized necking due to the strong dependency of the onset of necking with the strain path evolution that can encompass numerous complex interacting physical phenomena including mechanical properties degradation.

In this chapter, a integrated approach between the presented anisotropic damage model (Chapter 5) and the necking criterion proposed by Hora *et al.* [1996] is formulated. First, a brief review of the forming limit diagrams modelling activities is provided (a more complete review can be found in [Aretz 2004] and [Stoughton 2004]) and the most relevant criteria are presented. Subsequently, developments on forming limit calculation with damage consideration are also reviewed and, finally, the proposed approach is presented together with the corresponding evaluation of its performance in the calculation of forming limits for an aluminium alloy.

7.2 Forming limit diagrams modelling review

The forming limit diagram concept, introduced by Keeler and Backofen [1963] and later by Goodwin [1968], is a constructive concept for characterizing the sheet metal formability. It consists of a map, plotted in the principal in-plane strains space, which separates safe combinations of major and minor in-plane principal strains states, from more severe strains states, that a material could sustain without the risk of the occurrence of visible defects like necking and fracture. Although this concept has more than 40 years-old, still represents nowadays one of the most important safety criterions in sheet metal forming operations.

Since the experimental determination of FLDs requires a wide range of sheet forming tests, a large variety of expensive equipment and tremendous experimental effort, many attempts have been made to predict the FLDs, taking into account the theory of plasticity, material parameters and instability conditions. A large number of different theoretical approaches have been proposed to explain the localized necking in biaxial tensile fields and can be divided into two main frameworks [Banabic 2000]: the linear necking theory, based on the plastic instability of homogeneous sheet metals which describes the initiation of localized band of straining in an otherwise uniform sheet, and the theory of non-homogeneous sheet metals, based on the plastic instability of heterogeneous sheet metals, where it is assumed an initial weakness, imperfection or inhomogeneity in the sheet, which gradually develops into a neck as straining proceeds.

7.2.1 Hill's localized necking criterion

The earliest approaches to predict instabilities were based on the study of bifurcations. The first model is due to Hill [1952], who has described localized necking in thin sheets under plane stress states. Consider a specimen, with a thickness t, subjected to a proportional loading [Marciniak 2002], as seen in Figure 7.3.

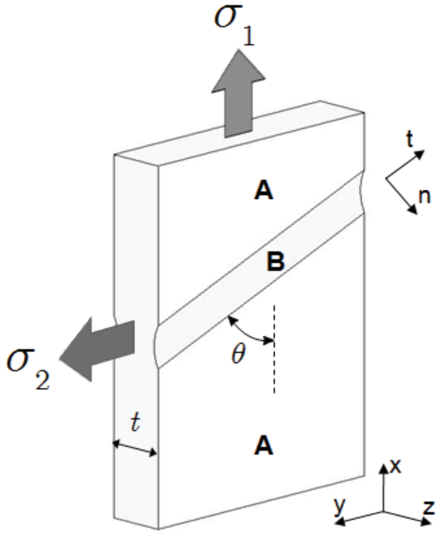

Figure 7.3 Local neck formed in a continuous sheet oriented at an angle θ to the maximum principal stress.

Let us first define the stress α and strain β ratios, given as relations between the major and minor principal in-plane stresses and strains, respectively, as:

$$\alpha = \frac{\sigma_2}{\sigma_1} \text{ and } \beta = \frac{d\varepsilon_2}{d\varepsilon_1}. \tag{7.1}$$

As the process is proportional, the stress ratio α and the strain ratio β will remain constant. The stress state can be given by:

$$\sigma_1 ;\ \sigma_2 = \alpha\sigma_1 ;\ \sigma_3 = 0. \tag{7.2}$$

The condition postulated by Hill [1952] for localized necking is that necking will start when the major tension, T_1, reaches a maximum. Therefore:

$$dT_1 = 0. \tag{7.3}$$

The major tension, T_1, is the maximum force per length along a section in a sheet and is equal to the product between the major stress, σ_1, and the thickness, t:

$$T_1 = \sigma_1 t\,. \tag{7.4}$$

Differentiating Equation (7.4), we obtain:

$$dT_1 = d\sigma_1 t + \sigma_1 dt \tag{7.5}$$

or, rearranging the equation dividing by T_1, Equation (7.4), one may write:

$$\frac{dT_1}{T_1} = \frac{d\sigma_1}{\sigma_1} + \frac{dt}{t}\,. \tag{7.6}$$

Using the definition of strain for the thickness direction, we know that:

$$d\varepsilon_3 = \frac{dt}{t} \tag{7.7}$$

and, we can substitute in Equation (7.6), obtaining:

$$\frac{dT_1}{T_1} = \frac{d\sigma_1}{\sigma_1} + d\varepsilon_3\,. \tag{7.8}$$

Using Equation (7.1) and assuming that material is incompressible, i.e., the volume remains constant during straining, the condition:

$$d\varepsilon_1 + d\varepsilon_2 + d\varepsilon_3 = 0 \tag{7.9}$$

is satisfied, and the strain increment in the thickness direction $d\varepsilon_3$ is given by:

$$d\varepsilon_3 = -\left(1+\beta\right) d\varepsilon_1\,. \tag{7.10}$$

Using Equation (7.3) and Equation (7.10), Equation (7.8) can be rewritten as:

$$\frac{d\sigma_1}{\sigma_1} - \left(1+\beta\right) d\varepsilon_1 = 0 \tag{7.11}$$

and finally as:

$$\frac{d\sigma_1}{d\varepsilon_1} = \left(1+\beta\right)\sigma_1\,. \tag{7.12}$$

This last equation corresponds to the criterion proposed by Hill [1952]. For a material that obeys the generalized stress-strain law given by:

$$\bar{\sigma} = K\left(\bar{\varepsilon}^{p}\right)^{n}, \tag{7.13}$$

it is possible to demonstrate that the equivalent stress, $\bar{\sigma}$, and the major principal stress ,σ_1, are equal, and differentiating Equation (7.13), we obtain:

$$\frac{1}{\sigma_1}\frac{d\sigma_1}{d\varepsilon_1} = \frac{n}{\varepsilon_1}\,. \tag{7.14}$$

Therefore, the major principal in-plane strain ε_1^* obtained for maximum tension is given by:

$$\varepsilon_1^* = \frac{n}{1+\beta} \tag{7.15}$$

and the corresponding minor principal in-plane strain ε_2^* as:

$$\varepsilon_2^* = \frac{\beta n}{1+\beta}. \tag{7.16}$$

This maximum tension criterion represents a line in the principal strains diagram (Figure 7.5) and provides a reasonable theoretical model for local necking strains when the strain ratio is negative ($\beta < 0$). This criterion states that the local neck can only develop along a line of zero extension. This statement can be explained by the fact that once the uniform region outside the neck (zone A in Figure 7.3) ceases to strain, implying that necking process has become catastrophic, strain increment parallel to the neck will be zero (in the t direction in Figure 7.3). Due to the geometric constraint, the strain increment in the t direction in the necking region (zone B in Figure 7.3) will also be zero. This “zero extension” direction of the neck can be easily found by imposing that the strain in t direction (Figure 7.3) is equal to zero.

7.2.2 Swift’s diffuse necking criterion (MFC)

The Hill's criterion predicts localized plastic deformation in the characteristic directions of zero extension, which can only happen for the strain states where one of the surface strains is negative. However, localized necking can be experimentally observed in biaxial stretched sheets, as both practical experience and later experiments have demonstrated [Barata da Rocha 1985]. To describe this experimental behaviour, Swift [1952] proposed a criterion for predicting the onset of diffuse necking with the assumption that plastic instability occurs at a maximum load for proportional loading, applying the Considère uniaxial analysis [Considère 1885] to determine the limit strains in a biaxial stress state. He analysed a sheet element loaded along two perpendicular directions and applied the Considère criterion [Considère 1885] for each direction.

Consider a specimen, with a length l, width w and thickness t, subjected to a proportional biaxial stretching loading [Marciniak 2002] as represented in Figure 7.4. Also, consider σ_1 and σ_2 to be the stresses along the two principal in-plane directions and the corresponding traction forces, F_1 and F_2.

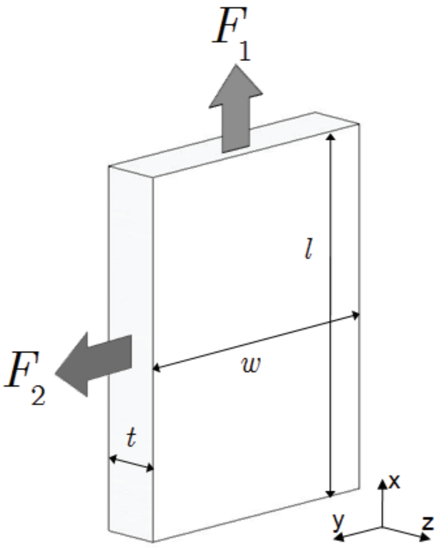

Figure 7.4 Sheet element subjected to a biaxial stretching loading.

Assuming a proportional loading, one can state that if the resultant force F reaches a maximum then also F_1 and F_2 attain a maximum value, simultaneously:

$$dF = 0 \Rightarrow \begin{cases} dF_1 = 0 \\ dF_2 = 0 \end{cases}. \tag{7.17}$$

Knowing that traction forces F_1 and F_2 are given by:

$$\begin{cases} F_1 = \sigma_1 wt \\ F_2 = \sigma_2 lt \end{cases}, \tag{7.18}$$

one may write that:

$$\begin{cases} dF_1 = d\sigma_1 wt + \sigma_1 dwt + \sigma_1 wdt = 0 \\ dF_2 = d\sigma_2 lt + \sigma_2 dlt + \sigma_2 ldt = 0 \end{cases} \tag{7.19}$$

or, rearranging, as:

$$\begin{cases} \dfrac{dF_1}{F_1} = \dfrac{d\sigma_1}{\sigma_1} + \dfrac{dw}{w} + \dfrac{dt}{t} = 0 \\ \dfrac{dF_2}{F_2} = \dfrac{d\sigma_2}{\sigma_2} + \dfrac{dl}{l} + \dfrac{dt}{t} = 0 \end{cases}. \tag{7.20}$$

Using the definition of strain for principal directions, we know that:

$$d\varepsilon_1 = \frac{dl}{l}\,;\; d\varepsilon_2 = \frac{dw}{w}\,;\; d\varepsilon_3 = \frac{dt}{t} \tag{7.21}$$

and, substituting in Equation (7.20), we obtain:

$$\begin{cases} \dfrac{d\sigma_1}{\sigma_1} = -d\varepsilon_2 - d\varepsilon_3 \\ \dfrac{d\sigma_2}{\sigma_2} = -d\varepsilon_1 - d\varepsilon_3 \end{cases}. \tag{7.22}$$

Assuming that material is incompressible, i.e., the volume remains constant during straining, the condition:

$$d\varepsilon_1 + d\varepsilon_2 + d\varepsilon_3 = 0 \tag{7.23}$$

verifies, and Equation (7.22) becomes:

$$\begin{cases} \dfrac{d\sigma_1}{\sigma_1} = d\varepsilon_1 \\ \dfrac{d\sigma_2}{\sigma_2} = d\varepsilon_2 \end{cases}. \tag{7.24}$$

It is interesting to note that this result has the same formalism of Considère criterion [Considère 1885]. After a straightforward manipulation and assuming an isotropic yield criterion and a power law hardening rule as:

$$\overline{\sigma} = K\left(\overline{\varepsilon}\right)^n, \tag{7.25}$$

the principal in-plane strains ε_1^* and ε_2^* for a maximum load are given by:

$$\begin{cases} \varepsilon_1^* = \dfrac{2n\left(1+\beta+\beta^2\right)}{\left(\beta+1\right)\left(2\beta^2-\beta+2\right)} \\ \varepsilon_2^* = \dfrac{2n\beta\left(1+\beta+\beta^2\right)}{\left(\beta+1\right)\left(2\beta^2-\beta+2\right)} \end{cases}. \tag{7.26}$$

It is important to remark that, at maximum load, the major in-plane strain ε_1^* is equal to the hardening exponent n for uniaxial tension, plane strain ($\beta = 0$) and equibiaxial stretching ($\beta = 1$). Figure 7.5 shows the forming limit curve obtained through the Swift criterion, being known as Swift curve or diffuse necking curve.

In contrast to Hill’s criterion [Hill 1952], Swift's analysis can be applied to the whole range or deformation, i.e., from uniaxial tension to equibiaxial stretching, but the predicted limit strains are much lower than the experimental data in the drawing zone, i.e., when the strain ratio is negative. Using the predictive capabilities of this criterion under positive strain ratios, Lee and Kobayashi [1975] and later Korhonen [1978] combined the Swift criterion and Hill’s analysis, making a distinctive calculation for negative and positive strain ratios. Main conclusions of their work was that a change towards equibiaxial tension increases forming limits and a change towards plane strain has the opposite effect, thus showing that instability is strain path dependent.

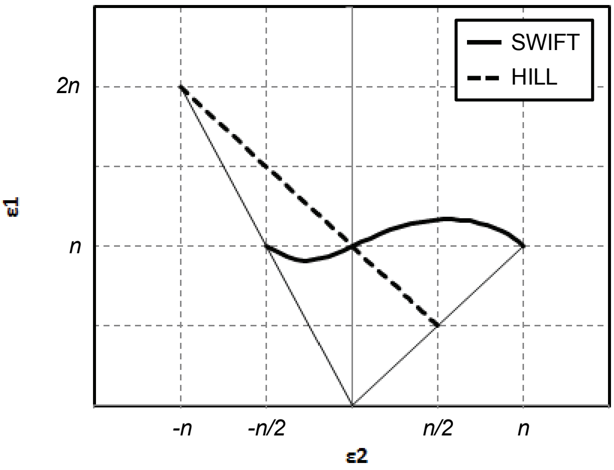

Figure 7.5 Hill's and Swift's forming limit curves.

7.2.3 Marciniak-Kuczynski analysis (M-K analysis)

In 1967, Marciniak and Kuczynski (M–K) [1967] proposed the first realistic mathematical model for theoretical determination of FLDs, based on the assumption that necking develops from local regions of initial heterogeneity. In order to define this heterogeneity, they supposed an infinite sheet metal containing a region of local imperfection where heterogeneous plastic flow develops and localizes. Rigid plasticity, plane stress condition and isotropic work hardening of the material are assumed. A detailed description of the theoretical M–K analysis, schematically illustrated in Figure 7.6, can be found in several publications [Marciniak 1967] [Barata da Rocha 1985] [Banabic 2000].

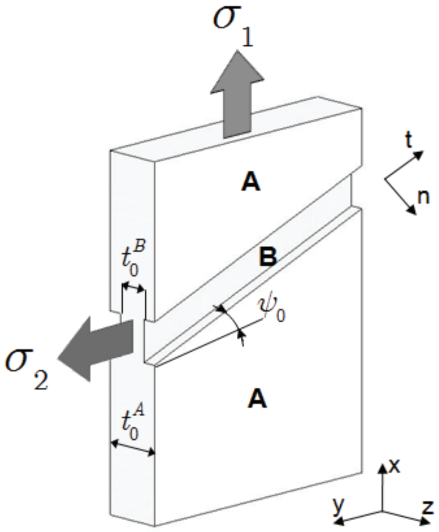

Figure 7.6 Schematic representation of M-K analysis [Marciniak 1967].

Essentially, the model is based on the growth of an initial defect in the form of a narrow band with an angle ψ_0 with respect to the principal axis, as represented by zone B in Figure 7.6 [Barata da Rocha 2009]. This two-zone material is subjected to plastic deformation by applying a constant incremental stretching $d\overline{\varepsilon}^A$ in the homogeneous part (zone A in Figure 7.6). In zone A, the stress tensor in the orthotropic referential frame of anisotropy $[\boldsymbol{\sigma}^A]_{xyz}$ is calculated as well as the corresponding stress matrix $[\boldsymbol{\sigma}^A]_{ntz}$ in the groove reference frame $\left(n,t,z\right)$ (see Figure 7.6) using the yield function ($\Phi^A = \overline{\sigma}^A - \sigma_Y^A = 0$) along with the stress ratio definition $\alpha = \sigma_2 \big/ \sigma_1$, within the framework of Theory of Plasticity. The flow rule permits the determination of the strain increment tensor $[d\boldsymbol{\varepsilon}^A]_{xyz}$ in the principal axis of anisotropy, which transposed in the strain matrix $[d\boldsymbol{\varepsilon}^A]_{ntz}$ in the groove reference frame, give the strain increment in the longitudinal direction of the groove $d\varepsilon_{tt}^A$.

In order to compute the equivalent increment strain $d\overline{\varepsilon}^B$ and the stress value in longitudinal direction of the groove σ_{tt}^B, the equilibrium and compatibility requirements are used. The equilibrium condition that indicates the same force perpendicular to the necking band in region A and B conforms to:

$$\begin{cases} \sigma_{nn}^A t^A = \sigma_{nn}^B t^B \\ \sigma_{nt}^A t^A = \sigma_{nt}^B t^B \end{cases} \tag{7.27}$$

where $\sigma_{nn}^A, \sigma_{nt}^A$ and $\sigma_{nn}^B, \sigma_{nt}^B$ are components of stress tensor in the groove reference frame $\left(n,t,z\right)$ for zones A and B, respectively, while t^A and t^B are the current sheet thickness outside and inside the groove respectively, given by:

$$\begin{aligned} t^A &= t_0^A \exp\left(\varepsilon_{zz}^A\right) \\ t^B &= t_0^B \exp\left(\varepsilon_{zz}^B\right) \end{aligned}. \tag{7.28}$$

The force equilibrium condition between zones A and B allows to calculate the flow stress value in the normal direction of the groove and the flow shear stress in the groove. The compatibility requirement assumes that the elongation in the direction of the necking band is identical in both regions:

$$d\varepsilon_{tt}^A = d\varepsilon_{tt}^B. \tag{7.29}$$

The strain matrix increment in the imperfection region (region B in Figure 7.6) $[d\boldsymbol{\varepsilon}^B]_{xyz}$ is determined in the orthotropic referential frame of anisotropy and, then, the deformation in the longitudinal direction of the groove is computed. Using the described requirements, the following two nonlinear equations in $d\overline{\varepsilon}^B$ and σ_{tt}^B can be written:

$$\begin{cases} G1\left(d\overline{\varepsilon}^B, \sigma_{tt}^B\right) = \overline{\sigma}^B - \overline{\sigma}_{YF}^B = 0 \\ G2\left(d\overline{\varepsilon}^B, \sigma_{tt}^B\right) = d\varepsilon_{tt}^A - d\varepsilon_{tt}^B = 0 \end{cases} \tag{7.30}$$

where $G1$ and $G2$ are two polynomial functions which represents the yield criterion and the deformation compatibility requirement in longitudinal direction of the necking band, respectively. From these equations, the iterative formula for Newton–Raphson's method [Butuc 2002] is described as follows:

$$\begin{bmatrix} d\overline{\varepsilon}_{i+1}^B \\ \sigma_{tt\,i+1}^B \end{bmatrix} = \begin{bmatrix} d\overline{\varepsilon}_{i}^B \\ \sigma_{tt\,i}^B \end{bmatrix} - \boldsymbol{J}^{-1} \begin{bmatrix} G1\left(d\overline{\varepsilon}_{i}^B, \sigma_{tt\,i}^B\right) \\ G2\left(d\overline{\varepsilon}_{i}^B, \sigma_{tt\,i}^B\right) \end{bmatrix} \tag{7.31}$$

where $\boldsymbol{J}$ represents the matrix of first partial derivatives of functions $G1$ and $G2$ in order to $d\overline{\varepsilon}^B$ and σ_{tt}^B. When absolute values of functions $G1\left(d\overline{\varepsilon}_{i+1}^B, \sigma_{tt\,i+1}^B\right)$ and $G2\left(d\overline{\varepsilon}_{i+1}^B, \sigma_{tt\,i+1}^B\right)$ becomes less than an imposed error, the solution of the problem is achieved. In this analysis, one assumes that plastic flow localization occurs when the equivalent strain increment in imperfection region ($d\overline{\varepsilon}^B$) is 10 times greater than in homogeneous zone ($d\overline{\varepsilon}^A$). So, when the necking criterion is reached the computation is stopped and the corresponding strains $\left(\varepsilon_{xx}^A, \varepsilon_{yy}^A\right)$ accumulated until that moment in the homogeneous zone are the necking limit strains. The analysis is repeated for different values of ψ_0 (between 0° and 90°) and the limit point on the FLD is obtained after minimization of the curve ε_{xx}^A versus ψ_0. The determination of forming limits in the case of complex strain paths, approximated by sequences of two-stage linear strain paths, involves a prestrain of the homogeneous zone and then a drastic change in strain path:

$$\begin{aligned} \beta &= \beta_1 \quad \text{if} \quad \varepsilon_1 < \varepsilon^* \\ \beta &= \beta_2 \quad \text{if} \quad \varepsilon_1 > \varepsilon^* \end{aligned} \tag{7.32}$$

where β_1 and β_2 are two distinct strain paths that are applied and ε^* is the prestrain value. As Barata da Rocha *et al.* [1985] have shown in previous work, the band orientation ψ which minimizes the critical strain depends on the level of prestrain and on the sequence of strain paths. The minimization of the critical strain is achieved as a function of the initial band orientation at the beginning of the first stage. If the initial band orientation ψ_0 is not a principal direction, rotation of the groove will occur during straining and the angle (that defines its orientation) at the beginning of the second strain path must be equal to the final band orientation at the end of the first stage. As for linear strain paths, the analysis is repeated for different values of ψ_0

(between 0° and 90°) at the beginning of the first stage and the limit point in the FLD is obtained after minimization of the curve ε_{xx}^{A} versus ψ_0.

After the pioneering work of Marciniak and Kuczynski [1967], many others researchers adopted this theory. Several enhancements were performed to the original theory: introduction of kinematic hardening [Tvergaard 1978] and mixed hardening models [Hiwatashi 1998] (associated with the dislocation structure using the Teodosiu-Hu model [Teodosiu 1995]), inclusion of strain rate sensitivity [Marciniak 1973], extension to describe necking in viscoplastic materials [Mesrar 1998] and implementation of several yield criteria (Hill48 [Hill 1948] by Sowerby and Duncan [1971] and Barata da Rocha *et al.* [1985]; Hill79 [Hill 1979] by Parmar and Mellor [1978] and Bassani *et al.* [1979]; Hill93 [Hill 1993] by Banabic [1996], Texture-based yield surface [Houtte 1995] by Hiwatashi *et al.* [1998], Yld96 [Barlat 1997b] by Butuc *et al.* [2002], etc.).

Other developments have focused on the extension of the model to predict limit strains under bilinear strain paths evolutions [Barata da Rocha 1985], new algorithmic strategies [Butuc 2002] and combined approaches with diffuse necking models [Tadros 1975].

The original model and the proposed enhancements were extensively studied in order to quantify the model's sensitivity to different mechanical properties (strain-hardening [Sowerby 1971], shape of the anisotropic yield surface [Bassani 1979], influence of anisotropic behaviour [Sowerby 1971] [Barata da Rocha 1985]), imperfection orientation [Hutchinson 1978a] [Barata da Rocha 1985] and also for strain paths changes [Barata da Rocha 1985] [Mesrar 1998] [Butuc 2002].

Especially important is the work developed by Hutchinson and Neale [1978b], who extended M–K theory using a J2 deformation theory and their predictions were in close agreement with experiments. This extension allowed that the left and right hand sides of the forming limit diagram could be calculated using M–K analysis. Their work represents an important contribution to gain insight into the roles of constitutive equations and plasticity theories on FLDs. Additionally, Hutchinson and Neale [1978a] [1978b] found that an orientation of the imperfection non-perpendicular to the principal strain direction, considered perpendicular in the original M-K model, gives the minimum limiting strain for each proportional strain path on the left hand side of FLDs. Later, Barata da Rocha *et al.* [1985] pointed out that the limiting strains are sensitive to the groove orientation, even on the right hand side of the FLD.

Although very popular among the sheet metal forming community, the main objection that can be posed to this framework is connected to the definition of the initial geometrical imperfection parameter f_0, calculated as the ratio between the initial thicknesses of the groove and homogeneous zones ,which evaluation remains rather questionable [Col 2006].

7.2.4 Modified maximum force criterion (MMFC)

Based on the classical formulation of the maximum force criterion (MFC) proposed by Swift [1952], Hora *et al.* [1996] have concluded that the proposed homogeneous stress condition is only correct at the beginning of diffuse necking but, after necking development, a multiaxial stress condition is settled inside the neck. So, they have proposed a new criterion, known as modified maximum force criterion (MMFC), which reads:

$$\frac{\partial\sigma_1}{\partial\varepsilon_1}+\frac{\partial\sigma_1}{\partial\beta}\frac{\partial\beta}{\partial\varepsilon_1}\le\sigma_1 \tag{7.33}$$

in order to take into account the experimentally confirmed fact that the onset of necking depends significantly on the strain ratio β. The fundamental principle of this modified maximum force criterion is based on the fact that, in addition to the purely material-related work hardening, another work hardening effect can appear, triggered by the deviation from the initial, homogeneous stress condition to the stress condition of local necking and, with this, to the point of plane strain, Figure 7.7 [Hora 1996].

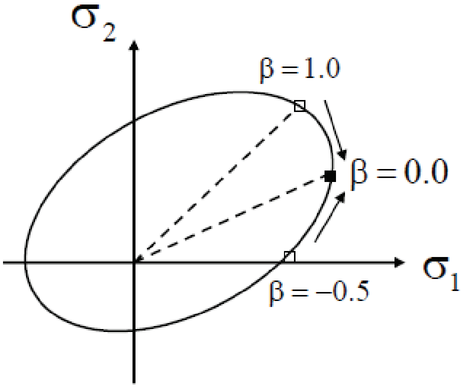

Figure 7.7 Additional hardening effect through change in deformation state.

After a straightforward mathematical manipulation and using the derivative chain rules, the MMFC equation can be rewritten in a form which is compatible with numerical implementation into computer codes as:

$$\frac{H'}{\sigma_Y}g(\alpha)-\frac{f'(\alpha)\beta(\alpha)g(\alpha)}{f(\alpha)\beta'(\alpha)\bar{\varepsilon}^p}\le 1 \tag{7.34}$$

defined in the principal stress directions for proportional straining ($\beta=\dot{\varepsilon}_2/\dot{\varepsilon}_1=\varepsilon_2/\varepsilon_1$), where α is the stress ratio, β the strain ratio, H' the tangent modulus to the hardening curve, σ_Y the current yield stress, $\bar{\varepsilon}^p$ the equivalent plastic strain, and the functions $f\left(\alpha\right)$ and $g\left(\alpha\right)$ are defined as:

$$\bar{\sigma} = \frac{1}{f\left(\alpha\right)}\sigma_1 \,;\; \bar{\varepsilon}^p = g\left(\alpha\right)\varepsilon_1 . \tag{7.35}$$

The terms $f'\left(\alpha\right)$ and $\beta'\left(\alpha\right)$ correspond to the partial derivatives of $f\left(\alpha\right)$ and $\beta\left(\alpha\right)$ in order to the stress ratio α.

A more general analytical form of this criterion can be establish by combining it with Hill's quadratic yield criterion [Hill 1948] for a general plane stress state [Brunet 1998]. Relative to coordinates along the principal directions of orthotropy, the quadratic yield criterion was originally cast in the form [Hill 1990]:

$$\begin{aligned} \bar{\sigma}^2 = {} & \frac{1}{4}\left(F+G\right)\left(\sigma_{11}+\sigma_{22}\right)^2 + \frac{1}{4}\left(F+G+4H\right)\left(\sigma_{11}-\sigma_{22}\right)^2 \\ & - \frac{1}{2}\left(F-G\right)\left(\sigma_{11}^2-\sigma_{22}^2\right) + 2N\sigma_{12}^2 \end{aligned} \tag{7.36}$$

where $\bar{\sigma}$ is the Hill's equivalent stress, σ_{11}, σ_{22} and σ_{12} are the in-plane components of Cauchy stress and F, G, H and N are the Hill's anisotropic parameters. In order to find the intrinsic formulation for a general plane stress case, Hill's quadratic criterion must be written in terms of principal stresses, σ_1 and σ_2. Replacing in Equation (7.36) the following relations:

$$\begin{aligned} \sigma_{11}+\sigma_{22} &= \sigma_1+\sigma_2 \\ \sigma_{11}-\sigma_{22} &= \left(\sigma_1-\sigma_2\right)\cos 2\theta \\ 2\sigma_{12} &= \left(\sigma_1-\sigma_2\right)\sin 2\theta \end{aligned} \tag{7.37}$$

where θ corresponds to the angle described between the orthotropic axes and the principal axes, the yield criterion expression can be rearranged to:

$$\bar{\sigma}^2 = a\left(\theta\right)\sigma_1^2 + b\left(\theta\right)\sigma_2^2 - 2c\left(\theta\right)\sigma_1\sigma_2 \tag{7.38}$$

with:

$$\begin{aligned} a\left(\theta\right) &= \frac{1}{4}\left[\left(F+G\right)+2N-2\left(F-G\right)\cos 2\theta+\left(F+G+4H-2N\right)\cos^2 2\theta\right] \\ b\left(\theta\right) &= \frac{1}{4}\left[\left(F+G\right)+2N+2\left(F-G\right)\cos 2\theta+\left(F+G+4H-2N\right)\cos^2 2\theta\right] \\ c\left(\theta\right) &= -\frac{1}{4}\left[\left(F+G\right)-2N-\left(F+G+4H-2N\right)\cos^2 2\theta\right] \end{aligned} \tag{7.39}$$

and angle θ can be determined by:

$$\theta = \frac{1}{2}\tan^{-1}\left(\frac{2\sigma_{12}}{\sigma_{11}-\sigma_{22}}\right). \tag{7.40}$$

Through the relation between the two principle in-plane stresses defined as $\sigma_2 = \alpha\sigma_1$, one obtains the equivalent stress $\bar{\sigma}$ as a function of the stress ratio α, orientation angle θ and the major in-plane principal stress σ_1 as:

$$\bar{\sigma}\left(\sigma_1,\alpha,\theta\right) = \left(a\left(\theta\right) + b\left(\theta\right)\alpha^2 - 2c\left(\theta\right)\alpha\right)^{\frac{1}{2}}\sigma_1 . \tag{7.41}$$

Therefore, the relation between the current yield stress and the major principal in-plane stress, denoted as f, is given by:

$$f\left(\alpha,\theta\right) = \left(a\left(\theta\right) + b\left(\theta\right)\alpha^2 - 2c\left(\theta\right)\alpha\right)^{-\frac{1}{2}} . \tag{7.42}$$

Evoking the associate flow rule of plasticity, one has:

$$\dot{\boldsymbol{\varepsilon}}^p = \dot{\gamma}\frac{\partial\bar{\sigma}}{\partial\boldsymbol{\sigma}} \tag{7.43}$$

which allows us to deduce the strain ratio β, expressed as:

$$\beta = \frac{\dot{\varepsilon}_2}{\dot{\varepsilon}_1} = \frac{\partial\bar{\sigma}/\partial\sigma_2}{\partial\bar{\sigma}/\partial\sigma_1} = \frac{b\left(\theta\right)\alpha - c\left(\theta\right)}{a\left(\theta\right) - c\left(\theta\right)\alpha} . \tag{7.44}$$

The function $g\left(\alpha,\theta\right)$ can also be given in an explicit form. Its inference is also made by using the associative flow rule. Knowing that:

$$\dot{\varepsilon}_1 = \dot{\gamma}\frac{\partial\bar{\sigma}}{\partial\sigma_1} \tag{7.45}$$

and that the equivalent plastic strain $\dot{\bar{\varepsilon}}^p$ is equal to the plastic consistency parameter $\dot{\gamma}$ for this yield criterion:

$$\dot{\gamma} = \dot{\bar{\varepsilon}}^p , \tag{7.46}$$

along with the definition presented in Equation (7.35), lead us to the following form for the function g,

$$g\left(\alpha,\theta\right) = \frac{\left(a\left(\theta\right) + b\left(\theta\right)\alpha^2 - 2c\left(\theta\right)\alpha\right)^{\frac{1}{2}}}{a\left(\theta\right) - c\left(\theta\right)\alpha} . \tag{7.47}$$

The partial derivatives $\partial f/\partial\alpha$ and $\partial\beta/\partial\alpha$ may be explicitly found from Equation (7.42) and (7.44), respectively.

The main advantage of this necking criterion is the fact that no additional material parameters are required, such as the ambiguous thickness ratio in the M-K analysis [Marciniak 1967] and critical strains can be directly calculated for a given strain path without the need to perform an incremental analysis. Also, due to its differential form, it can be used for necking prediction in non-linear strain paths evolutions [Tong 2002]. However, it is considered too conservative with regard to reality. To improve the performance of the MMFC, the same authors have introduced an extension to the MMFC, the so-called "Enhanced MMFC" (eMMFC) [Hora 2007] for plastic instability prediction in thermo-sensitive sheet metal forming processes by including the influence of sheet thickness and temperature in the necking occurrence, expressed as:

$$\frac{\partial \sigma_1}{\partial \varepsilon_1}\left[1+\frac{t}{2R}+e\left(E,t\right)\right]+\frac{\partial \sigma_1}{\partial \beta}\frac{\partial \beta}{\partial \varepsilon_1}+\frac{\partial \sigma_1}{\partial T}\frac{\partial T}{\partial \varepsilon_1}\leq \sigma_1 \tag{7.48}$$

where t is the sheet thickness, R is the sheet curvature radius, T is the temperature and function e is calculated as:

$$e\left(E,t\right)=E_0\left(\frac{t}{t_0}\right)^p \tag{7.49}$$

where t_0 is the initial sheet thickness and E_0 and p are material constants. The newly developed criterion has shown to predict better results for failure prediction for stainless steels when compared to the classical MMFC model [Krauer 2007].

Mattiasson *et al.* [2007] have also observed a general tendency of the MMFC to severely under predict critical strains on the right-hand side of the FLD, although good predictions are achieved by this criterion on the left-hand side. The explanation is due to the loss of accuracy that the MMFC incurs by the approximation of the derivative $\partial\beta/\partial\varepsilon_1$. So, to overcome this approximation, they proposed a new method, the "Extended MFC" (EMFC) [Mattiasson 2006], based on the MFC fundamental equation, where an incremental calculation scheme is performed after diffuse necking is achieved, defined by the original Swift criterion. According to authors, this new approach does not introduce additional approximations to the original Swift's work but, although better predictions were achieved by the newly developed approach, still some underestimation of the limit strains on the right hand side of the FLD was experienced [Mattiasson 2007].

Recently, Banabic *et al.* [2009] proposed an improvement to the MMFC by introducing two fitting coefficients (A and B) in the original MMFC equation, that are calibrated by using two experimental points that represent different limit states:

$$A\frac{\partial \sigma_1}{\partial \varepsilon_1}+B\frac{\partial \sigma_1}{\partial \beta}\frac{\partial \beta}{\partial \varepsilon_1}\leq \sigma_1\,. \tag{7.50}$$

They achieved better results in the stretching area of the FLD, due to the enforcement of the theoretical curve to catch two experimental points used for parameter identification.

Besides the underestimation of critical strains in the right-hand side of the FLD, another disadvantage of the MMFC is due to the fact that a singularity can occur if the yield locus used in necking simulation exhibits straight line segments [Aretz 2004], leading to singularities in the predicted forming limit curve or even in total failure in forming limit diagram prediction. Nevertheless, due to its simplicity and easiness to implement, this criterion is suitable to be used as a necking criterion in finite element codes.

7.2.5 Other theoretical methods of necking prediction

Although not so popular between the sheet metal forming community, other models were proposed to theoretically predict necking occurrence in sheet metals.

Storën and Rice [1975] (S-R) proposed the so-called "vertex theory" to predict localized necking over the entire range of the forming limit diagram. They have incorporated the J2 deformation theory into the classical bifurcation analysis. The proposed model postulates that localized necking is due to the development of a corner on the yield surface thus there is no theoretical restriction to localized necking. The analysis of the forming limit curve behaviour was done by imposing force equilibrium between the neck and non-necked region of the metal. Enhancement to this theory was later proposed by Gotoh [1985] who had a relevant contribution by using an original yield condition expressed as a polynomial function of fourth degree. Based on the S-R theory, Zhu *et al.* [2001] proposed a unified bifurcation analysis of sheet metal forming limits, by including the moment equilibrium in their study in addition to the force equilibrium condition. They have found that the shear terms due to the perturbation vanish inside the localized neck of a region of deformation, thus the two-dimensional problem could be simplified to a one-dimensional problem. Based on this simplified version of the vertex theory, Chow *et al.* [2003] developed a generalized method to predict forming limits of sheet metals considering several isotropic and anisotropic yield criteria. In their work, the influence of the yield function is only noticeable on the right hand side of the forming limit diagram and, typically, a higher order yield function leads to lower limit strains.

Motivated by experimental observations at the failure site, Bressan and Williams [1983] introduced the "Through Thickness Shear Instability Criterion" (TTIC). This model takes into account the experimental fact that the fracture plane lies in a direction near to that of maximum shear stress. The model proposed by Bressan and Williams [1983] takes into account this shear fracture mode and was applied in the determination of the onset of failure in sheet metal forming. A more general form of this criterion was presented by Brunet and Clerc [2007], considering that the principal stress directions do not coincide with the orthotropic anisotropy axes.

Jones and Gillis [1984] have proposed a new method (further known as "Jones-Gillis theory (J-G)") for calculating the right hand side of the forming limit diagram of a sheet metal. The prediction of localized necking was made by assuming that biaxial stretching occurs in the three stages of deformation: perfectly homogeneous deformation, strain concentration at constant load and finally localized necking due to a rapidly load decrease. Later, Choi *et al.* [1989] has extended the J-G theory to the negative strains ratios, allowing the modelling of the entire forming limit curve.

In 1991, Dudzinski and Molinari [1991] introduced the linearised theory of perturbations. They first used the concept of effective instability and successfully adopted the instability method for prediction of forming limit diagrams. The dependence of the limit strains on the value of the instability intensity parameter presents the same tendencies as the dependence of the limit strains on the amplitude of the initial defect in the M-K analysis.

Another branch of forming limit calculation method was recently proposed by Bai and Wierzbicki [2008], based on the concept of "cumulative forming severity". Such approach makes use of a representation of the forming limit diagram in the space of the equivalent strain to neck and the Lode angle parameter. For non-proportional loadings, they introduced a non-linear accumulation of the forming severity thus improving the prediction of the loading history effect. Although good results were obtained for an aluminium alloy and a steel material, no physical interpretation of the "accumulation of the forming severity" was provided.

7.3 Forming limit calculation with damage consideration review

Since damage mainly occurs as a result of nucleation, growth and coalescence of cavities around particles during sheet metal forming operations, the internal degradation phenomenon can have an important effect in the limit strains that can be achieved before the appearance of localized necking, and, therefore, forming limit analysis should account for this mechanical degradation. Early works related with this damage consideration dates back to the late 1970's and constitutes an important phase of the research works on the localized necking of sheet metals.

First considerations of damage in necking calculations was made by Needleman and Triandafyllidis [1978] by considering a micromechanics-based formulation to describe the internal damaging process. Their calculation was based on the concept of imperfection, similar to the M-K model, but defining the imperfection as the ratio between the initial volume concentration of voids inside and outside the necking band

and considering the damaging process governed by the Gurson's void growth model. This same approach was also employed by Chu and Needleman [1980], Jalinier and Schmitt [1982], Barata da Rocha [1989] and Barlat [1989b] in order to analyse the effects of internal damage on the limit strains. An extension of this work was later proposed by Huang *et al.* [2000] by including a macroscopic yield criterion for anisotropic porous sheet metals in order to develop a failure prediction methodology in anisotropic damaged metals. Using the same methodology but adopting another void growth model, namely the Cocks and Ashby's model [Cocks 1982], Tjotta [1992] and Hu *et al.* [1998] have also considered a combined approach between internal damage growth and the M-K model.

But, after the developments of the Continuous Damage Mechanics framework during the 1980's, several researchers began to use CDM models in the localization analysis, namely using a scalar continuous variable to describe the internal damage evolution [Bontcheva 1994] [Doghri 1995] [Rizzi 1995] [Schreyer 1996] [Benallal 1996] and including the micro-crack closure effect in the isotropic damage models [Ekh 2000]. Combined approaches between isotropic damage models and the M-K model were also proposed by Tai [1988], Lee *et al.* [1997] and Tang and Tai [2000] within the framework of Continuous Damage Mechanics theory. Another approach was exploited by Boudeau and Gelin [2000], who have applied the linearised perturbation technique [Dudzinski 1991] combined with an isotropic damage model to theoretically determine the necking occurrence.

Especially important contributions were the works developed by Brunet *et al.* and Chow *et al.* An attempt to improve the MMFC model [Hora 1996] has made by Brunet *et al.* [1998] by introducing softening behaviour in the MMFC model, described by the micromechanical-based damage model GTN, taking the necking criterion the following form:

$$\frac{\tilde{\bar{\sigma}}}{\sigma_Y}\left(\frac{\partial\sigma_1}{\partial\varepsilon_1}+\frac{\partial\sigma_1}{\partial\beta}\frac{\partial\beta}{\partial\varepsilon_1}\right)\leq\sigma_1 \tag{7.51}$$

where σ_Y is the yield stress of the fully dense material and $\tilde{\bar{\sigma}}$ is the effective stress of the Gurson's potential. They have found that a good correlation between predicted and experimental FLD is achieved using this coupled analysis for aluminium alloys and almost no damage effect was observed in the necking predictions for the investigated mild steel. Later, a more advanced model was proposed by the same authors [Brunet 2001] including the influence of a triaxial stress state in the incipient neck through a correction of the uniform major stress. An approximate method was defined for this correction based on geometrical considerations for the necking profile.

Coupling the incremental theory of plasticity with an anisotropic damage evolution law, Chow *et al.* [1997] proposed a unified approach for forming limit diagrams prediction, based on the definition of a critical damage to necking, valid for proportional and non-proportional loading conditions. In view of the two distinct physical phenomena governing the cases of positive and negative strain ratios, two instability criteria were proposed to predict localized necking under drawing ($\beta \leq 0$) and biaxial stretching ($\beta > 0$). Critical damage to necking is defined as a function of the strain ratio, damage tensor and an additional material parameter. This orthotropic damage model has been employed to predict the FLD of VDIF steel and an excellent agreement between the predicted and measured results has been achieved. Later, the same authors [Chow 2001a] [Chow 2001b] extended their theory to incorporate a viscoplastic constitutive model of anisotropic damage, taking into account the effect of rotation of the principal damage coordinates on the deformation and damage behaviour.

Based on the simplified version of the vertex theory [Zhu 2001] and in their previous work [Chow 2003], Chow *et al.* [2004] combined the same anisotropic damage model with the modified vertex theory to generate a damage-coupled localization criteria, applicable on both sides of FLD. Using this approach, critical damage value for necking can be calculated as a function of stress / strain states and strain paths. They concluded that damage has a definite effect on forming limits and its consideration on necking determination enables the theoretical prediction to yield a better correlation with test results.

Recently, Chow *et al.* [2005] developed a localized necking criterion based on the singularity of the acoustic tensor. This criterion, applicable to materials exhibiting strain-softening behaviour, assumes that the critical condition for localized necking can be treated as an eigenvalue problem of second-order acoustic tensor. This criterion was applied to predict the FLD of the aluminium alloy 6061 at high temperature (450ºC) and a good agreement with tests were achieved. Further investigations lead Chow *et al.* [2007] to include on the acoustic tensor method an anisotropic damage model. A review of the works developed by Chow *et al.* can be found in [Chow 2009].

Other recent developments are attributed to Haddag *et al.* [2009]. Although the Rice's localization criteria [Rudnicki 1975] is seldom applied to the to study ductility limit of metal sheets (more suitable to describe localization on pressure-sensitive dilatant materials), Haddag *et al.* [2009] used a combined approach between an isotropic damage model, an elastic-plastic constitutive behaviour with hardening described by the Teodosiu-Hu model [Teodosiu 1995] and Rice's localization criteria to predict forming limits for linear and two-path straining modes. The trends predicted by this coupled approach were in accordance with the results obtained by the M-K model.

7.4 Proposed damage-coupled criterion (MMFC+AD)

Following the works addressed in previous section, a new damage-coupled criterion is proposed in this section. It is based on an integrated approach between the anisotropic damage model (presented in Chapter 5) and the MMFC necking criterion, proposed by Hora *et al.* [1996] (presented in Section 7.2.4). The choice for the MMFC model is intrinsically related with its advantages: easiness to implement, no additional parameters are required and is independent from the strain path trajectory, due to its differential form [Tong 2002]. Naturally, the introduction of the anisotropic damage mechanics concept into the MMFC instability criterion requires the definition of a new set of relations (as the ones defined in Section 7.2.4). It is important to refer that the definition of new relations does not change the instability model concept; only establishes new dependencies for the variables. Therefore, including the described anisotropic damage model, the variables that were originally only a function of the stress ratio α, Equation (7.34), now become also dependent of the damage tensor $\boldsymbol{D}$, introduced in the instability model as a parameter, not as a variable. This means that functions f and g, the strain ratio β and the partial derivatives f' and β' with respect α must be now expressed in terms of the stress ratio, α, and damage components. Thus, the proposed damage-coupled criterion is represented by the relation:

$$\frac{H'}{\sigma_Y} g\left(\alpha;\boldsymbol{D}\right) - \frac{f'\left(\alpha;\boldsymbol{D}\right)\beta\left(\alpha;\boldsymbol{D}\right)g\left(\alpha;\boldsymbol{D}\right)}{f\left(\alpha;\boldsymbol{D}\right)\beta'\left(\alpha;\boldsymbol{D}\right)\bar{\varepsilon}^p} \leq 1 \tag{7.52}$$

where $\boldsymbol{D}$ is the damage tensor, α the stress ratio, β the strain ratio, σ_Y the current yield stress, H' the tangent modulus to the hardening curve and $\bar{\varepsilon}^p$ the equivalent plastic strain.

The consideration of the anisotropic damage model, instead of the isotropic one, introduces in the necking model a important feature related with the effective stress definition proposed by Lemaitre *et al.* [2000a]. An effective triaxial stress state $\tilde{\boldsymbol{\sigma}}$ is developed from a general damaged plane stress state $\boldsymbol{\sigma}$, with the appearance of an effective stress in the thickness direction (denoted by $\tilde{\sigma}_{33}$, being direction 3 the thickness direction). This effective triaxial stress state can be shown if one considers a damaged representative volume element (RVE) in the orthotropic frame $\left(\vec{x}_1,\vec{x}_2,\vec{x}_3\right)$ subjected to a monotonic biaxial loading in principal stress directions. Assuming an isotropic material, having his plastic behaviour described by the von Mises criterion, the Cauchy stress tensor $\boldsymbol{\sigma}$ is given by:

$$\boldsymbol{\sigma} = \begin{bmatrix} \sigma_1 & 0 & 0 \\ 0 & \sigma_2 & 0 \\ 0 & 0 & 0 \end{bmatrix} \tag{7.53}$$

and the corresponding plastic strain rate tensor as:

$$\dot{\boldsymbol{\varepsilon}}^p = \begin{bmatrix} \dot{\varepsilon}_1^p & 0 & 0 \\ 0 & \dot{\varepsilon}_2^p & 0 \\ 0 & 0 & \dot{\varepsilon}_3^p \end{bmatrix}. \tag{7.54}$$

Using the anisotropic damage evolution law, the damage tensor is:

$$\dot{\boldsymbol{D}} = \left(\frac{\bar{Y}}{S}\right)^s \begin{bmatrix} \left|\dot{\varepsilon}_1^p\right| & 0 & 0 \\ 0 & \left|\dot{\varepsilon}_2^p\right| & 0 \\ 0 & 0 & \left|\dot{\varepsilon}_3^p\right| \end{bmatrix} = \begin{bmatrix} D_1 & 0 & 0 \\ 0 & D_2 & 0 \\ 0 & 0 & D_3 \end{bmatrix}, \tag{7.55}$$

having three principal components D_1, D_2 and D_3. Applying the effective stress definition [Lemaitre 2000a], the components of the effective stress tensor $\tilde{\boldsymbol{\sigma}}$ will be given by:

$$\begin{aligned} \tilde{\sigma}_1 = & \left[\frac{3}{\left(1-\eta D_H\right)} + \frac{4}{\left(1-D_1\right)} + \frac{1}{\left(1-D_2\right)} + \frac{1}{\left(1-D_3\right)}\right]\frac{\sigma_1}{9} \\ & + \left[\frac{3}{\left(1-\eta D_H\right)} - \frac{2}{\left(1-D_1\right)} - \frac{2}{\left(1-D_2\right)} + \frac{1}{\left(1-D_3\right)}\right]\frac{\sigma_2}{9} \end{aligned} \tag{7.56}$$

$$\begin{aligned} \tilde{\sigma}_2 = & \left[\frac{3}{\left(1-\eta D_H\right)} - \frac{2}{\left(1-D_1\right)} - \frac{2}{\left(1-D_2\right)} + \frac{1}{\left(1-D_3\right)}\right]\frac{\sigma_1}{9} \\ & + \left[\frac{3}{\left(1-\eta D_H\right)} + \frac{1}{\left(1-D_1\right)} + \frac{4}{\left(1-D_2\right)} + \frac{1}{\left(1-D_3\right)}\right]\frac{\sigma_2}{9} \end{aligned} \tag{7.57}$$

$$\begin{aligned} \tilde{\sigma}_3 = & \left[\frac{3}{\left(1-\eta D_H\right)} - \frac{2}{\left(1-D_1\right)} + \frac{1}{\left(1-D_2\right)} - \frac{2}{\left(1-D_3\right)}\right]\frac{\sigma_1}{9} \\ & + \left[\frac{3}{\left(1-\eta D_H\right)} + \frac{1}{\left(1-D_1\right)} - \frac{2}{\left(1-D_2\right)} - \frac{2}{\left(1-D_3\right)}\right]\frac{\sigma_2}{9} \end{aligned}. \tag{7.58}$$

So, an effective stress state $\tilde{\boldsymbol{\sigma}}$ that contains two components in the in-plane principal directions and, additionally, a component in the thickness direction is obtained. The influence of this effective triaxial stress state and of the anisotropic damage evolution is introduced in the necking criterion by means of the functions $f\left(\alpha;\boldsymbol{D}\right)$ and $g\left(\alpha;\boldsymbol{D}\right)$, strain ratio $\beta\left(\alpha;\boldsymbol{D}\right)$ and partial derivatives $f'\left(\alpha;\boldsymbol{D}\right)$ and $\beta'\left(\alpha;\boldsymbol{D}\right)$. Taking function

f as an example, which is defined as the ratio between the major in-plane principal stress σ_1 and the current yield stress σ_Y, and replacing the stress $\boldsymbol{\sigma}$ by the effective stress $\tilde{\boldsymbol{\sigma}}$ in the von Mises yield criterion, one obtains:

$$f\left(\alpha;\boldsymbol{D}\right)=\frac{1}{\sqrt{p\left(\boldsymbol{D}\right)\alpha^2-q\left(\boldsymbol{D}\right)\alpha+r\left(\boldsymbol{D}\right)}} \tag{7.59}$$

where functions $p\left(\boldsymbol{D}\right)$, $q\left(\boldsymbol{D}\right)$ and $r\left(\boldsymbol{D}\right)$ are dependent upon principal damage values (D_1, D_2, D_3) and can be explicitly written as:

$$\begin{aligned}p\left(\boldsymbol{D}\right)=&\frac{1}{2}\left(\frac{1}{3\left(1-D_1\right)}+\frac{2}{3\left(1-D_2\right)}\right)^2+\frac{1}{2}\left(\frac{2}{3\left(1-D_2\right)}+\frac{1}{3\left(1-D_3\right)}\right)^2\\&+\frac{1}{2}\left(-\frac{1}{3\left(1-D_3\right)}+\frac{1}{3\left(1-D_1\right)}\right)^2\end{aligned} \tag{7.60}$$

$$\begin{aligned}q\left(\boldsymbol{D}\right)=&\left(\frac{2}{3\left(1-D_1\right)}+\frac{1}{3\left(1-D_2\right)}\right)\left(\frac{1}{3\left(1-D_1\right)}+\frac{2}{3\left(1-D_2\right)}\right)\\&+\left(\frac{2}{3\left(1-D_2\right)}+\frac{1}{3\left(1-D_3\right)}\right)\left(\frac{1}{3\left(1-D_2\right)}-\frac{1}{3\left(1-D_3\right)}\right)\\&+\left(\frac{1}{3\left(1-D_3\right)}+\frac{2}{3\left(1-D_1\right)}\right)\left(-\frac{1}{3\left(1-D_3\right)}+\frac{1}{3\left(1-D_1\right)}\right)\end{aligned} \tag{7.61}$$

$$\begin{aligned}r\left(\boldsymbol{D}\right)=&\frac{1}{2}\left(\frac{2}{3\left(1-D_1\right)}+\frac{1}{3\left(1-D_2\right)}\right)^2+\frac{1}{2}\left(-\frac{1}{3\left(1-D_2\right)}+\frac{1}{3\left(1-D_3\right)}\right)^2\\&+\frac{1}{2}\left(\frac{1}{3\left(1-D_3\right)}+\frac{2}{3\left(1-D_1\right)}\right)^2\end{aligned}\ . \tag{7.62}$$

Hence, if a distinctive damage evolution is considered, function f value will be affected by the damage values calculated for each direction. It is possible to infer from Equations (7.60) to (7.62) that a damage increase leads to an increase of the values of the functions $p\left(\boldsymbol{D}\right)$, $q\left(\boldsymbol{D}\right)$ and $r\left(\boldsymbol{D}\right)$ which, consequently, leads directly to a decrease of the value of function f. Furthermore, if no damage occurs, the effective stress, $\tilde{\sigma}_3$, along thickness direction is eliminated and functions $p\left(\boldsymbol{D}\right)$, $q\left(\boldsymbol{D}\right)$ and $r\left(\boldsymbol{D}\right)$ will be equal to:

$$\begin{aligned}p\left(\boldsymbol{0}\right)&=1\\q\left(\boldsymbol{0}\right)&=1\ ,\\r\left(\boldsymbol{0}\right)&=1\end{aligned} \tag{7.63}$$

recovering, therefore, as a limiting case, the classical definition for function f:

$$f\left(\alpha;\boldsymbol{0}\right)=\frac{1}{\sqrt{\alpha^2-\alpha+1}}. \tag{7.64}$$

A remark can be made concerning the use of the MMFC model coupled with an isotropic damage model. If damage is considered as an isotropic scalar variable D, the effective stress tensor $\tilde{\boldsymbol{\sigma}}$ is obtained from the Cauchy stress tensor by multiplying the factor $1/\left(1-D\right)$ as:

$$\tilde{\boldsymbol{\sigma}}=\frac{1}{1-D}\boldsymbol{\sigma} \tag{7.65}$$

and, in this case, the effective triaxial stress state is not established. For an isotropic yield material, the strain ratio β, its derivative in order to stress ratio β' and the function g, defined as the ratio between the current equivalent plastic strain and the major in-plane principal strain ε_1, are independent on the scalar damage value D. Function f and corresponding derivative f' are dependent on the scalar damage value:

$$f\left(\alpha;D\right)=\frac{1}{1-D}\left(1+\alpha^2-\alpha\right)^{-\frac{1}{2}} \tag{7.66}$$

$$f'\left(\alpha;D\right)=\frac{\partial f}{\partial\alpha}=\frac{1}{1-D}\left(\frac{1-2\alpha}{2}\right)\left(1+\alpha^2-\alpha\right)^{-\frac{3}{2}}. \tag{7.67}$$

However, its influence on the MMFC model is removed in the ratio f'/f and therefore the original MMFC is recovered:

$$\frac{H'}{\sigma_Y}g\left(\alpha\right)-\frac{f'\left(\alpha\right)\beta\left(\alpha\right)g\left(\alpha\right)}{f\left(\alpha\right)\beta'\left(\alpha\right)\bar{\varepsilon}^p}\leq 1. \tag{7.68}$$

To the author’s knowledge, the computational implementation of the above coupled approach has not been addressed yet. This is probably due to the fact that an increased degree of complexity is introduced by using a second-order definition for the damage variable and corresponding intricacy in effective stress calculation when compared with the isotropic damage model.

7.5 Application of MMFC+AD for forming limit diagrams prediction

The material selected to illustrate the performance of the proposed criterion is the aluminium alloy AA6014. The material data as well as the FLD data were taken from Mattiasson *et al.* work [2007]. According to Mattiasson *et al.* [2007], this material exhibits a distinct necking behaviour before fracture and shows minor strain rate dependence. The material mechanical properties are presented in Table 7.1, as well as the corresponding damage parameters for its characterization [Lemaitre 2005]. The material is assumed to have isotropic hardening described by the Voce law and Hill48 yield criterion was used to describe the orthotropic anisotropy of the rolled sheet. Two values are presented for the damage denominator parameter, 1.22 and 0.976 MPa, corresponding to the value identified by Lemaitre *et al.* [2005] for the isotropic model and the value identified for the anisotropic damage model using the cross identification procedure proposed by Desmorat and Otin [2008a] (see Section 6.2 for more details), respectively.

Table 7.1 Material parameters of AA 6014.

Property	**Symbol**	**Value**
Young modulus [GPa]	E	70
Poisson coefficient	υ	0.33
Initial yield stress [MPa]	σ_{Y0}	125
Yield stress [MPa]	σ_Y	$350.72 - 225.72e^{-5.738\bar{\varepsilon}^p}$
r-values	r_0, r_{45}, r_{90}	0.75, 0.5, 0.62
Damage denominator [MPa]	S	1.22,0.976
Damage exponent	s	2.0
Damage threshold	ε_D^p	0.05
Critical damage value (failure)	D_C	0.36
Damage hydrostatic parameter	η	2.6

In order to establish a starting point for the illustration of the performance of the proposed integrated approach, the computation of the theoretical FLDs calculated by using the M-K model [Marciniak 1967] and the original MMFC model [Hora 1996] were performed. A comparison between experimental necking points and theoretical FLDs for linear strain paths (LSP) is presented in Figure 7.8.

Using Hill's quadratic criterion and an imperfection factor of $f_0 = 0.990$, M-K analysis computes limit strains that follows the experimental tendency in the stretching zone, i.e., in the right hand side of FLD, but, near the equibiaxial stretching path, computed strains are heavily overestimated, Figure 7.8. It is known that the yield function has a strong effect on the shape of the yield surface and a tremendous effect on the level of the forming limit diagram in the biaxial region as previous studies also have shown [Barlat 1987] [Barata da Rocha 2009] and, thus, the use of more advanced constitutive models can lead to more satisfactory computed limit strains in this region [Butuc 2004].

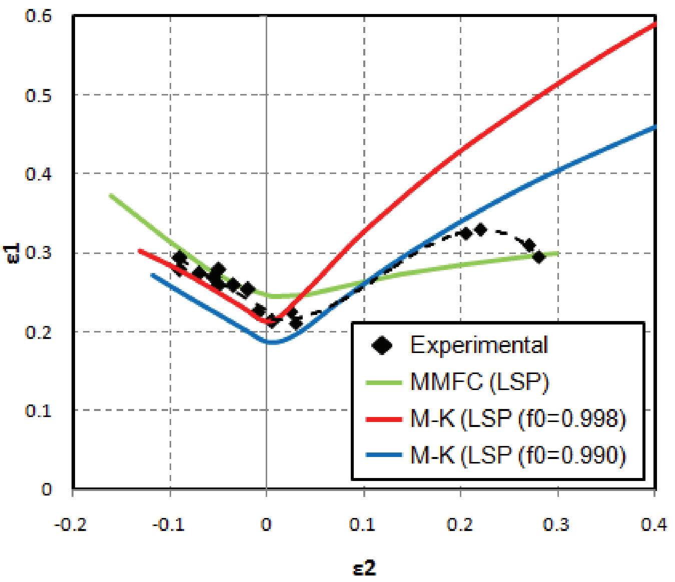

Figure 7.8 Comparison between experimental and theoretical FLDs for AA 6014.

Also, M-K analysis with an imperfection factor of 0.990 shows to be conservative in the drawing zone, i.e., in left hand side of FLD, predicting necking strains lower than the experimental ones. Using higher values for the imperfection factor f_0, the predicted forming limit curve has a shift to upper values of limit strains, improving the numerical predictions in the drawing zone and in the plane strain trajectory. Although better agreement is observed in the drawing zone, the overestimation of critical strains observed in the equibiaxial stretching path for a lower value of f_0 is extended to the entire biaxial stretching zone, as shown in Figure 7.8.

Concerning the forming limit curve computed by the MMFC model, it is shown that it is capable to represent reasonably well the experimental points at tension-compression state ($\beta < 0$) but, as already was observed by others authors [Mattiasson 2007], critical strains for tension-tension stress states ($\beta > 0$) are usually underestimated by this criterion, Figure 7.8. A better agreement in this region is achieved by using the proposed damage-coupled criterion (MMFC+AD), following more closely the experimental tendency in the biaxial strain region ($\beta > 0$), Figure 7.9.

The explanation for this behaviour is connected with the consideration of a distinctive tridimensional damage evolution that promotes the appearance of an effective triaxial stress state. Introducing the non-planar damage evolution, a correction is made in the variables of the original MMFC model that induces a delay in the necking criterion, postponing neck formation prediction and, therefore, allowing that an additional hardening effect occurs before necking condition is achieved, Figure 7.10.

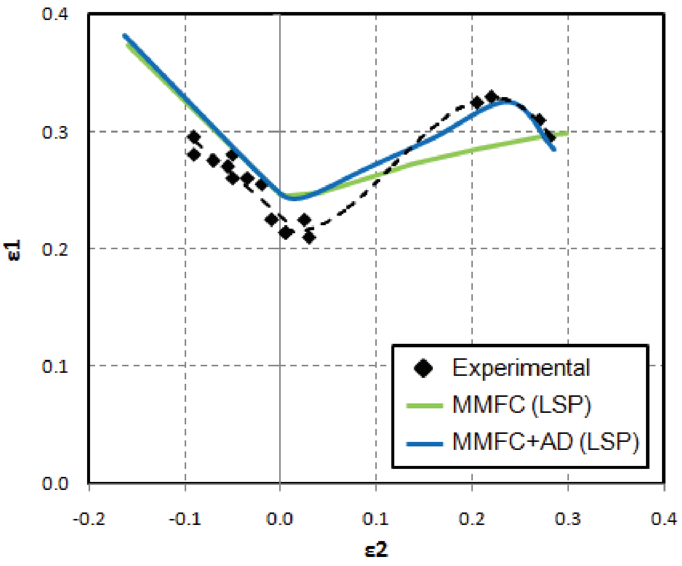

Figure 7.9 Comparison between experimental and theoretical FLDs for AA 6014.

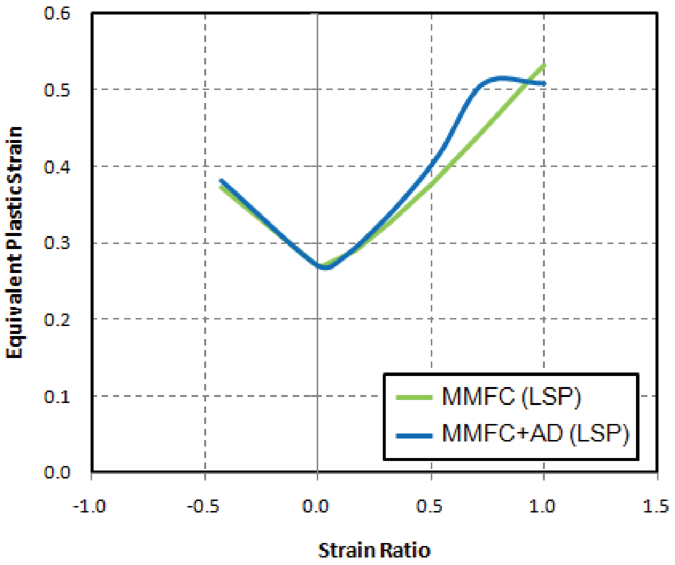

Figure 7.10 Additional hardening promoted by the introduction of anisotropic damage model into the MMFC criterion.

A similar additional hardening effect was also described by Gotoh *et al.* [1995], who has investigated the effect of out-of-plane stresses in forming limits. The theoretical study was shown that out-of-plane stress (even small compared to the equivalent stress) may notably raise the forming limit strain and, thus, it can be effectively used to avoid earlier failure during sheet metal forming. The main difference to the current study is that here there is no imposition of a triaxial stress state. The effective stress definition from the anisotropic damage law naturally develops a gradual non-planar effective stress, induced by the increase of damage in this direction, retarding necking prediction. As can be seen in Figure 7.9, this damage induced delaying effect has almost no importance on tension-compression states but its influence is clear in the biaxial stretching zone. To explain this, we need to recall the anisotropic damage evolution law (Section 5.3.1.3). The effective damage energy release rate $\overline{Y}$ variable, present in the evolution law, given as:

$$\overline{Y} = \frac{\tilde{\bar{\sigma}}^2}{2E}\left[\frac{2}{3}\left(1+\nu\right)+3\left(1-2\nu\right)\left(\frac{\tilde{\sigma}_H}{\tilde{\bar{\sigma}}}\right)^2\right] \tag{7.69}$$

is dependent on the stress triaxiality, defined by the ratio between the effective hydrostatic stress $\tilde{\sigma}_H$ and the von Mises equivalent stress $\tilde{\bar{\sigma}}$. Such dependence means that higher stress ratios will correspond to higher stress triaxialities and, thus, to faster damage growths under biaxial tension stress states. This increased damage evolution adds an increase influence of the damage values on the necking criterion, observed by the growing difference of the curves in Figure 7.10. Moreover, necking in biaxial tension is slowed down by a stabilization effect which allows attaining higher values of plastic strains and, therefore, higher values of damage will occur, turning the influence of anisotropic damage more pronounced. This can be seen in Figure 7.11, where higher damage values up to necking are calculated for higher strain ratios. Also, it is shown that it is not possible to define a constant critical damage value for necking, as is done for fracture, since the critical value depends on strain ratio and stress state.

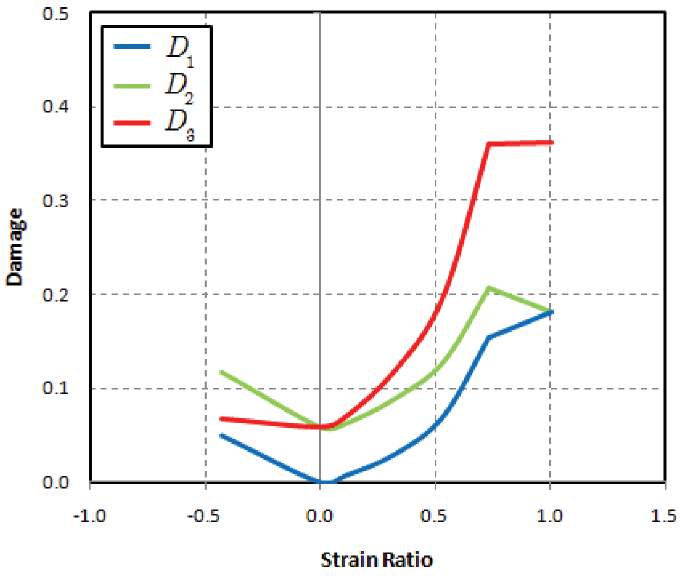

Figure 7.11 Critical damage values for necking. Damage value in thickness direction reaches more important values on the right hand side of the FLD.

In the plane strain path, the damage effect in the forming limit calculation is eliminated due to the fact that strain ratio β is equal to zero, thus eliminating all the second term of the first member in Equation (7.52), rewritten here:

$$\frac{H'}{\sigma_Y} g\left(\alpha;\boldsymbol{D}\right) - \frac{f'\left(\alpha;\boldsymbol{D}\right)\beta\left(\alpha;\boldsymbol{D}\right)g\left(\alpha;\boldsymbol{D}\right)}{f\left(\alpha;\boldsymbol{D}\right)\beta'\left(\alpha;\boldsymbol{D}\right)\bar{\varepsilon}^p} \leq 1 . \qquad (7.70)$$

This implies that theoretical predictions for this strain path using the proposed criterion are identical to the original MMFC model and, by the same reason, this last criterion reduces to Swift model [Swift 1952] and Hill model [Hill 1952] calculations.

An important phenomenon occurs near the equibiaxial stretching path. As indicated by the truncated shape of the experimental forming limit curve in Figure 7.9, one can expect that the material has failed in ductile fracture in this area [Mattiasson 2008]. Therefore, limit strains in this zone are governed by ductile failure rather than by local necking and a correction to the forming limit curve must be performed due to the abrupt failure. The calculations using only necking models will necessarily overestimate the limit strains in this region (Figure 7.8) since no fracture occurrence modelling is performed. The coupled approach of the proposed criterion allows us to model this “fragile” behaviour of the material, as seen in Figure 7.9. At these trajectories, the critical damage for failure is achieved before plastic instability, determined by the necking model, is attained and, therefore, fracture is the most restrictive event in this material under these loading conditions. This phenomenon illustrates the importance of the coupled calculation of forming limits considering not only the appearance of localized necking but also final fracture occurrence.

Also important is the contribution of each damage values on failure occurrence. In the drawing zone (left hand side of FLD), the damage component along the loading direction D_1 (in this case coincident with the principal stress and strain directions) is the most important value and is responsible for the activation of the critical damage criterion. The values attained in the transverse and perpendicular directions to the loading direction, D_2 and D_3 respectively, are significantly lower and assume distinct values, according to the anisotropic behaviour of the material. The importance of this component decreases gradually with increasing triaxiality and strain ratio until the plane strain path is reached. In this strain path, since plastic straining only occurs in loading and thickness directions, no damage will occur in the transverse direction, $D_2 = 0$ and, according to volume constancy condition, plastic strains in the loading and thickness direction, although with different sign, have the same absolute value and, therefore, same damage values for both directions are calculated $D_1 = D_3$, as seen in Figure 7.11. In the stretching zone, i.e., under positive strain ratios ($\beta > 0$), the contribution of the in-plane damage values are relegated to “second place”, assuming the damage value in the thickness direction D_3 the leading role as the most critical damage value. The importance of this component will be higher as higher strain ratios are considered and will be particularly relevant in materials that present a normal anisotropy value lower than one (as is the case with a $\overline{r} < 1$).

The proposed criterion allows also the determination of limit strains in complex strain paths evolutions, as those that are undergone by industrial parts during a single or multi-pass forming process. The assessment of sheet material behaviour under such non-linear strain paths is often examined by means of different combination of linear deformation paths.

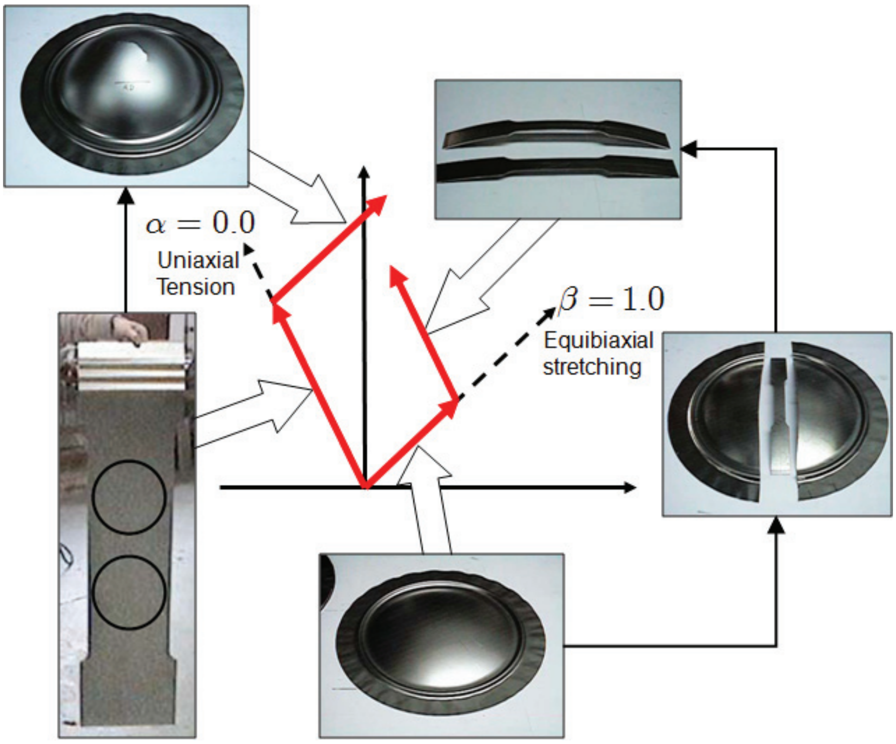

Figure 7.12 Experimental procedure and samples involved in determination of bilinear strain paths limits: uniaxial tension + equibiaxial stretching (UT-BS) and equibiaxial stretching + uniaxial tension (BS-UT).

Two different types of complex FLDs can be used to determine the effect of strain path changes on the formability of the material [Barata da Rocha 1985]: one preliminary deformation followed by proportional straining at different strain ratios and one linear prestrain up to different deformation levels and subsequent straining at a fixed strain ratio. Figure 7.12 shows the experimental procedure and required samples in order to determine forming limits in such bilinear strain paths evolution [Barata da Rocha 2009]. In Figure 7.13, the predicted forming limit curves for a complex FLD is presented, involving a bilinear strain path composed by prestraining in biaxial stretching followed by uniaxial tension (BS-UT).

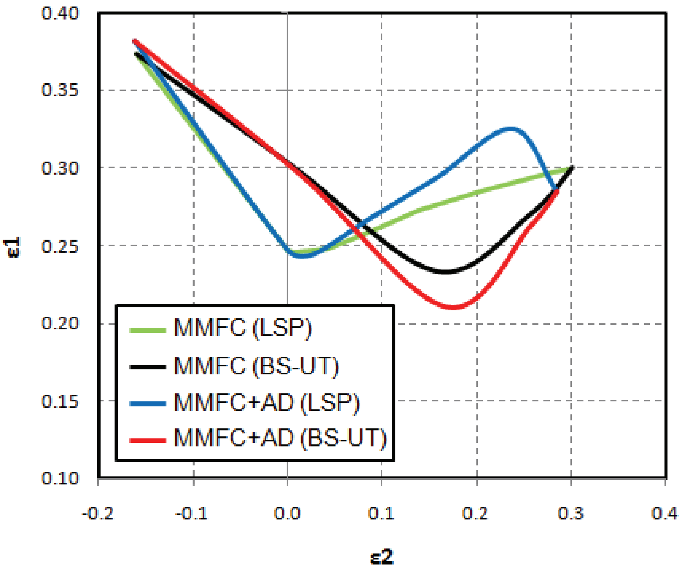

Figure 7.13 Theoretical FLDs for biaxial stretching followed by uniaxial tension (BS-UT) (AA 6014).

This strain path change (BS-UT) is usually characterized by premature instabilities occurrences, especially for higher values of prestrain in biaxial stretching. However, an enhancement of subsequent uniaxial tension limit strains is observed for small amounts of prestrain under biaxial stretching. Additionally, there is a shift of the FLD lowest point to higher values of ε_2 and, so, necking can occur with combinations of strains below the standard FLD, obtained under linear strain paths evolutions. For this particular case, the anisotropic damage effect is more pronounced for higher values of prestrain under biaxial stretching. The calculated forming limits using the proposed criterion give lower limit strains than the ones calculated using the original MMFC for such high prestrain levels. At those levels, high values of damage are attained in the first strain path and a drastic change to uniaxial tension causes early necking occurrence. To perceive this event, it is necessary to define a variable called risk factor k [Tong 2002], given by:

$$k = \frac{H'}{\sigma_Y} g\left(\alpha;\boldsymbol{D}\right) - \frac{f'\left(\alpha;\boldsymbol{D}\right)\beta\left(\alpha;\boldsymbol{D}\right)g\left(\alpha;\boldsymbol{D}\right)}{f\left(\alpha;\boldsymbol{D}\right)\beta'\left(\alpha;\boldsymbol{D}\right)\bar{\varepsilon}^{p}}, \tag{7.71}$$

which, according to the proposed criterion in Equation (7.52), necking is detected when:

$$k \leq 1. \tag{7.72}$$

The evolution of such risk factor k for the MMFC criterion and the proposed criterion (MMFC+AD) is presented in Figure 7.14 for a prestrain value of 0.32 under biaxial stretching.

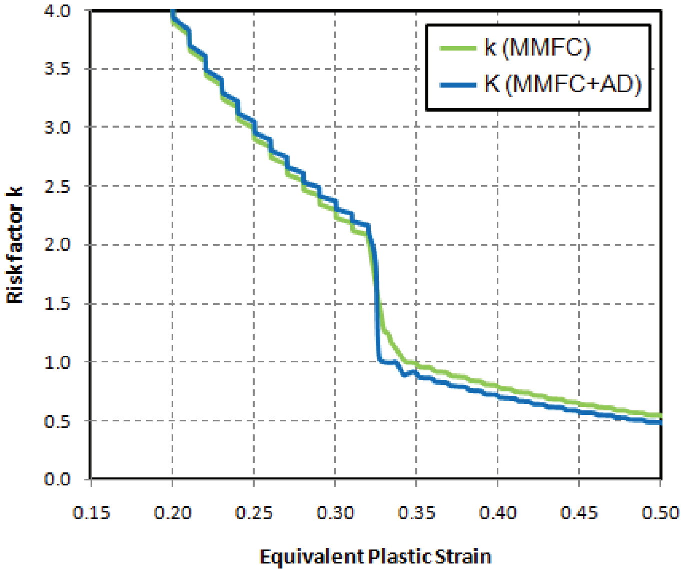

Figure 7.14 Risk factor evolution for a biaxial stretching followed by uniaxial tension strain path (prestrain of 0.32).

Before the strain path change, the risk factor k calculated by the MMFC+AD criterion is higher than the one calculated by the original MMFC criterion. This effect reveals the delay in necking formation prediction due to the damage evolution, similarly to the effect already observed during linear strain paths evolutions. But, when the drastic change to uniaxial tension takes place, risk factor calculated by the MMFC+AD criterion falls to a value lower than the one computed by the MMFC criterion and, following a similar evolution, necking is predicted for lower plastic strains with the proposed criterion. This indicates that, besides the additional hardening effect promoted by the increase of damage, the softening effect, originated by mechanical properties degradation that affects yielding, plays an inverse role in the analysis of the complex mechanism of triggering localized necking, causing the lowering of forming limits. Therefore, anisotropic damage establishes a combined effect between supplementary hardening and decrease of load-carrying capability. On one hand, the presence of a non-planar effective stress state and distinctive evolutions of damage is responsible for the increase of hardening, postponing necking formation but, on the other hand, damage induces a mechanical degradation that promotes early neck development. This combination of mechanisms has a strong influence on the FLD level and will be dependent on strain and stress history.

The other type of studied strain path change is the one defined by a prestrain in uniaxial tension until different deformation levels followed by straining in equibiaxial stretching up to necking / failure (UT-BS). The predicted forming limit curves for this strain path change are presented in Figure 7.15 using the original MMFC and the proposed criterion (MMFC+AD).

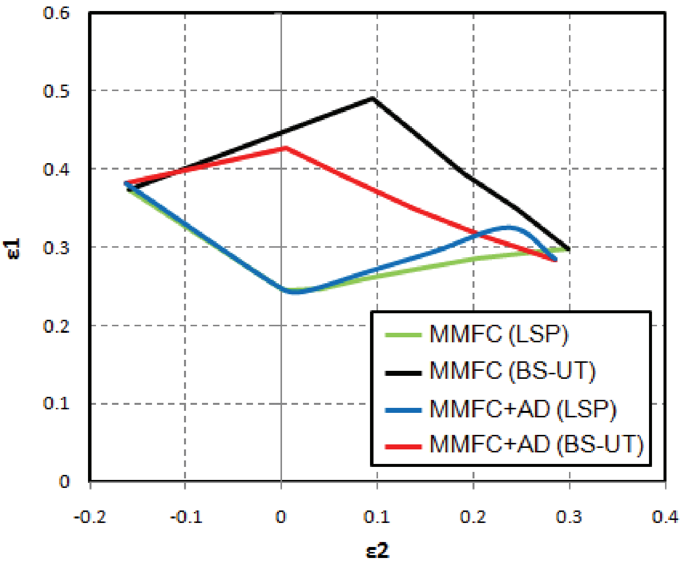

Figure 7.15 Theoretical FLDs for uniaxial tension followed by biaxial stretching (UT-BS) (AA 6014).

Imposing uniaxial tension as the preloading path, there is a considerable increase in forming limit strains and combinations of in-plane plastic strains are possible well above the standard FLD without risk of necking occurrence [Barata da Rocha 1985] [Butuc 2003] [Barata da Rocha 2009]. For this bilinear strain path, the proposed criterion (MMFC+AD) predicts that failure will occur before necking and the computed failure limit strains are significantly lower than the ones calculated by the original MMFC for necking, Figure 7.15. In this case, the influence of the anisotropic damage induced hardening effect, observed for linear strain paths evolutions under positive strain conditions, is negligible since the raise in limiting strains is hampered by the occurrence of premature failure.

Another question aroused in Figure 7.15 is the difference between the critical strains values attained for failure in linear and this bilinear strain path evolution, near equibiaxial stretching. To show this difference, Figure 7.16 presents the calculated fracture forming limit curves (FFLDs) for the linear and the bilinear strain path evolution, uniaxial tension followed by biaxial stretching. As can be seen in Figure 7.16, there is an effect of strain path change in the fracture forming limit locus. Considering the same final point in the principal strain space, higher values for damage are computed for the bilinear strain path combination when compared with the ones attained for a linear strain path evolution, and, therefore, a decrease on material ductility will be observed. This fact can be explained by the damage evolution law and its dependencies.

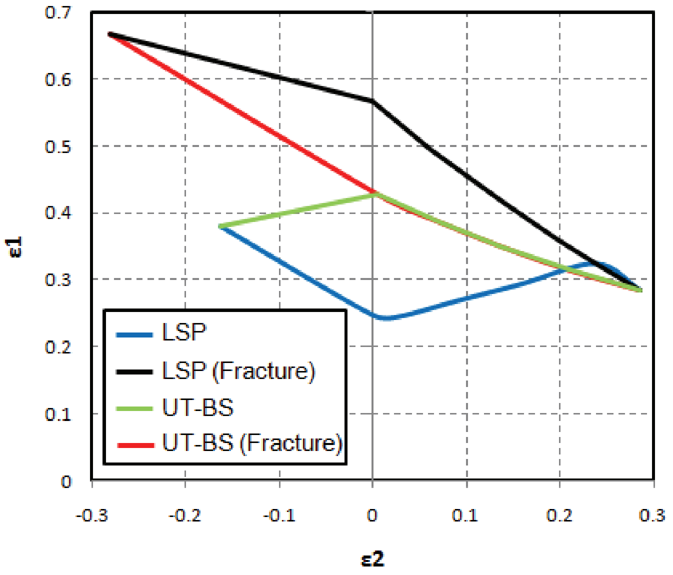

Figure 7.16 Theoretical FFLDs for linear strain paths and for uniaxial tension followed by biaxial stretching (UT-BS) strain paths using MMFC+AD (AA 6014).

At the beginning of the second strain path, material has already accumulated damage in all three directions, being the major value in the loading direction (in this case D_1). A change to a biaxial stretching loading condition will increase stress triaxiality, implying a higher damage rate, and, due to the fact that here we are not considering any healing effect, damage will grow rapidly under these conditions and will promptly attain the defined critical value. Naturally, the difference between the linear and the bilinear computed critical strains will be larger as more damage is accumulated during straining in the first strain path.

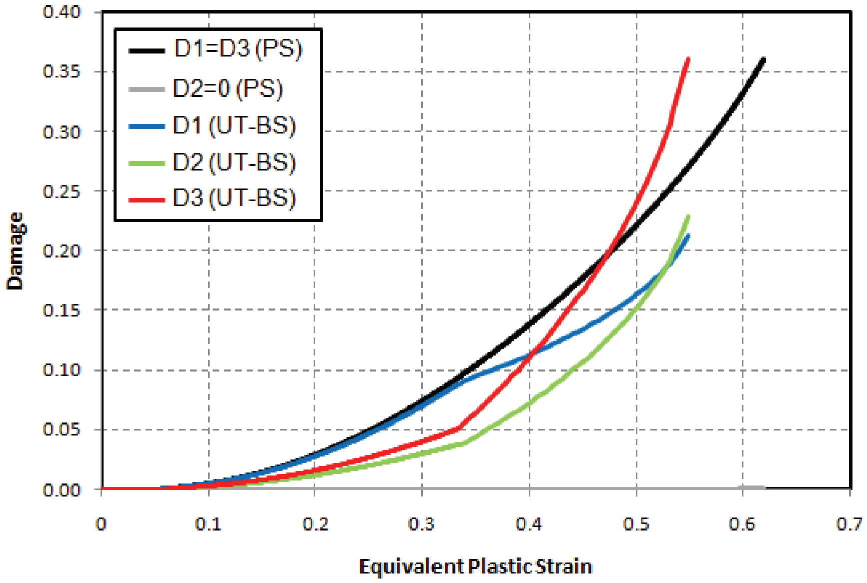

Figure 7.17 Damage evolution comparison between plane strain trajectory (PS) and bilinear strain path (UT-BS).

An example of such effect is shown for the plane strain trajectory (PS) and the bilinear strain path comprised by a prestrain of 0.33 in uniaxial tension followed by an equibiaxial stretching (UT-BS). Both of these strain path evolutions lead to predicted failure strains in the major plastic strain axis ($\varepsilon_2 = 0$). The latter strain path indicates that failure occurs for a major plastic strain of 0.428 while for the linear plane strain path, failure is detected for a higher major plastic strain, namely 0.566. Damage growth for both strain paths evolutions are presented in Figure 7.17. As shown in Figure 7.17, for the plane strain loading (PS), the evolution of damage in the loading and thickness directions are identical ($D_1 = D_3$) and, according to the plane strain condition, no damage is computed in the transverse direction ($D_2 = 0$). Under this loading condition, critical damage is attained simultaneously by D_1 and D_3 when an equivalent plastic strain of 0.618 is attained. Concerning the damage development in the non-linear path (UT-BS), it is necessary to distinguish between growth rates before and after the change in strain path, i.e., during uniaxial loading and during biaxial loading. During loading in uniaxial tension, there is an uneven increase of damage tensor components, being the component in the loading direction D_1 the one that has a more evident growth, mainly dominated by the plastic strain rate attained in this direction. But, after the change in the deformation path, there is a clear change in the growth of damage in the different directions. One witnesses an exponential growth of damage component in the thickness direction D_3, as a result of the higher established stress triaxiality and the higher plastic strain rate in the thickness direction. Although with a lower magnitude, also damage in transverse direction D_2 has an increase in the growth rate and a marked decrease in the growth rate is observed for the component under which pre-loading in uniaxial tension was made, D_1. These two in-plane components tend to achieve the same value, in accordance with the equality of corresponding plastic strains rates, proper of an equibiaxial stretching state. The exponential evolution of the component D_3 promotes a rapid material degradation and this component quickly reaches the condition for the macro-crack initiation and failure is detected. Therefore, computed critical strains will be largely dependent on the strain and damage state reached in the preloading path. In the linear strain path case, straining starts from an undeformed and undamaged material. Damage will evolve only after damage threshold is reached and his evolution rate will be proportional to the stress triaxiality for the specific loading path, which is lower than the value for equibiaxial stretching. This will lead to lower values of accumulated damage and, by its turn, to higher computed critical strains to failure, when compared to the ones obtained for a bilinear combination.

7.6 Concluding remarks

A model for necking and fracture initiation prediction was presented in this chapter. It is based on an integrated approach between the Modified Maximum Force criterion (MMFC) proposed by Hora *et al.* [1996] and the anisotropic damage evolution law proposed by Lemaitre *et al.* [2000a]. The main advantage of the proposed criterion is the fact that it allows the prediction of necking and fracture initiation, especially important in materials that may suffer abrupt fracture before any visible localized necking, raising questions in the applicability of the conventional forming limit curve. Another enhancement provided by the proposed model is the improved necking prediction, shown by the obtained good correlation between experimental FLDs and the predicted forming limits using the necking criterion coupled with anisotropic damage. This improvement can be related with the distinct damage evolution on different directions that promotes the appearance of an effective triaxial stress state and the correction of the functions in the MMFC model, which are responsible for the delay effect in the necking criterion, allowing the additional hardening before necking process. Besides the additional hardening effect promoted by the increase of damage, the softening effect originated by mechanical properties degradation also plays a significant role in the analysis of the complex mechanism of triggering localized necking. A lowering of forming limits due to the mechanical properties degradation was experienced for the bilinear strain path combination composed by equibiaxial stretching followed by uniaxial tension, denoting that anisotropic damage introduces a combined effect between supplementary hardening and decrease of load-carrying capability into the necking criterion. A dependence of the fracture forming limit curve level on the strain path evolution was also observed. The fracture forming limit curve calculated for a linear strain path evolution presents higher limits strains then the ones calculated for the bilinear strain path combinations. The higher dissimilarity is observed for the combination of uniaxial tension followed by biaxial stretching, explained by the imposed damage growth in the second deformation trajectory that imposes a more drastic reduction of the mechanical behaviour of the material, leading to a premature failure. The validation of this coupled approach using other materials and the evaluation of the model's performance on necking prediction under linear and non-linear strain paths evolutions is one of the future developments that will be analysed as well as the further investigation of the dependence of fracture strain limits on the strain path evolution.

8. CONCLUSION AND FINAL REMARKS

Some global conclusions of this work are presented. Additionally, it is also referred some future work perspectives.

8.1 General conclusions

The interest shown by industry in the use of numerical tools, especially by the automotive industry, is high. The main purpose of the use of these numerical tools in the simulation of sheet metal forming is to accurately predict the occurrence of any defects in the stamped component during its design and development phases. However, due to the high complexity, nonlinearity and interactivity of several phenomena involved in the deep drawing process, the numerical results may not match the experimentally observed behaviour. In the last decades, there has been a significant evolution of these numerical tools in order to reproduce in a reliable manner, the industrial reality. The introduction of new constitutive models for mechanical characterization, the growing desire to provide results in reasonable time from an industrial and economical standpoint, the correct prediction of residual stresses, the effects of springback and its compensation have been subject of intense research to meet the requirements placed by industry. One of the defects that can occur during a sheet metal forming operation is the rupture occurrence, which has assumed a prominent position in recent years. Usually, this phenomenon is preceded by the occurrence of a plastic instability, a localized neck, which is taken as the criterion for the rejection of stamped parts. Traditionally, the prediction of necking is performed by the analysis of the deformations of the final stamped part, comparing the achieved strain values with the forming limit curve, an experimental (or theoretical) curve that defines the limiting values for necking, according to the deformation trajectory undergone by each material point. However, the usage of new materials in sheet metal forming has brought new challenges to the stamping industry and to the numerical simulation of metal forming processes. These new materials are characterized by higher values of tensile strength but present lower ductility when compared to the so-called traditional materials. This lower ductility makes these materials particularly prone to breakage during processing, without any prior indication of necking occurrence. This unexpected fracture raises questions on the use of the conventional forming limit diagram concept to evaluate the formability of these materials and has promoted the need to introduce new failure criteria to predict such behaviour. Current trend is to replace the forming limit diagram concept by the use of theories that introduce ductile failure indicators based on the definition of an internal variable that represents the state and evolution of internal degradation of the mechanical properties of the material.

The work presented in this thesis follows this trend and interest shown by industry on such theories and aims to contribute to the improvement of numerical codes in determining fracture in sheet metal forming by adopting ductile damage models, within the framework of Continuum Damage Mechanics theory. For such purpose, the basic concepts of the Continuum Damage Mechanics theory were introduced and, using a scalar definition for the damage variable, a damage model including anisotropic flow behaviour was formulated. For the implementation of the devised model, two algorithms were proposed: a fully coupled algorithm, considering a strong link between the two dissipative phenomena, plasticity and damage, and a partially coupled algorithm, in which, although with damaging phenomenon affecting plasticity, the two phenomena are treated and integrated independently. In the latter algorithm, an additional enhancement to the original theory was introduced: the micro-crack closure effect, included in the damage evolution law by means of a tensile / compressive split of the stress tensor. This effect assumes that, when subjected to compressive stress states, micro-cracks may partially close and, thus, limits the damage growth under such conditions. This unilateral effect on damage growth has proved to be important in the deep drawing of a cylindrical cup, capturing the observed experimental behaviour. Also, a comparison between the fully coupled and partially coupled strategies performed in this benchmark has shown that the partial coupled algorithm can be adopted in explicit time integration codes for failure predictions in metal forming operations without a significant loss in the accuracy of the evolution of progressive plastic softening.

A higher order definition for the damage variable, namely a second order tensor definition, was further presented in order to describe the directional behaviour of micro-cracking, inevitably guided by the directions of loading and plastic flow. Analogously to the isotropic scalar damage variable, a model accounting for anisotropic plastic behaviour that characterizes the rolled sheet metals was formulated for the second-order damage definition and the corresponding integration algorithm addressed.

Concerning the comparison between the scalar and tensorial damage definitions, no significant differences were found in the predicted punch displacements to failure provided by the two approaches. For the presented numerical cases and using the considered aluminium alloy, one may conclude that the adoption of an isotropic scalar definition for damage can provide satisfactory failure predictions in accordance with experimental results, thus introducing a lower complexity in the constitutive model and, consequently, reducing computation time. However, this conclusion cannot be directly extrapolated to other sheet materials and more complex stamping cases, involving highly non-proportional loadings. A further study using more complicated examples and other sheet materials should be conducted.

A huge influence of the tribological conditions established between the blank and the active tool surfaces on the predicted failure site and computed critical punch displacements was revealed by the numerical examples. It was found that a small change in the friction coefficient can lead to unreliable failure predictions delivered by the implemented damage models. So, one may remark that it is crucial to impose higher requirements in the contact with friction modelling in order to obtain reliable failure predictions. These requirements may include the formulation of new frictional constitutive equations, the adoption of variable friction coefficients (dependent upon parameters such as pressure, sliding speed, temperature, slip direction, roughness evolution, etc.) and the development of experimental techniques that allow a reliable and systematic characterization of the tribological behaviour, taking into account the interactivity between the numerous phenomena involved in the sheet-tool contact.

The failure prediction ability, by itself, does not fulfil all the necessary requirements for formability assessment in sheet metal forming operations. A general formability criterion should also address the determination of the amount of useful deformation that can be imposed to a part before the occurrence of localized necking. With such purpose, an integrated approach between a plastic instability model and the anisotropic damage model was proposed. The new approach allows the prediction of the two last phases of plastic deformation, necking and failure, and is capable to determine which phase represents the most restrictive event in a sheet metal forming operation. Using the proposed methodology, numerical results have highlighted the importance of the coupled approach due to the occurrence of fracture before necking near equibiaxial stretching strain path. Also, results have shown that the introduction of distinctive damage evolutions in the plastic instability criterion produces improved necking predictions, following more closely the experimental tendency, due to the appearance of an effective triaxial stress state and correction of variables of the necking criterion that triggers an additional hardening effect.

8.2 Future work

Some perspectives concerning the continuity of the present work and potential topics for future research are the following:

- Extensive experimental program for damage models validation and parameters determination. An important effort should be devoted in the development of a methodology for identification of material parameters to be used in such models, throughout inverse techniques and minimization procedures to fully characterize the developed models and determine forming limit behaviour for different materials;

- Enhancement of local continuum theories by adopting scalar and high order regularization formulations. This is an ongoing research work that is being carried out within the group the author is involved with. However, a high order gradient non-local model for the anisotropic damage model is still needed to overcome its pathological effect of discretization dependence in size and orientation;

- Development and application of more advanced friction models (with possible introduction of dissipative and damaging behaviour), to improve contact-friction modelling and treatment;

- Fully thermo-mechanical analysis of forming operations and extension of the constitutive models by using more advanced plasticity models and including strain rate sensitivity and temperature dependency parameters towards the increase of accuracy in failure and necking predictions.

NOTATION, NOMENCLATURE AND ABBREVIATIONS

List of symbols

$\boldsymbol{0}$	- Second order null tensor
A	- Cross-sectional area
A_0	- Initial cross-sectional area
A_D	- Total area of defects in A
$\tilde{A}$	- Effective (resistant) cross-sectional area
$\boldsymbol{A}$	- Generic set of thermodynamical forces
$\mathcal{B}$	- Generic body
$\partial\mathcal{B}$	- Boundary of $\mathcal{B}$
$\boldsymbol{C}$	- Right Cauchy-Green strain tensor
C, ε_0, n	- Swift law parameters (isotropic hardening)
$\boldsymbol{d}$	- Rate of deformation tensor
$\boldsymbol{d}^e$	- Elastic rate of deformation tensor
$\boldsymbol{d}^e$	- Plastic rate of deformation tensor
D	- Scalar damage
D_C	- Critical damage value
D_H	- Hydrostatic damage
$\bar{D}$	- Non-local damage variable
$\boldsymbol{D}$	- Second order damage tensor
D_1, D_2, D_3	- Principal damage values
e	- Specific internal energy
E	- Young modulus
$\tilde{E}$	- Effective Young modulus
$\boldsymbol{\mathsf{E}}$	- Linear elasticity tensor
$\tilde{\boldsymbol{\mathsf{E}}}$	- Effective linear elasticity tensor

f_0	- Imperfection factor (M-K model)
F	- Generic uniaxial force
$\boldsymbol{f}$	- Body force vector field
$\boldsymbol{F}$	- Deformation gradient
$\boldsymbol{F}^e$	- Elastic deformation gradient
$\boldsymbol{F}^p$	- Plastic deformation gradient
$F ,G ,H ,L\ M ,N$	- Hill48 criterion anisotropic parameters
G	- Shear modulus or modulus of rigidity
$\boldsymbol{g}$	- Temperature gradient
h_C	- Micro-crack closure parameter
H'	- Hardening modulus
$\boldsymbol{H}$	- Second order damage effect tensor
$\boldsymbol{I}$	- Second order identity tensor
$\boldsymbol{\mathsf{I}}$	- Fourth order identity tensor
I_1, I_2, I_3	- First, second and third invariant of Cauchy stress tensor $\boldsymbol{\sigma}$
J	- Jacobian of the deformation map
$\boldsymbol{J}$	- Jacobian matrix
J_1, J_2, J_3	- First, second and third invariant of deviatoric stress tensor $\boldsymbol{s}$
k	- Risk factor (MMFC model)
K , n	- Power law parameters (isotropic hardening)
l	- Length scale value, Generic length
$\boldsymbol{l}$	- Velocity gradient tensor
$\boldsymbol{l}^e$	- Elastic velocity gradient tensor
$\boldsymbol{l}^p$	- Elastic velocity gradient tensor
$\boldsymbol{\mathsf{L}}$	- Fourth order damage effect tensor
$\boldsymbol{M}$	- Consistent mass matrix
$\boldsymbol{\mathsf{M}}$	- Hill'48 criterion fourth order operator
$\boldsymbol{n}$	- Generic normal vector
$\boldsymbol{N}$	- Plastic flow vector
$\tilde{\boldsymbol{N}}$	- Effective plastic flow vector
p	- Pressure
$\boldsymbol{p}$	- Generic material point
$\boldsymbol{P}$	- First Piola-Kirchhoff stress tensor
$\boldsymbol{q}$	- Heat flux vector field
$\boldsymbol{Q}$	- Generic orthogonal or rotation tensor
$\boldsymbol{\mathsf{Q}}$	- Fourth order tensor operator (anisotropic damage model)
r	- Density of heat production; isotropic hardening internal variable
R	- Isotropic hardening associated variable
$\tilde{R}$	- Effective isotropic hardening associated variable
$\boldsymbol{R}$	- Rotation tensor obtained from the polar decomposition of $\boldsymbol{F}$

r_0, r_{45}, r_{90}	- Lankford anisotropic coefficients
R_{sat}, C_R	- Voce law parameters (isotropic hardening)
s	- Exponent parameter from Lemaitre's damage evolution law; entropy
S	- Denominator parameter from Lemaitre's damage evolution law
$\boldsymbol{s}$	- Deviatoric stress tensor
$\boldsymbol{S}$	- Second Piola-Kirchhoff stress tensor
$\mathcal{S}$	- Generic surface
t	- Generic time (instant), Generic thickness
T	- Temperature
T_X	- Stress triaxiality
$\boldsymbol{t}$	- Surface traction
$\boldsymbol{v}$	- Velocity field
$\boldsymbol{u}$	- Displacement vector field
$\boldsymbol{U}$	- Right stretch tensor
$\mathcal{U}$	- Space of vectors in the three-dimensional Euclidean space
$\boldsymbol{v}$	- Velocity field
$\boldsymbol{V}$	- Left stretch tensor
$\boldsymbol{V}^e$	- Elastic left stretch tensor
$\boldsymbol{V}^p$	- Plastic left stretch tensor
$\mathcal{V}$	- Space of virtual displacements
W^p	- Plastic Work
W^e	- Elastic Work
w	- Generic width
$\boldsymbol{w}$	- Continuum spin or vorticity tensor
$\boldsymbol{x}$	- Generic point in space
$\boldsymbol{X}$	- Back stress tensor
$\tilde{\boldsymbol{X}}$	- Effective back stress tensor
Y	- Strain energy release rate
$\bar{Y}$	- Effective elastic energy density
$\boldsymbol{Y}$	- Elastic energy density tensor
Z	- Necking parameter
α	- Stress ratio
$\boldsymbol{\alpha}$	- Generic set of internal state variables
β	- Strain ratio
$\boldsymbol{\beta}$	- Back-strain tensor
δ	- Infinitesimal operator for iterative variations
Δ	- Finite operator for incremental variations
ε	- Uniaxial strain
$\bar{\varepsilon}^p$	- Equivalent plastic strain
ε_D^p	- Damage threshold accumulated plastic strain

$\boldsymbol{\varepsilon}$	- Generic strain tensor
$\boldsymbol{\varepsilon}^e$	- Elastic strain tensor
$\boldsymbol{\varepsilon}^p$	- Plastic strain tensor
$\varepsilon_1^p, \varepsilon_2^p, \varepsilon_3^p$	- Principal strain values of plastic strain tensor
$\boldsymbol{\varphi}$	- Deformation map
Φ	- Yield function
γ	- Consistence parameter; plastic multiplier
η	- Hydrostatic sensitivity damage parameter
$\boldsymbol{\eta}$	- Virtual displacement field
λ, μ	- Lamé coefficients
μ	- Friction coefficient
ν	- Poisson ratio
θ	- Temperature, Rotation angle (MMFC)
ρ	- Density
σ	- Uniaxial stress
$\tilde{\sigma}$	- Uniaxial effective stress
$\bar{\sigma}$	- Equivalent stress
$\tilde{\bar{\sigma}}$	- Effective equivalent stress
σ^*	- Damage equivalent stress
σ_H	- Hydrostatic stress
σ_{Y0}	- Initial yield stress
σ_Y	- Yield stress
$\sigma_1, \sigma_2, \sigma_3$	- Principal stress values of Cauchy stress tensor
$\tilde{\sigma}_1, \tilde{\sigma}_2, \tilde{\sigma}_3$	- Principal stress values of effective stress tensor
$\boldsymbol{\sigma}$	- Cauchy stress tensor
$\tilde{\boldsymbol{\sigma}}$	- Effective stress tensor
$\boldsymbol{\sigma}^+, \boldsymbol{\sigma}^-$	- Positive and negative components of stress tensor $\boldsymbol{\sigma}$
$\boldsymbol{\tau}$	- Kirchhoff stress tensor
ω	- Material integrity
$\boldsymbol{\Omega}$	- Angular velocity tensor
Ξ	- Dissipation potential
ψ	- Helmholtz specific free energy, band orientation (M-K model)
ψ^{ed}	- Elastic-damage component of Helmholtz specific free energy
ψ^p	- Plastic component of Helmholtz specific free energy
ψ_0	- Initial band orientation (M-K model)
Ψ	- Dissipation potential
Ψ^d	- Damage dissipation potential
Ψ^p	- Plastic dissipation potential

List of abbreviations

3DS	- Acronym of “Digital Die Design System”
AA	- Aluminium Alloy
AD	- Anisotropic Damage model
AHSS	- Advanced High Strength Steel
BS	- Equibiaxial Stretching strain path
BS+UT	- Bilinear strain path evolution composed by Equibiaxial Stretching followed by Uniaxial Tension
CAD	- Computer-Aided Design
CAE	- Computer-Aided Engineering
CAM	- Computer-Aided Manufacturing
CDM	- Continuous Damage Mechanics
DOF	- Numerical model Degrees Of Freedom
DP	- Dual Phase steel
eMMFC	- Enhanced Modified Maximum Force Criterion
EMFC	- Extended Maximum Force Criterion
FEM	- Finite Element Method
FFLC	- Fracture Forming Limit Curve
FFLD	- Fracture Forming Limit Diagram
FLC	- Forming Limit Curve
FLD	- Forming Limit Diagram
FLD-T	- Temperature dependent Forming Limit Diagram
GTN	- Gurson-Tvergaard-Needleman damage model
Hill48	- Hill 1948 yield criterion
Hill79	- Hill 1979 yield criterion
Hill93	- Hill 1993 yield criterion
HSS	- Conventional High Strength Steel
IBVP	- Initial Boundary Value Problem
ID	- Isotropic Damage model
J-G	- Jones-Gillis theory
LHS	- Left Hand Side of Forming Limit Diagram (drawing zone)
LSP	- Linear Strain Path
MFC	- Maximum Force Criterion
M-K	- Marciniak- Kuczynski model
MMFC	- Modified Maximum Force Criterion
MMFC+AD	- Modified Maximum Force Criterion with Anisotropic Damage consideration
MS	- Martensitic Steel
PS	- Plane Strain strain path
RD/TD/ND	- Rolling, Transverse Direction and Normal Direction to sheet metal plane
RHS	- Right Hand Side of Forming Limit Diagram (stretching zone)
TRIP	- Transformation Induced Plasticity steel

TTIC - Through Thickness Shear Instability Criterion
UT - Uniaxial Tension strain path
UT+BS - Bilinear strain path evolution composed by Uniaxial Tension followed by Equibiaxial Stretching
VDIF - Vacuum Degassed Interstitial Free steel
Yld96 - Barlat 96 yield criterion

LIST OF FIGURES

Figure 1.1 Deep drawing process. 2

Figure 1.2 Different types of steels and their mechanical characteristics: Advanced high strength steels (AHSS) compared to mild steels (MS) and low-resistance and conventional high-strength steels (HSS). 5

Figure 1.3 Localized necking prior to the rupture in a DP600 steel (left) and fracture without any visible necking in a DP980 steel (right) [Shi 2006]. 6

Figure 2.1 Configurations of a deformable body. 10

Figure 2.2 Schematic representation of the polar decomposition theorem. 11

Figure 2.3 Schematic representation of the multiplicative decomposition theorem. 14

Figure 2.4 Surface forces. The Cauchy stress. 16

Figure 3.1 Central difference scheme. 35

Figure 4.1 Schematic of ductile damage evolution. 47

Figure 4.2 Damaged representative volume element. 48

Figure 4.3 Uniaxial elastic model with damage and partial crack closure effect. 72

Figure 5.1 Damage of a bar under uniaxial tension; a) Initial undeformed and undamaged state; b) Current damaged state; c) Equivalent (fictitious) undamaged state. 83

Figure 5.2 Definition of a tridimensional damage state; a) Initial undamaged configuration; b) Current damaged configuration; c) Equivalent (fictitious) undamaged configuration. 84

Figure 5.3 Interpretation of damage tensor; a) Current damaged configuration; b) Equivalent (fictitious) undamaged configuration. 86

Figure 5.4 Influence of damage denominator parameter on stress and hydrostatic damage evolutions. 103

Figure 5.5 Influence of damage exponent parameter on stress and hydrostatic damage evolutions. 103

Figure 5.6 Influence of damage hydrostatic parameter on stress and hydrostatic damage evolutions. 104

Figure 5.7 Influence of damage hydrostatic parameter on Poisson ratio and Young modulus evolutions. 104

Figure 5.8 Influence of stress triaxiality on stress and hydrostatic damage evolutions. 105

Figure 5.9 Stress-strain curves for different hardening coefficients and hardening exponents. 106

Figure 5.10 Influence of hardening strength on stress and hydrostatic damage evolutions. 106
Figure 5.11 Influence of hardening exponent on stress and hydrostatic damage evolutions. 107
Figure 5.12 Influence of normal anisotropy on damage evolutions under uniaxial tension. 108
Figure 6.1 Uniaxial true stress – true strain curves of AA 5182-O. 112
Figure 6.2 Sheet tensile test specimen dimensions (in mm). 118
Figure 6.3 Adopted numerical mesh for tensile test. 119
Figure 6.4 Evolution of stress triaxiality. 119
Figure 6.5 Tensile test damage contour. 120
Figure 6.6 Tensile test equivalent plastic strain contour. 120
Figure 6.7 Stress-strain curves for tensile test. 120
Figure 6.8 Engineering stress- strain curve. 121
Figure 6.9 Tensile test equivalent stress contour (coupled analysis). 121
Figure 6.10 Tensile equivalent stress contour (uncoupled analysis). 121
Figure 6.11 Stress-strain curves for isotropic and anisotropic damage models. 123
Figure 6.12 Bulge test dimensions (in mm). 124
Figure 6.13 Adopted numerical mesh for bulge test. 124
Figure 6.14 Bulge test equivalent plastic strain contour (isotropic damage model) 126
Figure 6.15 Bulge test damage contour (isotropic damage model). 126
Figure 6.16 Bulge test stress triaxiality contour (isotropic damage model). 126
Figure 6.17 Bulge test equivalent stress contour (isotropic damage model). 127
Figure 6.18 Damage evolution comparison between tensile and bulge tests (isotropic damage model). 127
Figure 6.19 Bulge test equivalent plastic strain contour (anisotropic damage model). 128
Figure 6.20 Bulge test damage contour (anisotropic damage model). 129
Figure 6.21 Bulge test damage evolution comparison between isotropic and anisotropic damage models. 129
Figure 6.22 Experimental part without rupture (left) and failed part (right) (AA 5182-O, initial blank holder force 300kN). 130
Figure 6.23 U shape geometry experimental and numerical shapes (initial blank holder force 90 kN). 132
Figure 6.24 U shape geometry experimental and numerical profiles (initial blank holder force 90 kN). 132
Figure 6.25 U shape geometry equivalent plastic strain contour (initial blank holder force 90 kN). 133
Figure 6.26 U shape geometry stress contour (initial blank holder force 90 kN). 133
Figure 6.27 U shape geometry stress contour (initial blank holder force 300 kN). 134
Figure 6.28 U shape geometry equivalent plastic strain contour (initial blank holder force 300 kN). 134
Figure 6.29 U shape geometry damage contour (initial blank holder force 300 kN). 135
Figure 6.30 Influence of friction coefficient in predicted punch displacement to failure. 136
Figure 6.31 Experimental part with 152 kN holding force (left) and failed part with a holding force of 200 kN (right), AA5182-O. 137

Figure 6.32 Adopted numerical mesh for warping geometry. 138
Figure 6.33 Warping geometry experimental and numerical shapes (initial blank holder force 90 kN). 138
Figure 6.34 Warping geometry experimental and numerical longitudinal profiles (initial blank holder force 90 kN). 139
Figure 6.35 Warping geometry damage contour (initial blank holder force 90 kN). 139
Figure 6.36 Warping geometry equivalent plastic strain contour (initial blank holder force 90 kN). 139
Figure 6.37 Strain path evolution of critical element. 140
Figure 6.38 Warping geometry numerical and experimental crack evolution. 141
Figure 6.39 Axisymmetric cup tool geometry (in mm). 142
Figure 6.40 Experimental geometry: fully drawn and failure. 142
Figure 6.41 Adopted mesh for axisymmetric cup. 143
Figure 6.42 Axisymmetric cup equivalent plastic strain contour (high lubrication condition). . 145
Figure 6.43 Thickness and equivalent plastic strain vs. initial distance from cup center for rolling direction section (high lubrication condition). 145
Figure 6.44 Axisymmetric cup damage contours (high lubrication condition) 146
Figure 6.45 Damage vs. initial distance from cup center for rolling direction section (high lubrication condition). 147
Figure 6.46 Axisymmetric cup equivalent plastic strain contours (low lubrication condition). . 148
Figure 6.47 Thickness and equivalent plastic strain vs. initial distance from cup center for rolling direction section (low lubrication condition). 148
Figure 6.48 Axisymmetric cup damage contours (low lubrication condition). 149
Figure 6.49 Damage vs. initial distance from cup center for rolling direction section (low lubrication condition). 149
Figure 6.50 Axisymmetric cup major principal stress component (low lubrication condition). . 150
Figure 6.51 Axisymmetric cup middle principal stress component (low lubrication condition). 150
Figure 6.52 Axisymmetric cup minor principal stress component (low lubrication condition). . 150
Figure 6.53 Influence of friction coefficient in predicted punch displacement to failure. 151
Figure 6.54 Cross shape geometry tool and part dimensions (in mm). 152
Figure 6.55 Experimental failures: corner-cut of 85 mm and 105 mm. 153
Figure 6.56 Adopted numerical mesh for cross shape geometry. 153
Figure 6.57 Influence of friction coefficient in predicted critical punch displacement (corner-cuts 85 mm and 105 mm). 155
Figure 6.58 Cross shape geometry damage contours prior to failure for different friction coefficient values (corner-cut 85mm, isotropic damage model). 155
Figure 6.59 Cross shape geometry damage contours prior to failure for different friction coefficient values (corner-cut 105 mm, isotropic damage model). 156
Figure 6.60 Cross shape geometry stress triaxiality ratio contours prior to failure for different friction coefficient values (corner-cut 105 mm, isotropic damage model). 157
Figure 6.61 Cross shape geometry equivalent plastic strain contours prior to failure for

different friction coefficient values (corner-cut 105 mm, isotropic damage model). 157
Figure 6.62 Draw-in evolution for different friction coefficients (corner-cut 105 mm, isotropic damage model)......158
Figure 6.63 Influence of corner-cut length in predicted critical punch displacement (friction coefficient 0.10). 159
Figure 6.64 Cross shape geometry damage contours prior to failure for different corner-cut lengths (friction coefficient 0.1, isotropic damage model)......159
Figure 6.65 Mesh dependence in the cross shape geometry. 161
Figure 7.1 A high strength steel with a large number of inclusions can have a FFLD which will intersect the FLD [Keeler 1989]. 165
Figure 7.2 Fracture and local necking strains in aluminium alloy 5154-O. Under equibiaxial stretching, failure occurs by fracture before local necking [LeRoy 1978]. 165
Figure 7.3 Local neck formed in a continuous sheet oriented at an angle θ to the maximum principal stress. 167
Figure 7.4 Sheet element subjected to a biaxial stretching loading. 170
Figure 7.5 Hill's and Swift's forming limit curves. 172
Figure 7.6 Schematic representation of M-K analysis [Marciniak 1967]......172
Figure 7.7 Additional hardening effect through change in deformation state. 176
Figure 7.8 Comparison between experimental and theoretical FLDs for AA 6014. 189
Figure 7.9 Comparison between experimental and theoretical FLDs for AA 6014. 190
Figure 7.10 Additional hardening promoted by the introduction of anisotropic damage model into the MMFC criterion. 190
Figure 7.11 Critical damage values for necking. Damage value in thickness direction reaches more important values on the right hand side of the FLD. 191
Figure 7.12 Experimental procedure and samples involved in determination of bilinear strain paths limits: uniaxial tension + equibiaxial stretching (UT-BS) and equibiaxial stretching + uniaxial tension (BS-UT)......193
Figure 7.13 Theoretical FLDs for biaxial stretching followed by uniaxial tension (BS-UT) (AA 6014). 194
Figure 7.14 Risk factor evolution for a biaxial stretching followed by uniaxial tension strain path (prestrain of 0.32)......195
Figure 7.15 Theoretical FLDs for uniaxial tension followed by biaxial stretching (UT-BS) (AA 6014). 196
Figure 7.16 Theoretical FFLDs for linear strain paths and for uniaxial tension followed by biaxial stretching (UT-BS) strain paths using MMFC+AD (AA 6014)......197
Figure 7.17 Damage evolution comparison between plane strain trajectory (PS) and bilinear strain path (UT-BS). 197

LIST OF TABLES

Table 1.1 Typical forming defects classification. 5
Table 4.1 State variables for isotropic damage theory. 54
Table 5.1 State variables for anisotropic damage theory. 87
Table 5.2 Initial material properties. 102
Table 6.1 Material parameters of AA 5182-O. 112
Table 6.2 Mechanical characteristics of AA 5182-O. 116
Table 6.3 Isotropic damage model parameters for AA 5182-O. 117
Table 6.4 Tensile test numerical conditions. 118
Table 6.5 Anisotropic damage model parameters for AA 5182-O. 124
Table 6.6 Bulge test numerical conditions. 125
Table 6.7 U shape geometry numerical conditions. 131
Table 6.8 Warping geometry numerical conditions. 138
Table 6.9 Axisymmetric cup numerical conditions. 143
Table 6.10 Cross shape geometry numerical conditions. 154
Table 7.1 Material parameters of AA 6014. 188

LIST OF BOXES

Box 3.1 Dynamic Explicit (DE) solution strategy..37
Box 3.2 Objective Green-Nagdhi stress update procedure. 41
Box 4.1 Lemaitre's ductile isotropic damage model with anisotropic flow...................................63
Box 4.2 State update procedure for fully coupled Lemaitre's ductile isotropic damage model. ...68
Box 4.3 Newton-Raphson algorithm for return mapping system of equations for integration of fully coupled Lemaitre's ductile isotropic damage model. 69
Box 4.4 State update procedure for partially coupled Lemaitre's ductile isotropic damage model. 78
Box 5.1 Lemaitre's ductile anisotropic damage model with anisotropic flow. 93
Box 5.2 State update procedure for fully coupled Lemaitre's ductile anisotropic damage model. 100
Box 5.3 Newton-Raphson algorithm for return mapping system of equations for integration of fully coupled Lemaitre's ductile anisotropic damage model. 101

REFERENCES

ABAQUS (2008). ABAQUS Theory Manual. Providence, USA, Dassault Systèmes Simulia Corp.

Ajmar, A., M. Bertero and D. Conte (2001). Definition of forming defects. Digital Die Design Systems (3DS) Project, Work Package 1, Task 2 Report.

Al-Rub, R. K. A. (2004). Material length scales in gradient-dependent plasticity / damage and size effects: theory and computation. Department of Civil & Environmental Engineering. Lousiana, Louisiana State University. **Ph.D.**

Al-Rub, R. K. A. and G. Z. Voyiadjis (2003). "On the coupling of anisotropic damage and plasticity models for ductile materials " International Journal of Solids and Structures **40**(11): 2611-2643.

Alves, J. L. C. M. (2003). Simulação numérica do processo de estampagem de chapas metálicas: modelação mecânica e métodos numéricos. Departamento de Engenharia Mecânica. Guimarães, Escola de Engenharia, Universidade do Minho. **Ph.D.**

Aretz, H. (2004). "Numerical restrictions of the modified maximum force criterion for prediction of forming limits in sheet metal forming." Modelling and Simulation in Materials Science and Engineering **12**(4): 677-692.

Atkins, A. G. (1996). "Fracture in forming." Journal of Materials Processing Technology **56**(1-4): 609-618.

Bai, Y. and T. Wierzbicki (2008). "Forming severity concept for predicting sheet necking under complex loading histories " International Journal of Mechanical Sciences **50**(6): 1012-1022

Banabic, D. (1996). Forming Limit Diagrams predicted by using the new Hill's yield criterion. Proceedings of NUMISHEET '96 - 3rd International Conference and Workshop on Numerical Simulation of 3D Sheet Forming Processes. J. K. Lee, G. L. Kinzel and R. H. Wagoner. Dearbon, USA, The Ohio State University**:** 240-245.

Banabic, D., H. J. Bunge, K. Pohlandt and A. E. Tekkaya (2000). Formability of metallic materials: plastic anisotropy, formability testing and forming limits. Berlin, Germany, Springer-Verlag.

Banabic, D., L. Paraianu, G. Dragos, I. Bichis and D. S. Comsa (2009). An improved version of the Modified Maximum Force Criterion (MMFC) used for predicting the localized necking in sheet metals. Proceedings of the Romanian Academy, Series A, The Publishing House of The Romanian Academy. **10**.

Barata da Rocha, A. (1989). Theoretical forming limit diagrams of anisotropic sheets - Linear and nonlinear strain paths. Forming limit diagrams: Concepts, methods, and applications. R. H. Wagoner, K. S. Chan and S. P. Keeler, TMS press**:** 183–202.

Barata da Rocha, A., F. Barlat and J. M. Jalinier (1985). "Prediction of the forming limit diagrams of anisotropic sheets in linear and non-linear loading." Materials Science and Engineering **68**(2): 151-164.

Barata da Rocha, A., A. D. Santos, P. Teixeira and M. C. Butuc (2009). "Analysis of plastic flow localization under strain paths changes and its coupling with finite element simulation in sheet metal forming." Journal of Materials Processing Technology **2009**(11): 5097-5109.

Barlat, F. (1987). "Crystallographic texture, anisotropic yield surfaces and forming limits of sheet metals." Materials Science & Engineering **91**(C): 55-72.

Barlat, F. (1989b). Forming limit diagrams-predictions based on some microstructural aspects of materials. Forming Limit Diagrams: Concepts, Methods, and Applications. R. H. Wagoner, K. S. Chan and S. P. Keeler, TMS press**:** 275-301.

Barlat, F., H. Aretz, J. W. Yoon, M. E. Karabin, J. C. Brem and R. E. Dick (2005). "Linear transformation-based anisotropic yield functions." International Journal of Plasticity **21**(5): 1009–1039.

Barlat, F., D. J. Lege and J. C. Brem (1991). "A six-component yield function for anisotropic materials." International Journal of Plasticity **7**(7): 693-712.

Barlat, F., Y. Maeda, K. Chung, M. Yanagawa, J. C. Brem, Y. Hayashida, D. J. Lege, K. Matsui, S. J. Murtha, S. Hattori, R. C. Becker and S. Makosey (1997b). "Yield function development for aluminum alloy sheets." Journal of the Mechanics and Physics of Solids **45**(11-12): 1727-1763.

Bassani, J. L., J. W. Hutchinson and K. W. Neale (1979). On the prediction of necking in anisotropic sheets. Metal forming plasticity. H. Lippmann. Berlin, Springer**:** 1-13.

Bazant, Z. P. and M. Jirasek (2002). "Nonlocal integral formulations of plasticity and damage: Survey of progress." Journal of Engineering Mechanics **128**(11): 1119–1149.

Belytschko, T., W. K. Liu and B. Moran (2000). Nonlinear finite elements for continua and structures. West Sussex, England, John Wiley & Sons Ltd.

Benallal, A., R. Billardon and I. Doghri (1988). "An integration algorithm and the corresponding consistent tangent operator for fully coupled elastoplastic and damage equations." Communications in Applied Numerical Methods **4**(6): 731-640.

Benallal, A. and C. Comi (1996). "Localization analysis via a geometrical method." International Journal of Solids and Structures **33**(1): 99-119.

Bontcheva, N. (1994). "Plastic localization in anisotropically hardening damaged materials." European Journal of Mechanics. A. Solids **13**(6): 751-763.

Boudeau, N. and J.-C. Gelin (2000). "Necking in sheet metal forming. Influence of macroscopic and microscopic properties of materials." International Journal of Mechanical Sciences **42**(11): 2209-2232.

Bressan, J. D. and J. A. Williams (1983). "The use of a shear instability criterion to predict local necking in sheet metal deformation." International Journal of Mechanical Sciences **25**(3): 155-168.

Brunet, M. and P. Clerc (2007). Predictions of necking with analytical criteria and comparisons with experimental results. Proceedings of NUMIFORM'07, Materials Processing and Design:Modelling, Simulation and Applications. J. M. A. César de Sá and A. D. Santos. Porto, Portugal, American Institute of Physics. **908:** 81-86.

Brunet, M., S. Mguil and F. Morestin (1998). "Analytical and experimental studies of necking in sheet metal forming processes." Journal of Materials Processing Technology **80-81**(1): 40-46.

Brunet, M. and F. Morestin (2001). "Experimental and analytical necking studies of anisotropic sheet metals." Journal of Materials Processing Technology **112**(2-3): 214-226.

Brunig, M. (2003). "An anisotropic ductile damage model based on irreversible thermodynamics." International Journal of Plasticity **19**(10): 1679–1713.

Butuc, M. C. (2004). Forming limit diagrams: definition of plastic instability criteria. Departamento de Engenharia Mecânica e Gestão Industrial. Porto, Faculdade de Engenharia, Universidade do Porto. **Ph.D.**

Butuc, M. C., J. J. Gracio and A. Barata da Rocha (2003). "A theoretical study on forming limit diagrams prediction " Journal of Materials Processing Technology **142**(3): 714-724.

Butuc, M. C., A. B. d. Rocha, J. J. Grácio and J. F. Duarte (2002). "A more general model for Forming Limit Diagrams prediction." Journal of Materials Processing Technology **125-126**: 213-218.

Cazacu, O., B. Plunkett and F. Barlat (2006). "Orthotropic yield criterion for hexagonal closed packed metals." International Journal of Plasticity **22**(7): 1171–1194.

César de Sá, J. M. A., P. M. A. Areias and C. Zheng (2006). "Damage modelling in metal forming problems using an implicit non-local gradient model." Computer Methods in Applied Mechanics and Engineering **195**(48-49): 6646-6660.

Chaboche, J. L. (1988a). "Continuum Damage Mechanics: Part I—General concepts." Journal of Applied Mechanics, Transactions of the ASME **55**(1): 59-64.

Chaboche, J. L. (1988b). "Continuum Damage Mechanics: Part II—Damage growth, crack initiation, and crack growth." Journal of Applied Mechanics, Transactions of the ASME **55**(1): 65-72.

Chaboche, J. L. (2007). Damage mechanics. Comprehensive Structural Integraty. I. Milne, R. O. Ritchie and B. Karihaloo, Elsevier Science Ltd. **2:** 213-284.

Chen, Z. and X. Dong (2009). "The GTN damage model based on Hill'48 anisotropic yield criterion and its application in sheet metal forming." Computational Materials Science **44**(3): 1013–1021.

Choi, W., P. P. Gillis and S. E. Jones (1989). Forming Limit diagrams. Forming Limit Diagrams: Concepts, Methods, and Applications. R. H. Wagoner, K. S. Chan and S. P. Keeler, TMS press**:** 215-237.

Chow, C. L. and M. Jie (2004). "Forming limits of Al6022 sheets with material damage consideration - theory and experimental validation." International Journal of Mechanical Sciences **46**(1): 99-122.

Chow, C. L. and M. Jie (2009). "Anisotropic damage-coupled sheet metal forming limit analysis." International Journal of Damage Mechanics **18**(4): 371-392.

Chow, C. L., M. Jie and S. J. Hu (2003). "Forming limit analysis of sheet metals based on a generalized deformation theory." Journal of Engineering Materials and Technology, Transactions of the ASME **125**(3): 260-265.

Chow, C. L., M. Jie and X. Wu (2005). "Localized necking criterion for strain-softening materials." Journal of Engineering Materials and Technology, Transactions of the ASME **127**(3): 273-278.

Chow, C. L., M. Jie and X. Wu (2007). "A damage-coupled criterion of localized necking based on acoustic tensor." International Journal of Damage Mechanics **16**(3): 265-281.

Chow, C. L. and J. Wang (1987). "An anisotropic theory of elasticity for continuum damage mechanics." International Journal of Fracture **33**(1): 3-16.

Chow, C. L., X. J. Yang and E. Chu (2001a). "Viscoplastic constitutive modeling of anisotropic damage under nonproportional loading." Journal of Engineering Materials and Technology, Transactions of the ASME **123**(4): 403-408.

Chow, C. L., L. G. Yu and M. Y. Demeri (1997). "A unified damage approach for predicting forming limit diagrams." Journal of Engineering Materials and Technology, Transactions of the ASME **119**(4): 346-353.

Chow, C. L., L. G. Yu, W. H. Tai and M. Y. Demeri (2001b). "Prediction of forming limit diagrams for AL6111-T4 under non-proportional loading." International Journal of Mechanical Sciences **43**(2): 471-486.

Chu, C. C. and A. Needleman (1980). "Void nucleation effects in biaxially stretched sheets." Journal of Engineering Materials and Technology, Transactions of the ASME **102**(3): 249-256.

Cocks, A. C. F. and M. F. Ashby (1982). "On creep fracture by void growth " Progress in Materials Science **27**(3-4): 189-244.

Col, A. (2002). Presentation of the “3DS” research project. Proceedings of NUMISHEET 2002 - 5th International Conference and Workshop on Numerical Simulation of 3D Sheet Forming Processes. D.-Y. Yang, S. I. Oh, H. Huh and Y. Hwan. Jeju Island, Korea. **1:** 643–647.

Col, A. (2006). Summary report on the FLC'06 Conference, ETH Zürich.

Considère, A. (1885). "Use of the iron and steel in buildings." Annales des Ponts et Chaussées **9**: 547–575.

Cordebois, J. P. and F. Sideroff (1982). "Anisotropic damage in elasticity and plasticity." Journal De Mecanique Theorique Et Appliquee **Special Edition**: 45-60.

Desmorat, R. and S. Cantournet (2008). "Modelling microdefects closure effect with isotropic/anisotropic damage." International Journal of Damage Mechanics **17**(1): 65-96.

Desmorat, R. and S. Otin (2008a). "Cross-identification isotropic/anisotropic damage and application to anisothermal structural failure." Engineering Fracture Mechanics **75**(11): 3446-3463.

DIN EN 10002 (2001). Metallic materials – Tensile testing. Part 1: Method of test at ambient temperature.

Doege, E., T. El-Dsoki and D. Seibert (1995). "Prediction of necking and wrinkling in sheet-metal forming." Journal of Materials Processing Technology **50**(1-4): 197-206.

Doghri, I. (2000). Mechanics of deformable solids: Linear, nonlinear, analytical and computational aspects. Berlin, Germany, Springer-Verlag.

Doghri, I. and R. Billardon (1995). "Investigation of localization due to damage in elasto-plastic materials." Mechanics of Materials **19**(2-3): 129-149.

Duarte, J. F., F. Simões, P. Teixeira and A. Santos (2002). Experimental Benchmark # 7 - Cylindrical Cup – Earing. Digital Die Design Systems (3DS) Project, Work Package 2, Internal Report Porto, INEGI.

Dudzinski, D. and A. Molinari (1991). "Perturbation analysis of thermoviscoplastic instabilities in biaxial loading." International Journal of Solids and Structures **27**(5): 601-628.

Dunne, F. and N. Petrinic (2005). Introduction to computational plasticity. Oxford, UK, Oxford University Press.

Ekh, M. and K. Runesson (2000). "Bifurcation results for plasticity coupled to damage with MCR-effect." International Journal of Solids and Structures **37**(14): 1975-1996.

Gasser, A., P. Ladeveze and P. Peres (1998). "Damage modelling for a laminated ceramic composite." Materials Science and Engineering A **250**(2): 249-255.

Germain, P., Q. S. Nguyen and P. Suquet (1983). "Continuum thermodynamics." Journal of Applied Mechanics, Transactions of the ASME **50**(4b): 1010-1020.

Goodwin, G. M. (1968). Application of strain analysis to sheet metal forming problems in the press shop. Society of Automotive Engineers**:** Technical paper no. 680093.

Gotoh, M. (1985). "A class of plastic constitutive equation with vertex effect-III. Applications to calculation of FLD of metal sheets." International Journal of Solids and Structures **21**(11): 1131-1145.

Gotoh, M., T. Chung and N. Iwata (1995). "Effect of out-of-plane stress on the forming limit strain of sheet metals." JSME International Journal, Series A: Mechanics and Material Engineering **38**(1): 123-132.

Gurson, A. L. (1977). "Continuum theory of ductile rupture by void nucleation and growth: Part 1 - Yield criteria and flow rules for porous ductile media." Journal of Engineering Materials and Technology, Transactions of the ASME **99 Ser H**(1): 2-15.

Haddag, B., F. Abed-Meraim and T. Balan (2009). "Strain localization analysis using a large deformation anisotropic elastic–plastic model coupled with damage." International Journal of Plasticity **25**(10): 1970-1996.

Hill, R. (1948). "A theory of the yielding and plastic flow of anisotropic metals." Proceedings of the Royal Society of London. Series A, Mathematical and Physical Sciences **193**(1033): 281-297.

Hill, R. (1952). "On discontinuous plastic states, with special reference to localized necking in thin sheets." Journal of the Mechanics and Physics of Solids **1**(1): 19-30.

Hill, R. (1979). "Theoretical plasticity of textured aggregates." Mathematical Proceedings of the Cambridge Philosophical Society **85**(1): 179-191.

Hill, R. (1990). "Constitutive modelling of orthotropic plasticity in sheet metals." Journal of the Mechanics and Physics of Solids **38**(3): 405-417.

Hill, R. (1993). "A user-friendly theory of orthotropic plasticity in sheet metals." International Journal of Mechanical Sciences **35**(1): 19-25.

Hiwatashi, S., A. V. Bael, P. V. Houtte and C. Teodosiu (1998). "Prediction of forming limit strains under strain path changes: Application of an anisotropic model based on texture and dislocation structure." International Journal of Plasticity **14**(7): 647-669.

Hora, P., M. Merklein, L. Tong and J. Lechler (2007). Numerical and experimental evaluation of thermal dependent FLC (FLC-T). Proceedings of IDDRG'07 - International Deep Drawing Research Group Conference. M. Tisza. Gyor, Hungary, University of Miskolc**:** 23-30.

Hora, P., L. Tong and J. Reissner (1996). A prediction method for ductile sheet metal failure in FE simulation. Proceedings of NUMISHEET '96 - 3rd International Conference and Workshop on Numerical Simulation of 3D Sheet Forming Processes. J. K. Lee, G. L. Kinzel and R. H. Wagoner. Dearbon, USA, The Ohio State University**:** 252-256.

Houtte, P. V., A. V. Bael and J. Winters (1995). "The incorporation of texture-based yield loci into elasto-plastic finite element programs." Textures and Microstructures **24**(4): 255-272.

Hu, J., J. J. Jonas, Y. Zhou and T. Ishikawa (1998). "Influence of damage and texture evolution on limit strain in biaxially stretched aluminum alloy sheets." Materials Science and Engineering A **251**(1-2): 243-250.

Huang, H.-M., J. Pan and S. C. Tang (2000). "Failure prediction in anisotropic sheet metals under forming operations with consideration of rotating principal stretch directions." International Journal of Plasticity **16**(6): 611-633.

Hutchinson, J. W. and K. W. Neale (1978b). "Sheet necking II. Time- independent bahaviour." Mechanics of sheet metal forming, Plenum press New York – London: 127-153.

Hutchinson, J. W., K. W. Neale and A. Needleman (1978a). "Sheet necking I. Validity of the plane stress assumptions of the long-wavelenght approximation." Mechanics of sheet metal forming, Plenum press New York – London: 111-126.

IISI (2006). Advanced high strength steel (AHSS) application guidelines, International Iron & Steel Institute - Committee on Automotive Applications.

Jalinier, J. M. and J. H. Schmitt (1982). "Damage in sheet metal forming - II. Plastic instability." Acta Metallurgica **30**(9): 1799-1809.

Jones, S. E. and P. P. Gillis (1984). "An analysis of biaxial stretching of a flat sheet." Metallurgical Transactions A **15A**: 133-138.

Ju, J. W. (1989). "On energy-based coupled elastoplastic damage theories: constitutive modeling and computational aspects." International Journal of Solids and Structures **25**(7): 803–833.

Kachanov, L. M. (1958). "On the creep fracture time." Izv Akad, Nauk USSR Otd, Tekh. **8**(26-31).

Kazama, K. and N. Mori (2001). Report on experimental conditions for benchmarks. Digital Die Design Systems (3DS) Project, Work Package 2, Internal Report.

Keeler, S. P. (1989). Stamping and formability: Automotive sheet metal stamping and formability. Washington, USA, Automotive Applications Committee, American Iron and Steel Institute.

Keeler, S. P. and W. A. Backofen (1963). "Plastic Instability and fracture in sheets streched over rigid punches." Transactions of American Society for Metals **56**: 25-48.

Kestin, J. and J. Bataille (1977). Irreversible thermodynamics of continua and internal variables. Proceedings of the International Symposyum on Continuum Models of Discrete Systems, University of Waterloo Press**:** 39–67.

Khelifa, M., M. Oudjene and A. Khennane (2007). "Fracture in sheet metal forming: Effect of ductile damage evolution." Computers & Structures **85**(3-4): 205–212.

Klerck, P. A. (2000). The finite element modelling of discrete fracture in quasi-brittle materials. Swansea, School of Engineering, University of Wales. **Ph.D.**

Korhonen, A. S. (1978). "On the theories of sheet metal necking and forming limits." Journal of Engineering Materials and Technology, Transactions of the ASME **100**(3): 303-309.

Krajcinovic, D. (1983). "Constitutive equations for damaging materials." Journal of Applied Mechanics, Transactions of the ASME **50**(2): 355–360.

Krajcinovic, D. and G. U. Fonseka (1981). "The continuous damage theory of brittle materials, Part 1: General theory." Journal of Applied Mechanics, Transactions of the ASME **48**(4): 809-815.

Krauer, J., P. Hora, L. Tong and B. Berisha (2007). Forming limit prediction of metastable materials with temperature and strain induced martensite transformation. Proceedings of NUMIFORM'07, Materials Processing and Design: Modelling, Simulation and Applications. J. M. A. César de Sá and A. D. Santos. Porto, Portugal, American Institute of Physics. **908:** 1263-1268.

Ladevèze, P. and J. Lemaitre (1984). Damage effective stress in quasi unilateral conditions. Proceedings of the 16th International Congress of Theoretical and Applied Mechanics. Lyngby, Denmark.

Lange, K. (1985). Handbook of Metal Forming, Mcgraw-Hill.

Leckie, F. A. and D. R. Hayhurst (1974). "Creep rupture of structures." Proceedings of the Royal Society of London. Series A, Mathematical and Physical Sciences **340**: 323-347.

Lee, S. H. and S. Kobayashi (1975). Effects of strain paths on the stretching limit strains of sheet metal with planar anisotropy. Proceedings of the Third North American Metal Working Research Conference**:** 277-290.

Lee, W. B., W. H. Tai and C. Y. Tang (1997). "Damage evolution and forming limit predictions of an Al2024-T3 aluminium alloy." Journal of Materials Processing Technology **63**(1-3): 100-104.

Lee, Y.-W. and T. Wierzbicki (2005). "Fracture prediction of thin plates under localized impulsive loading. Part II: Discing and petalling." International Journal of Impact Engineering **30**(10): 1277-1308.

Lemaitre, J. (1984). "How to use damage mechanics." Nuclear Engineering and Design **80**(2): 233-245.

Lemaitre, J. (1985a). "Continuous damage mechanics model for ductile fracture." Journal of Engineering Materials and Technology, Transactions of the ASME **107**(1): 83-89.

Lemaitre, J. (1985b). "Coupled elasto-plasticity and damage constitutive equations." Computer Methods in Applied Mechanics and Engineering **51**(1-3): 31-49.

Lemaitre, J. (1996). A course on damage mechanics. Berlin, Germany, Springer-Verlag

Lemaitre, J., A. Benallal, R. Billardon and D. Marquis (2000b). Thermodynamics and phenomenology. Continuum thermomechanics: the art and science of modelling material behaviour. P. Germain, G. A. Maugin, R. Drouot and F. Sidoroff. Dordrecht, The Netherlands, Kluwer Academic Publishers**:** 209-223.

Lemaitre, J. and J.-L. Chaboche (1978). "Aspect phénoménologie de la rupture par endommagement." Journal Mécanique Appliquée **2**(3): 317-365.

Lemaitre, J. and J.-L. Chaboche (1990). Mechanics of solid materials. Cambridge, UK, Cambridge University Press.

Lemaitre, J., J.-L. Chaboche and B. Shrivastava (1994). Mechanics of solid materials. Cambridge, UK, Cambridge University Press.

Lemaitre, J. and R. Desmorat (2005). Engineering damage mechanics: ductile, creep, fatigue and brittle failures Amsterdam, The Netherlands, Springer-Verlag.

Lemaitre, J., R. Desmorat and M. Sauzay (1998). Some considerations about anisotropic damage. NTNU Workshop on Transient Loading and Response of Structures.

Lemaitre, J., R. Desmorat and M. Sauzay (2000a). "Anisotropic damage law of evolution." European Journal of Mechanics. A. Solids **19**(2): 187-208.

Lemaitre, J. and J. Dufailly (1987). "Damage measurements." Engineering Fracture Mechanics **28**(5-6): 643-661.

Lemaitre, J., J. P. Sermage and R. Desmorat (1999). "A two scale damage concept applied to fatigue." International Journal of Fracture **97**(1-4): 67-81.

LeRoy, G. H. and J. D. Embury (1978). The utilization of failure maps to compare the fracture modes occurring in aluminum alloys. Formability, analysis, modeling, and experimentation. S. S. Hecker, A. K. Ghosh and H. L. Gegel. New York, Metallurgical Society of AIME**:** 183-207.

LPMTM (2001). Selection and identification of elastoplastic models for the materials used in the benchmarks. Digital Die Design Systems (3DS) Project, Work Package 3, Task1, 18-Month Progress Report. Paris, University Paris 13.

Lubarda, V. A. and D. Krajcinovic (1995). "Constitutive structure of rate theory of damage in brittle elastic solids." Applied Mathematics and Computation **67**(1-3): 81-101.

Makinouchi, A. (2001). Recent developments in sheet metal forming simulation. Simulation of Materials Processing: Theory, Methods and Applications. K.-i. Mori, A.A. Balkema**:** 3-10.

Marciniak, Z., J. L. Duncan and S. J. Hu (2002). Mechanics of sheet metal forming. UK, Butterworth-Heinemann.

Marciniak, Z. and K. Kuczyński (1967). "Limit strains in the processes of stretch-forming sheet metal." International Journal of Mechanical Sciences **9**(9): 609-620.

Marciniak, Z., K. Kuczyński and T. Pokora (1973). "Influence of the plastic properties of a material on the forming limit diagram for sheet metal in tension " International Journal of Mechanical Sciences **15**(10): 789-800.

Mattiasson, K., M. Sigvant and M. Larsson (2006). Methods for forming limit prediction in ductile metal sheets. Proceedings of IDDRG'06 - International Deep Drawing Research Group Conference. A. D. Santos and A. Barata da Rocha. Porto, Portugal**:** 1-10.

Mattiasson, K., M. Sigvant and M. Larsson (2007). On the prediction of plastic instability in metal sheets. Proceedings of NUMIFORM'07, Materials Processing and Design:Modelling, Simulation and Applications. J. M. A. César de Sá and A. D. Santos. Porto, Portugal, American Institute of Physics. **908:** 129-134.

Mattiasson, K., M. Sigvant and M. Larsson (2008). "Issues in connection to the prediction of strain localization in metal sheets." International Journal of Material Forming **1**(Supplement 1): 245–248.

Mediavilla, J., R. H. J. Peerlings and M. G. D. Geers (2006). "A nonlocal triaxiality-dependent ductile damage model for finite strain plasticity." Computer Methods in Applied Mechanics and Engineering **195**(33-36): 4617-4634.

Mesrar, R., S. Fromentin, R. Makkouk, M. Martiny and G. Ferron (1998). "Limits to the ductility of metal sheets subjected to complex strain-paths." International Journal of Plasticity **14**(4-5): 391-411.

Mkaddem, A., F. Gassara and R. Hambli (2006). "A new procedure using the microhardness technique for sheet material damage characterisation." Journal of Materials Processing Technology **178**(1-3): 111–118.

Murakami, S. (1988). "Mechanical modeling of material damage." Journal of Applied Mechanics, Transactions of the ASME **55**(2): 280-286.

Murakami, S. and K. Kamiya (1997). "Constitutive and damage evolution equations of elastic-brittle materials based on irreversible thermodynamics " International Journal of Mechanical Sciences **39**(4): 473-486.

Murakami, S. and N. Ohno (1981). A continuum theory of creep and creep damage. Proceedings of 3rd IUTAM Symposium on Creep in Structures. A. R. S. Ponter and D. R. Hayhurst. Leicester, England, Springer-Verlag**:** 422–444.

Needleman, A. and N. Triandafyllidis (1978). "Void growth and local necking in biaxially stretched sheets." Journal of Engineering Materials and Technology, Transactions of the ASME **100**: 164-169.

Oliveira, M. C. C. d. (2005). Algoritmos e estratégias de gestão do problema de contacto com atrito em grandes deformações. Aplicação à estampagem de chapas metálicas. Departamento de Engenharia Mecânica, Faculdade de Ciências e Tecnologia da Universidade de Coimbra. **Ph.D.**

Ortiz, M. (1985). "A constitutive theory for inelastic behaviour of concrete." Mechanics of Materials **4**: 67-93.

Parmar, A. and P. B. Mellor (1978). "Predictions of limit strains in sheet metal using a more general yield criterion." International Journal of Mechanical Sciences **20**(6): 385-391.

Peerlings, R. H. J., R. De Borst, W. A. M. Brekelmans and J. H. P. De Vree (1996). "Gradient enhanced damage for quasi-brittle materials." International Journal for Numerical Methods in Engineering **39**(19): 3391-3403.

Pickett, A. K., T. Pyttel, F. Payen, F. Lauro, N. Petrinic, H. Werner and J. Christlein (2004). "Failure prediction for advanced crashworthiness of transportation vehicles " International Journal of Impact Engineering **30**(7): 853-872.

Pinto, M., A. D. Santos, P. Teixeira and P. J. Bolt (2008). "Study on the usability and robustness of polymer and wood materials for tooling in sheet metal forming." Journal of Materials Processing Technology **202**(1-3): 47-53.

Pires, F. M. A. (2001). Modelação por elementos finitos da iniciação da fractura dúctil nos processos de enformação plástica em massa. Departamento de Engenharia Mecânica e Gestão Industrial. Porto, Faculdade de Engenharia, Universidade do Porto. **M.Sc.**

Pires, F. M. A. (2005). Issues on the finite element modelling of degradation and prediction of failure in finitely straining ductile materials. Swansea, School of Engineering, University of Wales. **Ph.D.**

Pires, F. M. A., J. M. A. César de Sá, L. Costa Sousa and R. M. Natal Jorge (2003). "Numerical modelling of ductile plastic damage in bulk metal forming." International Journal of Mechanical Sciences **45**(2): 273–294.

Plunkett, B., O. Cazacu and F. Barlat (2008). "Orthotropic yield criteria for description of the anisotropy in tension and compression of sheet metals." International Journal of Plasticity **24**(5): 847–866.

Rabotnov, Y. N. (1963). On the equations of state for creep. Progress in Applied Mechanics, Prager Anniversary Volume. New York, MacMillan**:** 307-315.

Rizzi, E., I. Carol and L. Willam (1995). "Localization analysis of elastic degradation with application to scalar damage." Journal of Engineering Mechanics **121**(4): 541-554.

Roll, K. (2008). Simulation of sheet metal forming – necessary developments in the future. Proceedings of NUMISHEET 2008 - 7th International Conference and Workshop on

Numerical Simulation of 3D Sheet Forming Processes. P. Hora. Interlaken, Switzerland**:** 3-11.

Roll, K. and M. Rohleder (2002). Complex testing tool for the investigation of springback deviations. Proceedings of NUMISHEET 2002 - 5th International Conference and Workshop on Numerical Simulation of 3D Sheet Forming Processes. D. Y. Yang, S. I. Oh, H. Huh and Y. H. Kim. Jeju Island, Korea**:** 131-136.

Rudnicki, J. W. and J. R. Rice (1975). "Conditions for the localization of deformation in pressure-sensitive dilatant materials." Journal of the Mechanics and Physics of Solids **23**(6): 371-394.

Saanouni, K. and H. Badreddine (2006). Damage prediction in sheet metal forming: Theory, numerics and application. Proceedings of IDDRG'06 - International Deep Drawing Research Group Conference. A. D. Santos and A. Barata da Rocha. Porto, Portugal**:** 43-50.

Saanouni, K. and J. L. Chaboche (2007). Computational damage mechanics: Application to metal forming simulation. Comprehensive Structural Integraty. I. Milne, R. O. Ritchie and B. Karihaloo, Elsevier Science Ltd. **2:** 321-376.

Saanouni, K., K. Nesnas and Y. Hammi (2000). "Damage modeling in metal forming processes." International Journal of Damage Mechanics **9**(3): 196-240.

Santos, A. D. and P. Teixeira (2008). "A study on experimental benchmarks and simulation results in sheet metal forming." Journal of Materials Processing Technology **199**(1-3): 327-336.

Santos, A. D. d. (1993). Tool descriptions and contact strategies in static explicit finite element method for simulation of 3-D sheet metal forming processes. Department of Mechanical Engineering. Tokyo, University of Tokyo. **Ph.D.**

Schreyer, H. L. and M. K. Neilsen (1996). "Discontinuous bifurcation states for associated smooth plasticity and damage with isotropic elasticity." International Journal of Solids and Structures **33**(20-22): 3239-3256.

Shi, M. F. and S. Gelisse (2006). Issues on the AHSS forming limit determination. Proceedings of IDDRG'06 - International Deep Drawing Research Group Conference. A. B. d. R. Abel D. Santos. Porto, Portugal**:** 19-26.

Simo, J. C. and T. J. R. Hughes (1998). Computational inelasticity. New York, USA, Springer-Verlag.

Simo, J. C. and T. R. J. Hughes (1987). General return mapping algorithms for rate-independent plasticity. Constitutive Laws for Engineering Materials: Theory and Applications. C. S. Desai, Elsevier**:** 221-231.

Souza Neto, E. A. (2002). "A fast, one-equation integration algorithm for the Lemaitre ductile damage model." Communications in Numerical Methods in Engineering **18**(8): 541–554.

Souza Neto, E. A., D. Peric and D. R. J. Owen (1998). "Continuum modelling and numerical simulation of material damage at finite strains." Archives of Computational Methods in Engineering **5**(4): 311-384.

Souza Neto, E. A. d., D. Peric and D. R. J. Owen (1994). "Model for elastoplastic damage at finite strains: Algorithmic issues and applications." Engineering Computations **11**(3): 257-281.

Souza Neto, E. A. d., D. Peric and D. R. J. Owen (2008). Computational methods for plasticity: theory and applications. West Sussex, UK, John Wiley & Sons Ltd.

Sowerby, R. and J. L. Duncan (1971). "Failure in sheet metal in biaxial tension." International Journal of Mechanical Sciences **13**(3): 217-229.

Stören, S. and J. R. Rice (1975). "Localized necking in thin sheets." Journal of the Mechanics and Physics of Solids **23**(6): 421-441.

Stoughton, T. B. and X. Zhu (2004). "Review of theoretical models of the strain-based FLD and their relevance to the stress-based FLD." International Journal of Plasticity **20**(8-9): 705-731.

Swift, W. (1952). "Plastic instability under plane stress." Journal of the Mechanics and Physics of Solids **1**(1): 1-18.

Tadros, A. K. and P. B. Mellor (1975). "Some comments on the limit strains in sheet metal stretching." International Journal of Mechanical Sciences **17**(3): 203-210.

Tai, W. H. (1988). "A damage mechanics model for anisotropic material and its application to sheet metal forming." International Journal of Solids and Structures **24**(10): 1045-1057.

Tang, C. Y. and W. H. Tai (2000). "Material damage and forming limits of textured sheet metals." Journal of Materials Processing Technology **99**(1-3): 135-140.

Tasan, C. C., J. P. M. Hoefnagels and M. G. D. Geers (2009). "A critical assessment of indentation-based ductile damage quantification." Acta Materialia **57**(17): 4957-4966.

Teixeira, P., A. D. Santos, F. M. Andrade Pires and J. M. A. César de Sá (2006). "Finite element prediction of ductile fracture in sheet metal forming processes." Journal of Materials Processing Technology **177**(1-3): 278-281.

Teodosiu, C. and Z. Hu (1995). Evolution of the intragranular microstructure at moderate and large strains: modeling and computational significance. Proceedings of NUMIFORM'95, Simulation of Materials Processing: Theory, Methods and Applications. S. Shan-Fu and P. R. Dawson. Ithaca, New York, USA, Balkema**:** 173–182.

Tjotta, S. (1992). Formability and the growth of damage. Numerical Methods in Industrial Forming Processes. J.-L. Chenot, R. D. Woods and O. C. Zienkiewicz, A.A. Balkema**:** 187–192.

Tong, L., P. Hora and J. Reissner (2002). Prediction of forming limit with non-linear deformation paths using modified maximum force criterion. Proceedings of NUMISHEET 2002 - 5th International Conference and Workshop on Numerical Simulation of 3D Sheet Forming Processes. D. Y. Yang, S. I. Oh, H. Huh and Y. H. Kim. Jeju Island, Korea**:** 623-627.

Truesdell, C. (1969). Rational thermodynamics. New York, USA, McGraw-Hill.

Tvergaard, V. (1978). "Effect of kinematic hardening on localized necking in biaxially stretched sheets." International Journal of Mechanical Sciences **20**(9): 651-658.

Tvergaard, V. (1982). "Material failure by void coalescence in localized shear bands." International Journal of Solids and Structures **18**(8): 659-672.

Tvergaard, V. and A. Needleman (1984). "Analysis of the cup-cone fracture in a round tensile bar." Acta Metallurgica **32**(1): 157-169.

von Mises, R. (1913). "Mechanik der festen korper im plastisch deformablen zustand." Nachrichten von der Gesellschaft der Wissenschaften zu Göttingen, Mathematisch-Physikalische Klasse **1**: 582-592.

Voyiadjis, G. Z. and P. I. Kattan (2005). Damage mechanics. Boca Raton, USA, CRC Press, Taylor and Francis Group.

Voyiadjis, G. Z. and P. I. Kattan (2009). "A comparative study of damage variables in continuum damage mechanics." International Journal of Damage Mechanics **18**(4): 315-340.

Wouters, P., D. Daniel and C. Magny (2002). Selection and identification of friction models for the 3DS materials—Identification of the friction behaviour. Digital Die Design Systems (3DS) Project, Work Package 3, Deliverable 3b.

Wu, J.-Y. and J. Li (2008). "On the mathematical and thermodynamical descriptions of strain equivalence based anisotropic damage model." Mechanics of Materials **40**(4-5): 377-400.

Yang, D. Y., D. G. Ahn, C. H. Lee, C. H. Park and T. J. Kim (2002). "Integration of CAD/CAM/CAE/RP for the development of metal forming process." Journal of Materials Processing Technology **125-126**: 26-34.

Zhu, X., K. Weinmann and A. Chandra (2001). "A unified bifurcation analysis of sheet metal forming limits." Journal of Engineering Materials and Technology, Transactions of the ASME **123**(3): 329-333.

Zhu, Y. Y. and S. Cescotto (1995). "A fully coupled elasto-visco-plastic damage theory for anisotropic materials." International Journal of Solids and Structures **32**(11): 1607-1641.

Zienkiewicz, O. C. and R. L. Taylor (2000a). The finite element method. Volume 1: The basis, Butterworth-Heinemann.